



HAL
open science

Measurements of the Higgs boson mass and width in the four-lepton final state and electron reconstruction in the CMS experiment at the LHC

Mykhailo Dalchenko

► **To cite this version:**

Mykhailo Dalchenko. Measurements of the Higgs boson mass and width in the four-lepton final state and electron reconstruction in the CMS experiment at the LHC. High Energy Physics - Experiment [hep-ex]. Ecole Doctorale Polytechnique, 2014. English. NNT: . tel-01115325

HAL Id: tel-01115325

<https://pastel.hal.science/tel-01115325>

Submitted on 10 Feb 2015

HAL is a multi-disciplinary open access archive for the deposit and dissemination of scientific research documents, whether they are published or not. The documents may come from teaching and research institutions in France or abroad, or from public or private research centers.

L'archive ouverte pluridisciplinaire **HAL**, est destinée au dépôt et à la diffusion de documents scientifiques de niveau recherche, publiés ou non, émanant des établissements d'enseignement et de recherche français ou étrangers, des laboratoires publics ou privés.



Measurements of the Higgs boson mass and width in the four-lepton final state and electron recon- struction in the CMS experiment at the LHC

THÈSE

présentée pour obtenir le grade de Docteur en Sciences
de l'École Doctorale de l'École polytechnique (EDX)

par

Mykhailo Dalchenko

soutenue le 25 Septembre 2014 à l'École polytechnique
devant le jury composé de:

M. Jean-Claude Brient, président du jury

M. Marco Pieri, rapporteur

M. Reisaburo Tanaka, rapporteur

M. Fabrizio Caola, examinateur

Mme Stéphanie Baffioni, directrice de thèse

M. Claude Charlot, directeur de thèse

Palaiseau, France, 2014

Abstract

This thesis document reports measurements of the mass and width of the new boson recently discovered at the Large Hadron Collider (LHC), candidating to be the Standard Model Higgs boson. The analysis uses proton-proton collision data recorded by the Compact Muon Solenoid (CMS) detector at the LHC, corresponding to integrated luminosities of 5.1 fb^{-1} at 7 TeV center of mass energy and 19.7 fb^{-1} at 8 TeV center of mass energy. Set of events selecting Higgs boson via the $H \rightarrow ZZ$ decay channel, where both Z bosons decay to electron or muon lepton pairs, is used for the Higgs boson properties measurements. A precise measurement of its mass has been performed and gives $125.6 \pm 0.4(\text{stat}) \pm 0.2(\text{syst}) \text{ GeV}$. Constraints on the Higgs boson width were established using its off-shell production and decay to a pair of Z bosons, where one Z boson decays to an electron or muon pair, and the other to an electron, muon, or neutrino pair. The obtained result is an upper limit on the Higgs boson width of 22 MeV at a 95% confidence level, which is 5.4 times the expected value in the standard model at the measured mass. Throughout the thesis, a particular attention has been put on the electron momentum estimation. The combination of the momentum estimate with the tracker and the energy measurement with the electromagnetic calorimeter, allowing a significant improvement of the low transverse impulsion electrons measurement of the momentum, has been revisited and played an essential role in the Higgs boson discovery in the 4 leptons decay channel. The electron energy scale and resolution have been measured with very high precision using the Z boson decaying in electrons.

Résumé

Ce document de thèse traite de la mesure de la masse et de la largeur du nouveau boson découvert récemment au Large Hadron Collider (LHC), candidat pour être le boson de Higgs du modèle standard. L'analyse utilise les collisions protons-protons enregistrées par le détecteur Compact Muon Solenoid (CMS) au LHC, correspondant à des luminosités intégrées de 5.1 fb^{-1} à 7 TeV d'énergie dans le centre de masse et de 19.7 fb^{-1} à 8 TeV d'énergie dans le centre de masse. Les événements sélectionnant le boson de Higgs via sa désintégration en ZZ, ou les bosons Z se désintègrent en paires d'électrons ou de muons, ont été exploités pour la mesure des propriétés du boson de Higgs. Une mesure précise de la masse a été effectuée et vaut $125.6 \pm 0.4(\text{stat}) \pm 0.2(\text{syst}) \text{ GeV}$. Des contraintes sur la largeur du boson de Higgs ont été établies en utilisant sa production hors-masse et sa désintégration en une paire de bosons Z, ou un des Z se désintègre en paire d'électrons ou de muons, et l'autre en une paire d'électrons, de muons ou de neutrinos. Le résultat obtenu est une limite supérieure sur la largeur du boson de Higgs à 22 MeV à 95% de niveau de confiance, ce qui correspond à 5.4 fois la valeur attendue pour le modèle standard à la masse mesurée. Une attention particulière a été apportée à l'estimation de l'impulsion des électrons. La combinaison de l'estimation de l'impulsion par le trajectomètre et la mesure de l'énergie déposée dans le calorimètre électromagnétique, permettant une amélioration significative de la mesure de l'impulsion des électrons de basse impulsion transverse, a été ré-optimisée et a joué un rôle essentiel dans la découverte du boson Higgs dans le canal en quatre leptons. L'échelle d'énergie ainsi que la résolution en énergie des électrons a été mesurée avec une grande précision en utilisant les bosons de Z se désintégrant en électrons.

Acknowledgements

The three years I have spent in the Laboratoire Leprince-Ringuet were full of fun, meetings with very interesting people and super nice discussions. I would like to express now my deepest gratitude to all who was next to me during this long survey.

Thank you Claude and Stephanie for a limitless patience and attention you gave me. I appreciate very much a huge job you did to give me an opportunity to achieve such interesting results and to integrate them into the workflow of the Higgs analysis working group. I smile when I remember the ping-pong, pizza in Le Casanova or owl finalization of the talk on Higgs width at 1 am followed by ride from CERN to the hotel in a completely freezed car. Thank you for all this, you are more then just thesis supervisors for me.

I would like also to thank all the collective of the laboratory. First of all to the lab director, Jean-Claude Brient: thanks for leading and maintaining so nice and efficient collective. Then to my officemates: Christophe, Roberto, Nadir, JB, sometimes Alex. It was a pleasure to share office with you, guys. Thanks for useful tips, discussions, jokes, for some italian words (Roberto, I can better understand now some of my italian colleagues). Thanks to Yves, Philippe, Florian Pascal and Ludwik. The discussions with you helped me a lot to masterize the topic and improve the results. Thanks as well to the IT crew of the laboratory: David, Andrea, Pascale, Igor. My results would take ages without your help in the grid usage. Thanks to administration and director, for the support you provided me in a battle with burocracy. Thank you Ivo and Yacine for coffee breaks and especially for the support during thesis writing and defence preparation. You know very well what I mean. Thank you all the youngsters: Roko, Marko, Luca M., Luca C., Iurii, Stas, Kostya, Philipp, Alex T., Simon.

I would like also to express my deepest gratitude to the members of my thesis jury: Marco Pieri, Reisaburo Tanaka and Fabricio Caola. Your remarks on the manuscript helped me a lot as well as your questions and discussions.

A special thanks I want express to my friends who live at Ecole Polytechnique campus: poker, volleyball and borsch - everything was great, thank you guys!

And the final words I leave for my parents. I can't really express how I'm grateful to them. Their support during all my study and thesis writing was infinite. Thank you billion times!

Contents

Introduction	1
1 The Hitchhiker's Guide to the Particle Physics	3
1.1 The Standard Model of elementary particles	3
1.1.1 The Electroweak Theory	5
1.1.2 The Brout-Englert-Higgs Mechanism	8
1.1.3 Vector Boson Masses and Couplings	10
1.1.4 Fermion Masses and Couplings	11
1.1.5 The Higgs Boson Mass	12
1.2 The Higgs Boson Search at the LHC	15
1.2.1 The Higgs Boson Production	15
1.2.2 The Higgs Boson Decay	17
2 Experimental Setup	21
2.1 The Large Hadron Collider	21
2.1.1 Performance Goals	21
2.1.2 Nominal Center-of-mass Energy and Magnet Systems	24
2.1.3 Nominal Luminosity and Beam Parameters	24
2.1.4 Lattice Layout	25
2.1.5 The LHC Collision Detectors	25
2.1.6 Operation from 2010 to 2012	27
2.2 The Compact Muon Solenoid	28
2.2.1 The Coordinate System	30
2.2.2 The Magnet	32
2.2.3 The Inner Tracking System	32
2.2.4 The Electromagnetic Calorimeter	36
2.2.5 The Hadron Calorimeter	42
2.2.6 The Muon System	44
2.2.7 The Trigger System	46
2.2.8 Leptons And Photons Signatures In CMS	48
3 Electron Measurements At CMS	51
3.1 Measurement of the electron energy in the ECAL	52
3.2 Electron track reconstruction	53

Contents

3.2.1	Seeding	54
3.2.2	Track parameters estimation	55
3.3	Electron classification	56
3.4	Electron combination	64
3.5	Energy scale corrections	67
3.5.1	Energy scale corrections derivation	68
3.5.2	Energy scale corrections implementation	69
3.5.3	Energy scale corrections and resolution performance	70
4	Higgs Boson Search In The	
	$H \rightarrow ZZ^* \rightarrow 4\ell$ Channel and Its Mass Measurement	79
4.1	Data and Simulated Samples	80
4.1.1	Experimental data and online event selection	80
4.1.2	Simulated samples	81
4.2	Event Selection	82
4.2.1	Vertex Selection	82
4.2.2	Impact Parameter Selection	83
4.2.3	Lepton Isolation	83
4.2.4	Lepton Identification	83
4.2.5	Final State Radiation Recovery	84
4.2.6	Loose and Tight Lepton Selection	86
4.2.7	Best Candidate Selection	87
4.2.8	Selection Efficiency	87
4.3	Background Estimation	88
4.3.1	Irreducible Background	88
4.3.2	Reducible background	89
4.4	Systematic Uncertainties	92
4.5	Distribution Of Selected Events	93
4.6	The Higgs Boson Mass Measurements	96
4.6.1	Kinematical Discriminants	98
4.6.2	Per-event mass uncertainties	99
4.6.3	Signal Model	101
4.6.4	Results	104
5	The Higgs Boson Width Constraints From The Offshell Production	107
5.1	Off-shell Higgs Production	108
5.1.1	Gluon-induced Higgs boson production	109
5.1.2	$gg \rightarrow ZZ$ continuum production	111
5.1.3	Contributions of other production mechanisms	111
5.2	Analysis Strategy	112
5.3	Datasets	113
5.4	Signal and Background Cross-sections	116
5.4.1	Higher order corrections	117

5.4.2 Vector boson fusion samples	119
5.5 Backgrounds Estimation	119
5.6 Reweighting Procedure	120
5.7 First Preliminary Results on the Width Constraints	121
5.8 Matrix Element Likelihood Approach	122
5.9 2D Statistical Model	124
5.10 Systematic Uncertainties	125
5.11 Results	127
5.11.1 Combination with the $2\ell 2\nu$ analysis	128
5.11.2 Discussion and perspectives	129
Conclusion and Outlook	131
Appendix	134
References	151

Introduction

*I feel that matter has properties which
physics tells you*

G. Gamow

For decades, the main question engaging the High Energy Physics community has been the origin of the electroweak symmetry breaking (EWSB). One of the possible ways to introduce the EWSB is the Brought-Englert-Higgs (BEH) mechanism. It predicts the existence of a scalar boson (named the Higgs boson), but does not predict its mass. Besides, there are other theories which describe the EWSB in other ways. Some of them predict an extended Higgs sector (like the supersymmetry) and some do not include any Higgs field at all (like the technicolor). From the experimental side the main challenge has been the need to search for the Higgs boson (or another physics responsible for the EWSB) in a very large piece of the phase space with the ability to observe resonances at scales from hundreds GeV up to few TeV. The Large Hadron Collider (LHC) was designed to cover the above needs and opened a new era of experimental EWSB studies.

Like many, my choice of the PhD thesis topic has been inspired by the Higgs boson search. I have chosen the $H \rightarrow ZZ \rightarrow 4\ell$ decay channel. Besides the "physics analysis" part this thesis work also contains the "physics object reconstruction" part devoted to the electron momentum determination, which is related to the physics analysis part due to the presence of leptons in the chosen final state. The organisation of this document is near to exactly chronological. The first two chapters provide the playground to the study of the Higgs sector. The first chapter presents a theoretical overview of the Standard Model and the second describes the experimental setup: the Large Hadron Collider and the Compact Muon Solenoid experiment. The following three chapters are devoted to the physics analysis I participated in and to the results obtained.

At the beginning of this study (fall 2011) the LHC was already taking data at 7 TeV center-of-mass energy. The Higgs boson at that time was excluded in a large part of the phase space at the 95% confidence level. The remaining possible Higgs boson mass range was accessible mainly by $H \rightarrow ZZ \rightarrow 4\ell$ and $H \rightarrow \gamma\gamma$ decay modes. It was decided to start with the electron reconstruction because an optimal reconstruction of the final state is a key ingredient for the

Introduction

measurement of the Higgs properties and in particular of the Higgs mass. This part of the work is described in the chapter 3. When I was about to finish the "objects" part of my analysis, both multipurpose experiments at the LHC (ATLAS and CMS) reported about the observation of the new boson with a mass $m \simeq 125$ GeV candidating to be the Higgs boson. I concentrated then on the measurement of its properties. Following my expertise on the electron energy scale and resolution I joined the mass measurement of the new boson. An overview of the Higgs boson search in the four lepton final state and its mass measurements are presented in the chapter 4. An extremely good control of the lepton energy scale and resolution allows to measure the Higgs boson mass with a precision of few tenth of GeV. Another important characteristic of the Higgs boson is its decay width. Since the Higgs boson couples to all the massive particles, its total decay width is sensitive to an eventual physics beyond the Standard Model. The Standard Model predicts the Higgs width to be ~ 4 MeV for the $m_H \simeq 125$ GeV, which is about three orders of magnitude less than the experimental resolution. This makes impossible to put precise direct bounds on the resonance width. However a new possibility to constrain the Higgs boson width exploring its off-shell production was proposed. This study is presented in the chapter 5.

1 The Hitchhiker's Guide to the Particle Physics

The Standard Model of Elementary Particle Physics (SM) is one of the most successful theories in terms of predictive power. It describes the fundamental components of matter and how they interact. SM combines two complementary field theories: the theory of electroweak interactions (developed in the mid-60s by Weinberg, Glashow, and Salam) and the strong interactions theory (Quantum Chromodynamics or QCD). The gauge group of the Standard Model is $SU(3)_C \otimes SU(2)_L \otimes U(1)_Y$, where $SU(2)_L \otimes U(1)_Y$ is related to the couplings of the electroweak interaction, whilst $SU(3)_C$ is related to gauge couplings in quantum chromodynamics.

In this part, a short overview of the SM (Sec. 1.1) and of the electroweak theory (Sec. 1.1.1) is given, focusing on the ElectroWeak Symmetry Breaking (EWSB), the Brout-Englert-Higgs (BEH) mechanism and the Higgs boson (Sec. 1.1.2). Finally, in the next section the Higgs boson search at the Large Hadron Collider (LHC) and its properties determination are introduced.

Note that *natural units* are used, i.e. $\hbar = c = 1$, unless otherwise specified,

1.1 The Standard Model of elementary particles

The Standard Model of elementary particles as each modern theory should rely on one fundamental principle, so-called gauge invariance postulate. In order to introduce this postulate we need firstly to set the gauge transformation: any space-time transformation which doesn't change the action is called gauge transformation. For example, in case of electromagnetic field it is the gradient transformation:

$$A_\mu \rightarrow A_\mu + \partial_\mu \Lambda, \quad \Psi \rightarrow e^{ie\Lambda} \Psi, \quad \left(\partial_\mu = \frac{\partial}{\partial x^\mu} \right) \quad (1.1)$$

Now we can formulate the gauge invariance postulate: the physics (theory predictions) is invariant under the gauge transformations. This principle allows to prove that for each interaction the hamiltonian is uniquely determined. Before going further we should also mention a very important statement, the Noether theorem: for each continuous symmetry

there is an associated conserved current. Hence (accounting the gauge invariance postulate) the local (space-time dependent) symmetries determine the structure of all the fundamental interactions in nature. As it was just mentioned, the theory should be invariant under the local gauge transformations. But in general the quantum mechanics is invariant under the global gauge transformations (when the phase of transformation doesn't depend on x_μ) and not invariant under the local ones. However, we can restore the local gauge invariance by introducing an additional physical field which compensates the change in the Lagrange equation. The quanta of such fields are called the gauge bosons and are responsible for the mediation of the interaction between matter particles. On the other hand, the matter is described by the particles subjected to Fermi-Dirac statistics, i.e. fermions.

From all the elementary particles we can detach a special group of so-called fundamental particles which form all the known kinds of matter. There are 3 families of 4 fundamental particles, which have spin 1/2. Ordinary matter is composed only of the 1st family members, and other two families can be regarded as the replicas of the first one. The corresponding particles belonging to separate families are said to have different *flavours*, with the same coupling constants but with different masses. The fermions can be divided into two main groups, *leptons* and *quarks*. The corresponding classification is given in Table 1.1. Although anti-particles are not mentioned in this table, the same classification is applicable to them. Quarks are subject to both strong and electroweak interactions and do not exist as free states, but only as constituents of a wide class of particles, the *hadrons*, such as protons and neutrons. Leptons, instead, only interact by electromagnetic and weak forces.

Fermions	1st fam.	2nd fam.	3rd fam.	Charge	Interactions
Quarks	u	c	t	$+\frac{2}{3}$	all
	d	s	b	$-\frac{1}{3}$	
Leptons	e	μ	τ	-1	weak, electromagnetic
	ν_e	ν_μ	ν_τ	0	weak

Table 1.1 – Classification of the three families of the fundamental fermions.

The main characteristics of the bosons and corresponding interactions are summarised in Table 1.2 (the gravitational interaction is not taken into account, as it is not relevant at the scales of mass and distance typical of the particle physics).

As previously mentioned, the SM describes these interactions by means of two gauge theories: the Quantum Chromodynamics and the theory of the electroweak interaction (Glashow-Weinberg-Salam, or GWS model [1, 2, 3]), which unifies the electromagnetic and weak interactions. We describe in more details only the latter since the subject of the present work deals mostly with only electroweak processes.

1.1. The Standard Model of elementary particles

Quantum	Electromagnetic	Weak	Strong
	Photon (γ)	W^\pm, Z	Gluons
Mass [GeV]	0	80.4, 91.2	0
Coupling constant	$\alpha(Q^2 = 0) \approx \frac{1}{137}$	$G_F \approx 1.2 \cdot 10^{-5} \text{ GeV}^{-2}$	$\alpha_s(m_Z) \approx 0.1$
Range [cm]	∞	10^{-16}	10^{-13}

Table 1.2 – Fundamental interactions relevant in particle physics and corresponding carriers.

1.1.1 The Electroweak Theory

The gauge transformations form a Lie group - referred to as the symmetry (or the gauge) group of the theory. Each gauge field corresponds to the generator of this Lie group. The simplest example of the gauge group is $U(1)$ which determines the electromagnetic interaction.

The relativistic spin 1/2 fermion is described by a four component spinor Ψ via the Dirac equation

$$(i\gamma^\mu \partial_\mu - m)\Psi = 0, \quad (1.2)$$

where γ_μ are 4×4 Dirac matrices satisfying the Clifford algebra. This equation is not invariant under transformation 1.1 unless we replace the derivative with the covariant derivative

$$D_\mu \Psi \equiv (\partial_\mu + ieA_\mu)\Psi \Rightarrow (D_\mu \Psi)' = (\partial_\mu + ieA'_\mu)\Psi' = e^{ie\Lambda(x)} D_\mu \Psi \quad (1.3)$$

Therefore the Dirac equation in the electromagnetic field becomes

$$(i\gamma^\mu D_\mu - m)\Psi = (i\gamma^\mu \partial_\mu - e\gamma^\mu A_\mu - m)\Psi = 0, \quad (1.4)$$

Here the massless gauge boson called photon arises. Notice that if we try to introduce a mass term for it, the gauge invariance is broken. The Eq. 1.4 can be derived from the following lagrangian density:

$$\mathcal{L}_{QED} = \bar{\Psi}(i\gamma^\mu D_\mu - m)\Psi - \frac{1}{4}F_{\mu\nu}F^{\mu\nu} \quad (1.5)$$

The second Lagrange equation, complementary to the Eq. 1.4, is then

$$\partial^\mu F_{\mu\nu} = g\bar{\Psi}\gamma_\nu\Psi \equiv j_\nu, \quad (1.6)$$

where j_ν is the electromagnetic current of the charged fermion. From the Eq. 1.6 the charge conservation law can be derived.

$U(1)$ is a particular case of unitary abelian transformations. If the symmetry group is non-commutative, the gauge theory is referred to as non-abelian, the simplest case is $SU(2)$, proposed by Yang and Mills in 1954 [4]. The most usual representation of this group is a

doublet

$$\Psi = \begin{pmatrix} \Psi_1 \\ \Psi_2 \end{pmatrix}, \Psi' = U(\theta)\Psi, \text{ with } U(\theta) = e^{\frac{i}{2}g\theta_a\tau_a}, \quad (1.7)$$

where τ_a are the Pauli matrices and g is the $SU(2)$ gauge coupling. Then, three generators of $SU(2)$ form equal amount of gauge bosons W_μ^a . The most compact notation introduces a matrix

$$W_\mu = W_\mu^a \frac{\tau_a}{2} = \begin{pmatrix} W_\mu^3 & W_\mu^1 - iW_\mu^2 \\ W_\mu^1 + iW_\mu^2 & -W_\mu^3 \end{pmatrix} \equiv \begin{pmatrix} W_\mu^3 & \sqrt{2}W_\mu^+ \\ \sqrt{2}W_\mu^- & -W_\mu^3 \end{pmatrix}. \quad (1.8)$$

A theory reproducing both the electromagnetic and weak interaction phenomenology is achieved by unification of electromagnetic and Yang-Mills theories in form of the group $SU(2)_I \otimes U(1)_Y$. The generators of $SU(2)_I$ are the three components of the *weak isospin* operator, $t^a = \frac{1}{2}\tau^a$. The generator of $U(1)_Y$ is the *weak hypercharge* Y operator. The corresponding quantum numbers satisfy

$$Q = I_3 + \frac{Y}{2},$$

where I_3 is the third component of the weak isospin (eigenvalue of t^3).

The fermions can be divided in doublets of negative chirality (*left-handed*) particles and singlets of positive chirality (*right-handed*) particles, as follows:

$$L_L = \begin{pmatrix} \nu_{\ell,L} \\ \ell_L \end{pmatrix}, \quad \ell_R \quad Q_L = \begin{pmatrix} u_L \\ d_L \end{pmatrix}, \quad u_R, \quad d_R, \quad (1.9)$$

where $\ell = e, \mu, \tau$, $u = u, c, t$ and $d = d, s, b$.

In the Tab. 1.3, the I_3 , Y and Q quantum numbers of all fermions are reported.

	I_3	Y	Q
$\begin{pmatrix} u_L \\ d_L \end{pmatrix}$	$\begin{pmatrix} \frac{1}{2} \\ -\frac{1}{2} \end{pmatrix}$	$\begin{pmatrix} \frac{1}{3} \\ \frac{1}{3} \end{pmatrix}$	$\begin{pmatrix} \frac{2}{3} \\ -\frac{1}{3} \end{pmatrix}$
u_R, d_R	$0, 0$	$\frac{4}{3}, -\frac{2}{3}$	$\frac{2}{3}, -\frac{1}{3}$
$\begin{pmatrix} \nu_{\ell,L} \\ \ell_L \end{pmatrix}$	$\begin{pmatrix} \frac{1}{2} \\ -\frac{1}{2} \end{pmatrix}$	$\begin{pmatrix} -1 \\ -1 \end{pmatrix}$	$\begin{pmatrix} 0 \\ -1 \end{pmatrix}$
ℓ_R	0	-2	-1

Table 1.3 – Isospin (I_3), hypercharge (Y) and electric charge (Q) of the fermions in the 1st family. Other two families are exact replicas of the first one.

Again, imposing the requirement of the local gauge invariance with respect to the $SU(2)_I \otimes U(1)_Y$ group introduces four massless vector fields, $W_\mu^{1,2,3}$ and B_μ , which couple to the fermions with two different coupling constants, g and g' .

1.1. The Standard Model of elementary particles

However B_μ does not represent the photon field, because it arises from the $U(1)_Y$ group of hypercharge, instead of $U(1)_{EM}$ group of electric charge. The gauge invariant Lagrangian for the fermion fields can be written as follows:

$$\mathcal{L} = \bar{\Psi}_L \gamma^\mu \left(i\partial_\mu + g t_a W_\mu^a - \frac{1}{2} g' Y B_\mu \right) \Psi_L + \bar{\Psi}_R \gamma^\mu \left(i\partial_\mu - \frac{1}{2} g' Y B_\mu \right) \Psi_R, \quad (1.10)$$

where

$$\Psi_L = \begin{pmatrix} \psi_L^1 \\ \psi_L^2 \end{pmatrix}$$

and where Ψ_L and Ψ_R are summed over all the possibilities in Eq. 1.9.

Coming back to the compact representation introduced in Eq. 1.8 we get the charged physical fields

$$W_\mu^\pm = \sqrt{\frac{1}{2}} (W_\mu^1 \mp i W_\mu^2), \quad (1.11)$$

while the neutral bosons γ and Z correspond to

$$A_\mu = B_\mu \cos \theta_W + W_\mu^3 \sin \theta_W \quad (1.12)$$

$$Z_\mu = -B_\mu \sin \theta_W + W_\mu^3 \cos \theta_W, \quad (1.13)$$

obtained by mixing the neutral fields W_μ^3 and B_μ with a rotation defined by the *Weinberg angle* θ_W . In terms of the fields in Eqs. 1.11 and 1.13, the interaction term between the gauge fields and the fermions, taken from the Lagrangian in Eq. 1.10, becomes

$$\mathcal{L}_{int} = \frac{1}{2\sqrt{2}} g (J_\alpha^+ W^{(+)\alpha} + J_\alpha^- W^{(-)\alpha}) + \frac{1}{2} \sqrt{g'^2 + g^2} J_\alpha^Z Z^\alpha - e J_\alpha^{EM} A^\alpha, \quad (1.14)$$

where J^{EM} is the electromagnetic current, coupling to the photon field, while J^+ , J^- and J^Z are the three weak isospin currents. It is found that

$$J_\alpha^Z = J_\alpha^3 - 2 \sin^2 \theta_W \cdot J_\alpha^{EM}. \quad (1.15)$$

A_μ can then be identified with the photon field and, requiring the coupling terms to be equal, one obtains

$$g \sin \theta_W = g' \cos \theta_W = e \quad (1.16)$$

which represents the electroweak unification. The GWS model thus predicts the existence of two charged gauge fields, which only couple to left-handed fermions, and two neutral gauge fields, which interact with both left- and right-handed components.

1.1.2 The Brout-Englert-Higgs Mechanism

During the treatment of the electroweak unified theory we considered all the particles to be massless. However in order to correctly reproduce the observations we have to assign masses to the gauge bosons and fermions. Straightforward introduction of the explicit mass terms for the fermions would not violate the gauge invariance but the GWS model is also required to be invariant under the chiral transformations.

Following this we need to introduce some mechanism which break both $SU(2)_L$ and $U(1)_Y$ symmetries but stay invariant under the $U(1)_{EM}$ transformation group to keep the photon massless.

One of the many possible ways to introduce the spontaneous symmetry breaking is to add in the Lagrangian another scalar field. Masses are thus introduced with the so-called *Brout-Englert-Higgs (BEH) mechanism* [5, 6], which allows W^\pm, Z bosons and fermions to be massive¹, while keeping the photon massless.

Let us consider a doublet of complex scalar fields

$$\phi = \begin{pmatrix} \phi^+ \\ \phi^0 \end{pmatrix} = \frac{1}{\sqrt{2}} \begin{pmatrix} \phi^1 + i\phi^2 \\ \phi^3 + i\phi^4 \end{pmatrix}, \quad (1.17)$$

which is written in the form of the weak isospin doublet accordingly to Weinberg [2]. The additional term in the Lagrangian is therefore

$$\mathcal{L}_{EWSB} = (D^\mu \phi)^\dagger (D_\mu \phi) + V(\phi^\dagger \phi), \quad (1.18)$$

where $D_\mu = \partial_\mu - ig t_a W_\mu^a + \frac{i}{2} g' Y B_\mu$ denotes again the covariant derivative. The Lagrangian in Eq. 1.18 is invariant under the $SU(2)_I \otimes U(1)_Y$ transformations, since the kinetic part is written in terms of the covariant derivatives and the potential V only depends on the product $\phi^\dagger \phi$. The ϕ field is characterized by the following quantum numbers:

	\mathbf{I}_3	\mathbf{Y}	\mathbf{Q}
$\begin{pmatrix} \phi^+ \\ \phi^0 \end{pmatrix}$	$\begin{pmatrix} \frac{1}{2} \\ -\frac{1}{2} \end{pmatrix}$	$\begin{pmatrix} 1 \\ 1 \end{pmatrix}$	$\begin{pmatrix} 1 \\ 0 \end{pmatrix}$

We can choose the potential term in the following form:

$$V(\phi^\dagger \phi) = -\mu^2 \phi^\dagger \phi - \lambda (\phi^\dagger \phi)^2 \quad (1.19)$$

In case of the choice of $\mu^2 > 0$ and $\lambda > 0$ we end up with so-called "mexican hat" shape of the potential, which is crucial for the BEH mechanism. Such a choice of the potential, shown in

¹Rigorously speaking, the BEH mechanism is only needed to explain how W^\pm and Z acquire their mass. A *fermiophobic* Higgs boson, i.e. not coupling to fermions, is also looked for at the LHC [7, 8].

Fig. 1.1, has a minimum for

$$\phi^\dagger \phi = \frac{1}{2}(\phi_1^2 + \phi_2^2 + \phi_3^2 + \phi_4^2) = -\frac{\mu^2}{2\lambda} \equiv \frac{v^2}{2}. \quad (1.20)$$

This minimum is not found for a single value of ϕ , but for a manifold of non-zero values, which are symmetrical under the rotation in ϕ^+ , ϕ^0 plane. The choice of the single ground state point will break this symmetry. This is called the *spontaneous symmetry breaking*. If one chooses to fix the ground state on the ϕ^0 axis, the vacuum expectation value of the ϕ field become

$$\langle \phi \rangle = \frac{1}{\sqrt{2}} \begin{pmatrix} 0 \\ v \end{pmatrix}, \quad v^2 = -\frac{\mu^2}{\lambda}. \quad (1.21)$$

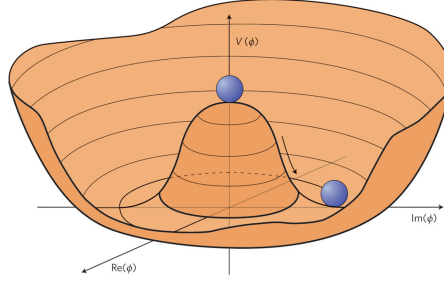


Figure 1.1 – Shape of the Higgs potential of Eq. 1.19.

The ϕ field can thus be rewritten in a generic gauge, in terms of its vacuum expectation value:

$$\phi = \frac{1}{\sqrt{2}} e^{i\phi^a t_a} \begin{pmatrix} 0 \\ H + v \end{pmatrix}, \quad a = 1, 2, 3$$

where the three fields ϕ^a and the fourth $\phi^4 = H + v$ are called *Goldstone fields*. Being scalar and massless, they introduce four new degrees of freedom, in addition to the six degrees due to the transverse polarizations of the massless vector bosons W^\pm and Z . The unitary gauge is fixed by the transformation

$$\phi' = e^{-\frac{i}{v}\phi^a t_a} \phi = \frac{1}{\sqrt{2}} \begin{pmatrix} 0 \\ H + v \end{pmatrix} = \frac{1}{\sqrt{2}} \begin{pmatrix} 0 \\ \phi^4 \end{pmatrix}.$$

Now we can rewrite the Lagrangian in Eq. 1.18 with the Higgs field in the unitary gauge. \mathcal{L}_{EWSB} results from the sum of three terms:

$$\mathcal{L}_{EWSB} = \mathcal{L}_H + \mathcal{L}_{HW} + \mathcal{L}_{HZ} \quad (1.22)$$

Under the approximation $V \sim \mu^2 H^2 + const$ and neglecting higher order terms, we get

$$\begin{aligned}\mathcal{L}_H &= \frac{1}{2} \partial_\alpha H \partial^\alpha H + \mu^2 H^2 \\ \mathcal{L}_{HW} &= \frac{1}{4} v^2 g^2 W_\alpha W^{\dagger\alpha} + \frac{1}{2} v g^2 H W_\alpha W^{\dagger\alpha} \\ &= m_W^2 W_\alpha W^{\dagger\alpha} + g_{HW} H W_\alpha W^{\dagger\alpha}\end{aligned}\quad (1.23)$$

$$\begin{aligned}\mathcal{L}_{HZ} &= \frac{1}{8} v^2 (g^2 + g'^2) Z_\alpha Z^\alpha + \frac{1}{4} v (g^2 + g'^2) H Z_\alpha Z^\alpha \\ &= \frac{1}{2} m_Z^2 Z_\alpha Z^\alpha + \frac{1}{2} g_{HZ} H Z_\alpha Z^\alpha.\end{aligned}\quad (1.24)$$

Eqs. 1.23 and 1.24 now contain mass terms for W^\pm and Z : each of the three gauge bosons has acquired a mass and an additional degree of freedom, corresponding to the longitudinal polarization. These additional degrees of freedom correspond to the three disappeared Goldstone bosons, thus preserving the total number of degrees of freedom. The only additional field not existing before is the H scalar field.

It can be shown that the Higgs field is still invariant under the $U(1)_{EM}$ transformation group which means that electromagnetic symmetry is unbroken and the photon remains massless. In summary, we have got a theory which explains how the weak gauge bosons could get masses while the photon remains massless and the whole theory stays renormalizable. The Higgs field as it is shown below can be also used to give masses to the fermions. The mass of the Higgs boson itself is not predicted by the theory.

1.1.3 Vector Boson Masses and Couplings

The Eqs. 1.23 and 1.24 introduce the masses of the vector bosons W^\pm and Z , which are related to the EWSB characterising parameter v and to the electroweak coupling constants:

$$\begin{cases} m_W = \frac{1}{2} v g \\ m_Z = \frac{1}{2} v \sqrt{g^2 + g'^2} \end{cases} \rightarrow \frac{m_W}{m_Z} = \frac{g}{\sqrt{g^2 + g'^2}} = \cos\theta_W. \quad (1.25)$$

From the same equations we can obtain the couplings of the vector bosons to the Higgs boson. They are found to be proportional to the square of m_W and m_Z

$$g_{HW} = \frac{1}{2} v g^2 = \frac{2}{v} m_W^2 \quad (1.26)$$

$$g_{HZ} = \frac{1}{2} v (g^2 + g'^2) = \frac{2}{v} m_Z^2. \quad (1.27)$$

Thus, it is easy to derive the ratio between partial decay rates of the Higgs boson to the pair of W or Z bosons:

$$\frac{BR(H \rightarrow W^+ W^-)}{BR(H \rightarrow Z Z)} = \left(\frac{g_{HW}}{\frac{1}{2} g_{HZ}} \right)^2 = 4 \left(\frac{m_W^2}{m_Z^2} \right)^2 \sim 2.4.$$

Finally, the EWSB energy scale can be determined from the relation between the v parameter and the Fermi constant G_F :

$$v = \left(\frac{1}{\sqrt{2}G_F} \right)^{\frac{1}{2}} \simeq 246 \text{ GeV}. \quad (1.28)$$

1.1.4 Fermion Masses and Couplings

As it was mentioned before, the Dirac mass terms do not preserve the $SU(2)_L$ symmetry. However we can introduce the fermions masses via Yukawa-type interactions using the Higgs field.

$$\mathcal{L}_f = -G_{Hf} \cdot \bar{l}_f \phi f_R + \bar{f}_R \phi^\dagger l_f.$$

After the electroweak symmetry breaking, Yukawa couplings generate quarks and leptons masses. In the unitary gauge, the first component of ϕ is zero, therefore a mass term arises from the Yukawa Lagrangian only for the second component of l_ℓ : this correctly reproduces the fact that the neutrinos are (approximately) massless.

$$\mathcal{L}_\ell = -\frac{G_{H\ell}}{\sqrt{2}} v \bar{\ell} \ell - \frac{G_{H\ell}}{\sqrt{2}} H \bar{\ell} \ell. \quad (1.29)$$

For what concerns the quark fields, the *down* quarks (d, s, b) are treated in the same way as leptons; the *up* quarks (u, c, t), instead, must couple to the charge-conjugate of ϕ

$$\phi^c = -i\tau_2 \phi^* = \frac{1}{\sqrt{2}} \begin{pmatrix} \phi^3 - i\phi^4 \\ -\phi^1 + i\phi^2 \end{pmatrix},$$

which becomes in the unitary gauge

$$\phi^c = \frac{1}{\sqrt{2}} \begin{pmatrix} \eta + v \\ 0 \end{pmatrix}.$$

The Yukawa Lagrangian is therefore

$$\mathcal{L}_Y = -G_{H\ell} \bar{L}_L \phi \ell_R - G_{Hd} \bar{Q}_L \phi d_R - G_{Hu} \bar{Q}_L \phi^c u_R + h.c.. \quad (1.30)$$

From Eq. 1.29, the mass of a fermion (apart from the neutrinos) and its coupling constant to the Higgs boson are found to be

$$m_f = \frac{G_{Hf}}{\sqrt{2}} v \quad (1.31)$$

$$g_{Hf} = \frac{G_{Hf}}{\sqrt{2}} = \frac{m_f}{v}. \quad (1.32)$$

Note that G_{Hf} are free parameters and hence the masses of the fermions cannot be predicted

by the theory.

At this point another important feature has to be mentioned. The above treatment doesn't account for the fact that in reality there are three families of quarks and leptons. This means that the weak mass eigenstates are not the same as the physical masses: the masses of the physical particles are linear combinations of the weak mass eigenstates. These transformations are described by the two unitary transformation matrices: Cabibbo–Kobayashi–Maskawa (CKM) [9, 10] and Pontecorvo–Maki–Nakagawa–Sakata (PMNS) [11, 12] matrices in cases of quarks and leptons respectively.

1.1.5 The Higgs Boson Mass

Among the 18 free parameters of the SM², the Higgs boson mass was the only still undetermined one at the beginning of my thesis work. Its mass is the function of the parameters v and λ . Although the former can be estimated by its relation with the G_F constant of the Fermi theory, the latter is the intrinsic characteristic of the field ϕ and cannot be determined other than measuring the Higgs mass itself. However, both theoretical and experimental constraints existed, including those from direct search at colliders, in particular Large Electron-Positron Collider (LEP).

Theoretical Constraints

An upper limit on the Higgs boson mass could be set using the so-called triviality condition[13]: let's define a scale Λ up to which the SM is valid, before the perturbation theory breaks down. Then, we require that the running quartic coupling of the Higgs potential λ remains finite up to this scale. This limitation is called triviality. A lower limit is found instead by requiring that λ remains positive after the inclusion of radiative corrections, at least up to Λ : this implies that the Higgs potential is bounded from below, i.e. the minimum of such potential is an absolute minimum (vacuum stability). A looser constraint is found by requiring such minimum to be local, instead of absolute (metastability). These theoretical bounds on the Higgs mass as a function of Λ are shown in Fig. 1.2.

In case of the validity of the SM up to the Planck scale ($\Lambda \sim 10^{19}$ GeV), the allowed Higgs boson mass range is between 130 and 190 GeV, while for $\Lambda \sim 1$ TeV the Higgs boson mass can be up to 700 GeV. The above means that experimentally we should look for a Higgs boson up to masses of ~ 1 TeV. If the Higgs particle is not found in this mass range, then another explanation for the EWSB mechanism will be needed.

² 9 fermion masses (+ 3 neutrino masses, if $m_\nu \neq 0$), 3 CKM mixing angles + 1 phase (+ 3 more angles + 1 additional phase for neutrinos), the electromagnetic coupling constant α_{EM} , the strong coupling constant α_S , the weak coupling constant G_F , the Z boson mass and the Higgs boson mass.

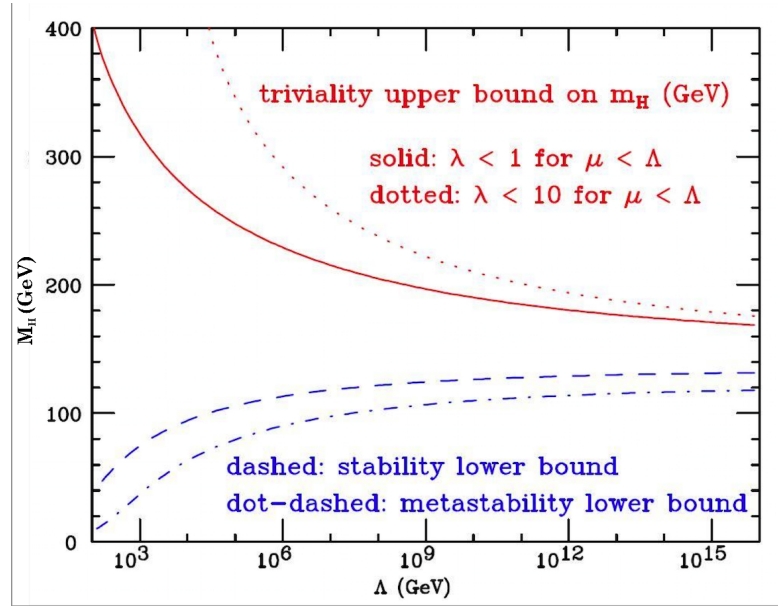


Figure 1.2 – Red line: triviality bound (for different upper limits to λ); blue line: vacuum stability (or metastability) bound on the Higgs boson mass as a function of the new physics (or cut-off) scale Λ [13].

Experimental Constraints

Bounds on the Higgs mass are also provided by the precise electroweak measurements at the LEP, SLC and Tevatron [14] (updated in 2010). Since the Higgs boson contributes to radiative corrections, many electroweak observables are logarithmically sensitive to m_H and can thus be used to indirectly constrain its mass. Direct searches at LEP-II have set the limit $m_H > 114.4$ GeV (95% C.L.) [15] and those performed at Tevatron have excluded the mass range $158 < m_H < 172$ GeV also at 95% C.L. [16] (see Fig. 1.3, top) before the start of the LHC.

The combined fit of the precise electroweak measurements from data collected by the four LEP experiments and by the SLD, CDF and DØ [17], assuming the SM as the correct theory and using the Higgs mass as a free parameter also contributes to the Higgs boson mass constraints. The result of this procedure is summarized in Fig. 1.3 (bottom), where $\Delta\chi^2 = \chi^2 - \chi_{min}^2$ and χ_{min}^2 corresponds to the global minimum of the χ^2 as a function of all the model parameters, is shown as a function of m_H .

The solid curve is the result of the fit, while the shaded band represents the theoretical uncertainty due to unknown higher order corrections. The indirectly determined value of the Higgs boson mass, corresponding to the minimum of the curve, is $m_H = 91_{-23}^{+30}$ GeV (68% C.L. for the solid line in Fig. 1.3, without taking the theoretical uncertainty into account).

However the latter constraints could not be treated as absolute ones since they are model-dependent: all the loop corrections account only for the contributions from already observed particles and the Higgs boson. This result hence is valid only in frames of the Standard Model and has to be confirmed by the direct observation of the Higgs boson.

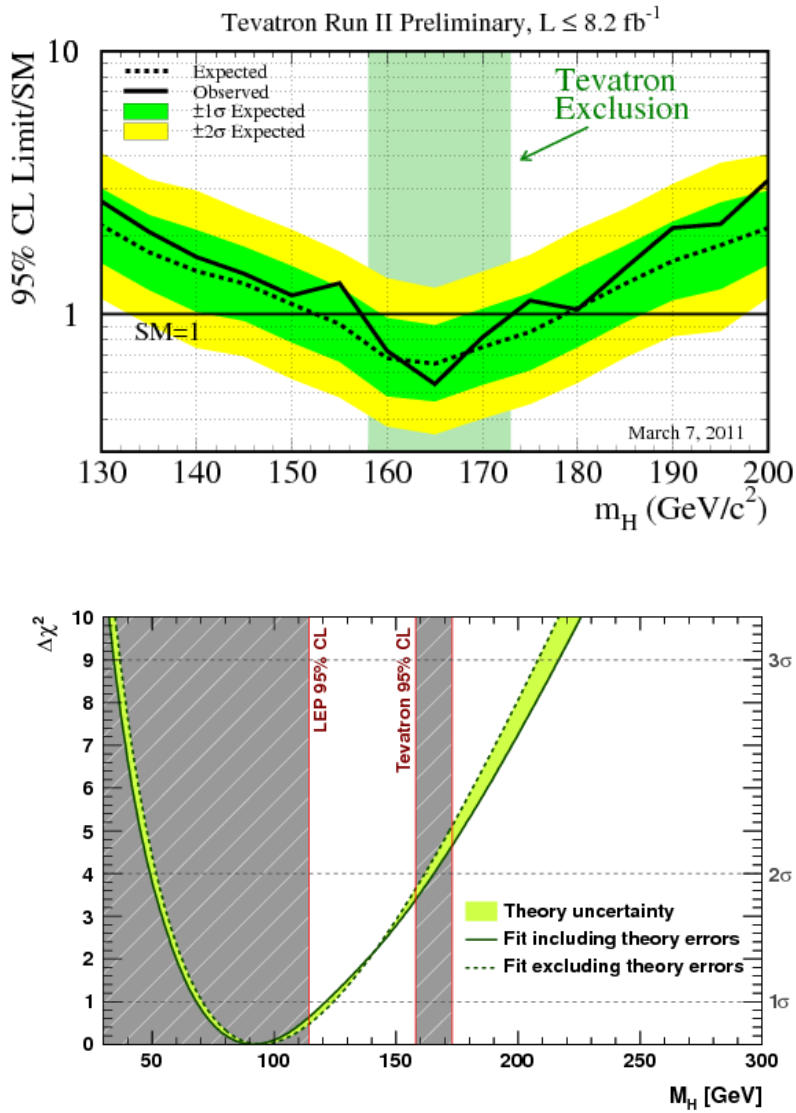


Figure 1.3 – Top: 2011 Tevatron exclusion at 95% C.L. in Higgs boson mass range from 158 to 172 GeV. Bottom: $\Delta\chi^2$ of the fit to the electroweak precision measurements of LEP, SLC, and Tevatron as a function of the Higgs mass (2012). The solid (dashed) lines give the results when including (ignoring) theoretical errors. The grey area represents the region excluded by direct searches at LEP and Tevatron.

1.2 The Higgs Boson Search at the LHC

Over the years, Higgs boson searches looked like the attempts to find a needle in a haystack. The almost total absence of any reasonable Higgs boson mass constraints even led theorists to end some of their articles like this: "We should perhaps finish our paper with an apology and a caution. We apologize to experimentalists for having no idea what is the mass of the Higgs boson, [...], and for not being sure of its couplings to other particles, except that they are probably all very small. For these reasons, we do not want to encourage big experimental searches for the Higgs boson, but we do feel that people doing experiments vulnerable to the Higgs boson should know how it may turn up" [18].

By 2011 still a huge piece of the phase space remained to be covered by searches at the LHC: from 114 GeV up to about 1 TeV. In this chapter we figure out which Higgs boson production and decay channels are most relevant for its searches at the LHC proton-proton collider. While the Higgs mass is not predicted by the theory, its couplings to the fermions or bosons in the Standard Model are proportional to the corresponding particle masses for fermions or squared masses for bosons. This implies that the Higgs boson production and decay processes are dominated by the channels involving the coupling of the Higgs boson to the heavy particles like W^\pm and Z bosons or third generation fermions.

1.2.1 The Higgs Boson Production

The lowest order Feynman diagrams of the main Higgs boson production processes at hadron colliders are shown in the Fig. 1.4. The corresponding cross section for center-of-mass energies of $\sqrt{s} = 7$ TeV and $\sqrt{s} = 8$ TeV (used by the LHC in 2011 and 2012) are represented in Fig. 1.5 [19].

Gluon Fusion

The gg fusion is the dominating mechanism for the Higgs boson production at the LHC. There are two reasons for this: firstly, the Higgs boson couplings to fermions are proportional to their masses (hence the couplings to all the quarks except the top quark are quite small) and secondly, roughly 50% of the proton momentum is carried by gluons and their luminosity increases with the centre-of-mass energy [20]. Also comparing to the Tevatron, we have a deficit of antiquarks at the LHC since it is a pp -collider, so that the ratio of the associated Higgs boson production modes to the gluon fusion one is even smaller.

The gg fusion process is shown in Fig. 1.4(top left), with a t -quark loop as the main contribution. Next-to-next-to-leading order QCD corrections have been found to increase the cross section for this process by a factor of ~ 2.5 . The uncertainties due to the higher order corrections are estimated to be within $\sim 10\%$. The choice of the parton distribution functions (PDF) adds another $\sim 10\%$ theoretical uncertainty.

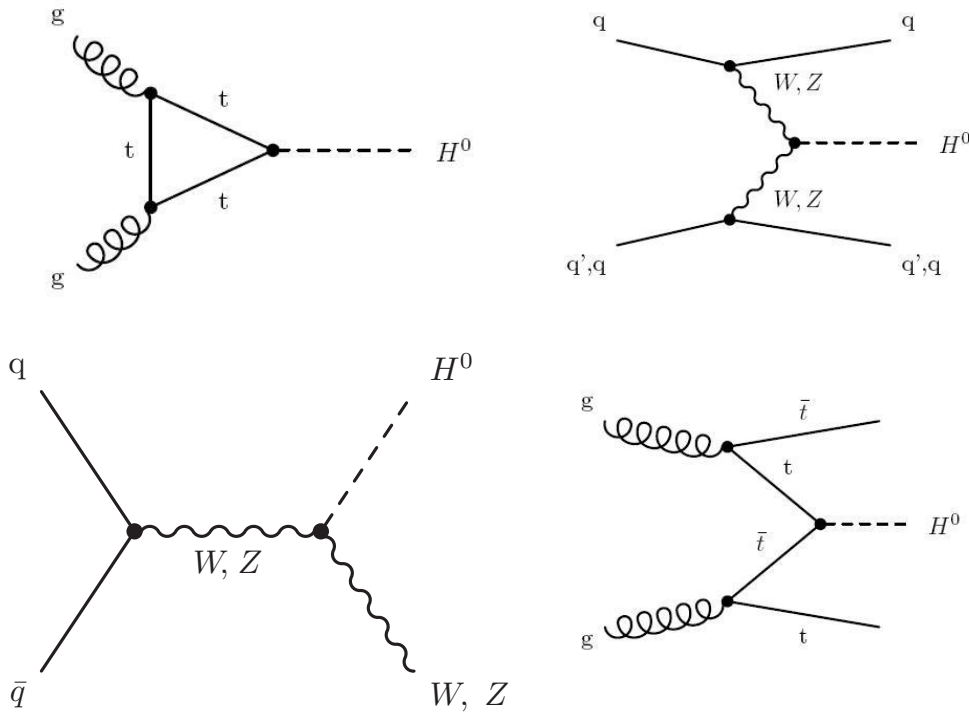


Figure 1.4 – The Higgs boson production mechanisms at lowest order in proton-proton collisions: gg fusion (top left); VV fusion (top right); W and Z associated production (or *Higgsstrahlung*) (bottom left); $t\bar{t}$ associated production (bottom right).

Vector Boson Fusion

The second largest Higgs boson production cross section is given by the vector boson fusion (VBF or VV fusion) shown in Fig. 1.4(top right). For a low-mass Higgs boson it is about one order of magnitude lower than the gg fusion, but it grows faster with the Higgs boson mass and the two processes become comparable at $m_H \sim 1$ TeV. Nevertheless this channel remains interesting at low mass as well because it provides a possibility to access the Higgs boson couplings to the vector bosons. It has quite clear experimental signature: two spectator jets with the high invariant mass in the forward region. This feature provides a good opportunity to tag the signal events and discriminate the background. Finally we should notice that both leading order and next-to-leading order cross sections for this process are known and the higher order QCD and EWK corrections are rather small.

Associated Production

There are two types of the Higgs boson associated production: the so-called *Higgsstrahlung* which is shown in Fig. 1.4(bottom left) and the Higgs boson production with a $t\bar{t}$ pair illustrated in Fig. 1.4(bottom right). In the *Higgsstrahlung* the Higgs boson is produced in association

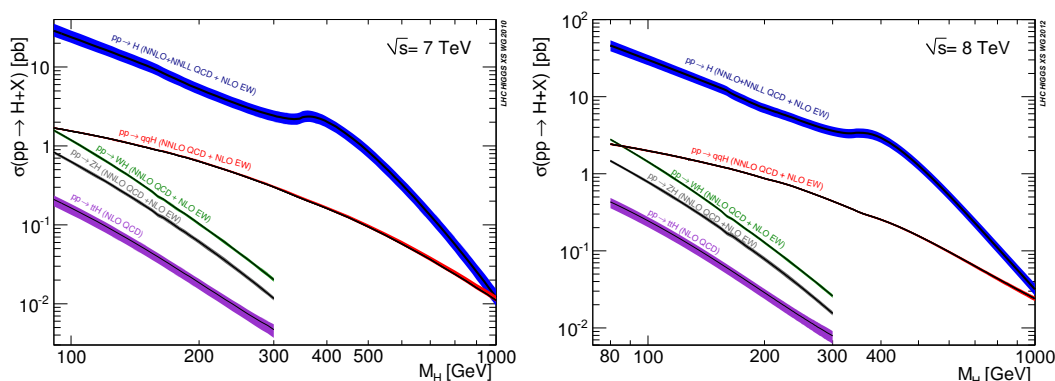


Figure 1.5 – The Higgs boson production cross sections at 7 TeV (left) and 8 TeV (right) center-of-mass energy as a function of the Higgs boson mass.

with a gauge vector boson (W^\pm or Z), which can be used to tag the event. The cross section for this process is about the same order of magnitude as the Vector boson fusion (VBF) mode around $m_H = 100$ GeV but then falls down rapidly with m_H . The QCD corrections are quite large and the next-to-leading order cross section results to be increased by a factor of 1.2–1.4 with respect to the leading order one. The cross section for the $t\bar{t}H$ process is even smaller, but the presence of the $t\bar{t}$ pair in the final state can provide a good experimental signature. The higher order corrections increase the cross section by a factor of about 1.2.

1.2.2 The Higgs Boson Decay

The Higgs boson branching fractions depend strongly on its mass. The low-mass region (up to ~ 150 GeV) is dominated by the fermionic decays while above the vector boson pair mass threshold (161 GeV for W^\pm and 182 GeV for Z) the largest branching fractions are assigned to the vector boson decays. At high masses (~ 350 GeV), also $t\bar{t}$ pairs can be produced. Fig. 1.6 shows the branching fractions of the different Higgs decay channels as a function of the Higgs boson mass.

We remind as well that the suitability of some channel for the Higgs boson discovery or for its properties determination depends not only on the corresponding branching fraction but also on the possibility of an efficient signal selection while rejecting the background. Below we present more detailed overview of different decay modes explored at the LHC experiments depending on the Higgs boson mass range.

High Mass Region

The situation is quite simple above the $2m_V$ threshold, which is ~ 160 GeV. The two main modes are $H \rightarrow WW$ and $H \rightarrow ZZ$. Also above the $t\bar{t}$ threshold we have $H \rightarrow t\bar{t}$ decay, but its branching fraction is still smaller than the for $H \rightarrow VV$ while the background is high. The most

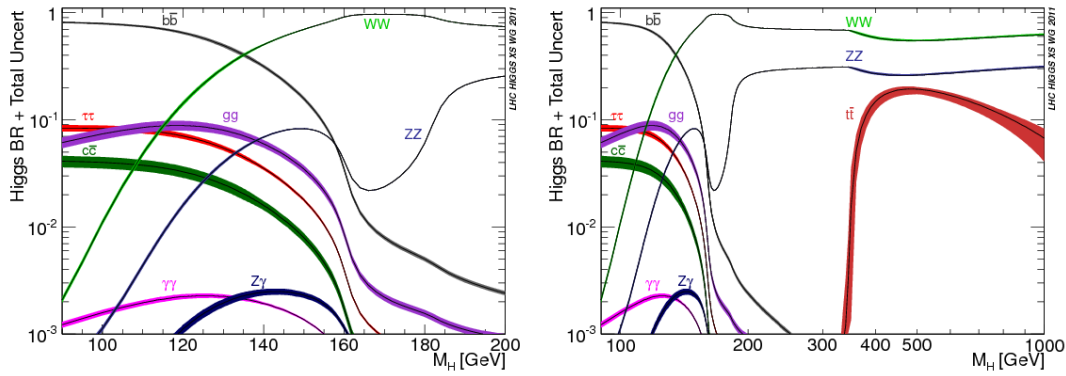


Figure 1.6 – Branching ratios for different Higgs decay channels as a function of the Higgs mass in low mass range (left) and full search range (right).

interesting decay channel at high mass region is so-called golden channel: $H \rightarrow ZZ \rightarrow 4\ell$ where ℓ denotes a charged lepton. Although its branching fraction is not large and several times lower than $H \rightarrow WW$, this channel provides extremely clean and fully reconstructable experimental signature.

Low and Intermediate Mass Region

Below the $2m_V$ threshold almost every channel can contribute to the Higgs boson search.

For a Higgs boson with $m_H < 120$ GeV, the channel $H \rightarrow \gamma\gamma$ is the most promising. It has quite low branching fraction, however the two high energy photons provide a very clear signature. Nevertheless, this channel suffers from the huge $q\bar{q} \rightarrow \gamma\gamma$ background.

The $b\bar{b}$ decay channel, dominating for the low-mass Higgs boson decays, has been exploited in the boosted regime³, in association with a vector boson decaying leptonically. This allows to discriminate the signal events from the large QCD di-jet background.

Another important decay channel is $H \rightarrow \tau\tau$. It has about the same branching fraction as $H \rightarrow b\bar{b}$ but allows for a more efficient background rejection due to the τ -tagging techniques.

For a Higgs boson mass value between 120 and 160 GeV, the Higgs boson decays into $WW^{(*)}$, $ZZ^{(*)}$ and $Z\gamma$ open up and their branching fractions increase with the Higgs boson mass. Also a significant contribution from the $\gamma\gamma$ decays is kept.

The branching fraction of the $H \rightarrow WW^{(*)}$ is higher than the $H \rightarrow ZZ^{(*)}/Z\gamma$, because of the higher coupling of the Higgs boson to the charged current with respect to the neutral current, however this channel is complicated because of the presence of the two neutrinos in the final state, which doesn't allow to reconstruct the Higgs boson mass. Such measurement can be

³ When the Higgs boson appears with high momentum.

performed instead when one W decays leptonically and the other one decays in two quarks. However, in this case, the final state suffers from the high hadronic background.

The decay $H \rightarrow ZZ^{(*)} \rightarrow 4\ell$, despite its lower branching fraction, has the highest sensitivity for $120 < m_H < 150$ GeV due to its clean signature and low background. To summarize, the two most promising low-mass channels are the $H \rightarrow \gamma\gamma$ and $H \rightarrow ZZ \rightarrow 4\ell$ which allow to perform the Higgs boson mass measurements, while the $H \rightarrow b\bar{b}$ and $H \rightarrow \tau\tau$ allow to probe the Higgs boson couplings to the fermions.

The Higgs Boson Total Decay Width

Among the Higgs boson properties, its decay width is particularly important since a sizeable deviation from the SM prediction would directly indicate new physics. The total width of the Higgs boson resonance, which is given by the sum over all the possible decay channels, is shown in Fig. 1.7 as a function of m_H [19]. Below the $2 m_W$ threshold, the Higgs width is of the order of a few MeV, then it rapidly increases, but remains lower than 1 GeV up to $m_H \simeq 200$ GeV.

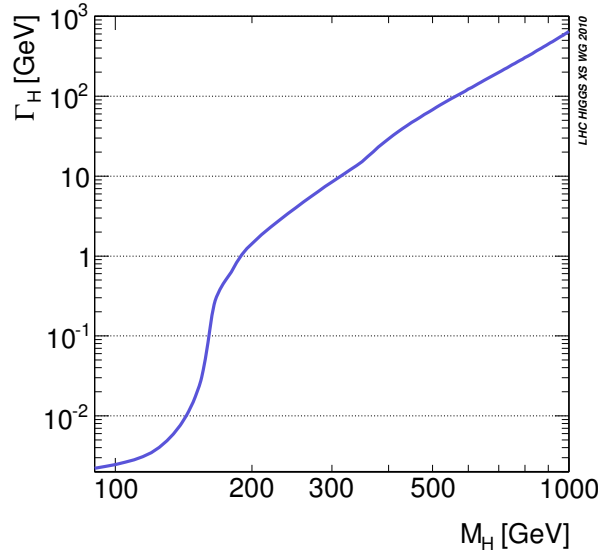


Figure 1.7 – The Higgs boson total decay width as a function of its mass.

In the high mass region ($m_H > 2 m_Z$), the total Higgs boson width is dominated by the $W^+ W^-$ and ZZ partial widths, which can be written as follows:

$$\Gamma(H \rightarrow W^+ W^-) = \frac{g^2}{64\pi} \frac{m_H^3}{m_W^2} \sqrt{1 - x_W} \left(1 - x_W + \frac{3}{4} x_W^2 \right) \quad (1.33)$$

$$\Gamma(H \rightarrow ZZ) = \frac{g^2}{128\pi} \frac{m_H^3}{m_Z^2} \sqrt{1 - x_Z} \left(1 - x_Z + \frac{3}{4} x_Z^2 \right), \quad (1.34)$$

where

$$x_W = \frac{4m_W^2}{m_H^2}, \quad x_Z = \frac{4m_Z^2}{m_H^2}.$$

As the Higgs boson mass increases, $x_W, x_Z \rightarrow 0$ and the leading term in Eqs. 1.33 and 1.34 grows proportional to m_H^3 . Summing over the $W^+ W^-$ and ZZ channels, the Higgs boson width in the high mass region can be written as follows:

$$\Gamma(H \rightarrow VV) = \frac{3}{32\pi} \frac{m_H^3}{v^2}. \quad (1.35)$$

From Eq. 1.35, it results that $\Gamma_H \simeq m_H$ for $m_H \simeq 1.4$ TeV. When m_H becomes larger than a TeV its width becomes larger than its own mass, hence the Higgs boson cannot be properly considered as a particle any more. In addition, if the Higgs mass is above 1 TeV, the SM predictions violate the unitarity (see Fig. 1.2). All these considerations suggest the TeV as a limit for the Higgs boson mass: at the TeV scale at least, the Higgs boson must be observed, or new physics must emerge.

The measurement of the Higgs boson width is very important in view of the search for new physics. While for the high mass Higgs boson we can measure its width directly, for the low mass Higgs boson it is a challenge, because the Higgs boson width ($\mathcal{O}(10)$ MeV) is dominated by the experimental resolution ($\mathcal{O}(1)$ GeV). However there are other methods allowing us constrain the Higgs boson width below experimental resolution as will be discussed in chapter 5.

2 Experimental Setup

2.1 The Large Hadron Collider

The Large Hadron Collider (LHC) was built between 1998 and 2008 at the European Organization for Nuclear Research (CERN). It is installed in the tunnel that had been constructed for the Large Electron-Positron Collider (LEP) machine, the world highest energy electron-positron collider ever built. This tunnel is 26.7 km long and located approximately 100 m underground. The LHC inherited the Proton Synchrotron (PS) and the Super Proton Synchrotron (SPS) accelerator systems shown schematically in Fig. 2.1. Following the LEP scheme four interaction regions were equipped, and host four main detectors: ATLAS, CMS, ALICE and LHCb.

There are two general purpose experiments, CMS (Compact Muon Solenoid) and ATLAS (A Torodial Large Apparatus), which study Standard Model physics processes (e.g. electroweak processes, physics of the top quark, etc.), looking also for deviations from the SM predictions. Their main goal was established to search for the Higgs boson and physics beyond the Standard Model. Two other experiments are dedicated to heavy ion collisions (ALICE) and flavor physics (LHCb).

The LHC is designed for two kinds of collisions: collisions of protons, and collisions of heavy ions (p-Pb and Pb-Pb). This section focuses on the case of proton collisions.

2.1.1 Performance Goals

Contrary to the leptonic colliders, the LHC is a hadronic machine. This means that it is not designed to perform precision measurements, but it can probe the scalar sector, and new physics beyond it. The unitarity constraint, mentioned in Sec. 1.1.2, sets upper limit on the Higgs boson mass: $m_H \lesssim 700$ GeV. In case of the absence of a fundamental Higgs boson, the application of the unitarity constraint to the tree-level amplitude for $W_L^+ W_L^- \rightarrow Z_L Z_L$ imposes that new physics should appear at a scale $\Lambda \lesssim 1.2$ TeV. It means that the LHC collisions should be able to produce Higgs bosons of masses lower than the TeV and/or they should provide

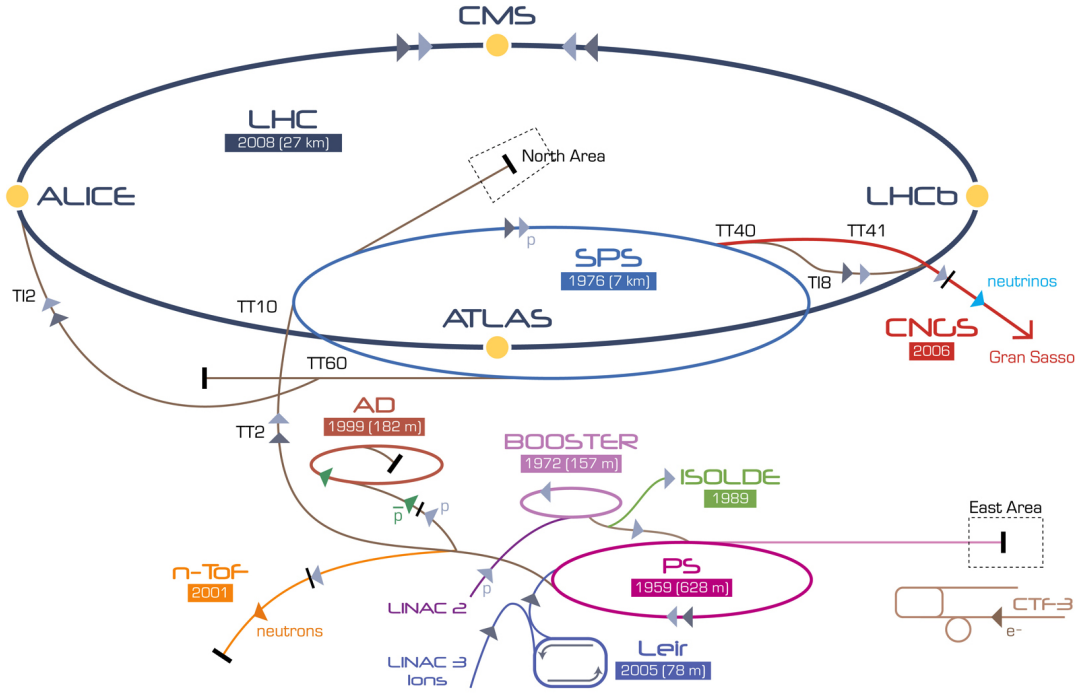


Figure 2.1 – The LHC accelerator complex. Proton acceleration starts from a linear accelerator (LINAC) that injects the protons to the Proton Synchrotron (PS), which accelerates them to 25 GeV. Following this, the Super Proton Synchrotron (SPS) accelerates the beams to 450 GeV and subsequently injects them into the LHC ring.

interactions of W_L bosons at a center-of-mass energy of the order of 1 TeV, in order to probe the unitarity constraint. The second requirement is tighter and requires a proton-proton center-of-mass energy of the order of 14 TeV.

The number of events of a given physics process that occur during one second, is related to the cross section of the corresponding process, $\sigma_{process}$, via the instantaneous luminosity \mathcal{L} of the machine:

$$N = \mathcal{L} \sigma_{process} \tag{2.1}$$

The relevant processes for physics searches such as Higgs physics and physics beyond the Standard Model, are predicted to have quite low production rates in proton-proton collisions. For example, the cross section for the production of a Higgs boson is several orders of magnitude smaller than the total inelastic cross section as it is shown on Fig. 2.2. However it increases more rapidly than the other ones with the center-of-mass energy of the collisions. Therefore, we need the center-of-mass energy to be as high as possible as well as collision luminosity to ensure reasonably high rate of interesting events.

The nominal center-of-mass energy for LHC collisions is $\sqrt{s} = 14 \text{ TeV}$ (7 TeV per beam), and the nominal peak luminosity is $\mathcal{L} = 10^{34} \text{ cm}^{-2}\text{s}^{-1}$ for the CMS and ATLAS experiments. One can

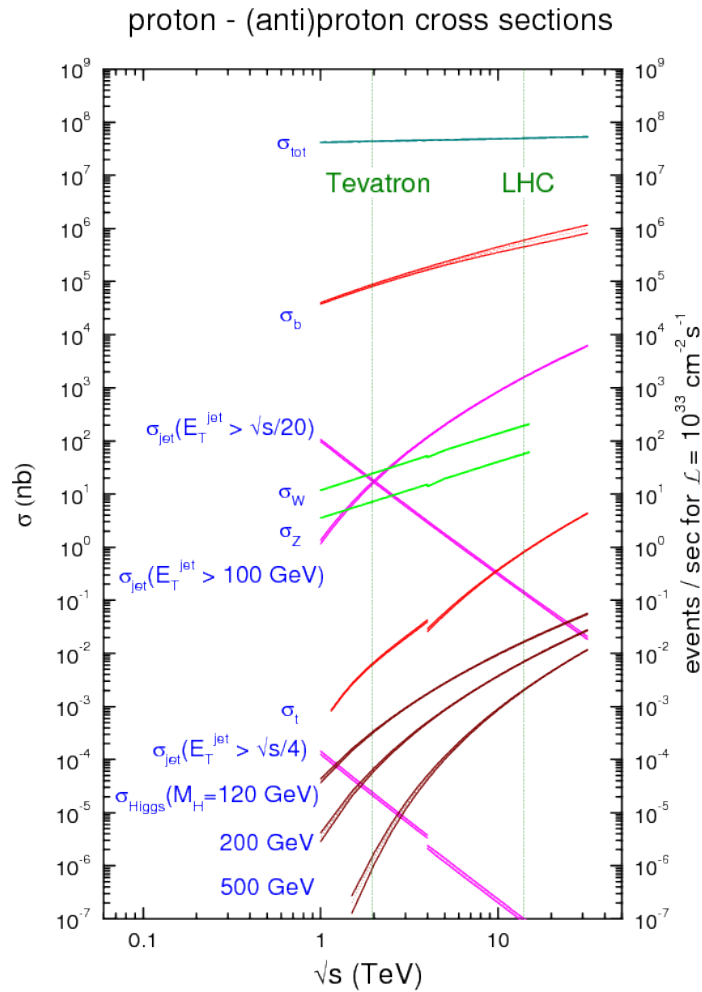


Figure 2.2 – Expected cross section as a function of energy in the centre of mass frame for proton-proton collisions. The cross sections are indicated in the left vertical axis. The right vertical axis shows the number of events expected per second for a luminosity of $\mathcal{L} = 10^{33} \text{ cm}^{-2} \text{ s}^{-1}$.

get from the right axis on Fig. 2.2 (note that it is given in units of $10^{33} \text{ cm}^{-2} \text{ s}^{-1}$, i.e. one should multiply by 10 the expected number of events) that for these values a Higgs boson with a mass of 200 GeV would be produced approximately every 10 s. In order to estimate the number of produced and recorded events in a particular decay channel, one must then take into account the Higgs boson branching ratio to this channel and the experiment reconstruction and (online and offline¹) selection efficiencies.

¹ The selection at the LHC experiments is done in two-step procedure: first, or online step is a preselection which is needed in order to reduce the event rate to a reasonable number we can further process, and second, offline selection, which is based on the physics analysis requirements

2.1.2 Nominal Center-of-mass Energy and Magnet Systems

Since the LHC is a proton accelerator with a constrained circumference, its maximal energy per beam depends on the strength of the dipole field that maintains the beams on the orbit.

The nominal LHC energy of 7 TeV per beam is possible thanks to a global magnet system at the edge of the technology. The system uses a total of about 9600 magnets.

The 1232 dipole magnets use niobium-titanium (NbTi) cables. They are kept at a temperature of 1.9 K, by pumping superfluid helium into the magnets. A total of 120 t of superfluid helium is used.

At that temperature², the dipoles are in a superconducting state. They provide a field of 8.33 T when conducting a current of 11850 A. Such a magnetic field is needed to bend the 7 TeV beams around the 27-km ring of the LHC.

In order to focus the beam, and maximize the probability of collision, quadrupole magnets are used.

2.1.3 Nominal Luminosity and Beam Parameters

The very high LHC design luminosity implies many constraints on the proton beam parameters. In the general case of two colliding beams, the luminosity \mathcal{L} writes:

$$\mathcal{L} = f_{rev} n_b \frac{N_1 N_2}{A} \quad (2.2)$$

Where f_{rev} is the revolution frequency, n_b is the number of bunches per beam, N_1 and N_2 are the number of particles in the bunches of each colliding beam, and A is the transverse cross section of the beams.

At the LHC, the bunches are filled with an identical number of protons, $N_b = N_1 = N_2$. The cross section of the beam writes:

$$A = 4\pi\epsilon_n \frac{\beta^*}{\gamma_r} \quad (2.3)$$

Where ϵ_n is the normalized transverse beam emittance³ (with a design value of $3.75 \mu\text{m}$), and β^* is the beta function at collision point⁴, which is then corrected by the relativistic gamma factor γ_r .

²NbTi becomes superconducting below a temperature of 10 K. At a temperature of 4.2 K (which is the temperature in the Tevatron collider magnets), the dipoles would produce a magnetic field weaker than 7 T.

³The beam emittance of a particle accelerator is the extent occupied by the particles of the beam in position and momentum phase space.

⁴It characterizes the beam focalization.

Finally, the expression in (2.2) has to be corrected by a geometric luminosity reduction factor, F , due to the crossing angle at the interaction point.

Hence, the final expression of the luminosity writes:

$$\mathcal{L} = \frac{f_{rev} n_b N_b^2 \gamma_r}{4\pi\epsilon_n \beta^*} F \quad (2.4)$$

Given the beam velocity ($v \sim c \sim 3 \cdot 10^8 \text{ m s}^{-1}$) and the LHC circumference (26.7 km), the revolution frequency is $f_{rev} = 11 \text{ kHz}$. Besides, the nominal value of the beta function at the impact point is $\beta^* = 0.55 \text{ m}$. Thus, the nominal luminosity is reached with $n_b = 2,808$ bunches per beam, and $N_b = 1.15 \cdot 10^{11}$ protons per bunch.

2.1.4 Lattice Layout

Such a high beam intensity could not be obtained with the antiproton beams⁵. This is why a 'simple' particle-antiparticle accelerator collider configuration⁶ is not used at the LHC.

Following this the LHC is designed with two rings and has two separate magnet fields and vacuum chambers, in a twin-bore magnet design. The only common sections are located at the insertion regions, equipped with the experimental detectors. The configuration is shown in Fig. 2.3.

A summary of the machine parameters [21] is given in Table 2.1. The numbers indicated correspond to the nominal values. In addition to the previously mentioned parameters, the luminosity lifetime is an important parameter at the LHC and colliders in general. The luminosity tends to decay during a physics run, because of the degradation of intensities and emittances of the circulating and colliding beams.

2.1.5 The LHC Collision Detectors

Targeted high luminosity and energy parameters demand the LHC to be a unique machine and impose important constraints for the detectors.

Under the nominal conditions, the LHC should produce $\sim 10^9$ inelastic collision events per second which means a bunch crossing rate of 40 MHz (or a bunch crossing spacing of 25 ns), with ~ 20 collision events expected per bunch crossing.

⁵In comparison, the highest luminosity achieved at the Tevatron proton-antiproton collider after the latest upgrades, is $3 \cdot 10^{32} \text{ cm}^{-2} \text{ s}^{-1}$.

⁶In such a configuration, both beams can share the same phase space, so a single ring can be used.

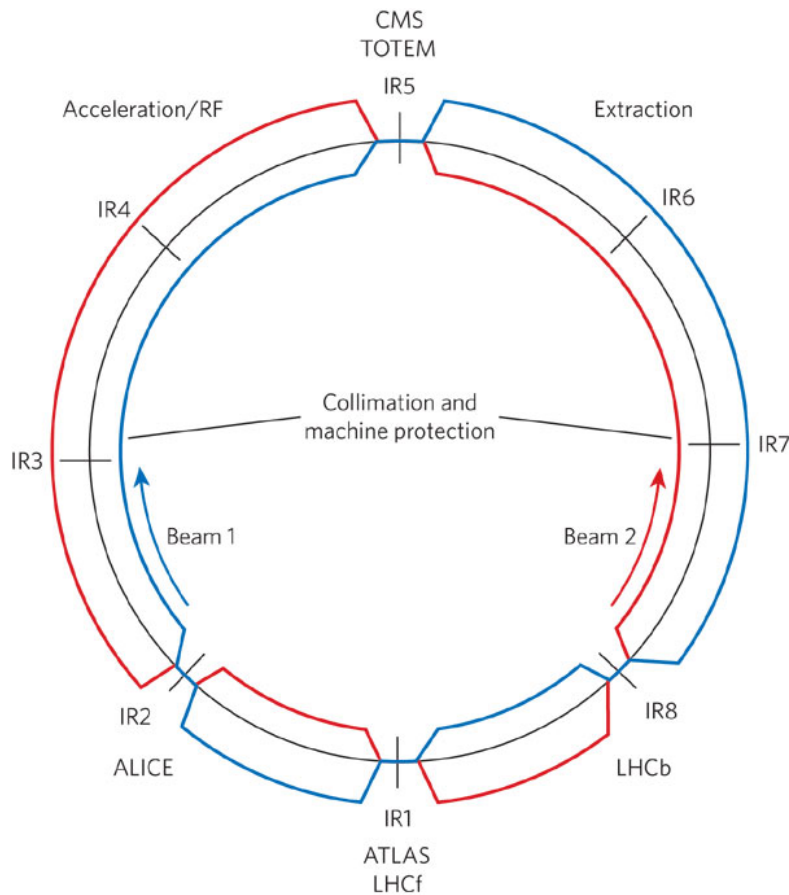


Figure 2.3 – Schematic layout of the LHC where Beam 1 is accelerated clockwise and Beam 2 anticlockwise.

Pile-up Events

As it was mentioned above the LHC should produce significant number of inelastic collisions at each beam crossing under the nominal conditions. To have the ability to separate these events one from another a high granularity of the detector is mandatory, which reflects in a large number of detector channels.

Moreover, the time for the detector response is limited by the order of one bunch spacing, i.e. 25 ns. Hence a good time resolution (few ns) is needed in order to distinguish the events from the two consecutive bunch crossings. This requires a precise synchronization of all the detector channels. The limit where two consecutive signals start to overlap is called out-of-time pile-up, and affects the shape of the signal, which is typically a few bunch crossings. This case must also be treated properly.

Circumference	26.659 km
Center-of-mass energy (\sqrt{s})	14 TeV
Nominal Luminosity (\mathcal{L})	$10^{34} \text{ cm}^{-2} \text{ s}^{-1}$
Luminosity lifetime	15 hr
Time between two bunch crossings	24.95 ns
Distance between two bunches	7.48 m
Longitudinal max. size of a bunch	7.55 cm
Number of bunches (n_b)	2808
Number of protons per bunch (N_b)	1.15×10^{11}
beta function at impact point (β^*)	0.55 m
Transverse RMS beam size at impact point (σ^*)	$16.7 \mu\text{m}$
Dipole field at 7 TeV (B)	8.33 T
Dipole temperature (T)	1.9 K

Table 2.1 – The LHC nominal parameter values for proton-proton collisions.

Collision Rate

Despite very large computing and storage facilities, events can only be recorded at a rate of ~ 300 Hz. This makes necessary to have an efficient online selection system that determines in a very small amount of time whether an event has to be recorded. This system should be not only fast but it should be very selective to reduce the event rate by seven orders of magnitude. Finally, this selection system must keep a very high efficiency on interesting collision events.

High Radiation

The large flux of particles emitted by the LHC collisions implies high radiation levels⁷. Hence the detectors must not only be hermetic, precise and selective, but as well highly resistant to the radiation. The same condition applies to their front-end electronics. The detectors were designed to operate during ten years of the nominal LHC collision conditions.

2.1.6 Operation from 2010 to 2012

The first injections of beams took place in September 10 2008, but due to an accident because of a faulty resistance of an interconnection between two magnets happened the 19th of the same month, the LHC stopped for more than one year for repairs and for the commissioning of further safety measurements. The injections restarted in November 2009 with the first 450 GeV beams circulating through the LHC. The beam energy then was raised by steps until it reached 3.5 TeV in March 2010 and the first physics run at the LHC finally started. The data taking proceeded smoothly through the whole 2010, with a steady increase of luminosity which

⁷For example, at nominal luminosity, the CMS electromagnetic calorimeter (located $\sim 2 - 3$ m from the collision point) is submitted to a radiation of ~ 0.2 to 6.5 Gy/h.

allowed the LHC to deliver a total of 47 pb^{-1} up to November 2010, when the proton-proton collisions stopped to start one month of Heavy Ions runs.

The proton-proton collisions restarted at the center-of-mass energy of 7 TeV in March 2011. The experience of machine operating accumulated during 2010 run allowed to increase the instantaneous luminosity, surpassing in few weeks the collected statistics of the whole 2010 and quickly approaching the design luminosity. During the 2011 run an integrated luminosity of about 6 fb^{-1} was delivered and collected by the experiments. During the Chamonix workshop in February 2012 it was decided to run the Large Hadron Collider (LHC) with an increased energy of 4 TeV per beam during 2012. In addition to this, the instantaneous luminosity has been constantly growing and reached $7.73 \times 10^{33} \text{ cm}^{-2}\text{s}^{-1}$. Fig. 2.4 shows the curve of the delivered luminosity and the luminosity, recorded by the CMS experiment in 2011 (a) and 2012 (b) summing up to a total of 29.6 fb^{-1} . Such high luminosity results in approximately 12 and 21 average number of events per beam crossing for 7 and 8 TeV data respectively.

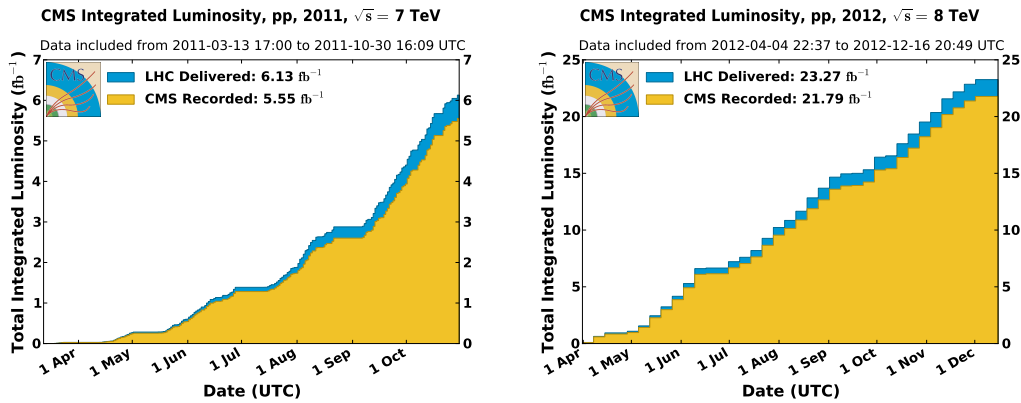


Figure 2.4 – Integrated luminosity delivered by the LHC (blue) and collected by the CMS (yellow) for 2011 (left) and 2012 (right).

2.2 The Compact Muon Solenoid

The Compact Muon Solenoid (CMS) apparatus was built as a multipurpose experiment and it was designed to cover a wide range of measurements in particle physics [21]. Since the question of the origin of the EWSB is one of the primary importance for the modern particle physics, the CMS detector was optimized in particular for the Higgs boson searches as well as for the search for production of supersymmetric particles and search for the resonances at the TeV scale. The geometry of the CMS detector is illustrated in Fig 2.5. A particular attention was drawn to the systems responsible for the detection of electrons, muons and photons.

The central feature of the CMS apparatus is a superconducting solenoid of 6 m internal diameter, providing a magnetic field of 4 T. Such a powerful magnet allows for accurate measurements of the momenta of the charged particles (muons in particular). This provides

2.2. The Compact Muon Solenoid

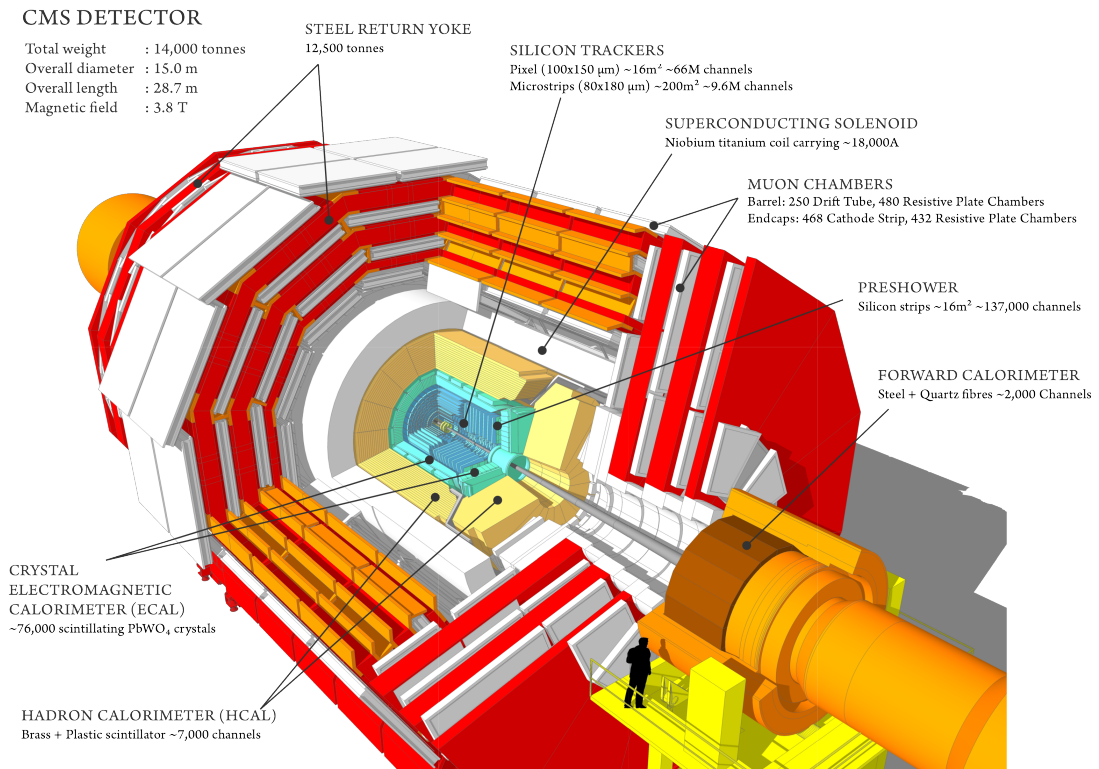


Figure 2.5 – A perspective view of the CMS detector with major subsystems indicated.

the possibility to conduct the measurements of the low-mass hadronic resonances, multi-lepton signatures of the Higgs boson and TeV resonances. For example, for the measurement of the properties of the Higgs boson in the 4μ or $2e2\mu$ final state ($H \rightarrow ZZ^* \rightarrow 4\mu$ or $H \rightarrow ZZ^* \rightarrow 2e2\mu$ decay channel) a very precise muon momentum estimation is needed up to transverse momentum values of ~ 100 GeV. CMS magnet then provides enough bending power for the accurate measurement of the muons track curvature in the inner tracker device.

The inner tracker detector is composed of pixel and silicon strip detectors. It measures the trajectories of all charged particles. Despite the powerful magnet, the measurement of the charged particles with high transverse momentum remains a challenge due to the straightening of the tracks.

Alongside with the silicon pixel and the strip tracker, two more detectors are located within the superconducting solenoid volume: a lead tungstate crystal electromagnetic calorimeter (ECAL) and a brass/scintillator hadron calorimeter (HCAL), each composed of a barrel and two endcap sections. The ECAL is a homogeneous detector consisting of lead tungstate ($PbWO_4$) scintillating crystals that are read out by the avalanche photodiodes or vacuum phototriodes. The photons and electrons develop electromagnetic showers which are nearly fully contained in the ECAL volume. The precision of e/γ energy estimation in the ECAL improves with the energy. The hadron calorimeter (HCAL) surrounds ECAL. It is a sampling calorimeter

Chapter 2: Experimental Setup

consisting of brass absorber plates interspersed with scintillator layers. It is designed to reconstruct the energy and position of the hadrons and jets.

Muons are measured in the gas-ionization detectors embedded in the steel flux-return yoke outside the solenoid. The return field extends to a distance of 1.5 m from the solenoid and allows an integration of four layers of muon detectors. Three different technologies are used: the drift tubes in the Barrel, the cathode strip chambers in the Endcaps and the resistive plate chambers to measure the bunch-crossing timing. All three subdetectors play as well a very important role in the trigger system. Extensive forward calorimetry complements the coverage provided by the barrel and endcap detectors.

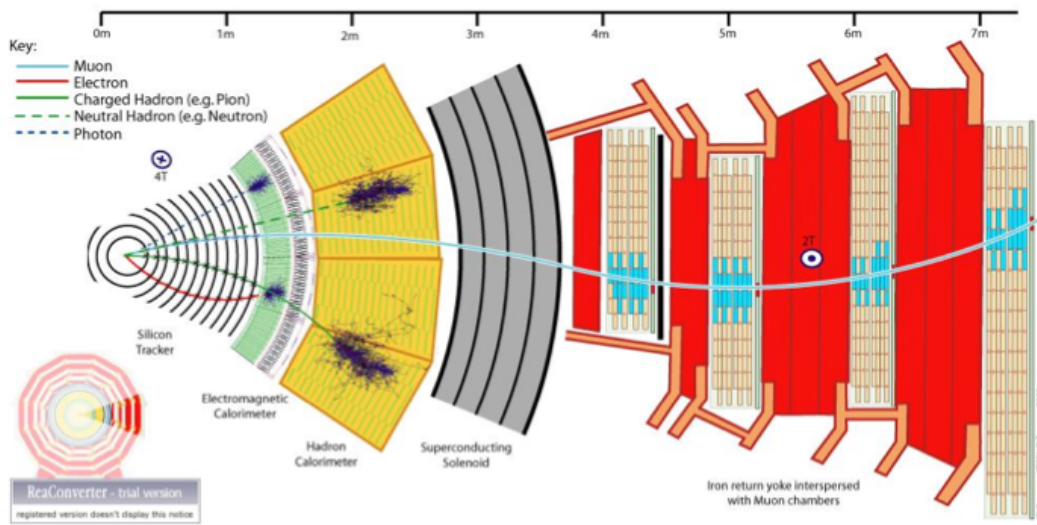


Figure 2.6 – The CMS detector transverse section and particle interactions in it.

Fig. 2.6 describes the interactions of various kinds of particles within the CMS subdetectors. The muons with sufficient transverse momentum cross the entire detector and their tracks are reconstructed both in the inner tracker and in the muon chambers. They essentially behave as minimum ionizing particles (MIPs) in the calorimeters, i.e. they deposit little energy (few hundreds of MeV) in them.

In the next sections a more detailed description of each subdetector listed previously is presented. Since the present thesis work deals in particular with the electron reconstruction, the emphasis is put on the electromagnetic calorimeter and on the tracker, whose measurements are used extensively in the subsequent chapters.

2.2.1 The Coordinate System

In this section we describe the coordinate system which is used in the CMS experiment and data analysis. This coordinate system is illustrated in Fig. 2.7.

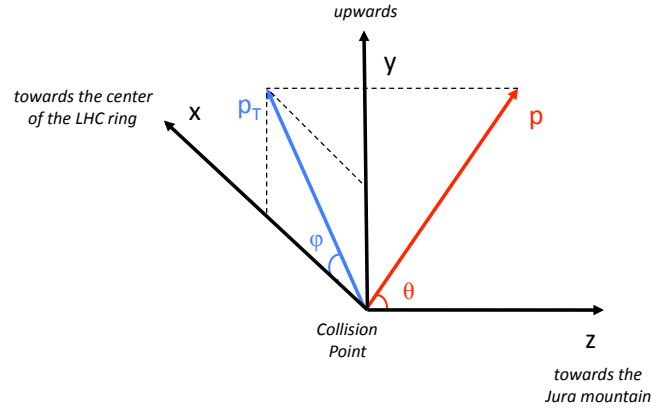


Figure 2.7 – The CMS coordinate system.

This coordinate system is orthogonal and right-handed. Its origin is located at the beams interaction point. The x axis is directed horizontally towards the center of the LHC accelerator ring, while the y axis points vertically upwards. Consequently, the longitudinal (z) axis direction corresponds to the tangent to the beam trajectory given at the interaction point and points towards the Jura mountain. The detector has a cylindrical shape around the beam axis (z axis).

In the transverse (x - y) plane, the azimuthal angle ϕ is measured from the x axis and the radial coordinate is denoted r . The polar angle θ is measured from the z axis. However it is more convenient to use the pseudorapidity⁸ η , defined as $\eta = -\ln \tan(\theta/2)$. These three variables (r, η, ϕ) form another full basis.

An inelastic collision event consist in the collision of two partons: one from a proton of the first beam, and one from a proton of the second beam. The energy of each parton can vary. It is some fraction of the proton energy, so the collision energy is not fixed. However the parton transverse momentum is negligible with respect to its longitudinal momentum since protons in the beam are highly boosted. Under the assumption that the detector is hermetic the total transverse momentum is conserved during an interaction, therefore the transverse momentum of the collision is expected to be negligible too. As a consequence, the particle trajectories are often described in the transverse plane, in particular their transverse energy writes: $E_T = E \sin \theta = \frac{E}{\cosh \eta}$. For a massless particle, the transverse energy is equal to its transverse momentum: $E_T = p_T$. For electrons and muons, and for the energies considered⁹, the masses are negligible, therefore they are considered as massless.

Another very important consequence of the transverse energy conservation is that in this way

⁸The pseudorapidity η is an approximation of the rapidity $\rho = \ln\left(\frac{E+p_z}{E-p_z}\right)$ in the relativistic limit ($\frac{mc^2}{E} \rightarrow 0$).

⁹In general, the studied leptons are reconstructed for $E_T \gtrsim 5$ GeV, and their transverse energy distribution is centered at $E_T \sim 40$ GeV, with a main contribution of leptons from the decays of W and Z bosons.

we can estimate the fraction of energy which is taken away by invisible particles. A particle escaping the detection creates an unbalance in the total transverse energy measurement, also called missing transverse energy (MET). If the detector is hermetic, this MET can be interpreted as the transverse energy of the particles that escape detection, such as neutrinos or new physics particles that interact as little as neutrinos with matter (e.g. neutralinos).

2.2.2 The Magnet

The CMS superconducting magnet is a solenoid, which has a diameter of 6 m and a length of 12.5 m. It is made of flat *NiTb* cable. It was designed to generate a uniform 3.8 T field in the inner barrel region, with a stored energy of 2.6 GJ at full current. Such a high magnetic field is necessary for a precise measurements of charged particles momenta. The magnet is operated at the temperature of 4 K in order to put *NiTb* in the superconducting state and produce a 20 kA current. A vacuum cylinder isolates the magnet from the external environment. A 10000 t return yoke closes the *B*-field lines. It consists of 5 barrel layers and of 3 disks in each of the two endcaps. The ratio between the stored energy and the cold mass is large (11.6 KJ/kg), which causes a rather large mechanical deformation (0.15 %) during the ramp-up phase. The parameters of the CMS magnet are summarized in Table 2.2.

2.2.3 The Inner Tracking System

The CMS tracker is designed for the charge and momentum measurements of charged particles. Surrounding the interaction point, it has a length of 5.8 m and a diameter of 2.5 m. It covers a pseudorapidity range of $|\eta| < 2.5$. The tracker material must be very resistant to the radiation due to its positioning in the vicinity of the collision point.

A very fine granularity in the innermost part is necessary in order to identify the different vertices in a bunch crossing: aside from the primary vertex, which corresponds to the interaction point of the triggered collision, there are other so-called secondary vertices. They can indicate other interactions that occurred during the same bunch crossing (pile-up), or the late decay of a particle.

The choice was made in favor of a full silicon detector technology which can fulfill the above conditions. However this modern and very powerful system has two large disadvantages: first of all, it implies a high power density of on-detector electronics, which requires an efficient cooling system. Secondly, such tracker device, due to the quite high density of silicon and amount of the surrounding mechanics, leads to large material budget as shown in Fig.2.8. For example, it corresponds to 1.9 radiation length at $|\eta| \simeq 1.5$ and to 0.4 at $\eta \simeq 0$.

The particles produced in the collisions interact with the corresponding high amount of dense material when they cross the tracker. This gives rise to multiple scattering, bremsstrahlung, photon conversion and nuclear interactions. Such processes result in complications in particle

2.2. The Compact Muon Solenoid

General Parameters	
Magnetic Length	12.5 m
Cold bore diameter	6.3 m
Central magnetic induction	4 T
Total Ampere-turns	41.7 MA - turns
Nominal current	19.14 kA
Inductance	14.2 H
Stored energy	2.6 GJ
Cold Mass	
Radial thickness of cold mass	312 mm
Radiation thickness of cold mass	3.9 X_0
Weight of cold mass	220 t
Maximum induction on conductor	4.6 T
Temperature margin wrt operating temperature	1.8 K
Stored energy/unit cold mass	11.6 kJ/kg
Iron Yoke	
Outer diameter of the iron flats	14 m
Length of Barrel	13 m
Thickness of the iron layers in Barrel	300, 630, 630 mm
Mass of iron in Barrel	6000 t
Thickness of iron disks in Endcaps	250, 600, 600 mm
Mass of iron in each Endcap	2000 t
Total mass of iron in return yoke	10 000 t

Table 2.2 – A summary of the main features of the CMS magnet.

reconstruction and losses of accuracy and efficiency. Detailed description of these effects and the way to recover the reconstruction quality will be given when dealing with electron objects, in particular in the chapter 3.

Under the nominal LHC conditions approximately 1000 particles every 25 ns will pass through the tracker. This results in a high hit density, which decreases when the distance to the center increases. This means that the tracker must have fine enough granularity and fast response. The hit density can reach values as reported in Tab.2.3.

Hit density	radius (cm)
1 MHz/mm ²	4
60 kHz/mm ²	22
3 kHz/mm ²	115

Table 2.3 – Silicon tracker hit densities.

Then, the tracker granularity is defined by the following condition: in order to ensure the good

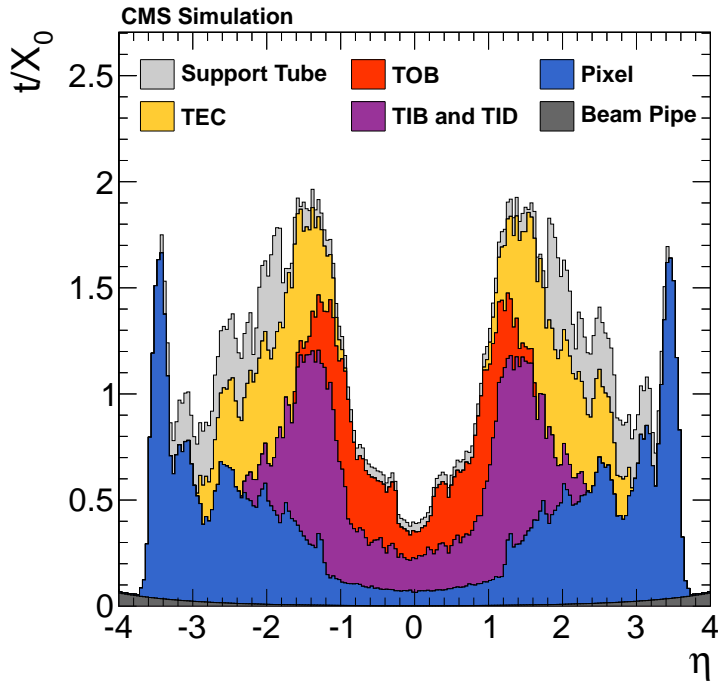


Figure 2.8 – Material budget profile of the tracker simulation: fraction of radiation length x/X_0 as a function of pseudo-rapidity for the different sub-detectors and structures: the beam pipe, the pixel vertex detector, the inner tracker (TIB+TID), the outer barrel (TOB) and endcaps (TEC), the outer structures (support tube, thermal screen and bulkheads).

performance, the occupancy of a detector cell must be kept at a level of $\sim 1\%$ or below.

Since the spatial density of particle tracks decreases with increased distance to the interaction point, it is convenient to have two different kinds of sensors, one for the innermost and another for the outermost. This scheme is implemented in the CMS tracker. Silicon pixels are located at the very core of the detector and deal with the highest intensity of particles. Thicker silicon strips sensors are used for the outer tracker region in order to maintain a signal to noise ratio well above 10. The CMS silicon tracker consists of 13 layers in the barrel region and 14 layers in the endcaps, as illustrated in Fig. 2.9. The innermost three layers consist of $100 \times 150 \mu m$ pixels, 66 million in total. For a primary particle, the pixels provide the three first hits of the track. They allow for a very precise measurement of a particle impact parameter and the identification of secondary vertices.

Some details about the detector sensors can be found in Table 2.4. Overall, the pixel detector covers an area of about 1 m^2 . The silicon strip tracker has a total of 9.3 million strips and 198 m^2 of active silicon area.

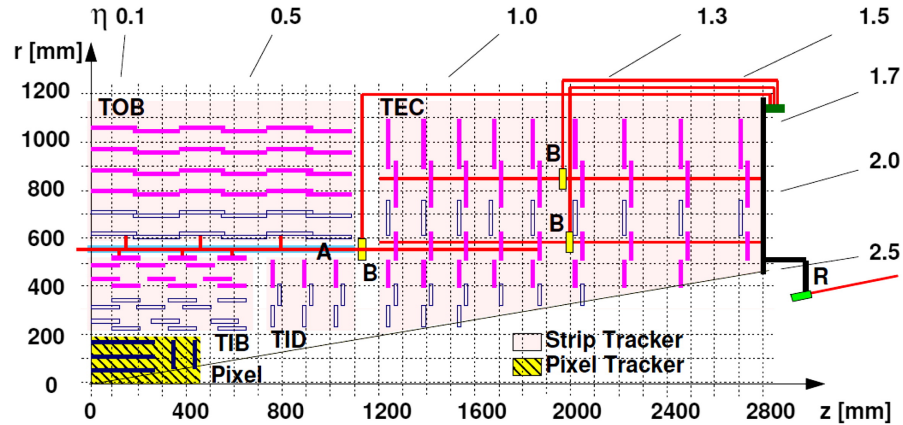


Figure 2.9 – Schematic cross-section of the CMS tracker. Each line represents a detector module. Empty dark blue rectangles indicate back-to-back modules which deliver stereo hits. The pixel detector contains barrel and endcap modules; the silicon strip detector contains two collections of barrel modules: the Tracker Inner Barrel (TIB) and the Tracker Outer Barrel (TOB), and two collections of endcap modules: the Tracker Inner Discs (TID) and the Tracker EndCaps (TEC). 'A' denotes an alignment tube of the laser alignment system, 'B' - beam splitters. The optical coming out from beam splitters are marked as red lines.

	region (as in Fig.2.9)	size in $r - \phi$ and z	occupancy
pixel detector	PIXEL	$100 \times 150 \mu\text{m}^2$	10^{-4} per pixel
silicon strip tracker (1)	TIB + TID	$10 \text{ cm} \times 80 \mu\text{m}^2$	2 – 3% per strip
silicon strip tracker (2)	TOB + TEC	up to $25 \text{ cm} \times 180 \mu\text{m}^2$	$\sim 1\%$ per cell

Table 2.4 – Structure of the Silicon Tracker Detector.

To prevent from overheating and thermal runaway¹⁰, the silicon tracker is coupled to a cooling system made of liquid Perfluorohexane (C_6F_{14}), and operates only at a temperature below -10°C except for short maintenance period.

The expected resolution of the tracker on several track parameters is shown in Fig. 2.10, for muons of different transverse momenta and as a function of the pseudorapidity. The muon transverse momentum resolution varies according to its direction and transverse momentum: a resolution of $\sim 1\%$ in the most central region, and raising to $\sim 3\%$ for high pseudorapidities, is expected in the p_T range of W and Z boson decays ($p_T \sim 40 \text{ GeV}$).

¹⁰The increased detector leakage current can lead to a dangerous positive feedback of the self-heating of the silicon sensor and subsequently to the exponential dependence of the leakage current on temperature.

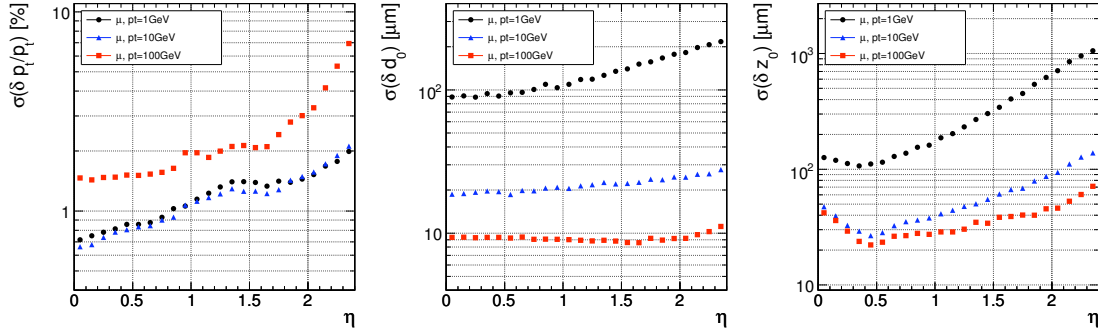


Figure 2.10 – Resolution of several track parameters as a function of the pseudorapidity for single muons with transverse momenta of 1, 10 and 100 GeV, using only the tracker information: transverse momentum (left), transverse impact parameter (middle), and longitudinal impact parameter (right).

2.2.4 The Electromagnetic Calorimeter

The Electromagnetic Calorimeter (ECAL) was mainly designed according to the requirements of the $H \rightarrow \gamma\gamma$ search. It is the only subdetector to provide information on photons. For a precise diphoton mass reconstruction, a very accurate position and energy measurement must be provided by the ECAL.

The ECAL is also of primary importance for the electron reconstruction in the Higgs boson analysis in a multi-lepton final state. The combination of its information with the one from the tracker allows for a very precise measurement of the electrons position and momentum and a significant background reduction. A good segmentation is essential to distinguish the shape of the energy deposit for an electromagnetic particle from the one of a hadronic particle.

The CMS ECAL is a hermetic and homogeneous calorimeter, that covers the rapidity range of $|\eta| < 3$. It is made of 75848 lead tungstate ($PbWO_4$) crystals, mounted in a barrel ($|\eta| < 1.479$) and two endcaps ($1.479 < |\eta| < 3.0$). The characteristics of the $PbWO_4$ ensure a fast response, a fine granularity, and a good radiation resistance of the detector.

The readout and amplification of the signal from the ECAL crystals is provided by two types of photodetectors. Avalanche photodiodes (APDs) are used in the barrel and vacuum phototriodes (VPTs) are used in the endcaps. The latter choice is motivated by the higher radiation in the endcaps.

A preshower detector, covering the $1.6 < |\eta| < 2.6$ pseudorapidity range, is installed in front of the ECAL endcaps. It is needed in order to ensure sufficient π^0/γ separation since the pion rate is particularly important in the forward region. The decay $\pi^0 \rightarrow \gamma\gamma$ gives two photons very close to each other, which is quite difficult to distinguish from a single photon.

A longitudinal view of the electromagnetic calorimeter is shown in Fig. 2.11.

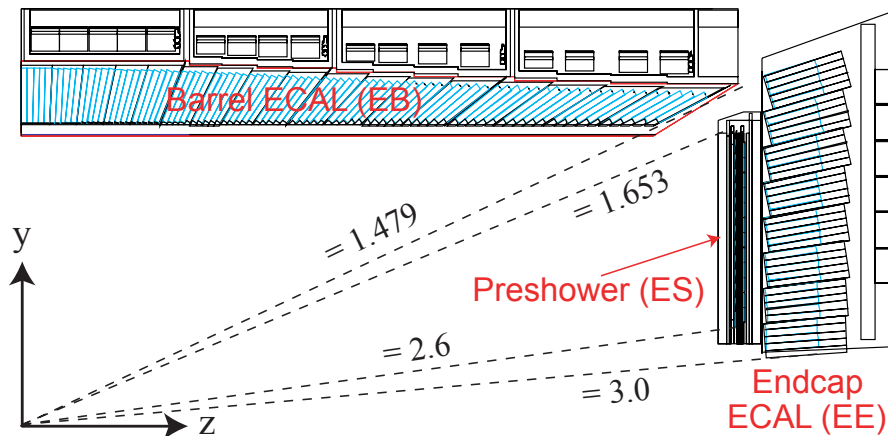


Figure 2.11 – Longitudinal view of part of the CMS electromagnetic calorimeter showing the ECAL barrel and an ECAL endcap, with the preshower in front.

ECAL Crystals and Geometry

The choice of ECAL crystals material is driven by general constraints assigned by the design of the CMS detector. Following these constraints, the calorimeters should be placed inside the magnet system which means it has to be very compact. In the language of electromagnetic interactions between the particles and matter this means that the ECAL material should have a short radiation length¹¹. The second requirement is the good separability of the electromagnetic showers. Since the ECAL is quite compact and located not far from the interaction point, this condition can be fulfilled only with a small Molière radius¹² of the used material. Finally, the scintillation decay time of the crystals should be fast enough for the context of LHC collisions rate.

The lead tungstate crystals are the good option which ensure all the above requirements. Lead tungstate high density (8.28 g/cm^{-3}) and short radiation length of 0.89 cm ensure the possibility to have reasonably short crystals. In the units of radiation length, crystals of $25.8 X_0$ are used in the barrel and $24.7 X_0$ in the endcaps. The Molière radius of 2.2 cm allows for an electromagnetic shower to be very compact in the transverse direction. Hence the use of thin crystals of typical face cross section $2.2 \text{ cm} \times 2.2 \text{ cm}$ (in the barrel, $2.6 \text{ cm} \times 2.6 \text{ cm}$ in the endcaps), which ensure a good shower separation.

Nevertheless the light output (i.e. the amount of light transferred to the photodetectors) is relatively low and varies with temperature. To ensure a stable response, a cooling system has

¹¹A material's radiation length is the mean distance over which a high-energy electron loses all but $1/e$ of its energy by bremsstrahlung; this is equal to $7/9$ of the mean free path for pair production by a high-energy photon.

¹²The Molière radius R_M is a characteristic constant of a material giving the scale of the transverse dimension of the fully contained electromagnetic showers initiated by an incident high energy electron or photon. It is defined as the mean deflection of an electron of critical energy after crossing a width $1X_0$. A cylinder of radius R_M contains on average 90% of the shower's energy deposition.

Chapter 2: Experimental Setup

been installed, maintaining the crystals and photodetectors at a temperature of $18^\circ\text{C} \pm 0.05^\circ\text{C}$, decoupled from the cold silicon tracker, and the readout electronics. The temperature is also monitored during data taking.

The barrel part of the ECAL covers the pseudorapidity range $|\eta| < 1.479$, with a granularity 360-fold in ϕ and (2×85) -fold in η . The centers of the front faces of the crystals are at a radius 1.29 m.

The endcaps cover the rapidity range $1.479 < |\eta| < 3.0$. The longitudinal distance between the interaction point and the endcap envelope is 315.4 cm.

A comparison of the number and dimensions of crystals in the barrel and the endcaps is given in Table 2.5.

	Barrel	Endcaps
number of crystals	61200	14648
crystal cross-section in (η, ϕ)	0.0174×0.0174	not fixed
crystal cross-section at the front face	$22 \times 22 \text{ mm}^2$	$28.62 \times 28.62 \text{ mm}^2$
crystal cross-section at the rear face	$26 \times 26 \text{ mm}^2$	$30 \times 30 \text{ mm}^2$
crystal length	230 mm	220 mm
	$25.8 X_0$	$24.7 X_0$

Table 2.5 – The ECAL crystals.

The crystals are mounted in a quasi-projective geometry with the tilts between them, so that their axes make a small angle (3° in the barrel, 2° to 8° in the endcaps) with respect to the vector from the nominal interaction vertex, in both the ϕ and η projections. This is needed in order to avoid the possibility for particles to cross the detector always being on the edge of the crystal.

Mechanically, the ECAL barrel is made of 36 identical *supermodules*, each covering half the barrel length ($-1.479 < \eta < 0$ or $0 < \eta < 1.479$), with a width of 20° in ϕ . Each *supermodule* is splitted into four *modules* in the η direction (see Fig. 2.12). The presence of acceptance gaps, called cracks, between *modules*, complicates the energy reconstruction. A larger crack is present in the border $\eta = 0$ between supermodules, and an even larger one marks the barrel-endcap transition.

Each ECAL endcap is made of two semi-circular plates called *dees* (see Fig. 2.12). Small cracks are also present between the endcap dees, but their effect is negligible.

In order to account for energy loss in the barrel cracks different sophisticated algorithms for electrons and photons were developed. They will be described in more details in the subsequent chapters.

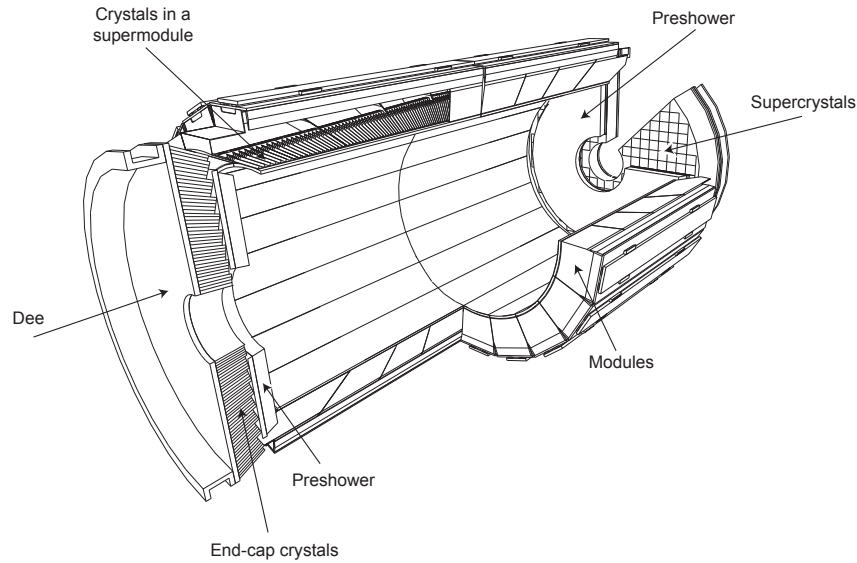


Figure 2.12 – Layout of the CMS electromagnetic calorimeter showing the arrangement of crystal modules, supermodules and endcaps, with the preshower in front.

Photodetectors

The photodetectors were developed specially for the CMS due to very high and quite unusual requirements for the photodetectors such as the ability to operate in the intense magnetic field and under the strong ionisation radiation. According to the different expected levels of radiation, two different kinds of photodetectors are used for the barrel and for the endcaps.

Avalanche photodiodes (APDs) are used in the barrel. Each APD has an active area of $5 \times 5 \text{ mm}^2$ and a pair is mounted on each crystal. They are operated at a gain of 50 and read out in parallel. The APDs are a good option for the ECAL barrel part, but cannot be explored in the ECAL endcaps due to the higher level of radiation.

Vacuum phototriodes (VPTs) are used in the endcaps. Each VPT is 25 mm in diameter, with an active area of $\approx 280 \text{ mm}^2$; one VPT is glued to the back of each crystal. They have a single gain stage, with a value of ~ 10.2 at zero magnetic field; a 4 T magnetic field lowers this value by less than 10%. Compared to the APDs, the lower quantum efficiency and internal gain of the VPTs is compensated by their larger coverage area on the back face of the crystals.

Preshower

The preshower is a 20-cm thick sampling device, made of two parts located at each end of the tracker, in front of each ECAL endcaps, in the pseudorapidity range $1.653 < |\eta| < 2.6$ (see Fig. 2.12). It has an absorber, made of lead radiators, which initiates electromagnetic showers

Chapter 2: Experimental Setup

from the incoming electrons and photons and two layers of silicon strip sensors positioned with orthogonal orientation behind each radiator. These sensors measure the energy deposit and the transverse shower profiles for a better identification of electromagnetic particles.

Each silicon sensor measures $63 \times 63 \text{ mm}^2$, with an active area of $61 \times 61 \text{ mm}^2$, divided into 32 strips. The nominal thickness of the silicon is $320 \mu\text{m}$.

An electron or a photon emitted in the direction of the preshower, deposits $\sim 5\%$ of its energy in the preshower, and the rest in the ECAL endcap.

Laser Monitoring

Despite the ECAL lead tungstate crystals are resistant to radiation they are not insensitive to it. Their optical transparency varies (decreases) by few percent during a run. This happens due to the production of color centers which absorb a fraction of the transmitted light.

The effect is neither constant nor uniform: it is more visible for higher radiations, e.g. higher luminosity, or higher pseudorapidity for a given luminosity. Moreover, at the ECAL temperature of 18°C , this effect tends to be compensated by an annealing effect¹³.

The LHC conditions are such that runs last ≈ 10 hours of collisions alternating with ≈ 1 hour machine refills breaks. Under such conditions the crystal transparency has a cyclic behavior, with a progressive degradation during the runs (when the radiation effect dominates), and a fast recovery during the breaks (because of the annealing).

The magnitude of the changes is dose-rate dependent, and is expected to range from $1 - 2\%$ at low luminosity in the barrel, to tens of percent in the high η regions of the endcaps at high luminosity.

Such evolutions must be taken into account for a proper calibration of the detector. Hence a regular measurement of the crystal transparency is performed, using laser pulses injected into the crystals via optical fibres. The response is normalized by the laser pulse magnitude measured using silicon PN photodiodes. The ratio of the crystal response to the photodiode measurement gives the crystal transparency. The corrections which accounts the transparency losses are then applied to the measured particle energy.

Detector Calibration

The main source of channel-to-channel deviations is the difference between the crystal scintillation light yields. The total variation among all barrel crystals is $\approx 15\%$; the dispersion is higher in the endcaps ($\approx 25\%$), because of non-negligible variations in the VPTs, like the gain.

¹³Annealing consists in heating a material to a temperature higher than the recrystallization temperature, maintaining a suitable temperature, and then cooling.

Corrections from laboratory measurements and calibration of crystal light yield and photodetector/electronics response reduced the initial channel-to-channel variation to less than 5% in the barrel and less than 10% in the endcaps.

A good precision on intercalibration constants was further achieved for the whole barrel ($< 2\%$) with the use of cosmic rays, with a further improvement for nine supermodules of the barrel ($\sim 0.5\%$) and 500 crystals in the endcaps ($< 1\%$), with electron test beams.

In order to reach the ultimate intercalibration precision, the data-driven techniques are used:

- the ϕ -symmetry method [22, 23], based on the assumption that the total transverse energy deposited from the minimum bias events should be the same for all crystals in a ring at a fixed pseudorapidity
- the π^0 calibration method [24], which consists in levelling the peak positions for individual crystals.

A global correction factor, corresponding to the detector energy scale is added to the intercalibration corrections. After application of all the corrections the energy scales in the ECAL barrel and ECAL endcap have been measured using $Z \rightarrow e^+ e^-$ events and systematic errors have been evaluated to be 0.1% for the barrel factor and 0.5% for the endcap factor. This will be described in details in the chapter 3

Energy Resolution

The energy resolution has been measured with electrons, during a test beam in 2004 [25]. The result is shown in Fig. 2.13. The resolution is composed of a stochastic, a noise and a constant contribution terms as follows:

$$\frac{\sigma(E)}{E} = \frac{2.8\%}{\sqrt{E}} \oplus \frac{0.12}{E} \oplus 0.30\%, \quad (2.5)$$

For electrons of energy higher than 15 GeV a resolution better than 1% is achieved while for typical electrons from Z boson, i.e. 40 GeV electrons it is of 0.6%.

These results correspond to optimal conditions: the electrons hit the center of a crystal, so the energy loss corresponding to crystal junctions, and the effect of the angle of incidence variation (due to the magnetic field), are minimized. The same tests applied on electrons hitting uniformly the crystal, showed that after a general energy correction the resolution is $\sim 0.15\%$ worse than the previous results (for 120 GeV electrons).

Position Resolution and Alignment

The ECAL position resolution reflects the fluctuations of the energy measurements, and follows the same dependence in energy as (2.5). The studies based on simulations demonstrate that a

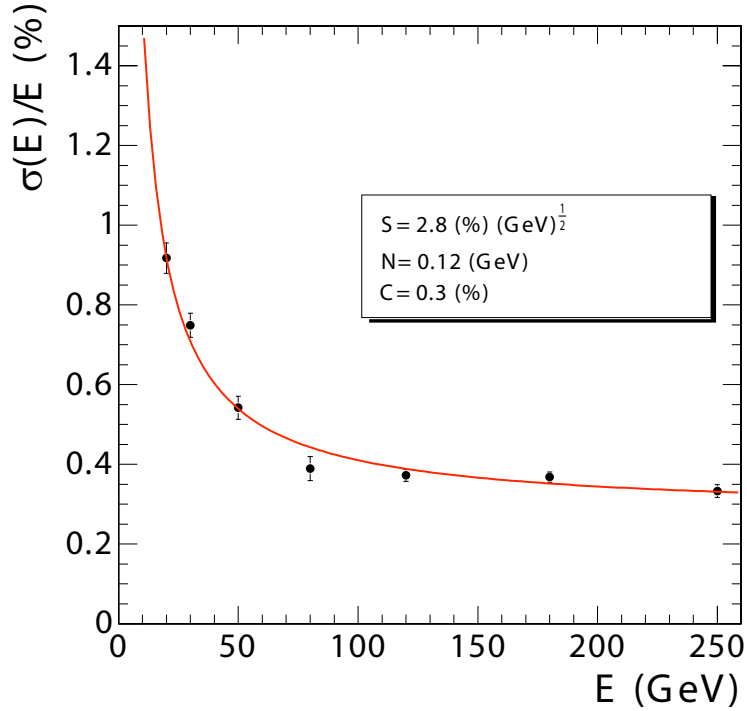


Figure 2.13 – ECAL barrel energy resolution, $\sigma(E)/E$, as a function of electron energy as measured from a test beam. The energy was measured in an array of 3×3 crystals with an electron impacting the central crystal. The stochastic, noise, and constant contributions are shown.

resolution of about 10^{-3} units in η and 1.6 mrad in ϕ can be reached on 35 GeV electrons; in terms of distance, this corresponds to ~ 2 mm for each coordinate (x, y) .

These expectations were confirmed by test beam experiments [25]. *In situ* measurements taken to align the ECAL and the tracker provide similar results.

2.2.5 The Hadron Calorimeter

The hadron calorimeter (HCAL) plays a major role in the measurement of hadron jets. It is located right after the electromagnetic calorimeter and completes the set of subdetectors located within the CMS magnet system.

From the point of view of a Higgs boson analysis in a multi-lepton final state, the HCAL measurement is very useful to distinguish electrons from hadron jets.

Like the ECAL, the HCAL contains a barrel part (HB) and two endcap parts (HE). It must provide a sufficient containment to stop hadron showers. Besides, the coverage in pseudorapidity, a wider than the ECAL one, is necessary to have a full description of the total collision

event, allowing for a reliable measurement of the missing transverse energy. To ensure a full containment and wide rapidity coverage, the HCAL is completed by two other calorimeters: the outer HCAL (HO) and the forward HCAL (HF).

The HCAL Barrel is a sampling calorimeter covering the pseudorapidity range $|\eta| < 1.3$. It is radially restricted, between the outer extent of the ECAL and the inner extent of the magnet coil: $1.77 \text{ m} < R < 2.95 \text{ m}$. Flat brass absorber plates are used in the HCAL Barrel, with a segmentation of $(\Delta\eta, \Delta\phi) = (0.087, 0.087)$. The HB effective thickness increases with polar angle (θ) as $1/\sin\theta$, resulting in $10.6 \lambda_I$ at $|\eta| = 1.3$, where λ_I is the nuclear interaction length¹⁴. The ECAL depth in front of HB in units of interaction length adds about 1.1λ of material.

The HCAL Endcaps cover a wide rapidity range: $1.3 < |\eta| < 3$. The forward hadron calorimeters (HF) placed at a distance of 11.2 m from the interaction point extend the pseudorapidity coverage up to $|\eta| < 5.2$.

The material in the HCAL Endcaps must handle high counting rates and are subjected to a consequent level of radiation. Due to the magnetic field, the absorber should be made from a non-magnetic material. Finally, the HE must fully contain hadronic showers. These considerations lead to the choice of C26000 cartridge brass. The total length of the calorimeter, including electromagnetic crystals, is about 10 interaction lengths.

Given the wide pseudorapidity coverage, the different calorimeter parts experience very different particle fluxes. This is the reason of the use of different material, depending on the radiation level, and on the particular goal of each part.

The structure of the Hadron Calorimeter is illustrated in Fig. 2.14.

The HO uses the solenoid coil as an additional absorber equal to $1.4/\sin\theta$ interaction lengths and is used to identify late starting showers and to measure the shower energy deposited after HB. Scintillation light from the tiles is collected using multi-clad Y11 Kuraray wavelength shifting (WLS) fibres.

On average, 760 GeV per proton-proton interaction is deposited inside the two forward calorimeters, compared to only 100 GeV for the rest of the detector. For that reason, the HF calorimeter uses a Cherenkov-based, radiation-hard technology, with quartz fibres.

In order to estimate the hadron energies all the calorimeter sub-detectors (electromagnetic calorimeter, hadron calorimeter and outer tail-catcher) are used. The resulting resolution in the barrel (provided by the combination of EB, HB and HO measurements) has been

¹⁴The nuclear interaction length is the mean path length in which the energy of relativistic charged hadrons is reduced by the factor $1/e$ as they pass through matter.

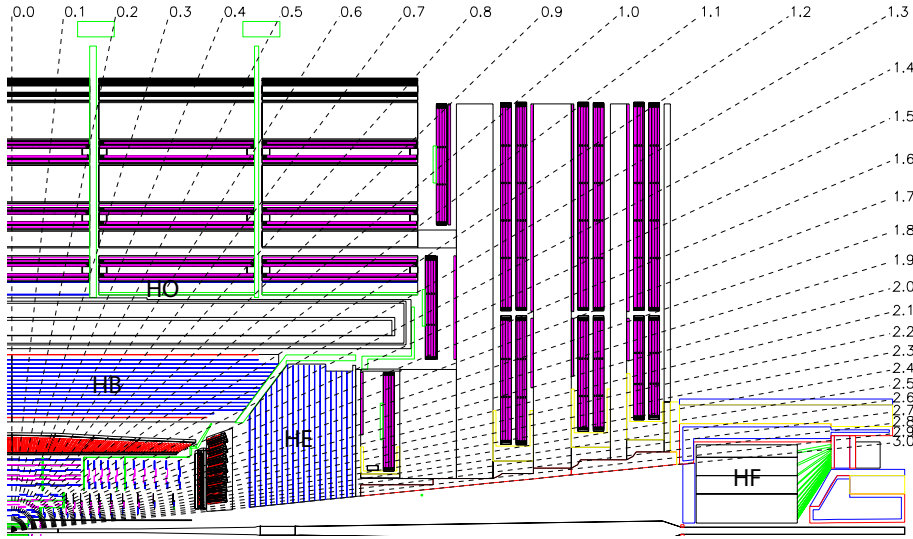


Figure 2.14 – Longitudinal view of the CMS detector showing the locations of the hadron barrel (HB), endcap (HE), outer (HO) and forward (HF) calorimeters.

determined with pions of varying energy (3 – 500 GeV) in test beams, and found to be:

$$\left(\frac{\sigma(E)}{E}\right) = \left(\frac{84.7\%}{\sqrt{E}}\right) \oplus 7.4\% . \quad (2.6)$$

This resolution is dominated by the HCAL contribution.

2.2.6 The Muon System

Given that muons behave like minimum ionizing particles (MIPs), they have a very specific and easily identified behaviour, but are not so easy to detect. Muons pass through tracker and both the calorimeters (ECAL and HCAL) almost without losing energy, whereas all the remaining particles are absorbed there. Therefore muon detectors are located outside of the CMS magnet.

Thanks to the high field solenoid magnet and its flux return yoke the accuracy of muons energy and position measurements remain good in a wide range of phase space. In addition, having a very clear signature of muons, muon system provides the possibility to have efficient muon triggers and a precise measurement of muon momentum and charge, even without relying on information from the tracking system.

Muons play a major role in many physics analyses, particularly in the Higgs boson search in a multi-lepton final state. The topology of the final state of $H \rightarrow ZZ \rightarrow 4\mu$ (and other such processes e.g. some SUSY particles decays) analysis motivates the construction of a muon

system with a wide angular coverage, with no acceptance gap.

Following the shape of the CMS solenoid, the muon systems is divided into a cylindrical barrel section, and two planar endcap regions. 25000 m² of detection planes are used in robust muon chambers.

The barrel region benefits from the almost uniform 4-T magnetic field (mostly contained in the steel yoke) and a comparably low muon rate. In the central barrel part the drift tube (DT) chambers are used, with the standard rectangular drift cells. They cover the pseudorapidity region $|\eta| < 1.2$. There are two types of chambers, measuring the muon coordinate in the $r - \phi$ bending plane and along z direction. The first three muon stations contain 8 chambers each: four chambers of each kind. Different chambers are alternating each other. The last one doesn't contain the z -measuring plane. The presence of cracks (dead spots in efficiency) is solved by introducing the offset of the drift cells between the neighbor chambers.

Contrary to the barrel, the endcaps cover a region of higher rates and non-uniformity of the magnetic field. Cathode strip chambers (CSC) are used there dealing with $0.9 < |\eta| < 2.4$ pseudorapidity range. They are multi-wire proportional chambers made of two cathode planes, one of which is segmented into strips, and of an array of anode wires laying between these two planes. Each of the four stations contains six layers of chambers and anode wires. The chambers are positioned perpendicular to the beam line and provide a precision measurement in the $r - \phi$ bending plane, whereas the anode wires provide measurements of η and the beam-crossing time of a muon.

Finally, a complementary system, consisting of resistive plate chambers (RPC) was added in both barrel and endcap regions. It covers a large portion of the rapidity range ($|\eta| < 1.6$). The RPCs are double-gap chambers, operated in avalanche mode to ensure a good operation at high rates: six layers are present in the barrel and three in each endcap. These chambers are not so accurate in position resolution as DTs or CSCs but produce a fast response, with a good time resolution. This allows RPCs to be used as an independent trigger system. Besides this, combining the hits from different chambers (and from the tracker) help to reduce ambiguities while reconstructing muon tracks.

In order to increase the precision of the muon measurements, sophisticated alignment system is used to measure the positions of each muon detector with respect to the others and to the inner tracker. A general representation of the muon system is shown in Fig. 2.15. The expected resolution of the transverse momentum of muons is of $\sim 10\%$ in the barrel and $\sim 20\%$ in the endcaps, for muons from W or Z boson decays ($p_T \sim 40$ GeV). For the global muon objects, the momentum is measured by the combination of the tracker and the muon system informations. Figure 2.16 shows the effect of this combination: in the p_T range below ~ 100 GeV, mainly the tracker contributes to the transverse momentum measurement. However for higher p_T values, the muon system information provides a significant improvement.

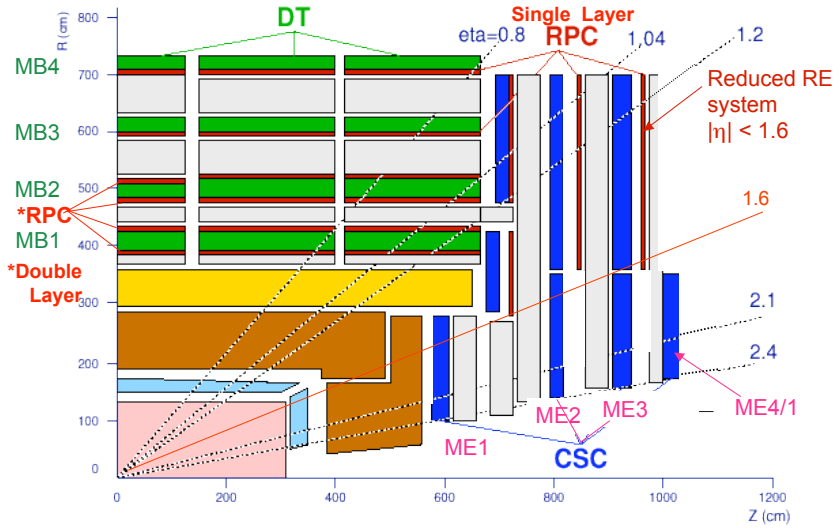


Figure 2.15 – Longitudinal view of the muon detectors: DT, RPC and CSC.

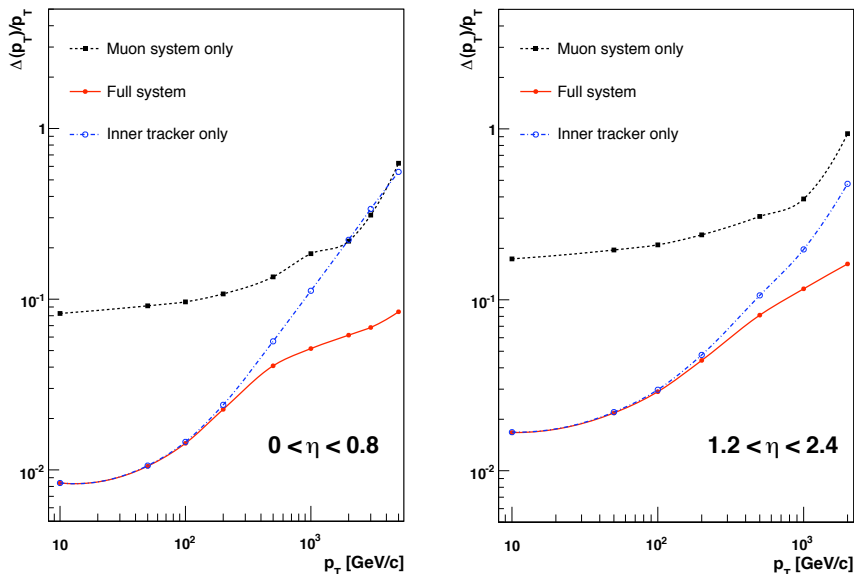


Figure 2.16 – The muon transverse momentum resolution as a function of the transverse momentum (p_T) using the muon system only (black dotted line), the inner tracker only (blue dashed line), and both (red solid line). Left panel: $|\eta| < 0.8$, right panel: $1.2 < |\eta| < 2.4$.

2.2.7 The Trigger System

The trigger system is a first event selection step. Unlike the different analysis selections, this one is not reversible so we should be very accurate in building of its algorithms. The bunch crossing rate at the CMS interaction point is 40 MHz, but no more than 300 Hz of data can be written on tape, since a typical raw event size is 1 MB. The trigger system must reduce this rate

in an optimal way, keeping as many interesting high-energy events as possible while discarding low-energy processes. Since the LHC bunch crossing time is 25 ns, the trigger decisions must be taken in a very short time. This is achieved by splitting the whole workflow in two steps or 'levels': L1 and High Level Trigger (HLT). Each of them reads out and processes only a limited fraction of the available information. The level-one step is totally hardware-based, whereas HLT is a set of software requirements. The HLT algorithms take as input relatively few events, therefore it is possible to analyse them in a more detailed way even if the available time is short.

The Level-1 Trigger

The L1 trigger consists of mostly custom-designed, programmable hardware capable of bringing down the event rate from the initial 40 MHz to 100 kHz. The full data content is stored in

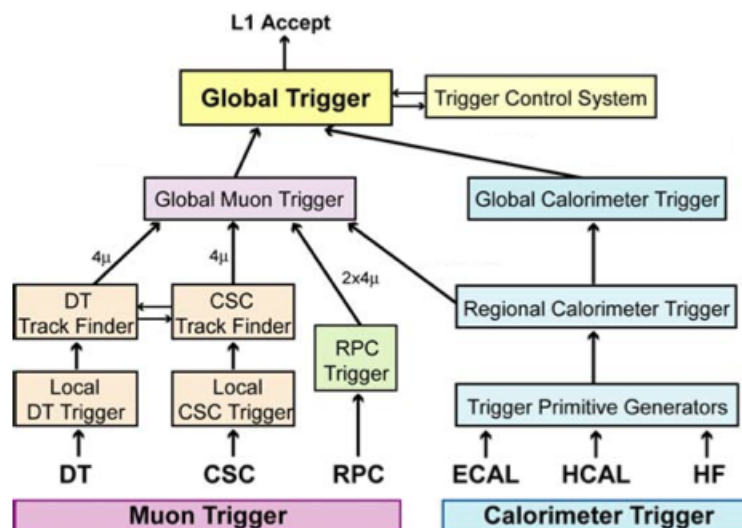


Figure 2.17 – Schematic representation of the CMS L1 trigger system.

the pipelines of processing elements until the trigger decision is taken. The maximum allowed latency is $3.2 \mu\text{s}$, after which, if the L1 accepts the event, the data starts being processed by the High Level Trigger. Since it would not be possible to read out and analyse the whole information contained in an event, mostly because of the time needed by tracking algorithms, only calorimeters and muon chambers are involved in the L1 step, as shown in Fig. 2.17.

The Calorimeter Trigger finds out the four 'best' candidates per event of each of the following categories: electrons, photons and jets. These candidates are handed over to the Global Calorimeter Trigger (GCT), along with the measured missing E_T .

The Muon Trigger is performed independently by DTs, CSCs and RPCs. The DT and CSC triggers carry out a local muon reconstruction by comparing the slopes of track segments built

in subsequent detector layers. The RPC trigger compares a given muon track with predefined hit patterns depending on the track p_T . The four best muon candidates are passed to the Global Muon Trigger system, which is in charge of matching those from DTs and CSCs with those from RPCs and of discarding low-quality tracks. The L1 electronics is installed partly directly on the detectors, partly in the underground control room about 20 m far from the experimental cavern.

The High Level Trigger

The HLT is a software system running on a farm of about 1000 CPUs, designed to reduce the event rate down to the final output of ~ 300 Hz that can be written on tape.

The HLT trigger makes use of the longer time available to process the event and exploits the data in pipelined memories in the front-end electronics as well as the information from the silicon tracker. It is subdivided into so-called "regional triggers" in order to reconstruct objects only in the useful regions. This allows to reject uninteresting events as soon as possible and gain time for more sophisticated calculations. The L1 and HLT schema lead to the development of three "virtual trigger" levels: at the first level only the full information of the muon system and of the calorimeters is used, in the second level the information of the tracker pixels is added and in the third and final level the full event information is available.

2.2.8 Leptons And Photons Signatures In CMS

Electrons and Photons

Electrons (here and after used as a generic term for electrons and positrons) are very light charged particles. Therefore they interact a lot with the silicon tracker material producing hits in the sensors on their trajectory. After crossing the inner tracker, electrons are absorbed by the ECAL. Due to the high magnetic field and the fact that the electron is charged, the trajectories of electrons in the tracker are bended. The orientation of the curvature allows the charge determination and its magnitude provides an estimation of the electron momentum. Thus, we have two complementary measurements: the momentum from the inner tracker and the energy deposit from the ECAL. However since electrons interact a lot with the tracker material they also emit significant amount of bremsstrahlung radiation which complicates the electron momentum determination as well as the energy deposit collection in the ECAL. Basically, we can draw the following picture: electron, being a charged object, leaves a track in the silicon tracker and then creates a high local deposit of energy in the ECAL. However we need to apply some more sophisticated reconstruction techniques in order to achieve the best accuracy and performance. All the phenomena related to the electron reconstruction and its momentum determination will be detailed in the following chapter.

The difference between the photons and the electrons is that the photon is neutral and doesn't leave any hit in the tracker. However due to the interaction with the surrounding matter a

photon could be converted into an e^+e^- pair and then we will see two tracks emerged from the same point in the tracker. If this happens all the further treatment is identical to the listed above treatment of electrons. Otherwise photon will make a very local energy deposit in the electromagnetic calorimeter and this is the only way to measure its energy. The methods of amelioration of the photon energy determination in the ECAL are quite similar to the ones used for electrons. However photons do not produce hits in the tracker and there is no complementary momentum estimation for photons as there is for electrons.

Muons

Muons (and antimuons), being charged particles, leave a track in the silicon tracker. They are minimum ionizing particles and hence cross the tracker and both the electromagnetic and hadron calorimeters almost without energy losses. Then they keep going through the muon systems located outside of the return yoke. Hence, muon (or antimuon) objects are the association of two tracks: one in the silicon tracker (or *tracker track*), and a second one in the muon systems (or *standalone track*). Notice that the curvatures have opposite signs because of different magnetic field directions inside and outside the magnet.

An ideal muon object, called *global muon*, is made of these two tracks: starting from a standalone track in the muon system, a matching tracker track is found and a global-muon track is fitted combining hits from the tracker track and standalone-muon track.

If no complete standalone track is reconstructed, the muon object is built from the inner track: this track is extrapolated to the muon system and matched to a muon segment (i.e. a short track stub made of DT or CSC hits): this is a *tracker muon*.

Finally, if only a standalone track is found, given the very low background rate in the muon systems, the object is also qualified as a muon: a *standalone muon*.

The degree of curvature gives the muon transverse momentum (p_T), while the orientation of the curvature determines its charge. For a global muon, these parameters are mainly based on the tracker information, because of the very precise inner tracking system. However at high p_T the muon system contributes more to the momentum determination due to the high lever arm.

3 Electron Measurements At CMS

The information needed to reconstruct electrons is provided by two CMS sub-detectors: the inner tracker and the electromagnetic calorimeter. The inner tracker allows to measure the electron charge and momentum while the ECAL allows to measure its energy. The combination of the tracker and ECAL measurements allows to increase the accuracy of the electron momentum determination. The ECAL energy resolution improves at higher energy while the tracker momentum resolution decreases due to the straightening of the electron trajectory. The tracker and ECAL resolution curves cross at the energy ~ 20 GeV. The contribution from each measurement to the combined momentum depends on their relative errors. The precision of measurement in the tracker and ECAL depends on the pattern of the electron energy loss. We provide a classification of electrons in order to ensure the best treatment of each case. When the electrons are split into classes and each one receives the proper estimation of its momentum in the tracker and energy in the ECAL, we combine these measurements and apply the final energy corrections, related to the detector operational conditions. Throughout the first part of my thesis period my work was concerning the reoptimization of the electron classification and the improvement of the tracker and ECAL measurements combination as well as electron energy scale corrections implementation. The final electron momentum estimation and energy resolution are important for the various physics analyses which involve electrons in the final state. In particular these results were used in the estimation of the per-lepton uncertainties for the Higgs boson mass measurements in the $H \rightarrow ZZ \rightarrow 4\ell$ decay channel, as it will be described in Sec. 4.6.

The above mentioned points determine the structure of the current chapter: firstly we set the playground for the electron reconstruction, listing the possible ways to measure the electron energy in the ECAL and momentum in the tracker and how we can get the electron candidate, then the electron classification and combination procedures are described and finally we present the electron energy scale corrections implementation.

3.1 Measurement of the electron energy in the ECAL

As it was mentioned in the Sec. 2.2.4, the CMS electromagnetic calorimeter consists of lead-tungstate crystals, assembled in supermodules. When traversing the material electrons start to develop an electromagnetic shower. The test beam measurements show that for an ECAL barrel supermodule electrons with an energy of $E^e = 120$ GeV impinging at the center of a crystal deposit about 97% of their initial energy in a cluster which consists of 5×5 crystal window [26]. The CMS operational conditions imply also large magnetic field, therefore the electron energy deposit is mainly spread in ϕ direction due to the bremsstrahlung emission along the electron trajectory in the tracker. Thus, in order to account for this spread and fully collect the electron energy we need to create a *supercluster*, combining the clusters in ϕ direction. There are two algorithms used on this purpose: the 'hybrid' algorithm (in the ECAL barrel) and 'multi 5×5 ' (in the ECAL endcaps).

The 'hybrid' algorithm is forming superclusters by grouping dominoes within a ϕ window around the starting crystal up to a maximum extension of 0.3 rad in both directions. The dominoes size $\eta \times \phi$ is 5×1 if the central crystal energy is greater than 1 GeV. Central crystal of each domino should have the same η coordinate as starting one. Schematically 'hybrid' algorithm is shown in Fig. 3.1 (left). Since the endcaps are not following the $\eta - \phi$ geometry,

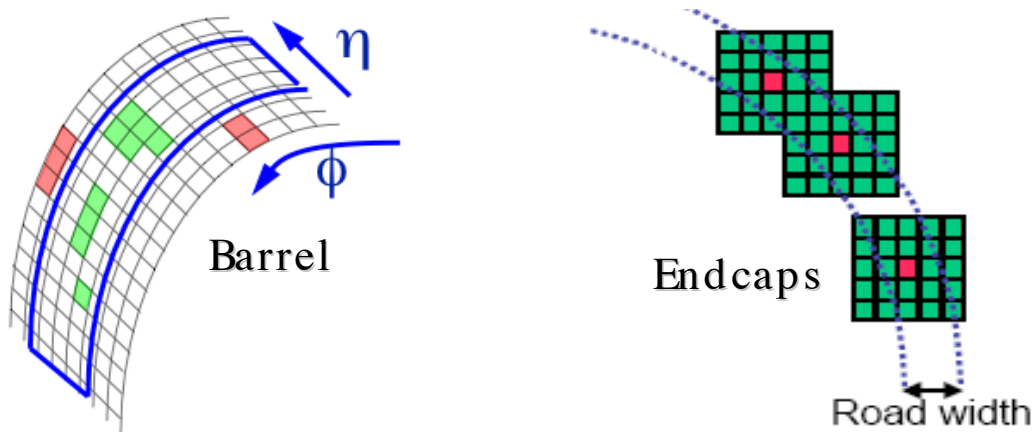


Figure 3.1 – Electron energy deposit shapes in the ECAL Barrel (left) and Endcaps (right)

the 'multi 5×5 ' algorithm is used there. In this case matrices of 5×5 crystals form the clusters

if the central crystal energy exceeds the threshold of 0.18 GeV and the cluster energy exceeds 1 GeV. The distance between these matrices in η and ϕ coordinates should be less than 0.07 and 0.3 rad respectively. An example of such energy deposit shapes is shown in Fig. 3.1 (right).

The energy of the supercluster is then the sum of the sub-clusters energies. Its position is calculated as the energy weighed mean of the sub-clusters. In case of non-isolated or low- p_T electrons the above algorithms suffer either from the additional energy deposit from other particles (if the electron is non-isolated) or from the early bremsstrahlung radiation which could not be found in the given η and ϕ ranges of the supercluster (in case of the low- p_T electrons). In such instances another algorithm, so-called "particle-flow" (PF) can be used complementary to the ones mentioned above [27]. The particle-flow algorithm firstly takes

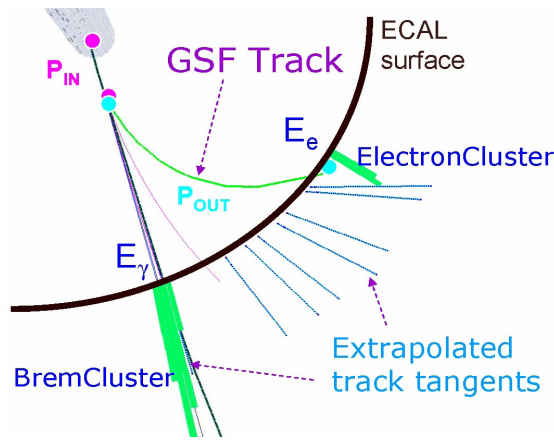


Figure 3.2 – Particle-flow clustering

the electron track. Then for each tracker layer a bremsstrahlung photon emission is sought by computing a tangent to the track up to the ECAL (see Fig. 3.2) and all the clusters satisfying this link condition are merging into the supercluster. This method allows to reconstruct a bremsstrahlung cluster which could be far away from the electron cluster and is not seen by the standard superclustering. But at higher p_T particle-flow algorithm tends to overestimate the electron energy.

3.2 Electron track reconstruction

In most of the cases the trajectories of the charged particles can be reconstructed using the Kalman Filter [28] technique which is the baseline for the CMS tracker. However, the Kalman Filter is a linear least-squares estimator and it is proved to be optimal for a Gaussian energy loss distribution. For electrons on the contrary the energy losses are highly non-Gaussian and described by a Bethe-Heitler distribution. Therefore the non-linear generalization of the Kalman Filter, the *Gaussian-sum Filter (GSF)* [29] has been implemented in the CMS reconstruction software. In this method the weighted sum of the multiple Gaussians is used

instead of a single Gaussian. Since the GSF method is time consuming, we should reduce the collection of tracks subjected to this procedure. The track seeding used on this purpose consists of finding and selecting two or three first hits in the tracker forming the initial part of the trajectory. The seeding is extremely important for the electron reconstruction because it has a direct impact on the electron reconstruction efficiency.

3.2.1 Seeding

There are two complementary algorithms used for the seeding of the electron tracks. Both of them should put in correspondence the electron track candidate and the ECAL cluster. The seeding can start either from the ECAL cluster (ECAL-driven seeding) or from the general tracks collection (tracker-driven seeding).

ECAL-driven seeding

The ECAL-driven seeding starts from the ECAL supercluster and explores its position and energy deposit in order to estimate the possible electron trajectory and selects the seed among the reconstructed ones. The barycentre of the supercluster is located on the helix which starts from initial electron 4-momentum. Both positive and negative charge hypotheses are considered. In this way the seeding hits are predicted. The predicted hits are then compared with the ones found in the tracker within the certain distance in ϕ and z (or transverse distance r_T in forward regions). The sizes of the windows are adjusted so that the maximal efficiency is kept while the number of candidates still can be handled by computing capabilities.

This ECAL-driven electron seeding strategy is very efficient for the isolated electrons with $p_T > 10$ GeV. However, for the low- p_T and non-isolated electrons certain difficulties with electron energy estimation in the ECAL arise, as it was discussed above. The tracker-driven seeding, developed in the context of the particle flow event reconstruction, is used in such cases.

Tracker-driven seeding

The tracker-driven seeding uses as starting point the tracks, reconstructed by the Kalman Filter algorithm. The Kalman Filter provides a reasonable estimation of the track parameters if an electron does not emit the bremsstrahlung radiation (or its fraction is sufficiently small). The quality of the tracks is allowed to be low (in terms of missing hits and χ^2) to keep in consideration the cases when electrons emit bremsstrahlung radiation and KF track cannot properly describe their trajectories. For each KF track the particle-flow supercluster is looked for. The low quality tracks are further refitted with a GSF method. Finally, the set of variables including the number of hits of the KF track, its quality (for both KF and GSF tracks) and ECAL-tracker geometry and energy matching, are passed to a multivariate analysis (MVA) in order to determine the electron seed.

Combination of the above seeding algorithms results in a high seeding efficiency. For the isolated electrons with $p_T > 10$ GeV the seeding efficiency is $\geq 92\%$ as predicted by the Monte-Carlo simulation. The drops of efficiency are mainly related to the detector geometry: they are located in the barrel-endcap transitions and at the very end of the tracker acceptance.

3.2.2 Track parameters estimation

Once the electron seeding is done, the electron track building starts with the combinatorial Kalman Filter method. In order to maintain high reconstruction efficiency, the compatibility between predicted and observed hits in each layer is set to be very loose, $\chi^2 < 2000$. As a consequence of the such loose found hits preselection, several trajectories could be developed. Their number is limited to 5 candidate trajectories per tracker layer. In case of a missing hit found, the requirement on the χ^2 is enforced to $\chi^2 < 90$ in order to avoid the reconstruction of a converted photon leg. Also at least 5 hits are required to create a track.

After the KF tracks reconstruction, the tracks refitting with the GSF filter is performed. The track parameters are extracted from the GSF fit as the most probable value. Having the electron track reconstructed up to the ECAL, we can estimate its parameters at the ECAL entrance. One of the most important for the electron classification parameters, the fraction of electron energy emitted by bremsstrahlung radiation, is determined as $f_{brem} = \frac{p_{in} - p_{out}}{p_{in}}$, where p_{in} and p_{out} are electron momentum estimations provided at the closest to the beam spot and at the ECAL entrance respectively.

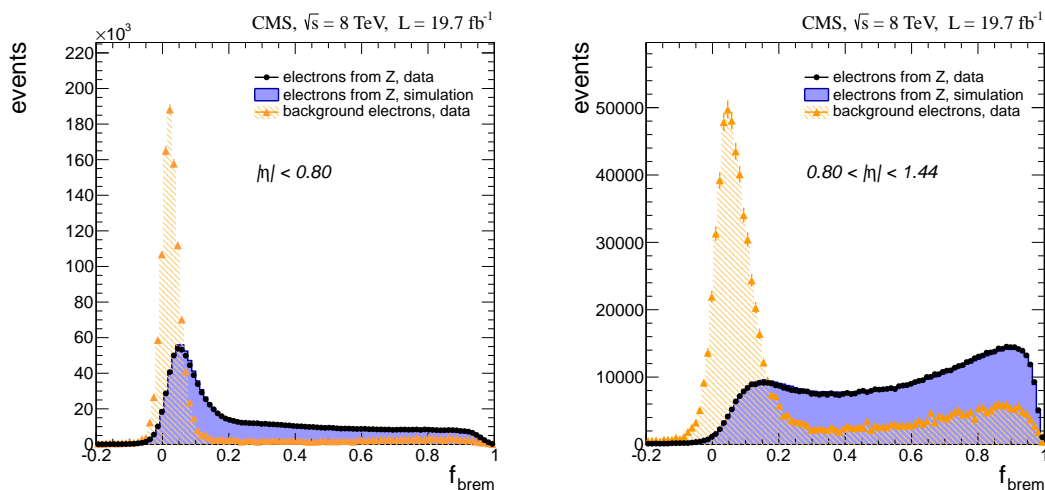


Figure 3.3 – Bremsstrahlung fraction in different parts of the ECAL barrel shown for data and simulated electrons from Z and for background data events. Left: central barrel $|\eta| \leq 0.8$. Right: outer barrel $0.80 \leq |\eta| \leq 1.44$.

Fig. 3.3., 3.4 show the comparison between predicted and measured bremsstrahlung fraction. A

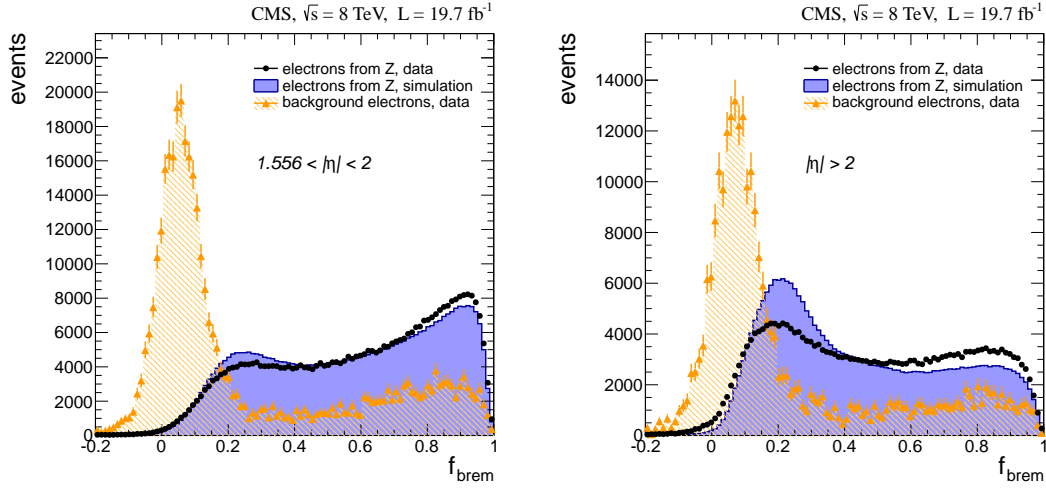


Figure 3.4 – Bremsstrahlung fraction in different parts of the ECAL endcaps shown for data and simulated electrons from Z and for background data events. Left: $1.556 \leq |\eta| \leq 2.0$. Right: $2.0 \leq |\eta|$.

reasonable agreement is found. Moreover, since the bremsstrahlung fraction strongly depends on the amount of material crossed by an electron, it is a perfect criteria for the quality of material budget simulation. Measuring the difference between the data and simulation some imperfections in the material budget description were found (especially in the ECAL endcaps).

Another important parameter of the electron is its charge. The most natural way to determine the charge of the electron is to explore the curvature of the GSF track. However the charge determination becomes more difficult in the presence of the bremsstrahlung radiation. The early converted bremsstrahlung photons complicate a lot the hit patterns and the conversion legs could be wrongly assigned to the electron track. Therefore two other charge estimators were developed: one using the curvature of the associated KF track and another, based on the sign of the difference in ϕ of the vector, pointing to the supercluster from the interaction point and the vector, starting at the same place and pointing to the first hit of the GSF track. Combining these three estimates, the electron charge is determined as the value, given by at least two out of three estimates in agreement. Such method allows to improve the misidentification rate by a factor ~ 2 with respect to the GSF curvature measurements alone.

3.3 Electron classification

The electron reconstruction (and, in particular, its momentum determination) is complicated by energy losses in the detector material placed before the ECAL. The CMS inner tracker being a very precise and high-granulated device, appears however as a source of the large material budget. The electrons are subject to the following phenomena when traversing the tracker material:

- ionization energy losses
- multiple Coulomb scattering
- bremsstrahlung energy losses

In fact the ionization energy losses are negligible at the energies $\gtrsim 100$ MeV and the dominant source of energy loss for electrons is the bremsstrahlung. Bremsstrahlung radiation complicates both the hit pattern in the track and the cluster topology in the calorimeter. Depending on the point where the bremsstrahlung photon was emitted, we can have different cluster patterns in the ECAL (the early radiated bremsstrahlung photon could be very far from the electron cluster, while very late bremsstrahlung radiation will be collinear to the electron and could be even recovered in the same cluster as the electron). Following this, we can establish the main observables, which reflect the quality of the electron reconstruction in the ECAL and the tracker subdetectors. First is the cluster topology: the electron supercluster can have inside one (in case of no or very late bremsstrahlung emission) or more clusters. Second is the bremsstrahlung fraction, as defined in previous section, and third is the ratio of measured in the ECAL energy to the momentum, measured in the tracker. On this basis, the first scheme of electron classification in the CMS experiment was provided in [30]. It was defined as the following:

- “golden”, or electrons with a small fraction of the energy lost because of the bremsstrahlung radiation and with a reconstructed track well matching the supercluster:
 - a supercluster formed by a single cluster (i.e. without observed bremsstrahlung sub-cluster),
 - a ratio $E/p > 0.9$,
 - a measured bremsstrahlung fraction $f_{brem} < 0.5$;
- “big brems”, or electrons with high bremsstrahlung fraction but without an evidence of the calorimetric energy loss effects:
 - a supercluster formed by a single cluster,
 - a ratio $E/p > 0.9$,
 - a measured bremsstrahlung fraction $f_{brem} > 0.5$;
- “showering”, or electrons with the energy pattern highly affected by the bremsstrahlung losses:
 - a supercluster formed by a single cluster not falling in the “golden” or “big brems” classes, or a supercluster formed by several sub-clusters.

In addition, “crack” electrons are defined as electrons whose supercluster’s starting crystal is close to an η boundary between the ECAL modules, or between the ECAL barrel and ECAL

endcap, or close to the end of the endcaps coverage. Fig. 3.5 shows the distribution of the electrons between the different classes as a function of the pseudorapidity.

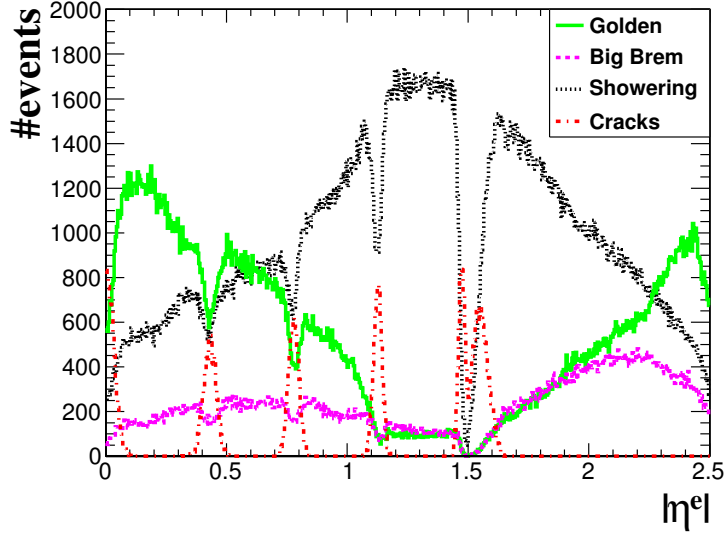


Figure 3.5 – Distribution of the class repartition as a function of $|\eta|$. The integrated fractions of reconstructed electrons in the different classes are as follows: 29.8% (golden), 12.2% (big brem), 53.3% (showering) and 4.7% (cracks).

This classification already allows a quite good reconstruction performance and electron energy estimation accuracy for the high- p_T and isolated electrons using a class dependent energy-momentum combination. The classification can be improved using additional information coming from the particle-flow reconstruction algorithm. These new developments are part of this thesis work.

The PF reconstruction provides the alternate method of building the electron superclusters in the ECAL. The difference between the ECAL-based clustering and the PF one arises from the differences in the bremsstrahlung photons reconstruction. Naively we can say that the PF algorithm should provide a better precision in case of low- p_T electrons where the ECAL-based clustering is not able to collect all the bremsstrahlung photons. On the other hand, if the track has a lot of missing hits or its χ^2 is high, it is possible that we have reconstructed a fake electron track (for example from a charged hadron or converted photon leg). In this case the tracker measurement will be wrong and we should see this also in the particle-flow supercluster composition. In order to quantify the differences in the supercluster composition (both in a number of hits and in a part of energy, which has been lost due to the bremsstrahlung radiation) let's introduce a new variable, called PF bremsstrahlung fraction:

$$f_{brem}^{PF} = \frac{PF\ SuperCluster\ Energy - Electron\ Cluster\ Energy}{PF\ SuperCluster\ Energy} \quad (3.1)$$

We can compare this variable with the previously defined f_{brem} . If the electron is "well-reconstructed", i.e. its trajectory has all the hits and it doesn't fall into the gap between the ECAL supermodules, then these two bremsstrahlung fraction estimators should give equal results. In case of a high-energy electron the PF bremsstrahlung fraction could be smaller than the tracker one due to the higher size of the cluster in the ECAL. If we look on the 2D plot with these two bremsstrahlung fractions, which is shown in Fig. 3.6, we can easily identify these two regions. The first region corresponds to the diagonal line on the plot and the latter is concentrated close to the x axis. Besides, one can identify another significant population

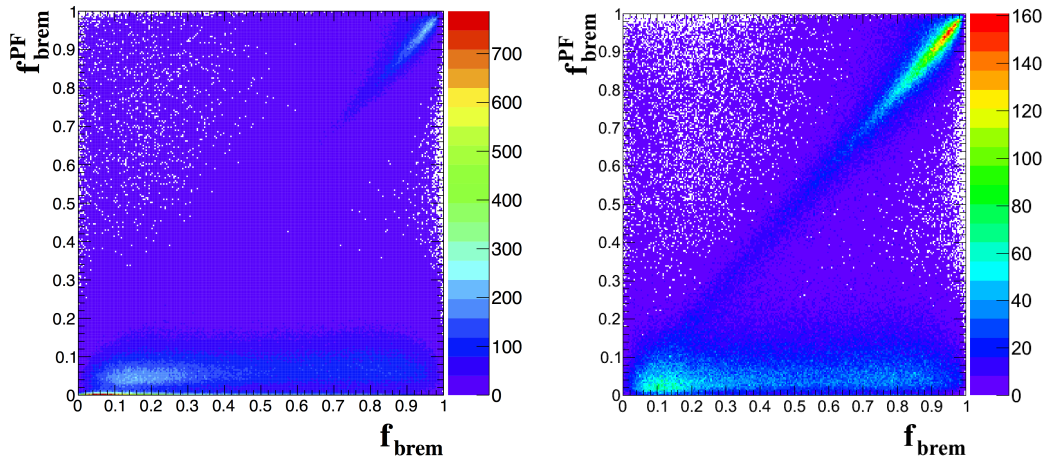


Figure 3.6 – 2D representation of f_{brem}^{PF} vs f_{brem} for all electrons (left) and showering electrons (right)

of electrons on this plot: the electrons with f_{brem}^{PF} higher than f_{brem} . It corresponds to the right tail of the $f_{brem}^{PF} - f_{brem}$ distribution, shown in Fig 3.7. As it was already mentioned, such

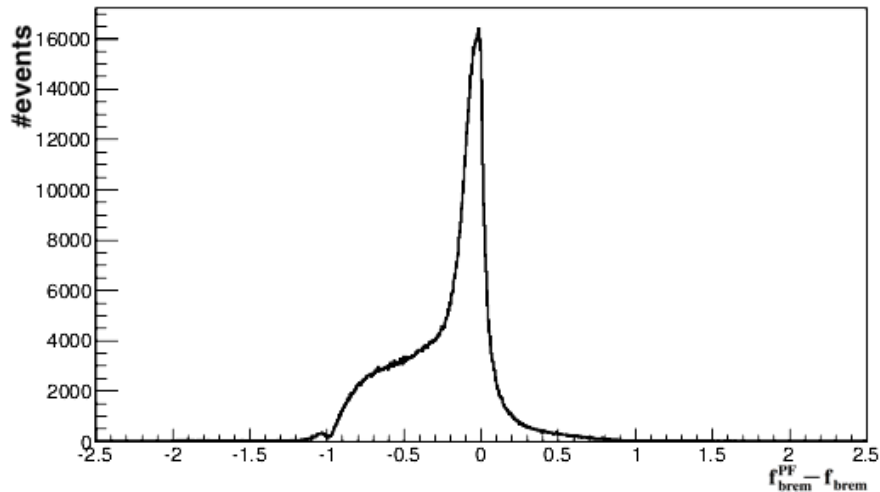


Figure 3.7 – Distribution of $f_{brem}^{PF} - f_{brem}$

situation can arise either in case of incorrectly assigned bremsstrahlung radiation, when the

photon cluster doesn't belong to the bremsstrahlung radiation, emitted by the electron, or in case of wrong track reconstruction. In the latter case PF clustering will follow the wrong trajectory and can reconstruct the clusters which are not related to the initial electron at all. Therefore, one of measurements (PF based on the electron track or ECAL-driven) will give correct result while the other will be wrong. Let's define three regions on the 2D plane $(f_{brem}^{PF}, f_{brem})$:

- Region 1: $f_{brem}^{PF} < 0.1$
- Region 2: $f_{brem}^{PF} - f_{brem} > 0.15$
- Region 3: the remaining part of the plane

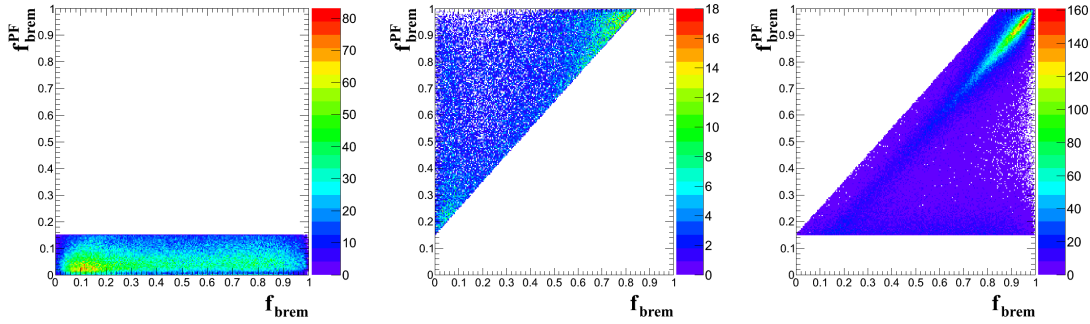


Figure 3.8 – The 2D representation of f_{brem}^{PF} vs f_{brem} for Region 1 (left), Region 2 (center) and Region 3 (right)

These regions are illustrated in Fig. 3.8 for the case of the showering electrons. The showering electrons are selected for the illustration as the category which have enough statistic for all the regions. The optimization of the requirement $f_{brem}^{PF} - f_{brem} > 0.15$ is discussed below.

In order to estimate the fraction of electrons which have correct ECAL or tracker measurements, we looked on the distributions of the E^{SC}/E_{true} and P/P_{true} where E^{SC} denotes the reconstructed ECAL energy, p - the momentum in the tracker and $E_{true}(P_{true})$ is the generated energy (momentum). A Monte-Carlo simulated sample with flat spectrum of the electrons transverse momenta varying from 2 to 100 GeV was used on this purpose. The results are shown in Fig 3.9 in case of the ECAL barrel part and in Fig 3.10 in case of the ECAL endcaps.

As we can see from these figures, the electron energy measurements for the region 2 electrons population (which is shown in red) are in general correct and peaked at the right place, while the momentum in the tracker is almost completely off. However in some cases (for example, showering electron on Fig. 3.9) the momentum distribution has a small peak at the correct value. The threshold on the $f_{brem}^{PF} - f_{brem}$ difference was adjusted to minimize this peak while preserving the contribution of the events with wrong momentum estimation. The regions 1 and 3 show quite similar behaviour and both the ECAL and tracker measurements for these regions are in a reasonable agreement.

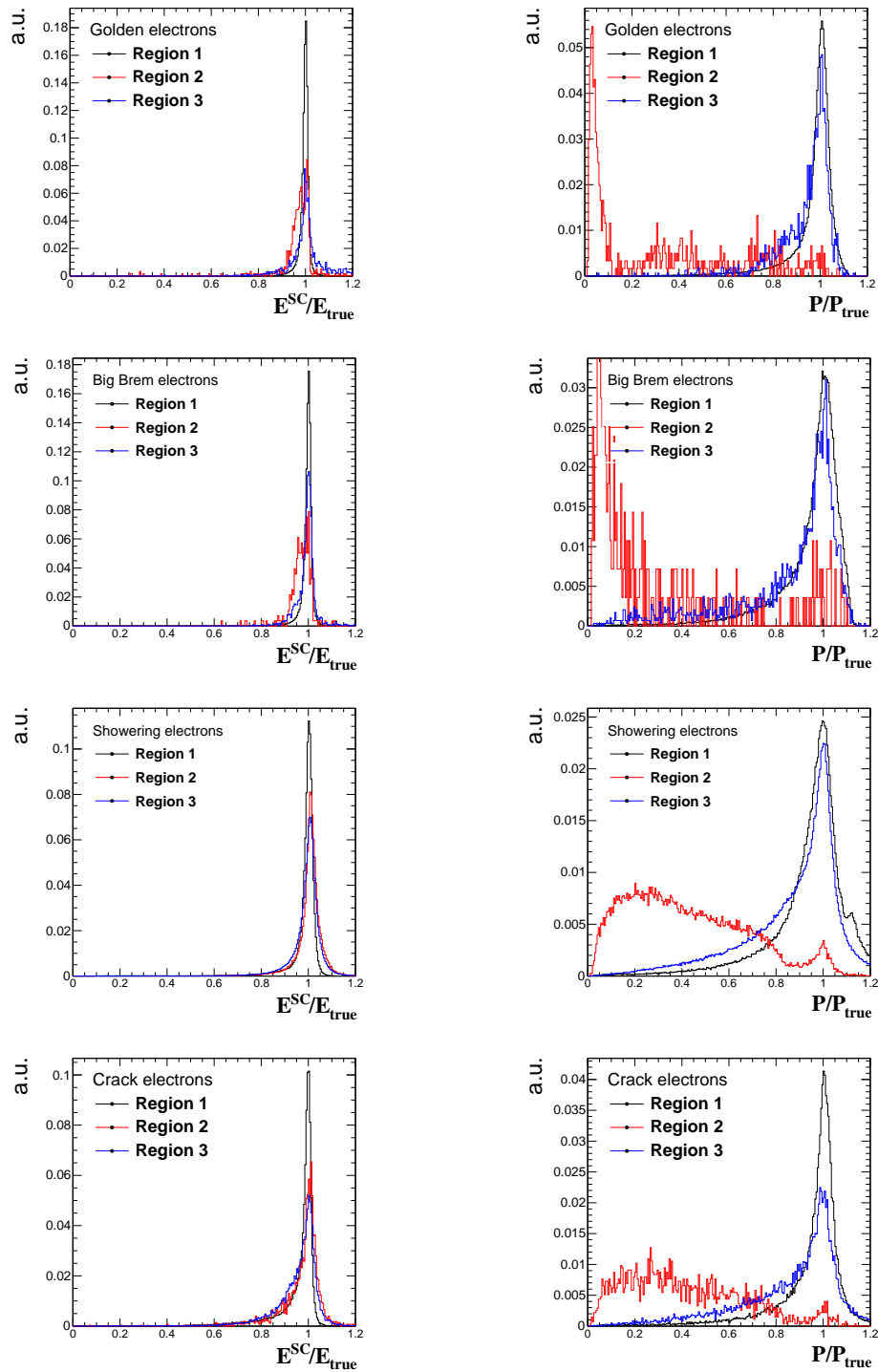


Figure 3.9 – Distribution of the E^{SC}/E_{true} (left) and P/P_{true} (right) for electrons in the ECAL barrel

Summarizing the above, we can pick out the population of electrons which have wrong momentum estimation in the tracker, meaning that purely ECAL measurements should be

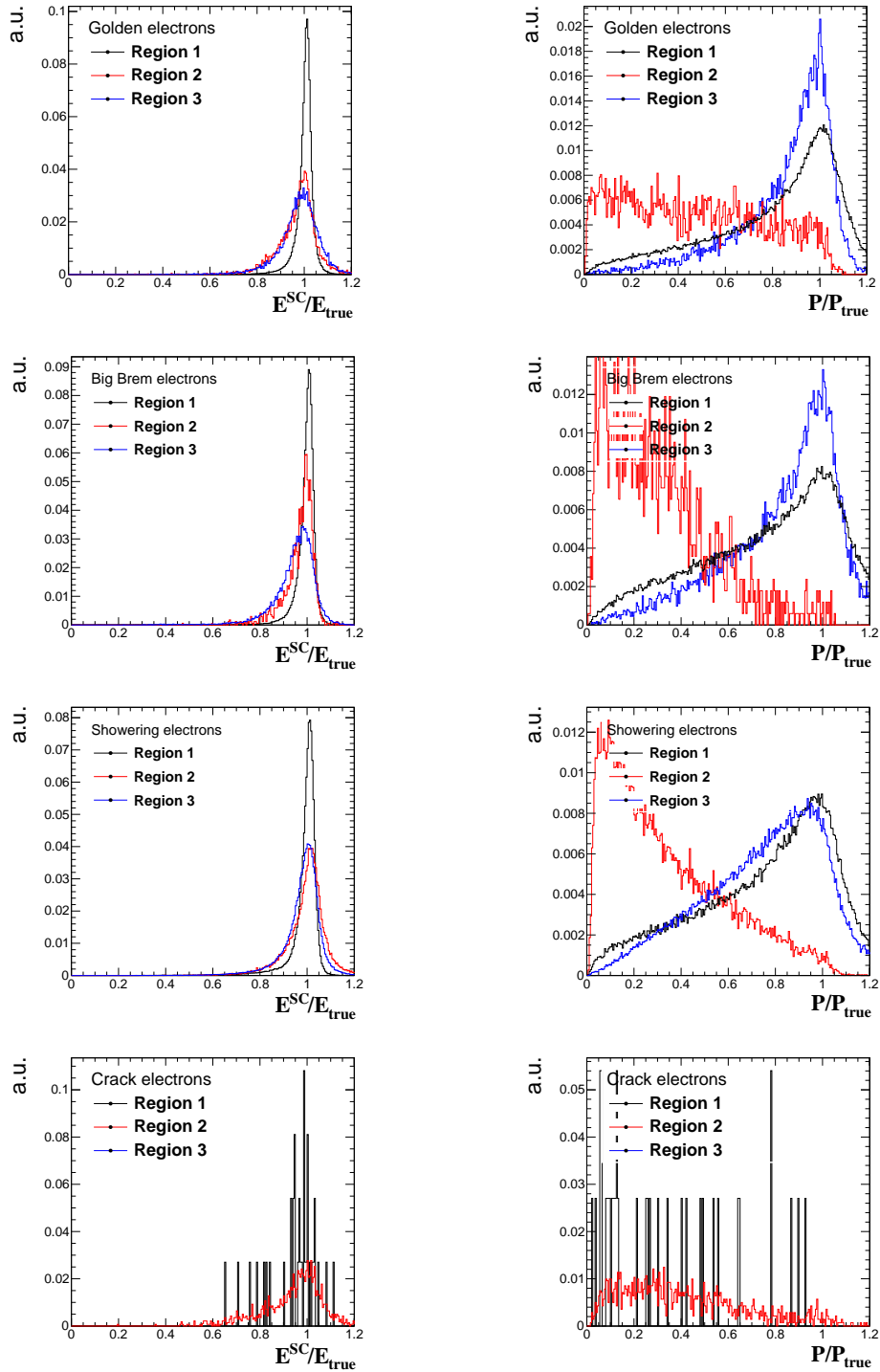


Figure 3.10 – Distribution of the E^{SC}/E_{true} (left) and P/P_{true} (right) for electrons in the ECAL endcaps

used in this case. Moreover, we also split the showering electrons into single-cluster and multi-cluster sub-classes and found that the single-cluster showering electrons give a measurement

accuracy very close to the golden and big brem ones. Following this we decided to revisit the electron classification picking out the electrons with wrong momentum estimation in a separate class and redistributing the showering single-cluster electrons between the golden and big brem classes by releasing the condition on E/p .

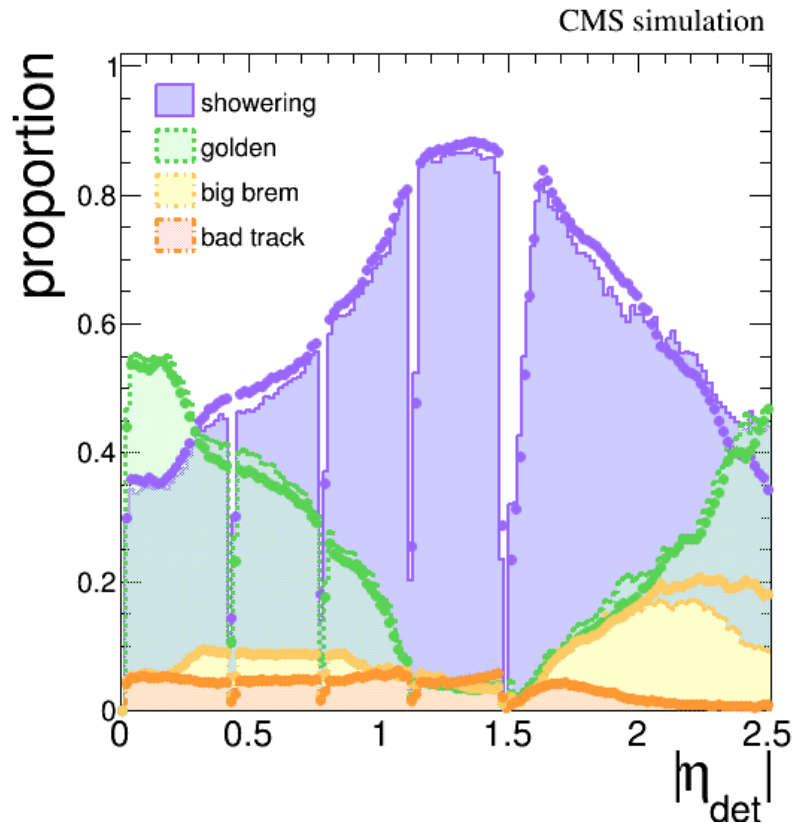


Figure 3.11 – The integrated fractions of reconstructed electrons in the different classes. The dots represent the data and the filled histograms represent the MC simulation. Crack electrons are not shown and the proportions are corrected respectively.

Finally, the new classification is:

- "golden"
 - a supercluster formed by a single cluster
 - a measured at the tracker bremsstrahlung fraction $f_{brem} < 0.5$
- "big brem"
 - a supercluster formed by a single cluster
 - a measured at the tracker bremsstrahlung fraction $f_{brem} > 0.5$
- "bad track"

- electrons matching to criteria $f_{brem}^{PF} - f_{brem} > 0.15$
- "showering"
 - a super-cluster formed by several sub-clusters
- "crack"
 - electrons whose supercluster's starting crystal is close to an η boundary between the ECAL barrel modules, or close to an η boundary between the ECAL barrel and ECAL endcaps

Fig. 3.11 shows the distributions of all the classes except crack as a function of the pseudorapidity. A good agreement is observed between the data and MC simulation.

3.4 Electron combination

In order to achieve the best possible precision on the electron momentum estimation we should explore both the tracker and ECAL measurements. The combination of the both detectors measurements has to account for the quality of the each one. This means that we should combine the measurements only in case of both are correct. Otherwise only one should be used. The classification, described in the section above provides the possibility to access the quality of the ECAL and tracker estimations. It is obvious that in case of "golden" electrons both measurements are fine, while in case of "bad track" class only the ECAL energy estimation should be taken. The measured momentum and energy themselves with the corresponding errors are used in the combination.

Fig. 3.12 presents the ratios E/E_{true} (left) and p/E_{true} (right) as a function of E/p for the barrel electron case, where E stands for the supercluster corrected energy and p is the track momentum at the innermost track position. A similar behaviour is found for the endcaps. The same MC simulation as in the previous section was used here. From this plot one can identify three main regions:

- cases with $E/P \approx 1$ where both the energy and momentum estimates are in good agreement with the generated value,
- cases with $E/P > 1$ where the tracker momentum measurement is almost always underestimated,
- cases with $E/P < 1$ where either the ECAL or the tracker measurement can be incorrect. Most of these cases correspond to showering electrons.

The combination zone requirements have been updated with respect to the old one, described in [30]. The electron momentum magnitude is defined as the weighted mean of E and p when

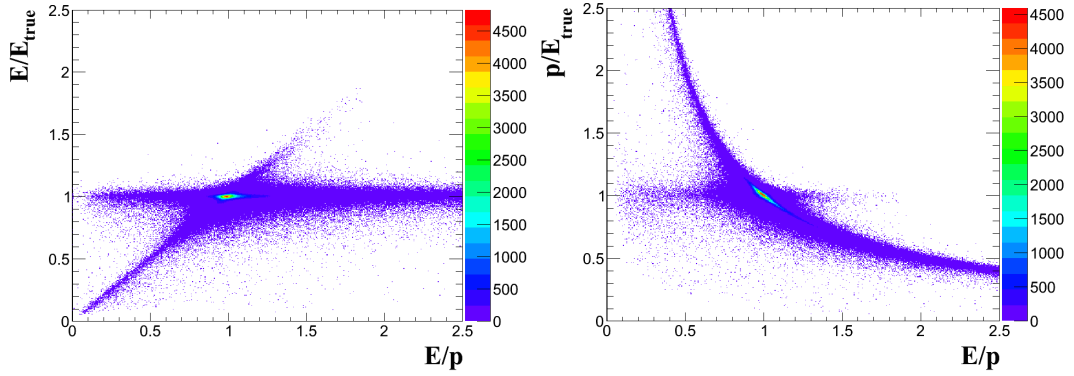


Figure 3.12 – Left (right): Ratio E/E_{true} (p/E_{true}) as a function of E/p for the barrel electrons

$|E/p - 1| < 2.5\sigma_{E/p}$ and $0.8 < E/p < 1.3$. The latter requirement was not present in the previous combination zone, giving the possibility to combine quite different measurements in case if one (or both) has large error. The weights are computed as the normalized inverse of the variance of each measurement:

$$p^{comb} = \frac{E/\sigma_E^2 + p/\sigma_p^2}{1/\sigma_E^2 + 1/\sigma_p^2} \quad (3.2)$$

If the electron doesn't satisfy the combination requirements, E or p is selected following the rules based on the above considerations:

- if $E/p > 1$ we take E for all electrons
- otherwise we have class-dependent choice thresholds:
 - golden: always take E
 - big brem: if $E < 36$ GeV we take p else we take E
 - bad track: always take E
 - showering: if $E < 30$ GeV we take p else we take E
 - crack: if $E < 60$ GeV we take p else we take E

The choice of the ECAL or tracker measurement arise from the fact that in general tracker measurements are more precise for the low- p_T electrons while at high- p_T part of the spectrum the ECAL measurements provide better results. The threshold values were adjusted in order to maximize the following ratio:

$$QR = \frac{\text{Number of electrons with } 0.9 < E_{comb}/E_{true} < 1.1}{\text{Number of all electrons}} \quad (3.3)$$

The performance of the new classification together with new combination in case of the ECAL-driven electrons is illustrated in Fig. 3.13. As one can see, it works good both for low-

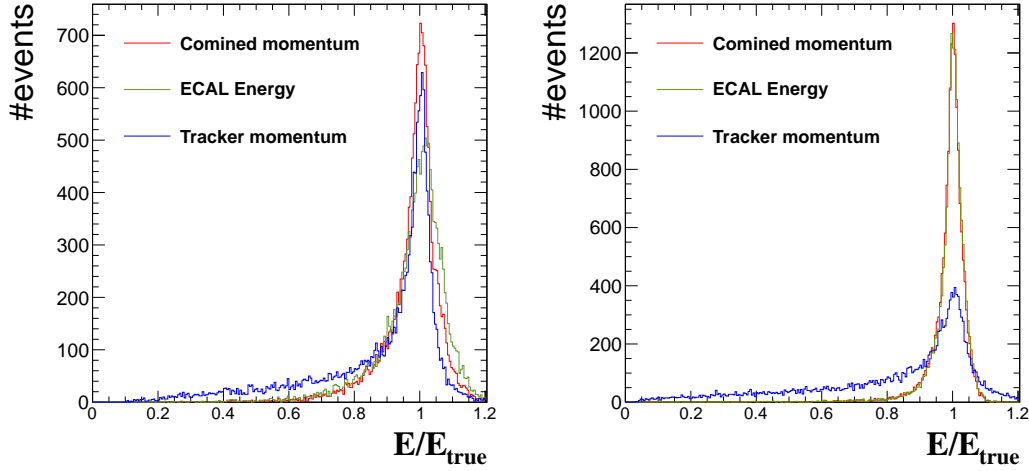


Figure 3.13 – Comparison of the combined momentum (in red), ECAL energy (in dark-green) and tracker momentum (in blue) normalized to the generated energy using $p_T = 10$ GeV (left) and $p_T = 35$ GeV (right) MC samples.

and high- p_T parts of spectrum, giving preference for the tracker measurements for low- p_T electrons and ECAL measurements at higher energies. It is also clear from the plot that the combination of the ECAL and tracker measurements allows better momentum estimation as well as better energy resolution at low p_T while maintaining the ECAL only resolution at higher p_T .

Once we developed the new combination algorithm we can also assess the effect of the new classification, which helps to get more proper treatment of each electron class. Fig. 3.14 shows the comparison of the mean values of P_{comb}/P_{true} distributions between the new and old approaches. P_{comb} denotes the combined momentum estimation. The accuracy of the momentum determination is improved in the barrel-endcap transition and over the whole ϕ range.

We also assess the effect on the relative resolution. From the Fig. 3.15 we can see that the resolution is improved in case of endcap electrons while remains the same in the barrel.

In case of pure tracker-driven electrons another combination scheme is used. This combination takes the weighted mean between the tracker and ECAL estimations in the same way as described above. The ECAL supercluster is provided by the particle-flow clustering algorithm and as the tracker measurement the GSF momentum estimation is usually taken. However there are two exceptions for the electron momentum estimation in the tracker. The track fit is not always sensitive to an early bremsstrahlung emission, while the corresponding photon can be recovered in the ECAL with the PF clustering. Therefore, if both the KF and GSF momenta (with the mode calculation) lack more than 5% of the energy with respect to the ECAL measurement, the electron energy is only determined from the ECAL. If the particle-flow supercluster lacks more than 10% of the energy with the respect to the track measurement,

and if the track is well measured, the momentum determination is based only on the GSF track measurement. When instead the GSF track is short ($N_{hits} < 8$), the momentum of the KF track is more precise than the GSF, and the track momentum estimation is performed using a weighted mean between the ECAL energy measurement and the KF track momentum at the vertex.

The combination algorithm described above has been used to produce the Higgs boson search in the four lepton final state results presented at the ICHEP'2012, HCP'2012 and Moriond'2013 conferences. However it has some disadvantages like the threshold effects when an electron goes in or away from the combination zone due to the re-reconstruction of an event with new conditions. Also this cut-based algorithm doesn't make use of all the information provided by the detector. Thus multivariate regression approaches for determining the ECAL energy of the electron and its combined momentum were later developed and deployed in the CMS reconstruction software. These algorithms include the information of a number of quality variables of both cluster and track. The main improvement is in the ECAL resolution, but for the very low p_T electrons the simultaneous use of the ECAL and tracker variables improves further the momentum and then the mass resolution of the 4ℓ invariant mass. The details of the method and its performance can be found in the references [31, 32]. In the following chapters all the results will use these recent developments.

3.5 Energy scale corrections

As it was discussed in Sec. 2.2.4, the ECAL crystals are subject to transparency losses during the data taking periods. Also different data taking conditions like pile-up affect the detector calibration. Such effects as well as detector intercalibration should be correctly accounted in the final electron scale calibration. This is implemented at a very basic reconstruction level, however some residual electron energy scale shifts are present. Moreover, since we use the

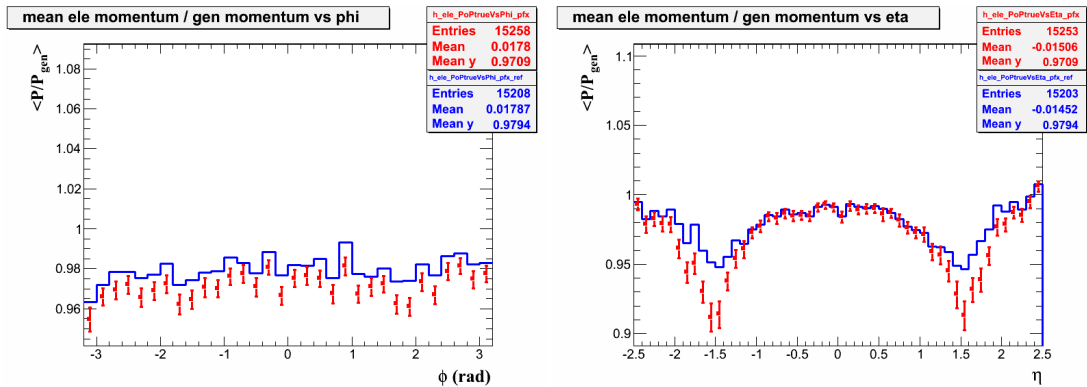


Figure 3.14 – Comparison of P_{comb}/P_{true} mean distributions for the old and new classification and combination as a function of ϕ (left) or η (right). Blue line represents the revisited results while red dots show the old ones.

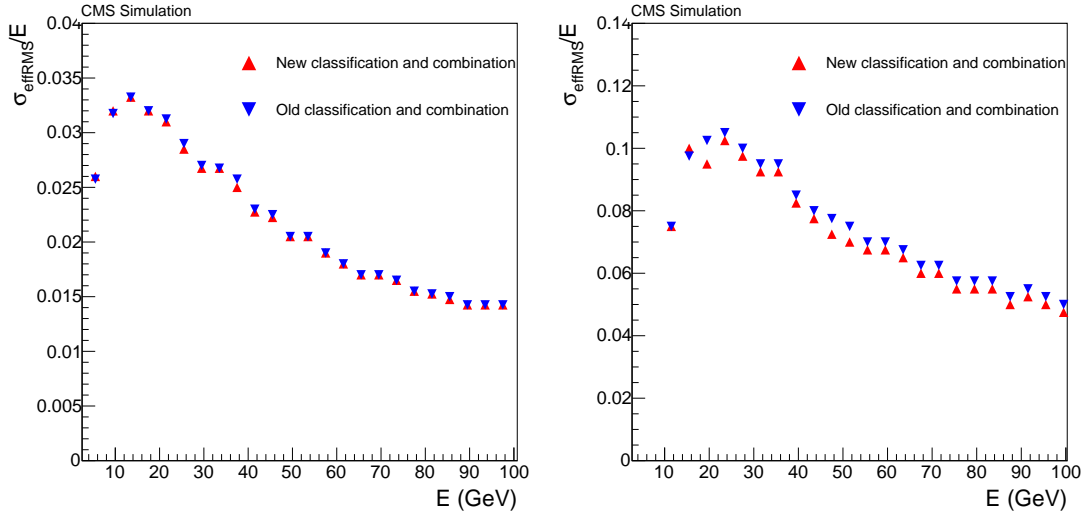


Figure 3.15 – Relative effective width of the combined momentum for the electrons in the barrel (left) and endcaps (right) as a function of the electron energy. Flat η simulated back to back electrons with a flat p_T distribution of $1 < p_T < 100$ GeV are used.

combined momentum estimation which accounts both the tracker and ECAL measurements, we should apply the final electron energy scale corrections to the combined momentum. There are different algorithms for the combined momentum estimation implemented in the different releases of the CMS software and the energy scale corrections should be applied according to the version of the combination algorithm used.

In this section the procedure of the electron energy scale corrections derivation, implementation and validation is described. In addition to the scale corrections applied to the data the additional gaussian smearing should be also applied to the Monte-Carlo simulated samples in order to properly match the data that show somewhat worse resolution than MC. Finally we will derive the energy scale uncertainties and electron momentum resolution. In order to derive the data corrections and MC smearings the events with a Z boson decaying to a pair of electrons were used both in the data and simulation.

3.5.1 Energy scale corrections derivation

The main source of the differences in the electron energy scale between the data and simulation is the loss of transparency of the ECAL crystals. This causes the time dependent discrepancy, which also depends on the pseudorapidity while remaining similar for different electron classes. Therefore at a first instance the energy scale is extracted per run range and in 4 pseudorapidity bins (two in the ECAL barrel part and two in the ECAL endcaps). The invariant mass of the dilepton pair in $Z \rightarrow ee$ events is fitted with a convolution of a Breit-Wigner (BW) function with a Crystal Ball (CB) function. This step is called “*fit method*”. Another source

of the energy scale difference is the mis-modelling of the material budget. This difference is looked for the whole run range, dividing electrons into high/low R_9 ¹ categories and in each pseudorapidity region. At this step additional smearing is also derived for the MC simulated sample in order to match the resolution in the data and simulation. This step is called “*MC smearing method*”. Finally the electron energy scale corrections are provided by a product of the corrections derived in the steps just described.

The electron energy scale corrections, obtained with *Winter13 re-reco* for 2012 data, which include our best knowledge of ECAL calibration conditions, are summarized in the Appendix.

3.5.2 Energy scale corrections implementation

Since the energy scale corrections and MC smearing depend on the run conditions, they also depend on the conditions used at the primary reconstruction level. This means that for each reco- or re-reco step as well as for each data taking period the individual set of corrections has to be applied. For example, during the preparation for the Moriond’2013 conference we had re-reconstructed dataset corresponding to the data accumulated by the end of summer and prompt reconstruction of the later accumulated data. Therefore the mixture of the different gaussian smearings had to be applied while combining the data in order to correctly account for the different reconstruction conditions. A special variable *LumiRatio* was introduced to maintain this. A dedicated software module called *ElectronEnergyCalibrator* was developed to implement the scale corrections assignment. The scale correction values are passed to this module from a csv-type² files. The run and reco- period is given by the input parameters so that proper corrections are applied for each case. This module was integrated in the CMS software and is extensively used by different physics analyses. A version of this module was developed as well to cope with the Physics Analysis Toolkit (PAT)³ data format. Since different ways of the electron momentum determination were developed and used⁴ all these possibilities should be available in the implementation of the module. Fig. 3.16 shows the workflow of the module.

All the technical information about the module was also documented and maintained in dedicated Twiki pages. In addition to the electron energy scale corrections described above, a special set of linearity corrections was added in order to account for a residual dependency of the electron energy scale on the electron transverse momentum. Detailed explanation of them will be given at the end of the current section.

¹ R_9 is a shower-shape variable, defined as the ratio of energy deposited in 3×3 crystals (centered at the seed crystal) to the supercluster energy. It assesses the amount of emitted bremsstrahlung radiation using the ECAL energy deposits alone.

² csv is a comma-separated values text data format.

³ PAT is a high-level analysis layer, which provides easy access to the object reconstruction algorithms.

⁴ Some analyses, in particular the ones which use very high energy electrons, don’t use the combined ECAL-tracker momentum estimation, preferring the ECAL-based one.

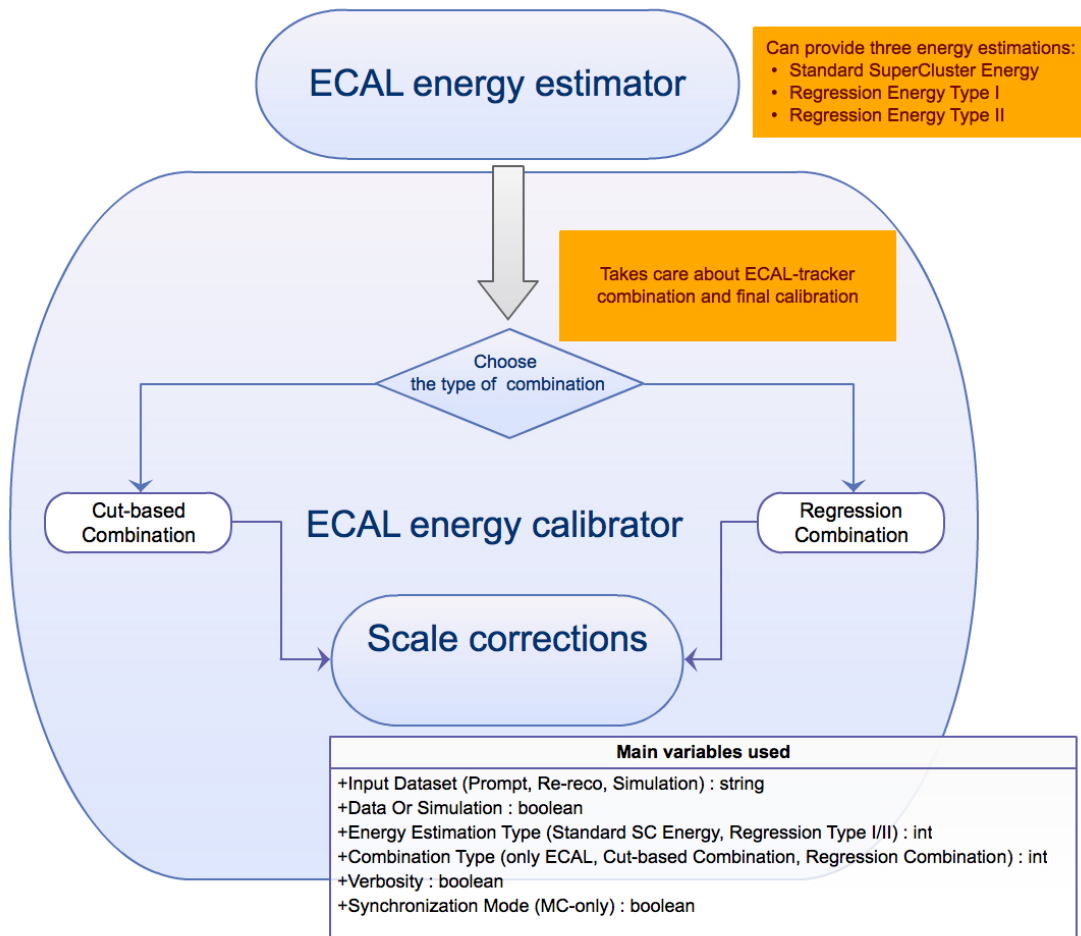


Figure 3.16 – Electron energy calibrator module workflow.

3.5.3 Energy scale corrections and resolution performance

In order to validate the scale corrections and provide the scale uncertainties and resolution for the physics analyses we use again $Z \rightarrow ee$ simulated samples and corresponding selection in the data. For the electrons, the $Z \rightarrow ee$ invariant mass can be built in different categories in η and separating the electrons with different momentum estimation precision using the electron classification. Also we must check the pile-up dependency of the scale uncertainties and resolution, therefore the events are looked at as well in the low and high pile-up regimes. The distributions are fitted with a Breit-Wigner function convoluted with a Crystal Ball function. The peak position and the width of the Breit-Wigner distribution are fixed to 0 and the PDG value for the Z boson ($\Gamma_{BW} = 2.495$ GeV) correspondingly, while the central value of the Crystal Ball is set to a Z boson mass ($m_{CB} = 91.188$ GeV). All the other parameters of the CB are just constrained in a reasonable vicinity of the expected ones. For the p_T dependency studies a generalized extension of a Crystal Ball function is used, providing left and right gaussian cores

around the peak and two different power-law tails at the left-hand and right-hand sides of the distribution. Fig 3.17 shows the results obtained in this way using 2012 data and comparing to the MC expectations for the best and worst categories of electrons. All the fits for all categories can be found in Fig.3.18.

The systematic uncertainties on the electron energy scale can be extracted from these results. They are estimated as the maximal deviations between the data and MC of fitted $Z \rightarrow ee$ peak position in different categories of η and electron classes. Since none of the parameters of the fit function describe the peak position, it was estimated as a maximal value of the fit. The error on the peak position was calculated by scaling the error on the m_{CB} parameter to the difference between PDG value of the Z boson mass and the observed one. Averaging on all electrons, the data and MC agree within 0.2%. Splitting by the ECAL regions, we reach 0.1% for the electrons in the ECAL barrel, and up to 0.3% for the electrons in the ECAL endcaps.

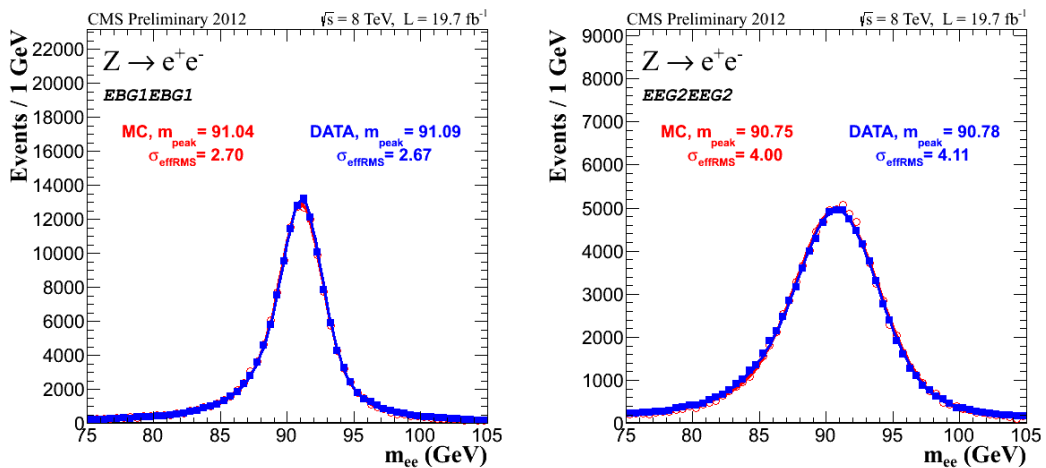


Figure 3.17 – $Z \rightarrow ee$ events categorized regarding the electrons classification for the best category of events, with both electrons belonging to golden or big bremsstrahlung class in the ECAL barrel (denoted EBG1EBG1) (left) and the worst category, with both showering, bad track or crack electrons in the ECAL endcaps (denoted EEG2EEG2) (right). Blue squares are 2012 data with a fit superimposed (blue line). Red open circles represent simulation with a fit superimposed (red line). The values of the effective resolution of the fit functions are also shown.

The dependency of the electron momentum scale with respect to the pile-up has been also checked. The $Z \rightarrow ee$ events were split into 6 bins according to the number of primary vertices observed in the event. The bins composition is the following: (0-5), (5-10), (10-15), (15-20), (20-25), (>25). No other categorization was applied. The fits of the distributions were performed with the same function as described above with the same initial conditions. Fit results for each pile-up bin are presented in Fig. 3.19.

The final scale dependency on the pile-up was extracted from these fits. No significant variation of the Z peak position with the number of vertices as well as data-MC difference

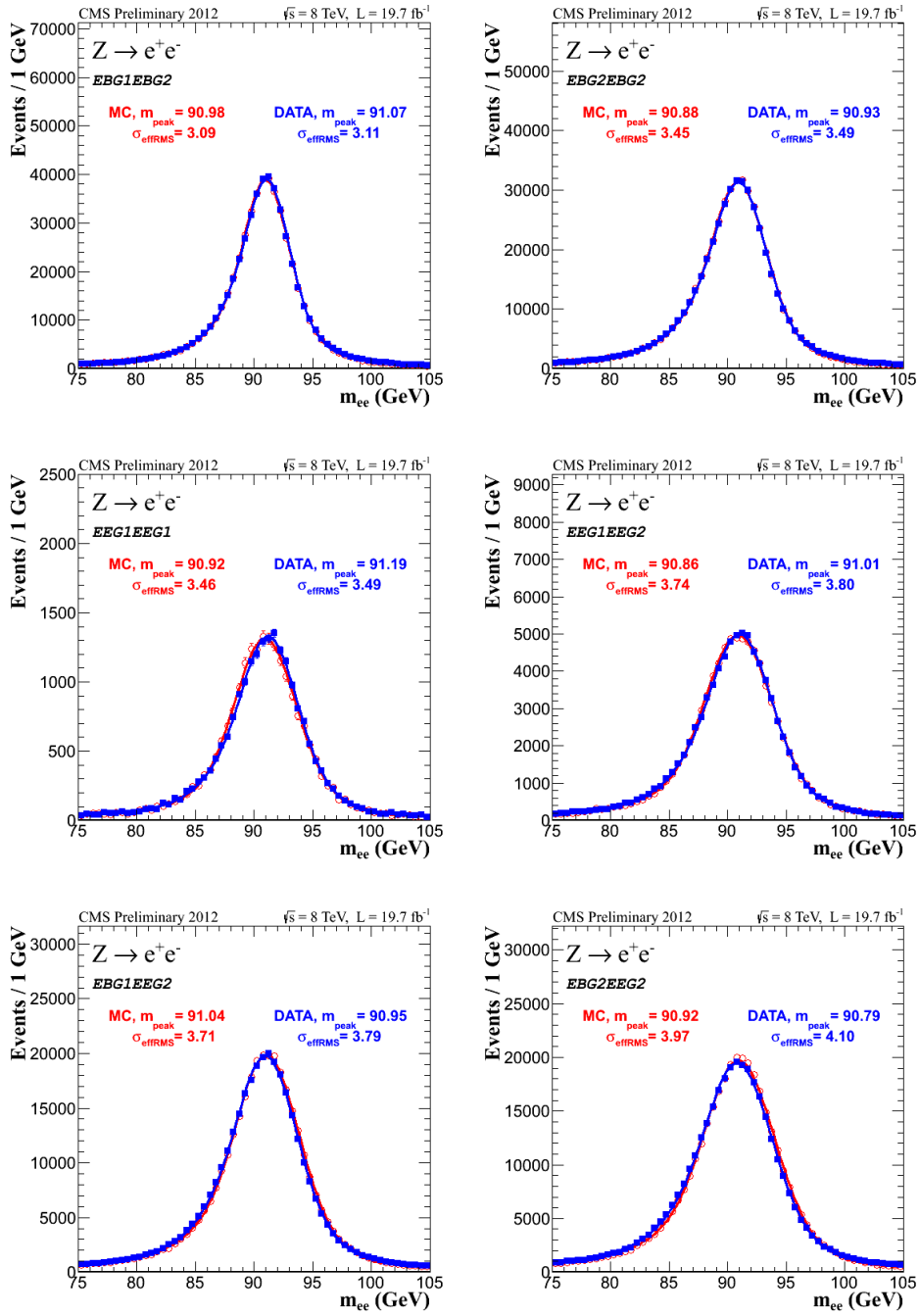


Figure 3.18 – $Z \rightarrow ee$ events categorized regarding the electrons classification. "EB" ("EE") denotes that electron comes from barrel (endcap) and G1("G2") denotes golden/big brems category (other categories). Blue squares are 2012 data with a fit superimposed (blue line). Red open circles represent simulation with a fit superimposed (red line). The values of measured effective resolution of the fit functions are also shown.

3.5. Energy scale corrections

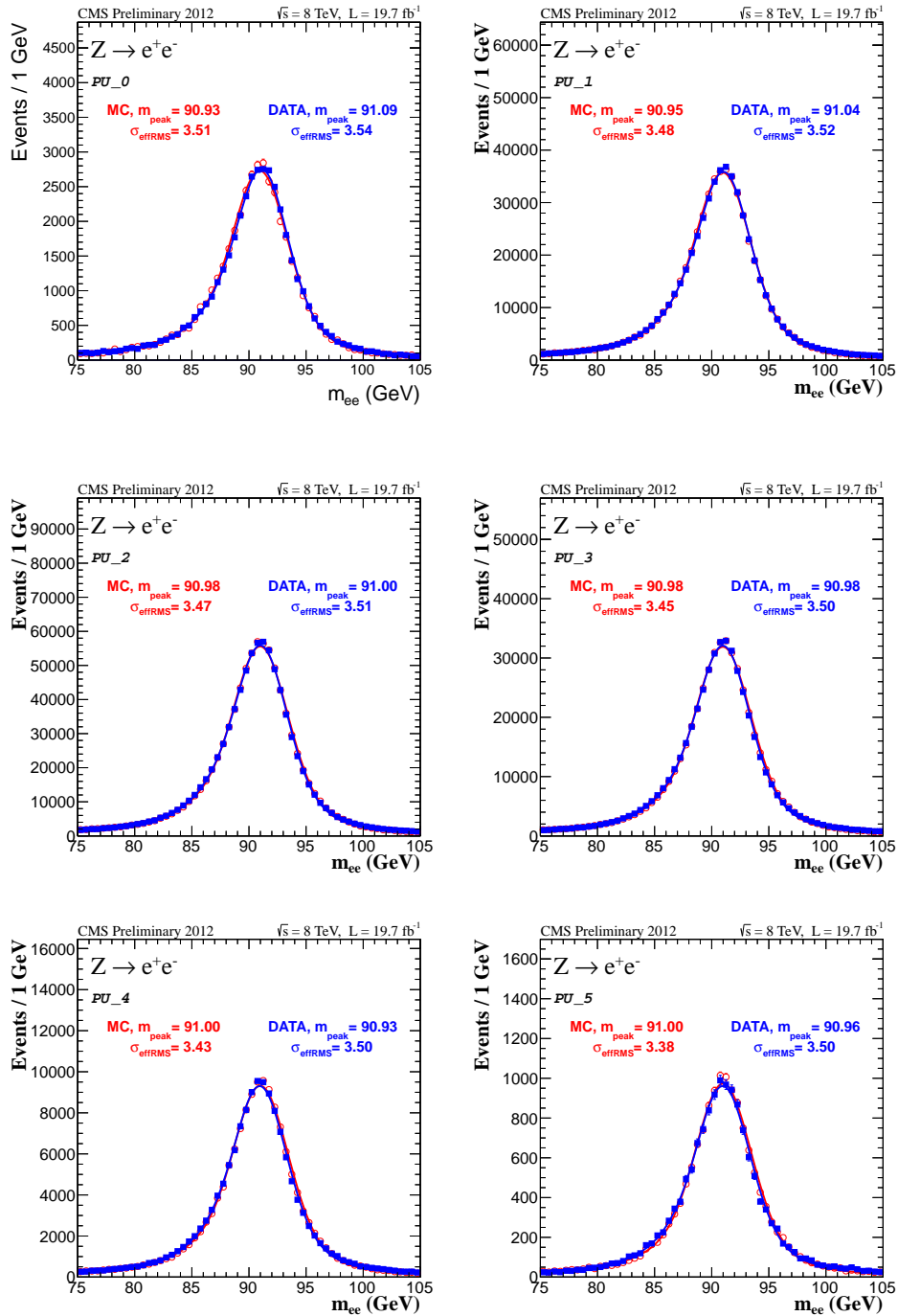


Figure 3.19 – $Z \rightarrow ee$ events categorized regarding the pile-up conditions. Blue squares are 2012 data with a fit superimposed (blue line). Red open circles represent simulation with a fit superimposed (red line).

variation was found, as can be appreciated from Fig. 3.20.

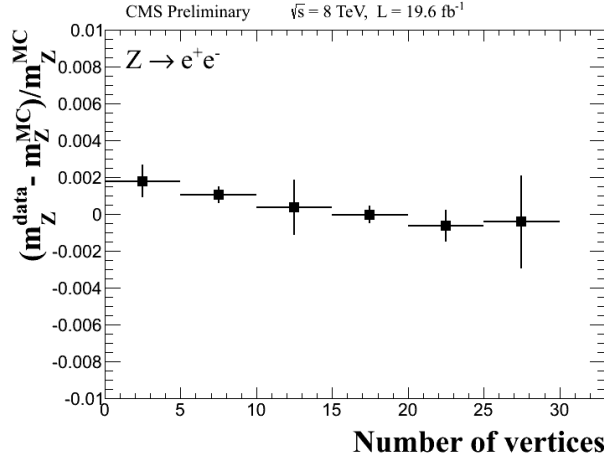


Figure 3.20 – Relative electron momentum scale uncertainty as a function of the number of vertices.

Another important survey was done in order to scrutinize the p_T dependency of the electron energy scale. The samples used for this study include:

- Low-mass resonances: J/ψ , Υ are used for low- p_T dependency determination.
- $Z \rightarrow ee$ samples are used mainly for high- p_T part of spectrum, but also cross-check of low- p_T dependency was provided.

The events were categorized with respect to the transverse momentum of the leptons as well as with respect to their η coordinate. The errors on the peak position were calculated varying the fit parameters within 1σ around their central values. A typical result of such variation is shown in the Fig. 3.21 for the case of $10 < p_T(\ell) < 15$ GeV, which represent the low- p_T electrons and in case of $30 < p_T(\ell) < 35$ GeV, which is typical for electrons from Z .

A small but clear linear trend was observed in the scale dependency on the electron transverse momentum, as it is shown in Fig. 3.22 (left). This was accounted by providing a linear scale corrections implemented in the calibrator module as it was discussed above. The distribution of the final electron energy scale as a function of the electron transverse momentum is shown in Fig. 3.22 (right). The dependency was almost eliminated and the residual one at the low- p_T is related to the fact that the fit function used cannot describe well the region $35 < p_T < 45$ GeV and low- p_T part of spectrum simultaneously.

For the resolution, a similar strategy has been adopted. The measured resolution of the di-electron spectra contains also intrinsic Z -boson resolution which is quite large (~ 2.5 GeV) and has to be subtracted. We can use then two measurements:

- σ_{CB} parameter of the CB function (the gaussian core)

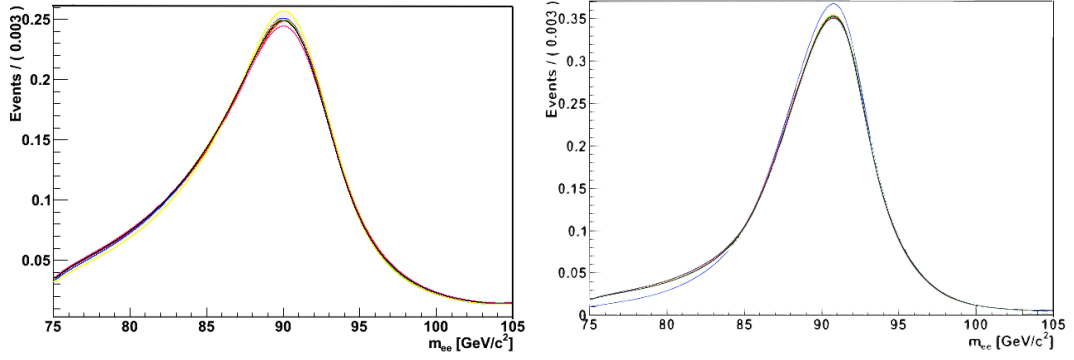


Figure 3.21 – 1σ variation of the fit parameters for the $Z \rightarrow ee$ events with $10 < p_T(\ell) < 15$ (left) and $30 < p_T(\ell) < 35$. Different colors correspond to variations of different parameters while other parameters remain the same.

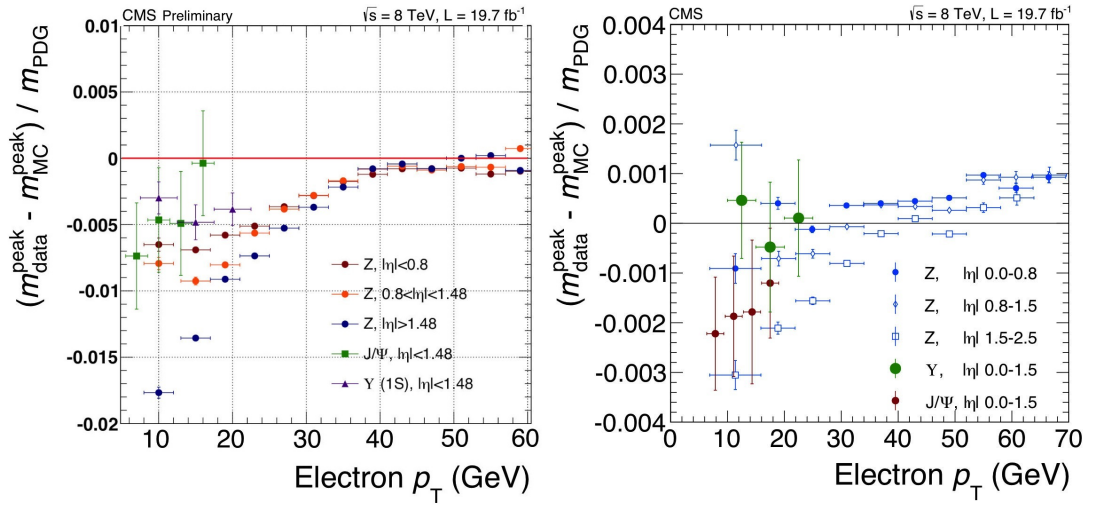


Figure 3.22 – Electron energy scale distribution as a function of the electron transverse momentum before the linearity corrections (left) and after the linearity corrections (right).

- effective resolution of the CB function

We can compare fitted σ_{CB} parameters of the CB functions between the data and MC. The largest relative difference amounts to 4% for the worse case. However this approach has two disadvantages: the σ_{CB} correlates with other parameters of the Crystal Ball function and also gives slightly underestimated resolution value since it doesn't account for higher left tail of the distribution due to bremsstrahlung losses. Fig. 3.23 shows the difference between CB and gaussian width.

Second, a correlation-free estimation was provided exploring the effective resolution of the $Z \rightarrow ee$ lineshape. The effective resolution is calculated as a half-width of the distribution

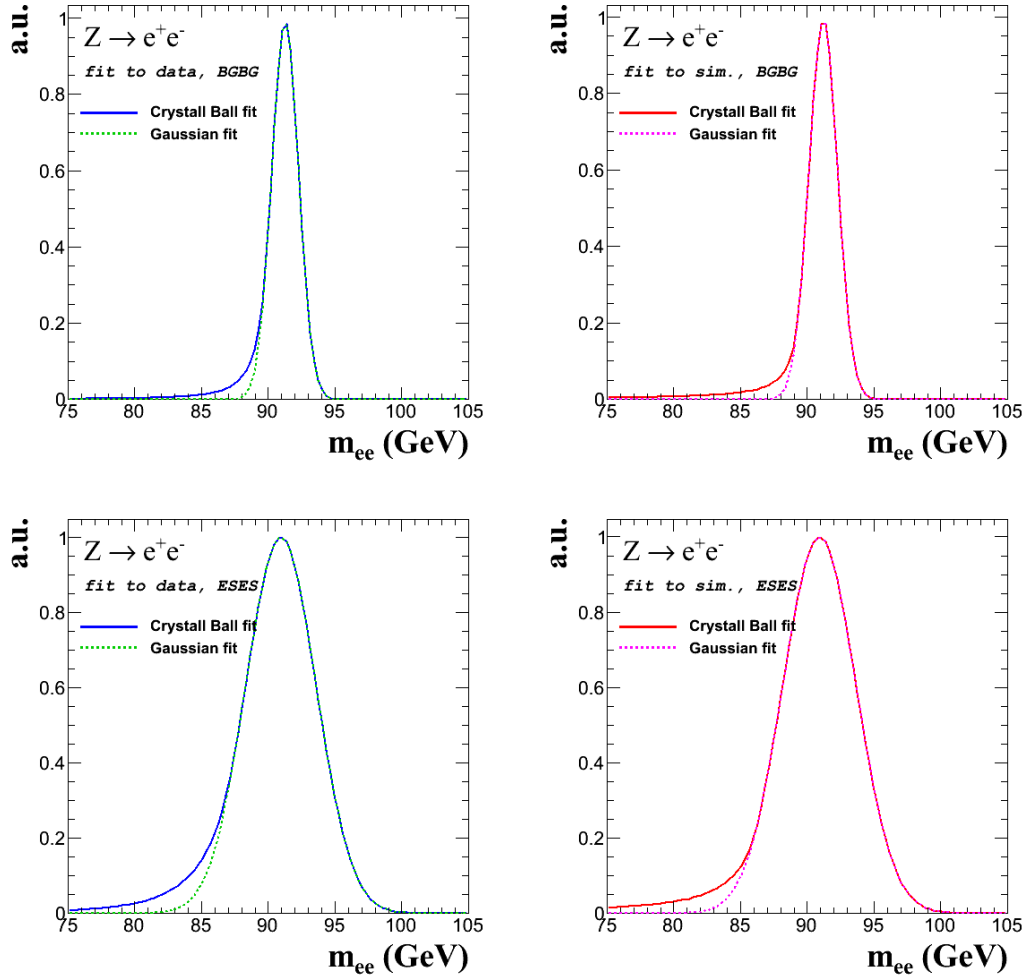


Figure 3.23 – Comparison of the CB fit and its gaussian core for $Z \rightarrow ee$ events categorized regarding the electrons classification for the best category of events, with both electrons belonging to golden or big brems class in the ECAL barrel (denoted BGBK) (top) and the worst category, with both showering, bad track or crack electrons in the ECAL endcaps (denoted ESES) (bottom). Left figures correspond to data results and right ones to the simulation.

containing 68% of the events. The relative difference between the resolutions, obtained from data and simulation, is shown in Fig. 3.24 (left).

This study shows that the corrected simulation matches well the resolution in the data and validates the applied additional gaussian smearing.

Summarizing the above, we can provide the systematic uncertainties on the electron energy scale and resolution. The propagation of the uncertainties depends on the particular physics analysis. In this thesis work we concentrate on the $H \rightarrow ZZ \rightarrow 4\ell$ study. Averaging by the electron transverse momentum we have almost no electron energy scale uncertainty. Additional

systematic uncertainty on the electron energy scale arises because of the p_T dependency of the scale, which we account for by applying linearity corrections. In case of the $H \rightarrow ZZ \rightarrow 4\ell$ analysis we propagate this dependency into the signal simulation and the four lepton invariant mass scale shift of 0.3% (0.1%) for the $4e$ ($2e2\mu$) final state is assigned as the systematic uncertainty. The systematic uncertainty on the resolution is taken as the difference between the predicted and measured values. The comparison between the predicted and measured effective resolution of the CB function (i.e. instrumental resolution) is shown in Fig. 3.24 (right) as a function of the electron category. The propagation of the relative resolution uncertainties

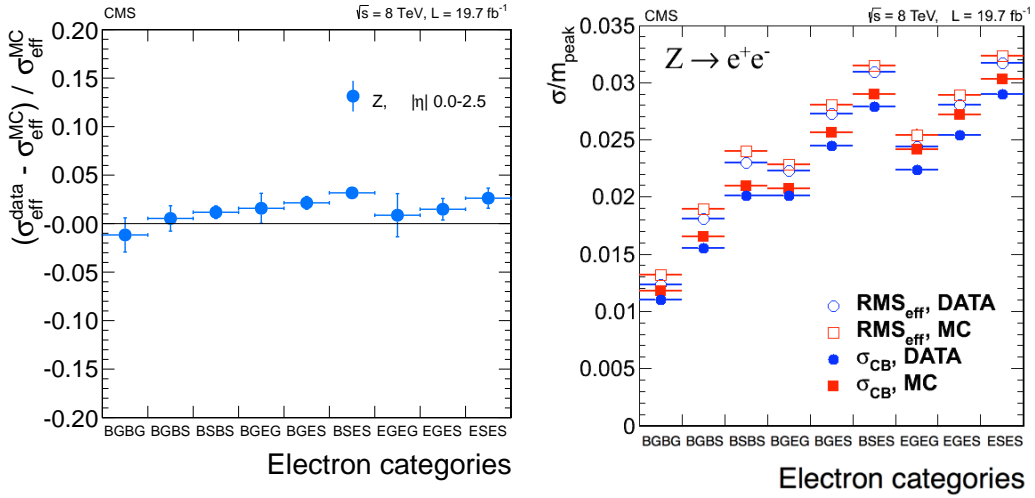


Figure 3.24 – Left: relative difference between the effective resolution, measured in data and simulation respectively. Right: relative instrumental dielectron effective resolution as measured from $Z \rightarrow ee$ events and compared to simulation. Events are categorized according to the electron class and pseudorapidity region of each leg (G : golden electron category, S : showering electron, B : electron in the $|\eta|$ range of the ECAL barrel, E : electron in the $|\eta|$ range of the ECAL endcaps). Results are presented for data collected at $\sqrt{s} = 8$ TeV.

in the $H \rightarrow ZZ \rightarrow 4\ell$ analysis is detailed in the next chapter.

The present study shows good performance of the electron reconstruction and momentum determination. After the application of the scale corrections and the additional smearing for the MC samples we can see a very nice agreement between the data and simulation. This is of primary importance in particular for the Higgs boson search since we use the electrons with transverse momentum starting from 7 GeV and require very high precision of electron momentum measurement. Having the final scale corrections we can provide the resolution dependency on the electron energy. The events from the MC simulated sample with flat p_T spectrum from 1 to 100 GeV was divided in bins with respect to the generated energy. In each bin the resolution was obtained from the fit of $P^{\text{comb}}/P_{\text{true}}$. The examples of the fit for the generated energies 16 GeV and 86 GeV are shown in Fig. 3.25. The final results are presented in Fig. 3.26.

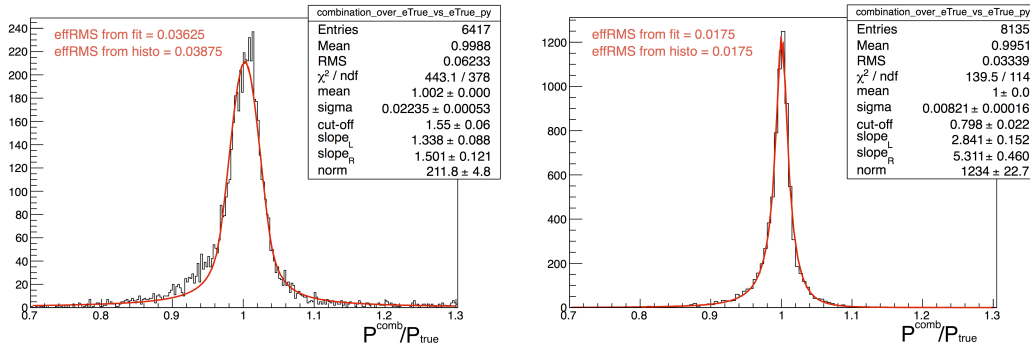


Figure 3.25 – Distribution of P^{comb}/P_{true} for electrons with the generated energy 16 GeV (left) and 86 GeV (right).

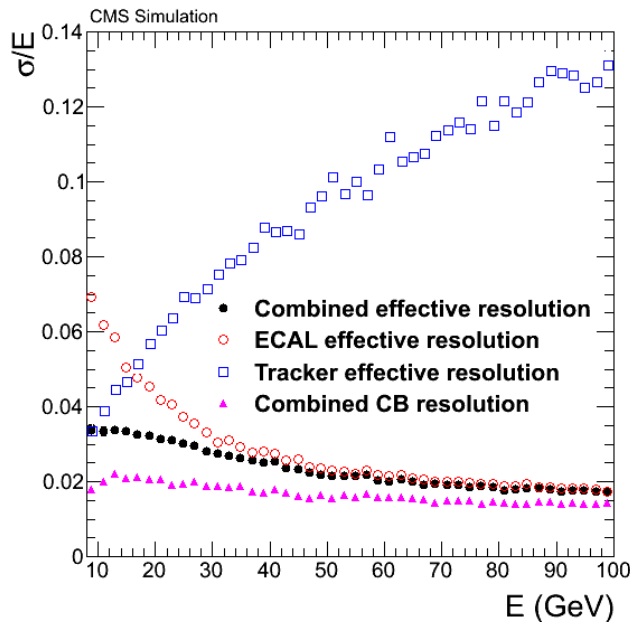


Figure 3.26 – Relative effective width for electrons in the barrel as a function of the electron energy, for the combined momentum, compared to the supercluster corrected energy and the tracker momentum. The Gaussian width is also shown for the combined momentum. Flat η simulated back to back electrons with a flat p_T distribution of $1 < p_T < 100$ GeV are used.

Concluding this chapter, we should say that the scale and resolution appear to be well modeled by the MC after the corrections. Overall, the data-MC scale is within 2‰ in general for all categories (golden/showering and barrel/endcap). The resolution difference between the simulation and data is within 5% while the relative effective resolution is kept below 4.4%. Such precision allows to perform a very accurate Higgs boson mass measurement as it is presented in the next chapter.

4 Higgs Boson Search In The $H \rightarrow ZZ^* \rightarrow 4\ell$ Channel and Its Mass Measurement

As it was mentioned in the Sec. 1.2, the $H \rightarrow ZZ^* \rightarrow 4\ell$ channel is one of the most powerful in the Higgs boson searches both at high and low mass phase space regions. Looking ahead we can say that this channel played a major role in the Higgs boson discovery at the LHC. Despite the fact that the $H \rightarrow ZZ \rightarrow 4\ell$ offers a very clear and fully reconstructable final state, the measurements in this channel under the low-mass Higgs boson hypotheses are complicated by the low branching fraction. This requires a very efficient event selection and background rejection. The backgrounds include irreducible $4\ell^1$ contributions from the $q\bar{q} \rightarrow ZZ^{(*)}$ and $gg \rightarrow ZZ^{(*)}$ di-boson production and instrumental backgrounds in which hadronic jets or secondary leptons are misidentified as primary leptons. The main possible sources of instrumental background contributions are the $Z + \text{jets}$ production with the $Z \rightarrow \ell^+ \ell^-$ decays, the $Zb\bar{b}$ (and $Zc\bar{c}$) associated production with the $Z \rightarrow \ell^+ \ell^-$ decays, and the production of top quark pairs in the decay mode $t\bar{t} \rightarrow WbW\bar{b} \rightarrow \ell^+ \ell^- \nu\bar{\nu}b\bar{b}$.

I began to work on this analysis not long before both the CMS and ATLAS experiments reported about the observation of the new particle, candidating to be a Higgs boson. My contribution to the discovery was not in the physics analysis, however the results of my studies of electron momentum determination, reported in the previous section, were used there. The most important results regarding the electron energy scale and resolution uncertainties were included in the first public presentation and publication of the new particle observation. Following my expertise on the electron scale and resolution determination, I worked on the Higgs boson mass measurements. Within the group I then contributed to the propagation into the analysis of per-lepton uncertainties in case of electrons and provided the independent cross-check of the mass measurement and associated errors compatibility. In this chapter I describe the Higgs boson search analysis and my contribution to its mass measurement.

¹ ℓ denotes any charged lepton, e, μ or τ

4.1 Data and Simulated Samples

4.1.1 Experimental data and online event selection

The data sample used in this analysis was recorded by the CMS experiment during the Run I data taking period. It corresponds to the integrated luminosity $\mathcal{L} = 5.1 \text{ fb}^{-1}$ recorded in 2011 at 7 TeV and $\mathcal{L} = 19.7 \text{ fb}^{-1}$ recorded in 2012 at 8 TeV. The CMS standard selection of runs and luminosity sections is applied ensuring high quality data with a good functioning of the different sub-detectors.

The analysis makes use of primary datasets (PDs) which are produced centrally and correspond to various combinations of High Level Triggers (HLT) menus.

For the 2011 data, the analysis relies on the so-called *DoubleElectron* and *DoubleMuon* PDs [33]. These PDs are formed by an OR between various triggers with symmetric or asymmetric trigger thresholds for the two leptons, with or without additional identification and isolation requirements. They also include triggers requiring three leptons above a low p_T threshold. For the 2011 data, the $2e2\mu$ events were selected from the *DoubleElectron* and *DoubleMuon* datasets avoiding the double-counting by vetoing the *DoubleElectron* triggers in the *DoubleMuon* PD. In 2012 the cross-triggers are added to recover few percents of inefficiency in the $2e2\mu$ channel at low Higgs boson masses, forming the so-called *MuEG* PD. We also use the tri-electron triggers for both 2011 and 2012 data to recover most of the inefficiency of the *DoubleElectron* trigger.

The PDs and trigger paths used for this analysis are summarized in Table 4.1.

Datasets	
2011	2012
/DoubleElectron/ /DoubleMu/	/DoubleElectron/ /DoubleMu/ /MuEG/
Muon triggers	
HLT_DoubleMu7 OR HLT_Mu13_Mu8 OR HLT_Mu17_Mu8	HLT_Mu17_Mu8
Electron triggers	
HLT_Ele17_CaloTrk_Ele8_CaloTrk OR HLT_Ele17_CaloTrk_Ele8_CaloTrk	HLT_Ele17_CaloTrk_Ele8_CaloTrk HLT_Ele15_Ele8_Ele5_CaloIdL_TrkIdVL
Cross triggers	
	HLT_Mu17_TkMu8 OR HLT_Mu8_Ele17_CaloTrk OR HLT_Mu17_Ele8_CaloTrk

Table 4.1 – Datasets and triggers used in the analysis. CaloTrk = CaloIdT_CaloIsoVL_TrkIdVL_TrkIsoVL

The triggers names have key values, that should be interpreted as follows:

- HLT - High Level Trigger
- Ele(Mu)XX - electron or muon, passing the p_T threshold given by XX in GeV

- Double(Triple)Ele(Mu)XX - two or three leptons of corresponding flavour, passing the same p_T threshold given by XX in GeV
- CaloIdT(CaloIdL) - tight or loose identification requirement imposed in the ECAL
- CaloIsoVT(CaloIsoVL) - tight or loose isolation requirement imposed in the ECAL. VT denotes Very Tight and VL - Very Loose
- TrXXX - the same as above, applied to the tracker measurements

The detailed description of the identification and isolation requirements is provided in [34].

The trigger efficiency has been measured with the Tag&Probe method² on data and compared to the MC simulation. The results in case of the DoubleElectron trigger with p_T threshold of 17 and 8 GeV are presented in Fig. 4.1. Overall, the expected trigger efficiency for $H \rightarrow ZZ \rightarrow 4\ell$

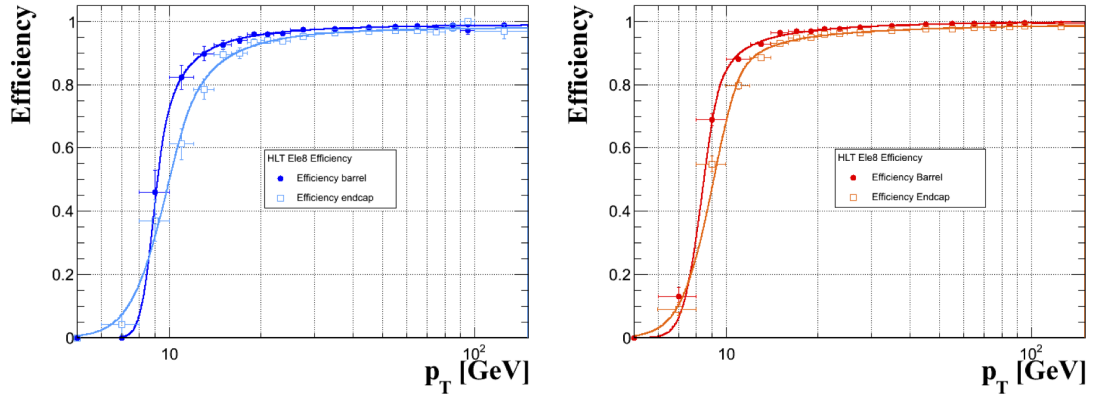


Figure 4.1 – Trigger efficiency for the Ele17Ele8 filter, measured with 2012 data (left) and in MC simulation (right)

events within the geometrical acceptance of this analysis is greater than 98% for a Higgs boson signal with $m_H > 110$ GeV.

4.1.2 Simulated samples

Detailed Monte Carlo (MC) simulations were used in order to provide various SM Higgs boson samples as well as electroweak and QCD-induced SM background processes. All MC datasets were subjected to the full reconstruction and skimming³ procedure. This includes the precise detector simulation and a reconstruction procedure identical to the one applied on data.

² The Tag&Probe method consist in tagging the resonance (e.g. Z boson) decay by one lepton with a tight selection and searching for a second lepton requiring a very loose selection (probe). Then, efficiency is estimated as the number of probe electrons which pass the enforced selection with respect to the very loose probe selection.

³ The skimming is the process of selection of the events that pass some loose selection criteria before performing the detailed study for each physics process.

Chapter 4: Higgs Boson Search In The $H \rightarrow ZZ^* \rightarrow 4\ell$ Channel and Its Mass Measurement

These samples have been used in the analysis for the comparisons with the measurements, the evaluation of acceptance corrections and systematic uncertainties, and for the background evaluation procedure where the measurements in a "background control" region are extrapolated to the "signal" region.

All the signal and background processes cross sections are re-weighted to the next-to-leading order (NLO) cross section calculations. In case of the Higgs boson production via the gluon fusion mechanism, the most recent NNLO+NNLL calculations of the cross sections are included [35].

The general multi-purpose Monte Carlo event generator PYTHIA [36] is used in order to generate some hard processes at the leading order (LO) and for the hadronization and showering when the hard processes are generated at higher orders.

In latter cases few different Monte Carlo event generators are used. The MadGraph (MadEvent) Monte Carlo [37] event generator is used to generate the multi-parton amplitudes and events for some di-boson and V+jets background processes. The POWHEG NLO generator [38] is used for the Higgs boson signal and for the ZZ and $t\bar{t}$ background. The Higgs boson decay is modeled with JHUGEN 3.1.8 [39, 40, 41] and includes proper treatment of the interference effects associated with permutations of identical leptons in the four-electron and four-muon final states. Finally, the dedicated tool GG2VV [42] is used to generate the $gg \rightarrow ZZ$ contribution to the ZZ^* cross section.

4.2 Event Selection

Since the branching fraction of the $H \rightarrow ZZ^*$ is quite low below the $2m_Z$ threshold (from $\sim 1\%$ for $m_H = 120$ GeV to $\sim 7\%$ for $m_H = 140$ GeV), it is extremely important to have high efficiency of the event selection in order to preserve reasonably high event rate. In addition, the possible final state radiation must be reconstructed and recovered to have the correct kinematics of the event. In this section the phase space selection will be described alongside with the final state radiation (FSR) recovery technique. Besides this, the dedicated event categorization used to separate the different production modes is shown.

4.2.1 Vertex Selection

The selection starts by the requirement of at least one good primary vertex (PV) fulfilling the following criteria: high number of degrees of freedom ($N_{PV} > 4$), collisions restricted along the z -axis ($z_{PV} < 24$ cm) and small radius of the PV⁴ ($r_{PV} < 2$ cm).

⁴Radius of the PV is the distance between the PV and the point ($x = 0; y = 0$) in the transverse plane

4.2.2 Impact Parameter Selection

The selection on the impact parameter is needed in order to remove leptons from in-flight decays of hadrons and muons from cosmic rays. All leptons are required to have a common primary vertex. This is achieved by requiring $|SIP_{3D}| < 4$, where $SIP_{3D} \equiv IP_{3D}/\sigma_{IP_{3D}}$ is the ratio of the impact parameter of the lepton track in three dimensions (IP3D) with respect to the chosen primary vertex position and its uncertainty.

4.2.3 Lepton Isolation

The particle-flow based isolation is used in this analysis. This algorithm shows the best performance in terms of the separation from the fake lepton candidates. It is defined by performing the scalar sum of the transverse momenta of the particle flow candidates reconstructed in a $\Delta R = \sqrt{\Delta\eta^2 + \Delta\phi^2}$ cone of 0.4 around the lepton direction at the interaction vertex, defined as:

$$\text{RelPFiso} = \frac{\sum^{\text{chargedhadron}} p_T + \sum^{\text{neutralhadron}} p_T + \sum^{\text{photon}} p_T}{p_T^{\text{lepton}}} \quad (4.1)$$

The contribution from the pile-up in the isolation cone is subtracted from the RelPFiso. Different techniques are used for the electrons and muons. For the electrons we can represent the correction as $p_T^{PU}(e) \equiv \rho \times A_{eff}$, where ρ is the median of the energy density distribution for the neutral particles within the area of any jet in the event and A_{eff} is the geometric area of the isolation cone, scaled by a factor that accounts for the residual dependence of the average pile-up deposition on the electron η . For the muons $p_T^{PU}(\mu) \equiv 0.5 \times \sum p_T^i$, the scalar sum of transverse momenta of the charged hadron PF candidates not originating from the primary vertex. The factor 0.5 in the sum accounts for the different fraction of the charged and neutral particles in the isolation cone.

4.2.4 Lepton Identification

For the electron identification a Boosted Decision Tree (BDT) multivariate technique is used. The variables entering the BDT involve the ones sensitive to the bremsstrahlung radiation emitted by an electron, shower-shape variables and the geometrical and momentum matching between the electron trajectory and associated clusters. The training was done on the simulated Higgs boson samples and on the $W + 1$ -fake electron data sample for the background.

For the muons a different identification algorithm is applied. They are splitted into three categories: isolated, PF-tight and PF-loose. The isolated muons have by definition little neighbouring activity. Hence the particle-flow technique is not needed to resolve additional particles in their vicinity. The remaining muons are divided between the PF-tight and PF-loose subsets. The identification of non-isolated muons takes place before the other categories of particles. The PF-tight selection requires a minimum number of hits in the muon track and

Chapter 4: Higgs Boson Search In The $H \rightarrow ZZ^* \rightarrow 4\ell$ Channel and Its Mass Measurement

compatibility between the muon segment and calorimeter deposits. Other reco muons can be recovered by the PF-loose selection. In this selection, the requirement on the number of hits is relaxed, and the compatibility between the muon segment and calorimeter deposits requirement is replaced by a matching requirement between the track and the hits in the muon stations.

4.2.5 Final State Radiation Recovery

In case of the presence of a FSR photon candidate we must take it into account modifying properly the event kinematics as well as the isolation sum. Events with electrons in the final state are less affected by FSR than the ones with muons due to the inclusion of nearby FSR photons in the electromagnetic supercluster. Therefore the four muon final state is affected the most. Including the FSR recovery algorithm in the analysis chain we gain in selection efficiency because of the subtraction of the photon from the isolation annulus of the leptons and increased efficiency of the di-lepton mass requirements.

Only the photons with p_T^γ in excess of $2 \text{ GeV}/c$ and well in the tracker acceptance ($|\eta| < 2.4$) are considered, and tentatively assigned to a lepton and to a Z from the candidate Higgs boson decay. The association of the FSR photon candidate to a lepton goes as follows:

- (i) Photons are considered only if the minimum ΔR distance with respect to any of the Z leptons is smaller than $\Delta R < 0.5$.
- (ii) In order to remove the photons which arise from a pile-up or from the underlying event, in case of the distance of the photon to the closest lepton is between 0.07 and 0.50 we must tighten the p_T^γ cut to $4 \text{ GeV}/c$. Also the photon is required to be somewhat isolated from other particles: the relative PF isolation including the pile-up contribution is required to be smaller than 1.0.
- (iii) For both Z candidates, only the photons that make a mass with a lepton pair closer to the nominal Z mass (taken here to be 91.2 GeV) but with a maximum $m_{\ell\ell\gamma} < 100 \text{ GeV}$ are kept.
- (iv) After the photons have been selected with the above criteria the best photon is selected as follows:
 1. If there is at least one photon with $p_T > 4 \text{ GeV}$ the one with the highest transverse momentum is associated to the Z boson
 2. If there is no photon with $p_T > 4 \text{ GeV}$ the closest photon to any of the leptons is associated to the Z

Finally, the invariant mass criteria defined in Sec. 4.2.7 are applied using the four-vector defined as the sum of the four-vectors of the two leptons and the photon.

After the FSR recovery an event can have zero, one or two selected FSR photon candidates. If there is one or two selected FSR candidates we should modify the lepton isolation by removing the selected photons from the corresponding lepton isolation cones (if in the isolation cones) and redefine the Z candidate masses with the corresponding lepton pair and the associated photon. Then, the default four lepton analysis applies.

The performance of the FSR identification algorithm is quantified using the samples from the simulation and data. The gain of the FSR algorithm is composed from the two parts:

- Events with associated photons move towards to the nominal reconstructed mass improving the resolution.
- New events migrate into the sample due to the higher isolation efficiency and the improved definition of the mass of the Z candidate.

The FSR identification algorithm is tested on simulated Higgs signal events with a mass of 126 GeV with an average PU of 20 interactions. The total efficiency is compared by running the full selection with and without the FSR algorithm applied. The Fig. 4.2 shows the comparison of the invariant mass distribution before and after the FSR recovery for events with an identified FSR photon and overall events. The FSR algorithm recovers performance by moving the events from the FSR tail back to the Higgs boson peak bulk distribution. In the case of the Higgs

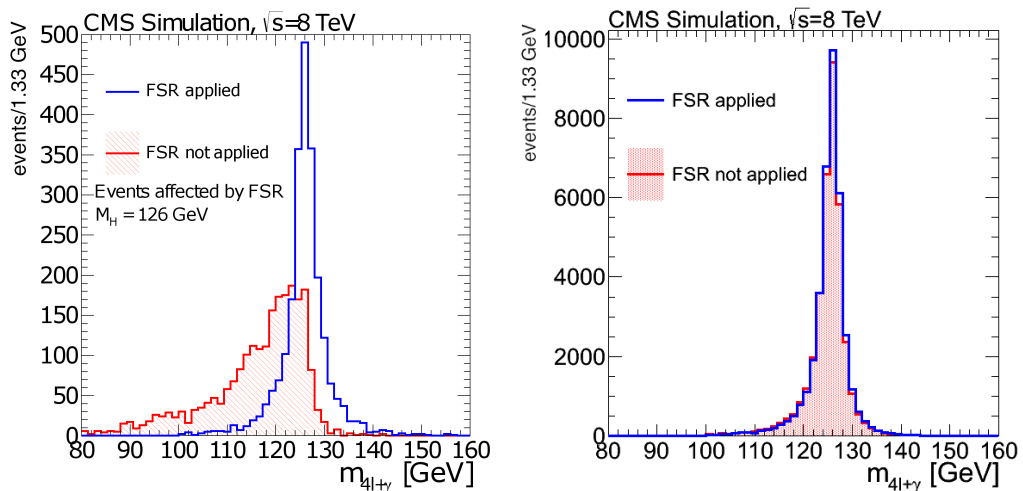


Figure 4.2 – Invariant mass reconstruction of the Higgs boson candidate of the events with an identified FSR photon (left) and all events (right) for the Higgs boson signal with $m_H = 126$ GeV

boson signal, the tails are reduced and the arithmetic RMS is improved from 7.1% to 6.9% while the Gaussian RMS is not modified showing that the effect on the width distribution due to the impurity is negligible. The rate⁵, gain in the event selection efficiency and purity⁶ for

⁵Rate means fraction of events with reconstructed FSR photons

⁶Purity means fraction of genuine FSR photons among the reconstructed ones

**Chapter 4: Higgs Boson Search In The
 $H \rightarrow ZZ^* \rightarrow 4\ell$ Channel and Its Mass Measurement**

the Higgs boson signal and SM ZZ continuum are presented in Tab.4.2.

final state	rate (%)	purity (%)	gain (%)
$H \rightarrow ZZ(\text{all})$	6.0	80	2.0
$H \rightarrow ZZ \rightarrow 4\mu$	9.1	82	3.0
$H \rightarrow ZZ \rightarrow 2e2\mu$	5.0	78	0.6
$H \rightarrow ZZ \rightarrow 4e$	1.4	72	1.8
SM ZZ(all)	6.7	81	2.1
SM ZZ $\rightarrow 4\mu$	10.1	83	3.0
SM ZZ $\rightarrow 2e2\mu$	6.5	77	0.6
SM ZZ $\rightarrow 4e$	1.8	72	1.8

Table 4.2 – Rate, purity and gain in the event selection efficiency for signal and ZZ background

The FSR recovery algorithm also affects the reducible background. In that case, fake π^0 inside jets can be identified as FSR photons, which modify both the yield and the shape of the reducible background. Those effects are studied in detail in a control region consisting of a tagged Z candidate and two loosely identified same sign leptons.

4.2.6 Loose and Tight Lepton Selection

Two flavors of leptons on which the selection steps act on are defined:

1. **loose leptons:** electrons within the geometrical acceptance of $|\eta^e| < 2.5$, with $p_T^e > 7 \text{ GeV}/c$ and having 0 or 1 expected missing inner hits, muons (global or tracker) satisfying $|\eta^\mu| < 2.4$, $p_T^\mu > 5 \text{ GeV}/c$. Both electrons and muons should satisfy loose requirements on the transverse ($d_{xy} < 0.5 \text{ cm}$) and longitudinal ($d_z < 1 \text{ cm}$) impact parameters with respect to the primary vertex. Non-global tracker muons must be arbitrated and a requirement on the shared segments is asked. In addition, the requirement on a minimal distance between the leptons $\Delta R > 0.02$ is imposed. The *loose leptons* are used in the estimation of reducible background.
2. **tight leptons:** these are *loose leptons* on which additional criteria are imposed. Namely:
 - electrons should pass the electron identification criteria as described above, muons should meet the Particle Flow Muons requirements;
 - Relative PFIso < 0.4 ;
 - the significance of the impact parameter to the event vertex, SIP_{3D}, is required to satisfy $|\text{SIP}_{3D}| = \left| \frac{\text{IP}_{3D}}{\sigma_{\text{IP}_{3D}}} \right| < 4$ for each lepton

The cross cleaning among the leptons is assured by the particle flow isolation, for which we veto all the particle flow leptons reconstructed within the isolation cone of $\Delta R = 0.4$. For electrons, for which there are rare cases where the particle flow electron does not match with the selected electron, extra vetoes are applied in the isolation procedure.

4.2.7 Best Candidate Selection

We impose the following sequence of selection requirements:

1. **First Z:** a pair of tight lepton candidates of the opposite charge and matching flavour (e^+e^- , $\mu^+\mu^-$) with the reconstructed mass $m_{1,2}$ closest to the nominal Z boson mass is retained and denoted Z_1 . The selected pair should satisfy $40 < m_{Z_1} < 120$ GeV.
2. **Three or more leptons:** at least another tight lepton candidate of any flavour or charge.
3. **Four or more leptons and a matching pair:** a fourth tight lepton candidate with the flavour of the third lepton candidate from the previous step, and with the opposite charge.
4. **Choice of the best 4ℓ and Z_1, Z_2 assignment:** retain a second lepton pair, denoted Z_2 , among all the remaining $\ell^+\ell^-$ combinations. If more than one Z_2 combination satisfies all the criteria, the one built from the leptons of highest p_T is chosen. The selected pair should satisfy $4 < m_{Z_1} < 120$ GeV. At this stage, it is required that at least two leptons from the four selected have $p_{T,i} > 20$ GeV and $p_{T,j} > 10$ GeV.
5. **QCD suppression:** the reconstruction mass of the each opposite-sign and same-flavor lepton pair must satisfy $m_{\ell\ell} > 4$ GeV.
6. **Higgs phase space** is defined by requiring $m_{Z_2}^{min} \equiv 12$ GeV, $m_{Z_1}^{min} \equiv 40$ GeV and $m_{4\ell}^{min} \equiv 100$ GeV. This provides a best sensitivity for masses $m_H < 130$ GeV.

In order to raise the sensitivity to the $Z \rightarrow 4\ell$ events, which are used to cross-check many of the measurements for the low mass Higgs boson due to the proximity of the phase space, a looser selection for the $Z_{1,2}$ is defined, as follows:

- $Z \rightarrow 4\ell$ **phase space** is defined by requiring $m_{Z_2}^{min} \equiv 4$ GeV and $m_{Z_1}^{min} \equiv 40$ GeV, $m_{4\ell}^{min} \equiv 70$ GeV and $m_{4\ell}^{max} \equiv 110$ GeV.

4.2.8 Selection Efficiency

The selection efficiencies for the different signal production modes and final states were estimated using the Monte-Carlo simulated samples with different values of the hypothetical Higgs boson mass. The signal events were generated with $|\eta^\ell| < 5$ and invariant mass of the dileptons from both the Z_1 and the Z_2 boson decays $m_{\ell^+\ell^-} > 1$ GeV. The overall signal detection efficiencies, including geometrical acceptance, grows rapidly as a function of m_H up to approximately $2m_Z$. After this threshold both the Z bosons are on shell, and the selection efficiency flattens. The residual rise for $m_H > 300$ GeV is mostly due to the increased acceptance. The efficiency within the geometrical acceptance for the gluon fusion production is $\approx 32\%$ (61%), 43% (73%), and 62% (87%) for the $4e$, $2e2\mu$ and 4μ respectively, for $m_H = 126$ (200) GeV as it is shown in

Chapter 4: Higgs Boson Search In The $H \rightarrow ZZ^* \rightarrow 4\ell$ Channel and Its Mass Measurement

Fig. 4.3 (left). The Fig. 4.3 (right) shows the efficiency times the geometrical acceptance curves for the gluon fusion Higgs boson production mode, and it is very similar for other production modes. A simple polynomial function interpolating the m_H points for which we have the simulation is used.

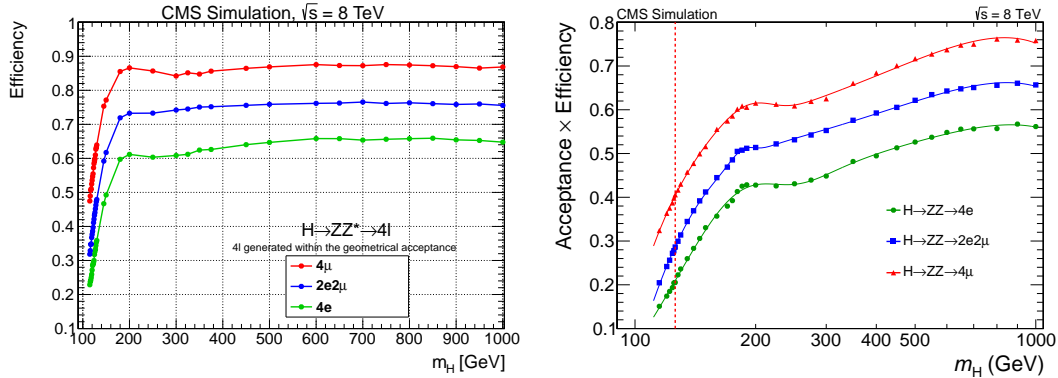


Figure 4.3 – Selection efficiency within the geometrical acceptance (left) or geometrical acceptance times selection efficiency (right) for the SM Higgs boson signal as a function of m_H in the three final states for the gluon fusion production. Points represent the efficiency estimated from the full CMS simulation; lines represent a smooth polynomial curve interpolating the points, used in the analysis. The vertical dashed line represents $m_H = 126$ GeV.

4.3 Background Estimation

The main background contributions come from the direct ZZ production via $q\bar{q}$ annihilation and gluon fusion. These backgrounds have very similar kinematics to the $H \rightarrow ZZ \rightarrow 4\ell$ and are irreducible. The remaining contributions are subleading and arise from the reducible multilepton sources like $Z + \text{jets}$, $t\bar{t}$ and $WZ + \text{jets}$.

4.3.1 Irreducible Background

We use the Monte Carlo simulation to determine the expected yield and shape of the ZZ background. The generator MCFM [43] was used to calculate the cross sections for $q\bar{q} \rightarrow ZZ$ (at next-to-leading order) and GG2VV for $gg \rightarrow ZZ$ (at leading order).

The relative contribution of the LO $gg \rightarrow ZZ$ with respect to the NLO $q\bar{q} \rightarrow ZZ$ is about 2% at four-lepton mass $m_{4\ell} = 126$ GeV and about 6% at 1 TeV. The expected contribution of the ZZ processes to the total background, in the region $100 < m_{4\ell} < 1000$ ($121.5 < m_{4\ell} < 130.5$) GeV, is approximately 91%, 94%, and 97% (58%, 71%, and 86%) in the $4e$, $2e2\mu$, and 4μ channels, respectively. The main theoretical uncertainties on the ZZ background shape come from the PDF and QCD scale uncertainties. They are accounted by varying the QCD scale and PDF parameters accordingly to the LHCXSWG recommendations [19]. The shape uncertainties

arising from imperfect simulation of the P_T^ℓ and η^ℓ dependence of the efficiency and other experimental sources are completely overshadowed by the systematic uncertainties on the normalization, such that shape variations have negligible effects.

The irreducible four-lepton background arising from double-parton interactions (DPI), $Z + \text{Drell-Yan}$ (DY), is estimated to be much smaller than normalization uncertainties on any other irreducible or reducible background source. It was evaluated using PYTHIA 6.4.24 with the overall cross section calculated as $\sigma_{\text{DPI}} = \sigma_Z \cdot \sigma_{\text{DY}} / \sigma_{\text{pheno}}$, where the phenomenological effective cross section, measured at $\sqrt{s} = 7 \text{ TeV}$, is $\sigma_{\text{pheno}} = 15 \text{ mb}$ [44], and the cross sections σ_Z and σ_{DY} are taken from the simulation. Hence this background is neglected in the analysis.

4.3.2 Reducible background

The reducible background (named $Z + X$ since it is dominated by $Z + \text{jets}$ process) in this analysis is estimated using a data-driven technique. There are two independent methods denoted as opposite-sign (OS) and same-sign (SS) leptons, cross-checking and complementing each other. In both methods the study is performed in the dedicated control regions, formed by the requirement of the Z_1 candidate selection and two additional leptons, opposite sign (OS) or same sign (SS), satisfying certain relaxed identification requirements. Such selections provide one prompt Z boson candidate and one misidentified. Hence, it is natural to impose an additional condition on the second dilepton pair invariant mass to be larger than 12 GeV in order to preserve the consistency with the signal selection. Thereafter we extrapolate the obtained results from the control regions to the signal region using the lepton misidentification probability, $f(\ell, p_T^\ell, |\eta^\ell|)$, which is defined as the fraction of non-signal leptons identified with the analysis selection criteria, estimated in an enriched sample of non-genuine electrons and muons. The sample used to determine this rate is composed of three-lepton events in the data where two leptons, forming the Z candidate, pass the *tight* selection requirements and exactly one lepton passes the *loose* selection. The mass of the Z_1 candidate is required to satisfy $|m_{\ell\ell} - m_Z| < 10 \text{ GeV}$ for the OS leptons method and $|m_{\ell\ell} - m_Z| < 40 \text{ GeV}$ for the SS leptons method. Such strong requirement in the OS leptons method is needed to suppress the contribution of events with the FSR where the photon converts and one of the conversion products is not reconstructed. In order to suppress the contribution from WZ and $t\bar{t}$ processes, which have a third lepton, the missing transverse energy (\cancel{E}_T) is required to be less than 25 GeV. The \cancel{E}_T is defined as the modulus of the vector sum of the transverse momenta of all reconstructed PF candidates (charged or neutral) in the event. In order to reject contributions from low-mass resonances, such as J/ψ , the invariant mass of the loose lepton and the opposite-sign lepton from the Z_1 candidate, if they have the same flavor, is required to be greater than 4 GeV.

Overall, such requirements result in a sample enriched with events consisting of Z boson and a misidentified additional lepton. Hence, the fraction of these events in which the additional lepton passes the analysis identification and isolation requirements gives a rate $f(\ell, p_T^\ell, |\eta^\ell|)$

Chapter 4: Higgs Boson Search In The $H \rightarrow ZZ^* \rightarrow 4\ell$ Channel and Its Mass Measurement

that ranges between 1%–15% (5%–10%) depending on the p_T^ℓ and $|\eta^\ell|$ of the electron (muon).

Method using opposite-sign (OS) leptons

In order to define the control region in this method events with a Z_1 candidate and two additional leptons with the same flavor and opposite charge are used. Depending on the additional leptons characteristics two subsets of events are considered. If none of the additional leptons satisfies the tight selection (remember that the ones forming the Z_1 candidate must) we call this category 2P2F which means that two leptons pass and two fail the tight selection (but pass the loose one). It is used to estimate the contribution from backgrounds that have only two prompt leptons by construction (Z + jets, $t\bar{t}$). The contribution of these background processes in the signal region is estimated by weighting each 2P2F event i by a factor $\frac{f_3^i}{1-f_3^i} \frac{f_4^i}{1-f_4^i}$, where f_3^i and f_4^i are the $f(\ell, p_T^\ell, |\eta^\ell|)$ for the leptons which pass only loose selection.

Following the same logic we call 3P1F category the subset of events where exactly one additional lepton passes the tight selection criteria. This category is used to estimate the contribution from backgrounds with three prompt leptons and one misidentified lepton (WZ + jets and $Z\gamma$ + jets with the photon converting to an e^+e^- pair). Analogously to the 2P2F case we must weight each 3P1F event in the control region by a factor $\frac{f_a^j}{1-f_a^j}$, where f_a^j is the $f(\ell, p_T^\ell, |\eta^\ell|)$ for the third or fourth lepton to fail the analysis selection. This control region also has a contribution from the ZZ events where one of the lepton fails the tight selection and from the events where two leptons should have failed tight selection but one is nevertheless passing the tight requirement. In the first case we must apply a reducing factor of $1 - n_{3P1F}^{ZZ}/N_{3P1F}$, where n_{3P1F}^{ZZ} is ZZ contribution estimated from simulation and N_{3P1F} is the number of events of the 3P1F control region. The latter case contribution is represented by the sum of probabilities to misidentify non-prompt lepton to be a prompt which results in the following expression: $\sum_i (2 \frac{f_3^i}{1-f_3^i} \frac{f_4^i}{1-f_4^i})$. This also has to be subtracted from the background event yield estimation. Finally, the expected yield for the reducible background in the signal region, $N_{SR}^{\text{reducible}}$, becomes

$$N_{SR}^{\text{reducible}} = \left(1 - \frac{n_{3P1F}^{ZZ}}{N_{3P1F}}\right) \sum_j \frac{f_a^j}{1-f_a^j} - \sum_i \frac{f_3^i}{1-f_3^i} \frac{f_4^i}{1-f_4^i}. \quad (4.2)$$

Method using same-sign (SS) leptons

In case of the SS method we consider the control region formed from events with a Z_1 candidate and two additional leptons with the same flavor and same charge. Like in the OS method the $f(\ell, p_T^\ell, |\eta^\ell|)$ is measured using a $Z_1 + 1\ell_{\text{loose}}$ sample, but with the looser requirement to the invariant mass of the Z_1 candidate. It is set to $|m_{\ell\ell} - m_Z| < 40 \text{ GeV}$. These released requirements significantly increase the contribution from the events with the FSR photon in the control region. Hence we need to account for the probability of electron misidentification due to the FSR photons. This is done by exploiting the observed linear dependence

of the $f(e, p_T^e, |\eta^e|)$ on the fraction of loose electrons with tracks having one missing hit in the pixel detector, $r_{\text{miss}}(p_T^e, |\eta^e|)$, which points to a possible photon conversion. The fraction $r_{\text{miss}}(p_T^e, |\eta^e|)$ is estimated using the samples with different FSR contributions obtained by varying the requirements on $|m_{\ell\ell} - m_Z|$ and $|m(\ell, \ell, e_{\text{loose}}) - m_Z|$ ⁷. Then, the corrected $\tilde{f}(e, p_T^e, |\eta^e|)$ is calculated using the value $r_{\text{miss}}(p_T^e, |\eta^e|)$ measured in the control sample where the method is applied. Finally, the expected number of reducible background events in the signal region is obtained as:

$$N_{\text{SR}}^{\text{reducible}} = r_{\text{OS/SS}} \cdot \sum_i^{N_{2\text{P}2\text{L}_{\text{SS}}}} \tilde{f}_3^i \cdot \tilde{f}_4^i, \quad (4.3)$$

where $N_{2\text{P}2\text{L}_{\text{SS}}}$ is the number of observed events in the region $2\text{P}2\text{L}_{\text{SS}}$, in which both the additional leptons fulfill the loose selection requirements for leptons, having the same flavor and charge. The ratio $r_{\text{OS/SS}}$ between the number of events in the $2\text{P}2\text{L}_{\text{OS}}$ and $2\text{P}2\text{L}_{\text{SS}}$ control regions is taken from the simulation.

Combination of the two methods

The predictions of the reducible background yields from both methods are in a reasonable agreement within their statistical uncertainties (5.23 ± 0.71 (4.89 ± 0.68) in the first method and 5.66 ± 0.96 (4.52 ± 0.75) in the second method in case of $2e2\mu$ ($4e$) final state), however limited number of events in the control regions as well as in the region where the correction factor for $\tilde{f}(e, p_T^e, |\eta^e|)$ is computed lower the accuracy of the estimation. On the other hand these two methods are statistically independent since they are using different control regions and therefore their results can be combined.

We extract the shape of the $m_{4\ell}$ distribution for the $Z+X$ background from the OS method. The fits with empirical functional forms built from Landau and exponential distributions are done for $2\text{P}2\text{F}$ and $3\text{P}1\text{F}$ events separately. The systematic uncertainty in the $m_{4\ell}$ shape is determined by the envelope that covers both alternative functional forms and alternative binning for the fit used to determine $m_{4\ell}$ shape parameters.

The prediction for the $Z+X$ background yield with combined statistical and systematic uncertainties is shown in Fig. 4.4 (right). Besides the $m_{4\ell}$ shape uncertainty, the total uncertainties account for the difference in the composition of the $Z_1 + 1\ell_{\text{loose}}$ sample used to compute $f(\ell, p_T^\ell, |\eta^\ell|)$ and the control regions in the two methods used to estimate the $Z+X$ background. The systematic uncertainty is estimated to be 20%, 25%, and 40% for the $4e$, $2e2\mu$, and 4μ decay channels, respectively. Both methods have been also validated using the dedicated control regions in the data. The Fig. 4.4 (left) shows the validation of the OS method.

⁷For example, imposing the requirement $|m(\ell, \ell, e_{\text{loose}}) - m_Z| < 5 \text{ GeV}$ provides a sample enriched with FSR

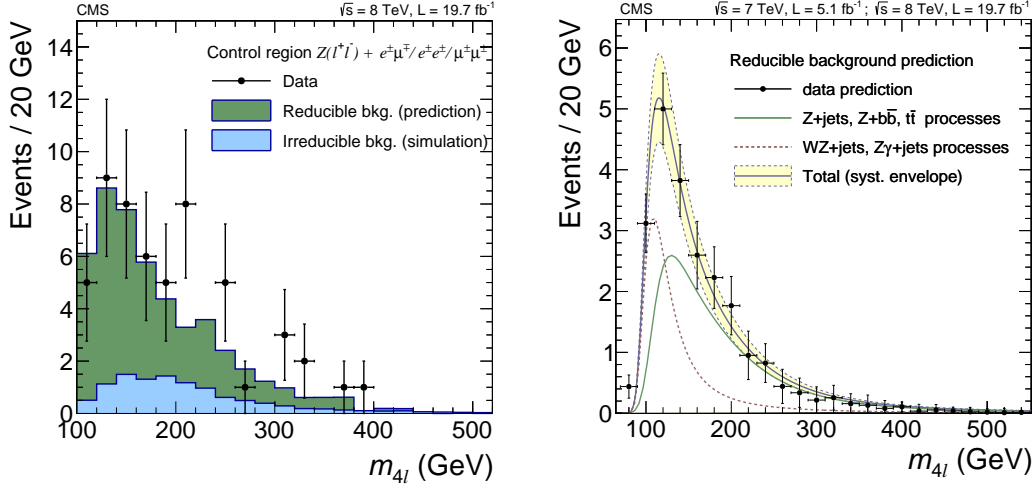


Figure 4.4 – (left) Validation of the OS method using the SS control sample. The observed $m_{4\ell}$ distribution (black dots), prediction of the reducible background (dark green area), and expected contributions from ZZ (light blue area) are shown. (right) Prediction for the reducible background in all three channels together (black dots) fitted using an empirical shape (blue curve) with indicated total uncertainty (yellow band). The contributions from the 2P2F-like (solid green) and 3P1F-like (dashed red) processes are fitted separately.

4.4 Systematic Uncertainties

The systematic uncertainties assigned to the reducible background have been already discussed in the Sec. 4.3.2. For the irreducible backgrounds the situation is different since they are fully simulated. The sources of theoretical uncertainties are parton distribution functions (PDF), coupling constant of strong interaction (α_s) and QCD scale uncertainties. The MCFM generator was used in order to estimate these uncertainties for $q\bar{q} \rightarrow ZZ \rightarrow 4\ell$ at NLO and $gg \rightarrow ZZ \rightarrow 4\ell$ at LO approximations. Following the prescription from the LHCXSWG, the PDF+ α_s and QCD scale uncertainties are treated as uncorrelated, while the uncertainties for different run periods (including both 7 and 8 TeV) are assumed to be 100% correlated.

In order to estimate PDF+ α_s uncertainties three PDF sets were used: CT10 [45], MSTW08 [46], NNPDF [47]. The $m_{4\ell}$ dependency of the systematic errors can be parametrized in the following way:

$$ZZ@NLO : \kappa(m_{4\ell}) = 1 + 0.0035\sqrt{(m_{4\ell} - 30)} \quad (4.4)$$

$$gg \rightarrow ZZ : \kappa(m_{4\ell}) = 1 + 0.0066\sqrt{(m_{4\ell} - 10)} \quad (4.5)$$

The results together with the parametrization are shown in Fig. 4.5.

The QCD scale systematic uncertainties were obtained from the variations in the differential cross section $d\sigma/dm_{4\ell}$ calculated with changing the renormalization and factorization scales

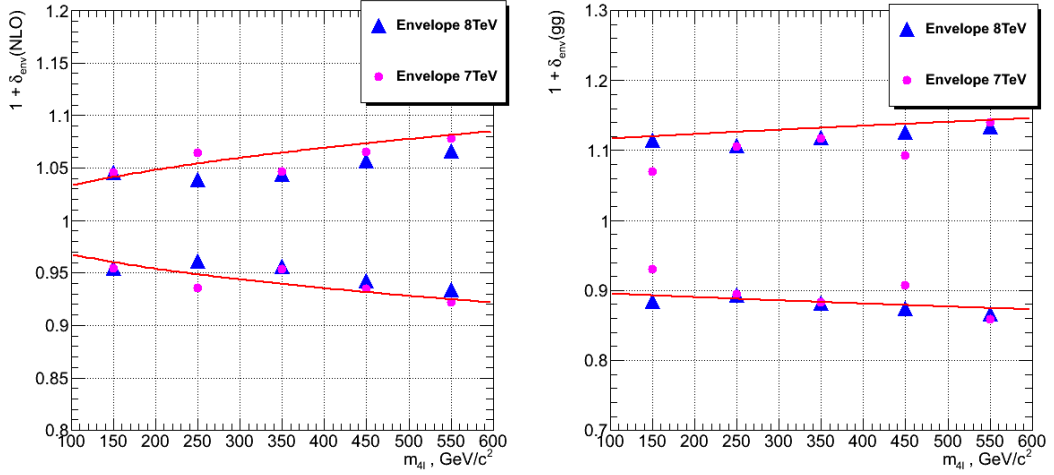


Figure 4.5 – PDF+ α_s uncertainties for (left) $q\bar{q} \rightarrow ZZ \rightarrow 4\ell$ at NLO and (right) $gg \rightarrow ZZ \rightarrow 4\ell$ processes. The points are the evaluated uncertainties. The curves are the analytical parametrizations $\kappa(m_{4\ell})$ which are used in the statistical analysis.

by a factor of two up and down from their nominal value $\mu_R = \mu_F = m_Z$. These errors also depend on $m_{4\ell}$ and can be described as follows:

$$\text{ZZ@NLO} : \kappa(m_{4\ell}) = 1.00 + 0.01\sqrt{(m_{4\ell} - 20)/13} \quad (4.6)$$

$$\text{gg} \rightarrow \text{ZZ} : \kappa(m_{4\ell}) = 1.04 + 0.10\sqrt{(m_{4\ell} + 40)/40} \quad (4.7)$$

The Fig. 4.6 presents the ratio of cross-sections for the different QCD scales settings as a function of four lepton invariant mass with corresponding analytical parametrizations on top.

The experimental systematic uncertainties in the normalization of the signal and the irreducible background processes arise from the triggers efficiencies uncertainties and lepton reconstruction, identification and isolation efficiencies. They are evaluated from the data using the Tag&Probe method. The trigger uncertainties contribute at the level of 1.5%, the combined lepton reconstruction, identification, and isolation efficiencies contribution vary from 5.5% to 11% in the $4e$ final state and from 2.9% to 4.3% in the 4μ one, depending on the considered m_H . The uncertainties related to the lepton energy scale and resolution are discussed in details in the following section.

4.5 Distribution Of Selected Events

Now, having established and discussed all the ingredients of the model such as signal production, background sources and event selection, we are ready to go to the final results and their

Chapter 4: Higgs Boson Search In The $H \rightarrow ZZ^* \rightarrow 4\ell$ Channel and Its Mass Measurement

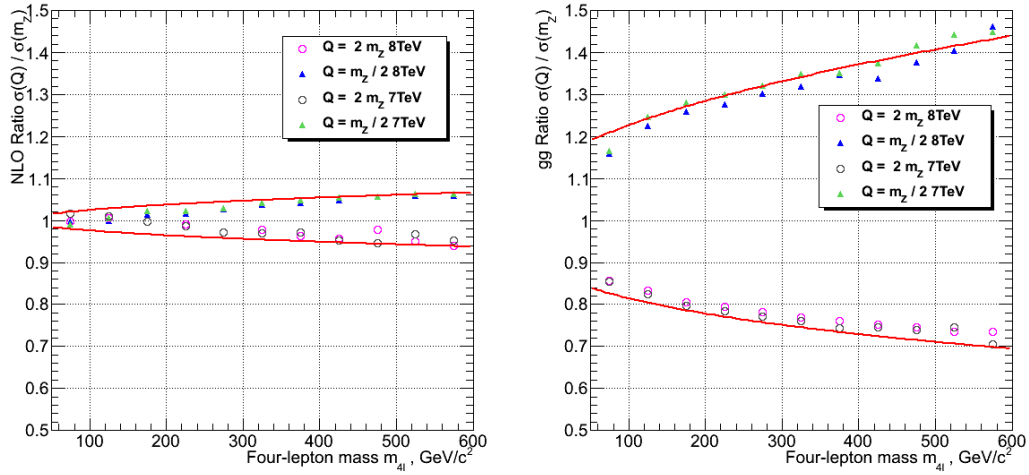


Figure 4.6 – QCD scale uncertainties for (left) $q\bar{q} \rightarrow ZZ \rightarrow 4\ell$ at NLO and (right) $gg \rightarrow ZZ \rightarrow 4\ell$ processes. The points are the evaluated uncertainties. The curves are the analytical parametrizations $\kappa(m_{4\ell})$ which are used in the statistical analysis.

interpretation. The breakthrough in the Higgs boson search has been made in July 2012 after analysing the data collected by the LHC experiments during 2011 and first half of 2012 run periods. The two biggest CERN experiments, CMS and ATLAS, have reported about the new boson discovery with a mass around 126 GeV[48, 49]. The new boson was observed with a local significance greater than 3σ in $H \rightarrow \gamma\gamma$ and $H \rightarrow ZZ \rightarrow 4\ell$ channels. In the Fig.4.7 the invariant mass distributions obtained in summer 2012 for the $H \rightarrow \gamma\gamma$ (left) and $H \rightarrow ZZ \rightarrow 4\ell$ (right) are shown. The results correspond to the data collected up to summer 2012

The presence of a signal is quantified by the background-only p -value, i.e. the probability for the background to fluctuate and give an excess of events as large or larger than the observed one. The local p -values, representing the significance of a local excess relative to the background expectation for different Higgs boson decay channels and their combination are shown as a function of m_H in Fig. 4.8. The local minimum of the p -value in the data has occurred at $m_H = 125.6 \text{ GeV}$ and has had significance of 3.2σ in the $H \rightarrow ZZ \rightarrow 4\ell$ decay channel. Combined result with the $H \rightarrow \gamma\gamma$ channel raised the local significance to 5.0σ . No other significant excess of events has been found in the other parts of the phase space.

This major achievement allows to focus on the determination of the characteristics of the observed new particle. Since the Higgs boson discovery we collected $\sim 15 \text{ fb}^{-1}$ more data at $\sqrt{s} = 8 \text{ TeV}$. Also some parts of the analysis technique were improved as well as the objects reconstruction. The following results correspond to the final ones obtained with the full LHC Run I period dataset.

After the event selection the background mostly consists of ZZ and $Z + X$ processes. Reducible background parameters (shape and yield) are estimated from the control regions in the data

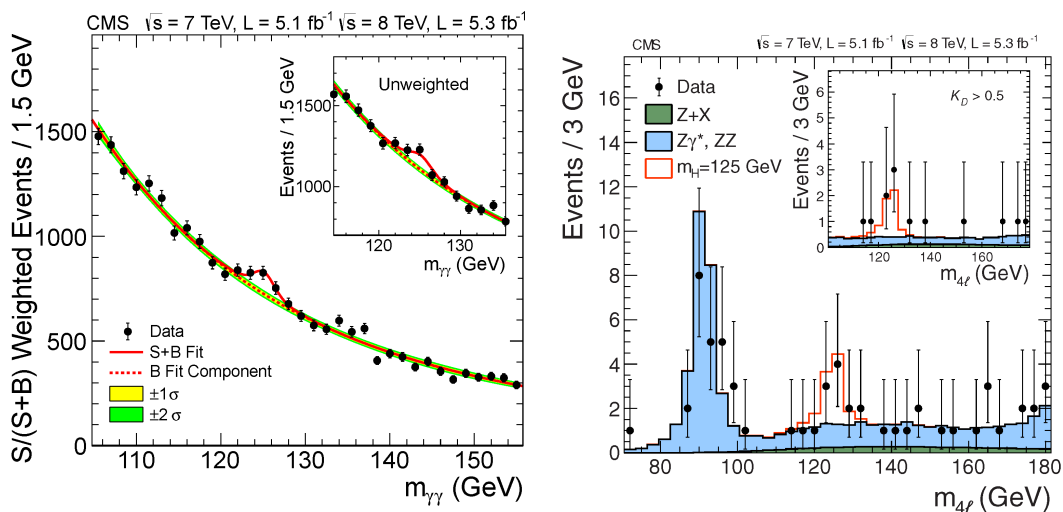


Figure 4.7 – (left) The diphoton invariant mass distribution with each event weighted by the $S/(S+B)$ value of its category. The lines represent the fitted background and signal, and the coloured bands represent the ± 1 and ± 2 standard deviation uncertainties in the background estimate. The inset shows the central part of the unweighted invariant mass distribution. (right) Distribution of the four-lepton invariant mass for the $ZZ \rightarrow 4\ell$ analysis. The points represent the data, the filled histograms represent the background, and the open histogram shows the signal expectation for a Higgs boson of mass $m_H = 125 \text{ GeV}$, added to the background expectation. The inset shows the $m_{4\ell}$ distribution after selection of events with $K_D > 0.5$, a kinematical discriminant, explained in Sec 4.6.1.

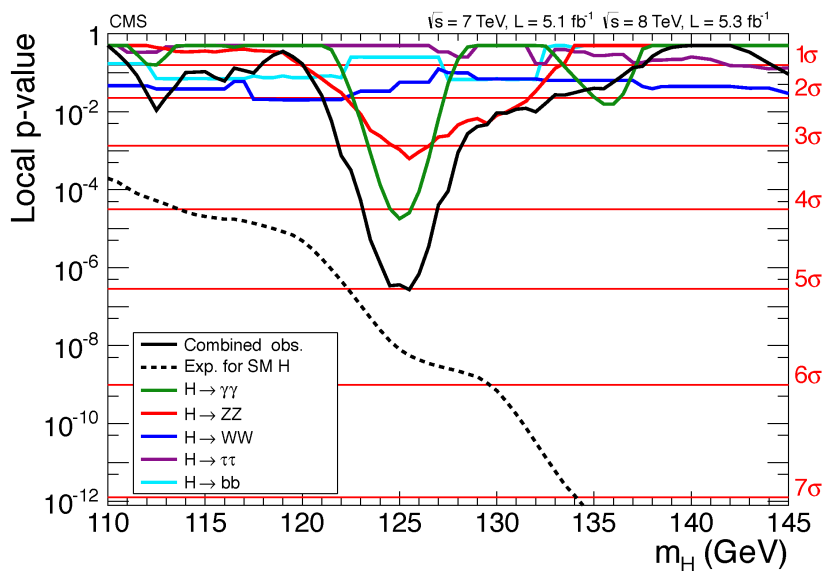


Figure 4.8 – The observed local p -value for the five decay modes and the overall combination as a function of the SM Higgs boson mass. The dashed line shows the expected local p -value for a SM Higgs boson with a mass m_H . The results corresponds to the data collected up to summer 2012.

Chapter 4: Higgs Boson Search In The $H \rightarrow ZZ^* \rightarrow 4\ell$ Channel and Its Mass Measurement

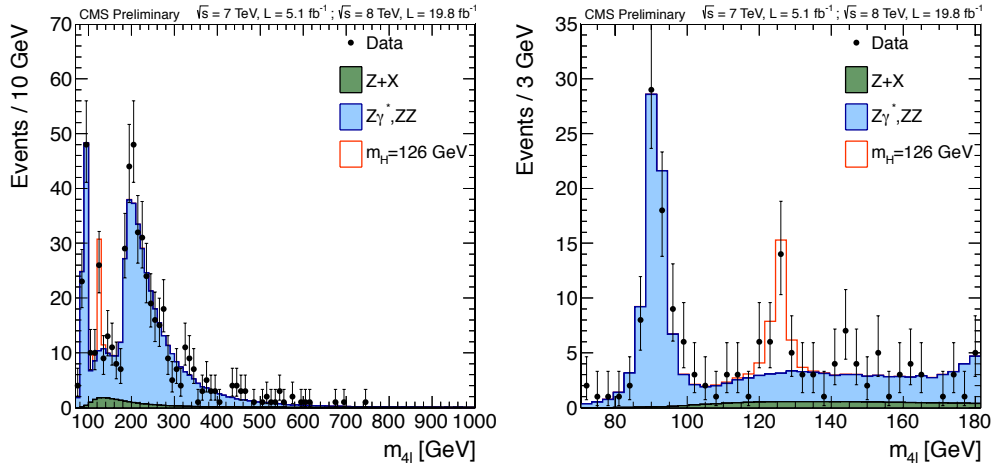


Figure 4.9 – Distribution of the four-lepton reconstructed mass for the full 2011+2012 dataset, compared to SM background expectations in full mass range (left) and low-mass range (right).

while irreducible part of background and signal are taken from the MC simulation. For the signal simulation m_H is set to 126 GeV. The error bars on data points are asymmetric Poisson uncertainties that cover the 68% probability interval around the central value [50]. Fig.4.9 shows the distribution of the reconstructed invariant mass in the 4ℓ final state. A clear peak, unexpected from the background is visible around $m_H = 126$ GeV.

We can also split 4ℓ final state by lepton flavours and check whether we can see the peak in all the subchannels ($4e$, 4μ and $2e2\mu$) or not. The distributions in Fig.4.10 shows that the peak at low mass is present in each possible final state and compatible with the presence of a Higgs boson signal with $m_H \simeq 126$ GeV.

4.6 The Higgs Boson Mass Measurements

Now we are almost ready to go for the measurement of the new boson mass. Before doing so we should recall that the $H \rightarrow ZZ \rightarrow 4\ell$ has a fully reconstructable final state. This means that we can explore the kinematics of the 4ℓ system in order to increase the accuracy of our measurements. Details of how can we benefit from the lepton kinematics are given in Sec. 4.6.1. Besides this, our decay channel has quite small branching fraction and hence the statistics is limited, which translates into significant uncertainties on the the peak position determination. In order to reduce these uncertainties we introduce the mass measurement uncertainties on per-event basis. This procedure is described in Sec. 4.6.2.

4.6. The Higgs Boson Mass Measurements

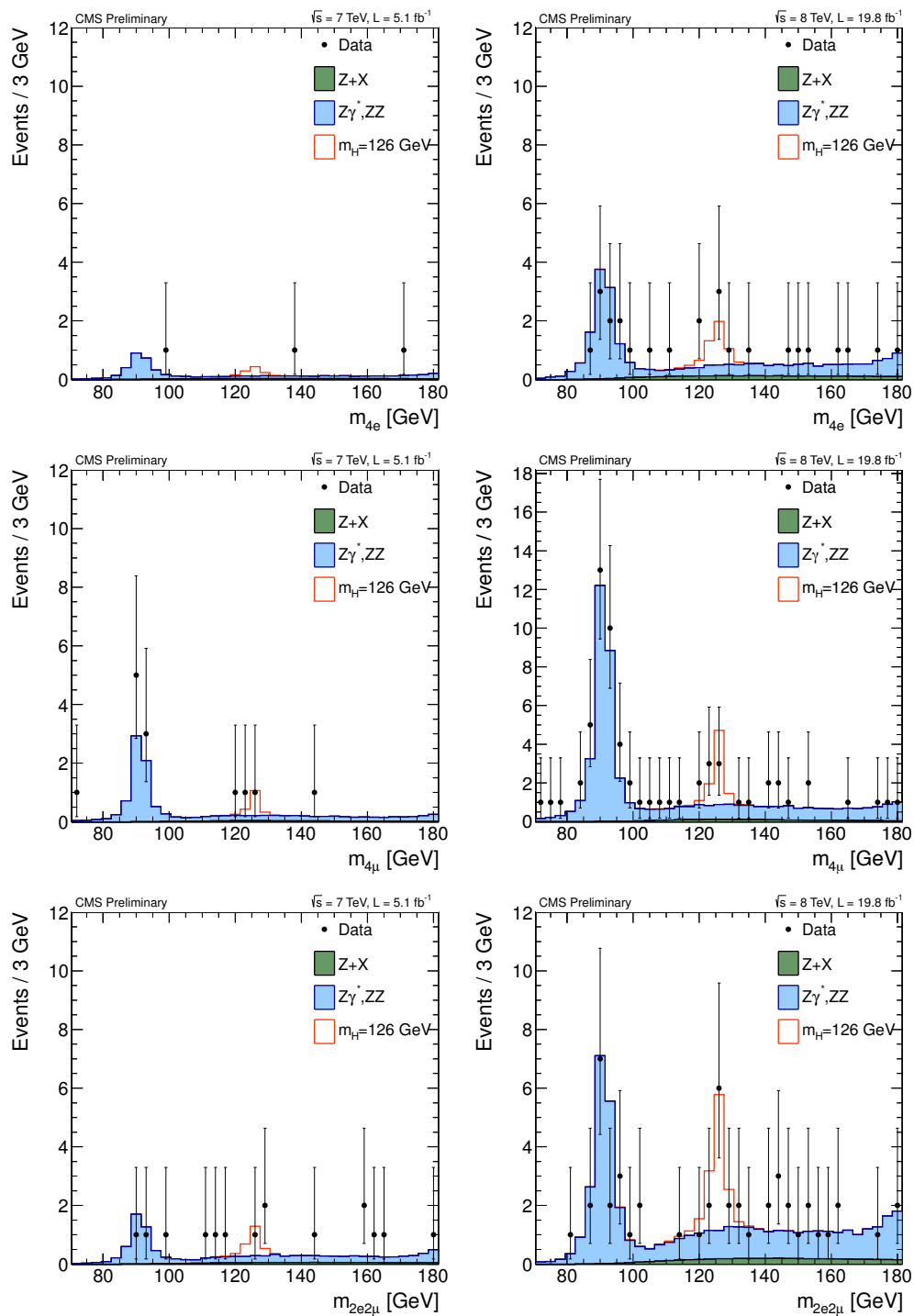


Figure 4.10 – Distribution of the four-lepton reconstructed mass in the low-mass range in several sub-channels: $4e$ (top), 4μ (middle), $2e2\mu$ (bottom), for 7 TeV (left) and 8 TeV (right).

4.6.1 Kinematical Discriminants

The kinematics of the cascade decays of the type $\Phi \rightarrow V_1(\ell_1, \ell_2)V_2(\ell_3, \ell_4)$ has been extensively studied in the literature in application to the studies of the Higgs boson or other exotic particles as well as in the vector meson studies, see for example Refs. [40, 51]. In the CMS experiment a special technique called the matrix element likelihood approach (MELA) was introduced to implement these developments. It relies on the probability for an event to come either from the signal or background with a set of observables which fully characterize the event topology in its center-of-mass frame [48, 52]. These observables are chosen to be $(m_{4\ell}, m_1, m_2, \vec{\Omega})$, where $\vec{\Omega}$ are five angles defined in Ref. [39] and shown in Fig. 4.11.

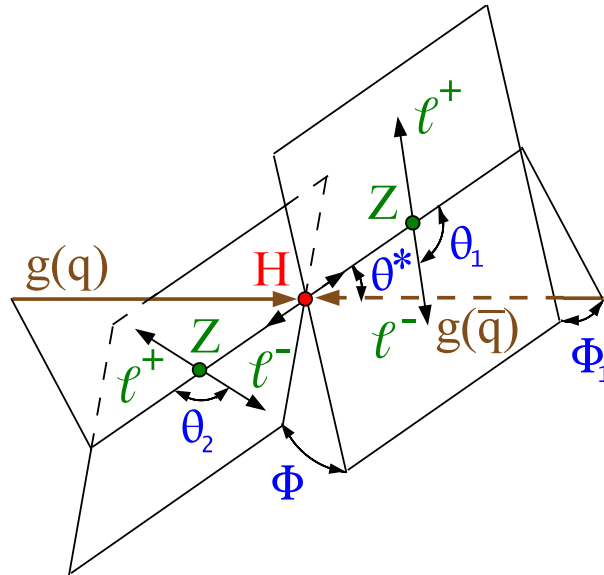


Figure 4.11 – Illustration of a particle H production and decay $g(q)g(\bar{q}) \rightarrow H \rightarrow Z_1 Z_2 \rightarrow 4\ell$ with the two production angles θ^* and Φ_1 shown in the H rest frame and three decay angles θ_1 , θ_2 , and Φ shown in the $Z^{(*)}$ rest frames [39]. Here H stands either for a SM Higgs boson, an exotic particle, or in general the 4ℓ system (e.g. background).

Several implementations of the matrix element approach were developed and also several implementations of the machine trained techniques. Their results were cross-checked and found to be essentially identical.

Given several signal (SM and J^P) and background ($q\bar{q} \rightarrow ZZ$ and $gg \rightarrow ZZ$) hypotheses, there are several effective probabilities that event come from a given process, that one can calculate

for each event:

$$\mathcal{P}_{\text{SM}} = \mathcal{P}_{\text{SM}}^{\text{kin}}(\vec{\Omega}, m_1, m_2 | m_{4\ell}) \times \mathcal{P}_{\text{sig}}^{\text{mass}}(m_{4\ell} | m_H) \quad (4.8)$$

$$\mathcal{P}_{J^P} = \mathcal{P}_{J^P}^{\text{kin}}(\vec{\Omega}, m_1, m_2 | m_{4\ell}) \times \mathcal{P}_{\text{sig}}^{\text{mass}}(m_{4\ell} | m_H) \quad (4.9)$$

$$\mathcal{P}_{q\bar{q}ZZ} = \mathcal{P}_{q\bar{q}ZZ}^{\text{kin}}(\vec{\Omega}, m_1, m_2 | m_{4\ell}) \times \mathcal{P}_{q\bar{q}ZZ}^{\text{mass}}(m_{4\ell}) \quad (4.10)$$

$$\mathcal{P}_{ggZZ} = \mathcal{P}_{ggZZ}^{\text{kin}}(\vec{\Omega}, m_1, m_2 | m_{4\ell}) \times \mathcal{P}_{ggZZ}^{\text{mass}}(m_{4\ell}), \quad (4.11)$$

where \mathcal{P}^{kin} is the probability as a function of angular and mass observables $(\vec{\Omega}, m_1, m_2)$ and is calculated with the matrix element approach, while $\mathcal{P}^{\text{mass}}$ is the probability as a function of the four-lepton reconstructed mass. Since the kinematics for the instrumental background $Z + X$ cannot be parametrized from the first principles this background is treated empirically in analysis. The Higgs boson mass is assumed to be $m_H = 126$ GeV but can be easily adjusted to any hypothetical mass.

From the above probabilities, several discriminant observables can be computed, such as

$$\mathcal{D}_{\text{bkg}}^{\text{kin}} = \frac{\mathcal{P}_{\text{SM}}^{\text{kin}}}{\mathcal{P}_{\text{SM}}^{\text{kin}} + c \times \mathcal{P}_{q\bar{q}ZZ}^{\text{kin}}} = \left[1 + c(m_{4\ell}) \times \frac{\mathcal{P}_{q\bar{q}ZZ}^{\text{kin}}(m_1, m_2, \vec{\Omega} | m_{4\ell})}{\mathcal{P}_{\text{SM}}^{\text{kin}}(m_1, m_2, \vec{\Omega} | m_{4\ell})} \right]^{-1} \quad (4.12)$$

$$\mathcal{D}_{\text{bkg}} = \frac{\mathcal{P}_{\text{SM}}}{\mathcal{P}_{\text{SM}} + c \times \mathcal{P}_{\text{bkg}}} = \left[1 + c(m_{4\ell}) \times \frac{\mathcal{P}_{\text{bkg}}^{\text{kin}}(m_1, m_2, \vec{\Omega} | m_{4\ell}) \times \mathcal{P}_{\text{bkg}}^{\text{mass}}(m_{4\ell})}{\mathcal{P}_{\text{SM}}^{\text{kin}}(m_1, m_2, \vec{\Omega} | m_{4\ell}) \times \mathcal{P}_{\text{sig}}^{\text{mass}}(m_{4\ell} | m_H)} \right]^{-1} \quad (4.13)$$

$$\mathcal{D}_{J^P} = \frac{\mathcal{P}_{\text{SM}}}{\mathcal{P}_{\text{SM}} + c_{J^P} \times \mathcal{P}_{J^P}} = \left[1 + c_{J^P} \times \frac{\mathcal{P}_{J^P}^{\text{kin}}(m_1, m_2, \vec{\Omega} | m_{4\ell})}{\mathcal{P}_{\text{SM}}^{\text{kin}}(m_1, m_2, \vec{\Omega} | m_{4\ell})} \right]^{-1} \quad (4.14)$$

$$\mathcal{D}_{ggZZ} = \frac{\mathcal{P}_{ggZZ}^{\text{kin}}}{\mathcal{P}_{ggZZ}^{\text{kin}} + c_{ggZZ} \times \mathcal{P}_{q\bar{q}ZZ}^{\text{kin}}} = \left[1 + c_{ggZZ}(m_{4\ell}) \times \frac{\mathcal{P}_{q\bar{q}ZZ}^{\text{kin}}(m_1, m_2, \vec{\Omega} | m_{4\ell})}{\mathcal{P}_{ggZZ}^{\text{kin}}(m_1, m_2, \vec{\Omega} | m_{4\ell})} \right]^{-1} \quad (4.15)$$

where the constants c_x are tuned to adjust relative normalization of probabilities, for the optimal appearance of the event distributions after the detector acceptance effects. The $\mathcal{D}_{\text{bkg}}^{\text{kin}}$ and \mathcal{D}_{bkg} observables emphasize the separation of the signal from background. They differ only by inclusion (\mathcal{D}_{bkg}) or not ($\mathcal{D}_{\text{bkg}}^{\text{kin}}$) of the $m_{4\ell}$ probability. The $\mathcal{D}_{\text{bkg}}^{\text{kin}}$ is designed to be used together with $m_{4\ell}$ in a fit, while \mathcal{D}_{bkg} can be used stand-alone for optimal background rejection power. The \mathcal{D}_{ggZZ} is used only as a cross-check of the $q\bar{q} \rightarrow ZZ$ and $gg \rightarrow ZZ$ background contributions at high mass. Finally, the \mathcal{D}_{J^P} can be calculated for a number of alternative spin-parity J^P signal hypotheses.

4.6.2 Per-event mass uncertainties

Imperfect calibration of the ECAL response and uncertainties on the GSF track fit due to possible high-bremsstrahlung emissions lead to uncertainties on the measured momenta of electrons. In case of muons uncertainties on the track fit arise because of the multiple

Chapter 4: Higgs Boson Search In The $H \rightarrow ZZ^* \rightarrow 4\ell$ Channel and Its Mass Measurement

scattering of the muons in the material of the inner tracker. These uncertainties depend on the lepton energy and direction as well as on possible mis-measurements specific to a given lepton. For electrons a multivariate regression similar to the one used in their momentum estimation is used to assess the quality of the ECAL supercluster and the GSF track fit and determine the momentum uncertainty. In case of muons the properties of hits in the tracker and in the muon system are used. If event has an identified FSR photons their uncertainties, assessed by the quality of the ECAL clusters, are also accounted for.

The momentum uncertainties for each of the four leptons in an event are then propagated into a relative uncertainty $\sigma_{m_{4\ell}}/m_{4\ell}$ in the four-lepton mass. Since the uncertainties on the different leptons are fully uncorrelated the total per-event mass uncertainty is given as the sum in quadrature of the individual mass uncertainty contributions from each lepton and any identified FSR photon candidate. A calibration of the per-lepton uncertainties is derived using large $J/\psi \rightarrow \mu^+\mu^-$, $Z \rightarrow \mu^+\mu^-$, and $Z \rightarrow e^+e^-$ event samples. The lineshape of these resonances is modeled with a BW convolved with a double-sided CB function, where the resolution is estimated as $\lambda \times \sigma(m_{4\ell})$. Here $\sigma(m_{4\ell})$ is fixed to the value computed using the uncertainties on the individual momenta of the leptons, and the calibration constant λ is a floating parameter. It is derived for electrons and muons in several bins of the p_T^ℓ and η^ℓ : $J/\psi \rightarrow \mu^+\mu^-$ is used for muons with $p_T^\mu < 20$ GeV, and $Z \rightarrow e^+e^-$ events are used in the entire p_T^e range. Obtained λ values are 1.2 and 1.1 for electrons and muons correspondingly, in the entire kinematic range of the leptons used in this analysis.

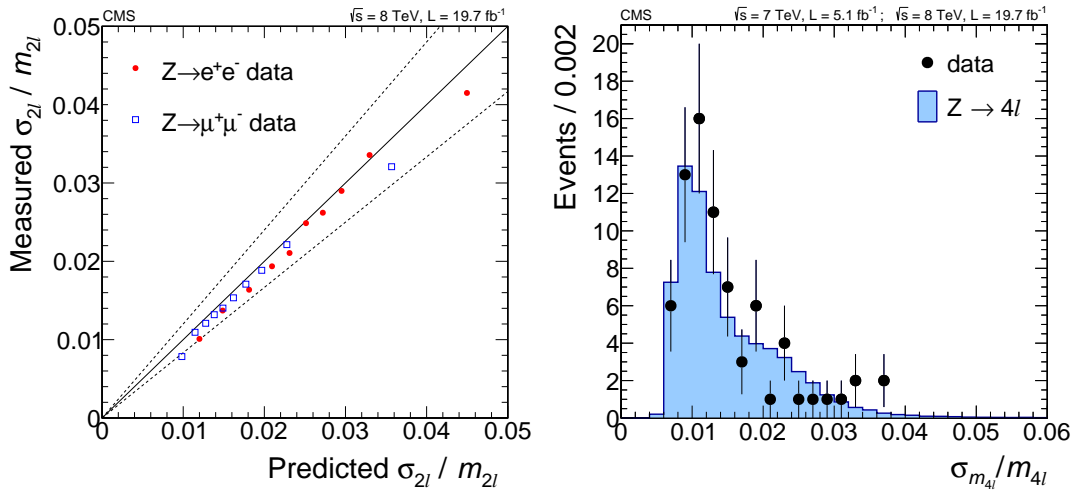


Figure 4.12 – Measured versus predicted relative mass uncertainties for $Z \rightarrow \mu^+\mu^-$, and $Z \rightarrow e^+e^-$ events in data. The dashed lines represent the $\pm 20\%$ envelope, used as systematic uncertainty in the resolution (left). Relative mass uncertainty distribution for data and simulation in the $Z \rightarrow 4\ell$ mass region of $80 < m_{4\ell} < 100$ GeV (right).

To validate how well the final per-event mass uncertainties are predicted a closure test with $Z \rightarrow \ell\ell$ events is provided. The $Z \rightarrow \ell\ell$ events are grouped into subsets based on their per-

event predicted dilepton mass resolution and fitted with the Z line shape in each subset as described above. A systematic uncertainty of $\pm 20\%$ is assigned to the per-event mass uncertainty for both electrons and muons based on the agreement between per-event computed and observed mass resolutions as shown in Fig. 4.12 (left). The comparison between the data and simulation of the $\sigma_{m_{4\ell}}/m_{4\ell}$ observable in the $Z \rightarrow 4\ell$ mass region is shown in Fig. 4.12 (right).

Another way to access the adequacy of the obtained per-event errors is to look at the pull distributions. The pull for the Higgs boson mass, defined as:

$$\text{pull}_m = \frac{m_{4\ell} - m_H}{\sigma(m_{4\ell})}, \quad (4.16)$$

where m_H is the reference Higgs mass hypothesis, $\sigma(m_{4\ell})$ is the per-event mass uncertainty, should be distributed as a standard Gaussian centered at zero and having the unit width. The Fig. 4.13 shows the distributions of the pulls in each sub-channel (4μ , $2e2\mu$ and $4e$) and the combined one. The reference Higgs mass was set to $m_H=126$ GeV, for which we have fully simulated and reconstructed MC sample. The event selection is identical to analysis one with an additional requirement on $m_{4\ell}$ to be within $121.5 < m_{4\ell} < 130.5$ GeV. The fit of data points was performed using the maximum likelihood method. Overall, a good agreement is observed between measured pull parameters and expected ones. The 4μ final state shows a small deviation ($\sim 2\sigma$) towards lower Higgs boson mass with respect to 126 GeV, which is consistent with the fitted central value in this final state (see Tab. 4.3). The precision of the test is limited by the statistic.

In the Fig. 4.14 the fitted pull distributions for the MC predictions for background plus signal hypotheses are shown.

From the fit parameters we can conclude that our data pull is well consistent with the signal plus background simulation. The fits are also well consistent with the Gaussian with the zero mean and unit width.

4.6.3 Signal Model

Since the total decay width of the Standard Model Higgs boson depends strongly on its mass, different description of the signal lineshape should be provided under the different mass hypothesis. Typically, the $m_{4\ell}$ phase space can be divided into two parts:

- $m_{4\ell} < 400$ GeV, where the Higgs boson can be treated as a narrow resonance
- $m_{4\ell} > 400$ GeV, where we should account for substantial out-of-pole production

Since this analysis concentrates on the study of the low-mass Higgs boson properties, only the signal model for this region will be presented.

Chapter 4: Higgs Boson Search In The $H \rightarrow ZZ^* \rightarrow 4\ell$ Channel and Its Mass Measurement

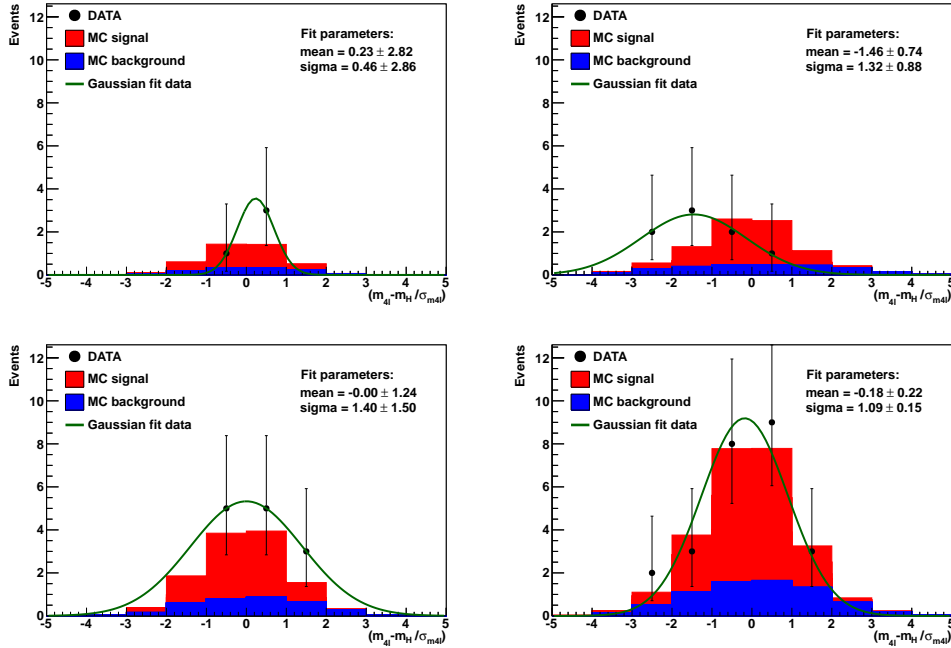


Figure 4.13 – Distribution of the pulls of the mass, defined as in Eqn. 4.16, for the separate channels: $4e$ (top left), 4μ (top right), $2e2\mu$ (bottom left), and the combination of all the 4ℓ channels (bottom right). A Gaussian fit to the data is shown.

The lineshape of the narrow-width resonance is described by the relativistic Breit-Wigner function. Besides, we should account for the detector-induced effects. This is implemented by convoluting the Breit-Wigner function with a special empirical function. This empirical function has to account for the Gaussian resolution of the core of the $m_{4\ell}$ distribution and for the tails caused by the radiative effects. The simplest function which describes the detector effects well was found to be a double-sided Crystal Ball (dCB): two-tails generalization of the regular CB function. It is defined as follows:

$$dCB(\xi) = N \cdot \begin{cases} A \cdot (B + |\xi|)^{-n_L}, & \text{for } \xi < \alpha_L \\ A \cdot (B + |\xi|)^{-n_R}, & \text{for } \xi > \alpha_R \\ \exp(-\xi^2/2), & \text{for } \alpha_L \leq \xi \leq \alpha_R \end{cases} \quad (4.17)$$

where $\xi = (m_{4\ell} - m_{H^*} - \Delta m_{H^*}) / \sigma_m$.

The parameters of the BW function are fully determined by the hypothetical Higgs boson mass, while the dCB parameters are obtained from simulations. There are six independent parameters in the dCB function: Gaussian core resolution σ_m , systematic mass shift of the peak Δm_{H^*} , left and right tail parameters $\alpha_{L,R}$ and $n_{L,R}$. The A and B parameters are defined by requiring the dCB function to be continuous and smooth. The fit is performed at the each Higgs mass hypothesis point. For the intermediate mass values the interpolation of the dCB parameters is used. The examples of the signal lineshape for the signal hypothesis with

4.6. The Higgs Boson Mass Measurements

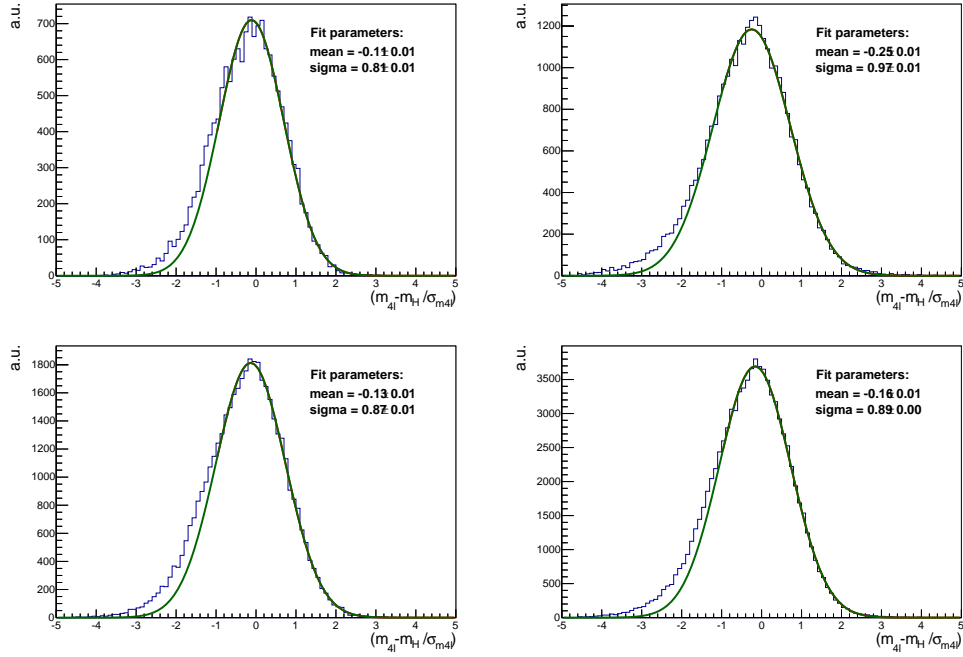


Figure 4.14 – Distribution of the pulls of the mass, defined as in Eqn. 4.16, for the separate channels: $4e$ (top left), 4μ (top right), $2e2\mu$ (bottom left), and the combination of all the 4ℓ channels (bottom right). A Gaussian fit to the Higgs boson signal at $m_H = 126$ GeV (right) is shown.

$m_H = 126$ GeV in different final states are shown in Fig. 4.15.

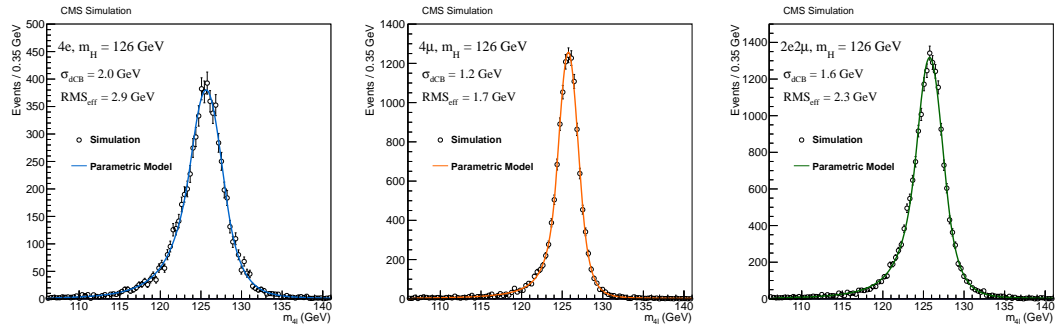


Figure 4.15 – Probability density functions $f(m_{4l}|m_H)$ for signal with $m_H = 126$ GeV at the reconstruction level after the full lepton and event selections are applied. The distributions obtained from 8 TeV MC samples are fitted with the model described in the text for $4e$ (left), 4μ (center) and $2\mu 2e$ (right) events.

The systematic uncertainties arising from the signal lineshape modelling are naturally divided into two groups: theoretical lineshape uncertainties and instrumental uncertainties on the detector resolution function. We neglect the first ones since in the low mass region the predicted width is order of few MeV and much smaller than the detector resolution. The instrumental uncertainties are taken from the dedicated scale and resolution studies, for

Chapter 4: Higgs Boson Search In The $H \rightarrow ZZ^* \rightarrow 4\ell$ Channel and Its Mass Measurement

which $Z \rightarrow ee$ and $Z \rightarrow \mu\mu$ events are used. The contribution of the muon energy scale systematic error for the 4μ and $2e2\mu$ final states is 0.1% and that of the electrons is 0.4% and 0.2% for the $4e$ and $2e2\mu$ final states respectively. Higher uncertainties in case of electrons are motivated by the fact that both ECAL and tracker measurements contribute in this case. The uncertainty on the resolution is taken as 20% overall as it was mentioned in Sec 4.6.2.

4.6.4 Results

The baseline for the mass measurements of the Higgs boson is a 3D likelihood fit, which explores the four lepton invariant mass, relative event-by-event errors (denoted as \mathcal{D}_m) and kinematical discriminant. However, this method has some mild dependency on the model due to the kinematical discriminant. Therefore, the 2D results using only $m_{4\ell}$ and associated event-by-event errors, which are fully model-independent, are provided. In order to ensure that there is no additional systematic effects, a cross-check is done using a simplest 1D fit of the $m_{4\ell}$.

The fits are performed with the CMS Combination Tool, accounting all statistical and systematic uncertainties. The signal strength μ^8 is profiled as all the other nuisance parameters of the model. Fig. 4.16 shows the 1D likelihood scans for 1D, 2D and 3D models in each final state ($4e$, $2e2\mu$ and 4μ) as well as their combination as a function of the Higgs boson mass. The plots show good consistency between the different models as well as between different final states. Some offset of the minimum position of order 1.6 GeV is observed in the 4μ final state with respect to the $4e$ and $2e2\mu$ results. Despite this, the results lie well within one standard deviation. The best fit values and associated 2σ uncertainties for all the fits are summarized in table 4.3. The performance gain due to the exploration of event-by-event mass errors and the

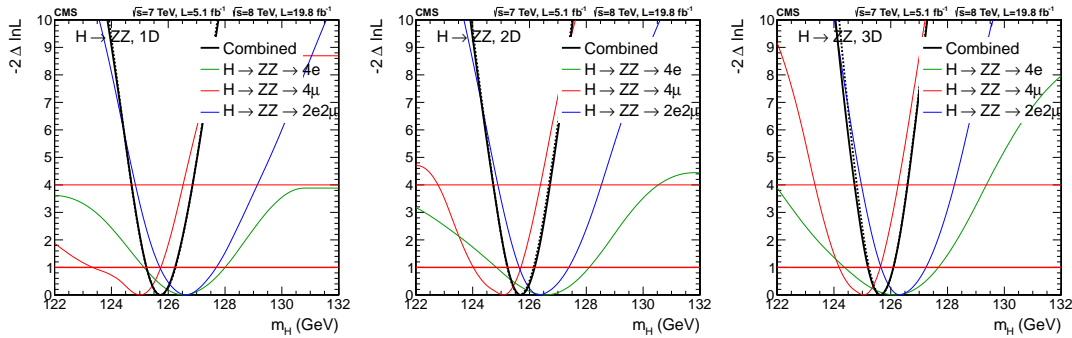


Figure 4.16 – 1D likelihood scan as a function of mass including statistical and systematic uncertainties for the 1D (left), 2D (middle) and 3D (right) models. Colors represent the different final states, black curve the combination. Both 7 and 8 TeV data are considered. Solid lines represent the scan with full uncertainties included, dashed lines include statistical errors only.

kinematical discriminant is illustrated in Fig 4.17. A visible improvement in the computation

⁸ The signal strength is the ratio of the observed signal cross section to the SM expectation value.

4.6. The Higgs Boson Mass Measurements

Table 4.3 – Best fit values for the mass of the new boson measured in the 4ℓ , $\ell = e, \mu$ final states, with 1D, 2D and 3D fit, respectively. For the 1D and 2D we give the total uncertainty only, while for the nominal 3D fit the contributions from statistical and systematic uncertainties are separated.

Channel	1D: $\mathcal{L}(m_{4\ell})$ (GeV)	2D: $\mathcal{L}(m_{4\ell}, \mathcal{D}_m)$ (GeV)	3D: $\mathcal{L}(m_{4\ell}, \mathcal{D}_m, \mathcal{D}_{\text{bkg}}^{\text{kin}})$ (GeV)
4μ	$125.01^{+0.73}_{-1.23}$ (tot.)	$125.08^{+0.62}_{-1.05}$ (tot.)	$125.05^{+0.60}_{-0.79}$ (stat.) $+0.15$ (syst.)
$4e$	$126.55^{+1.45}_{-1.41}$ (tot.)	$126.56^{+1.54}_{-1.73}$ (tot.)	$126.15^{+1.70}_{-1.38}$ (stat.) $+0.76$ (syst.)
$2e2\mu$	$126.62^{+1.08}_{-0.91}$ (tot.)	$126.34^{+1.05}_{-0.70}$ (tot.)	$126.32^{+0.96}_{-0.65}$ (stat.) $+0.24$ (syst.)
4ℓ	$125.72^{+0.52}_{-0.49}$ (tot.)	$125.69^{+0.50}_{-0.45}$ (tot.)	$125.63^{+0.47}_{-0.39}$ (stat.) $+0.09$ (syst.)

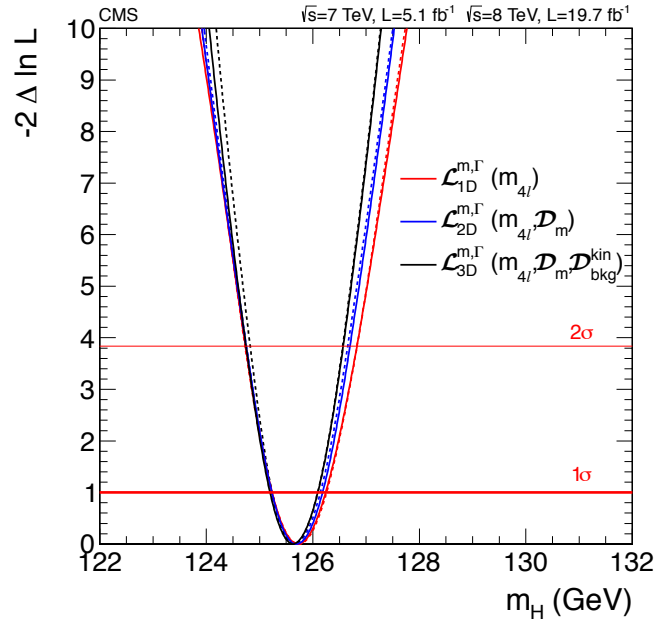


Figure 4.17 – 1D likelihood scan as a function of mass for the different fit scenarios for the combination of all final states, 7 and 8 TeV data. Solid lines represent the scan with full uncertainties included, dashed lines statistical error only.

of the 2σ vicinity band is found while the best fit position remains almost unchanged. Also it should be mentioned that no additional systematic effect is found. Finally, another representation of the best fit values and their corresponding 1σ bands is shown in Fig 4.18. This plot illustrates very well the good compatibility of all the results regardless of the fit model and particular final state. The baseline final result, as it was mentioned before is taken from the 3D model likelihood scan of the full data sample and amounts to $125.6 \pm 0.4(\text{stat}) \pm 0.2(\text{syst})$ GeV.

**Chapter 4: Higgs Boson Search In The
 $H \rightarrow ZZ^* \rightarrow 4\ell$ Channel and Its Mass Measurement**

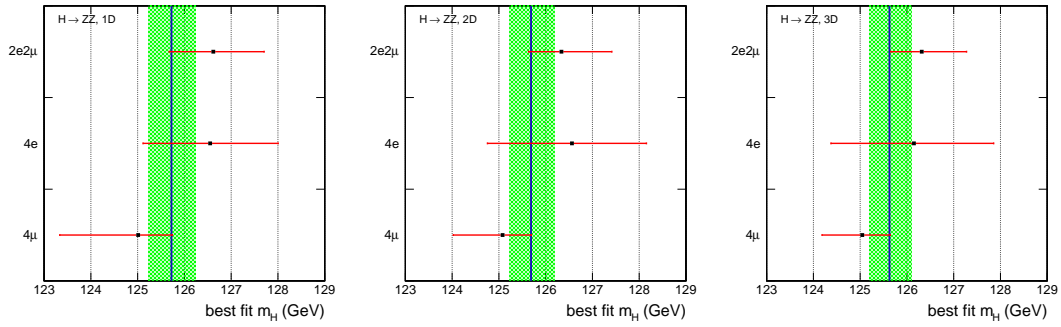


Figure 4.18 – The best fit values for the Higgs boson mass in the different channels (points) and for the combination of the three channels (line, with the bar representing the 1σ uncertainty) for the different fit configurations: 1D ($\mathcal{L}(m_{4\ell})$) (left), 2D ($\mathcal{L}(m_{4\ell}, \mathcal{D}_m)$) (middle) and 3D ($\mathcal{L}(m_{4\ell}, \mathcal{D}_m, \mathcal{D}_{\text{bkg}}^{\text{kin}})$) (right). The red lines on each point represent the total uncertainty.

5 The Higgs Boson Width Constraints From The Offshell Production

After having discovered the new boson which is a candidate to be the last piece of the Standard Model, we should concentrate on its properties determination. We have already discussed the new boson mass. The spin-parity properties have been also extensively studied in CMS and favour the scalar hypothesis [53]. A fundamental parameter being not discussed yet is the boson width. Constraining it is very challenging since the SM Higgs boson width is very small (~ 4 MeV for $m_H = 126$ GeV). It is about two orders of magnitude smaller than the experimental resolution in the most precise Higgs decay channels, $H \rightarrow ZZ \rightarrow 4\ell$ and $H \rightarrow \gamma\gamma$.

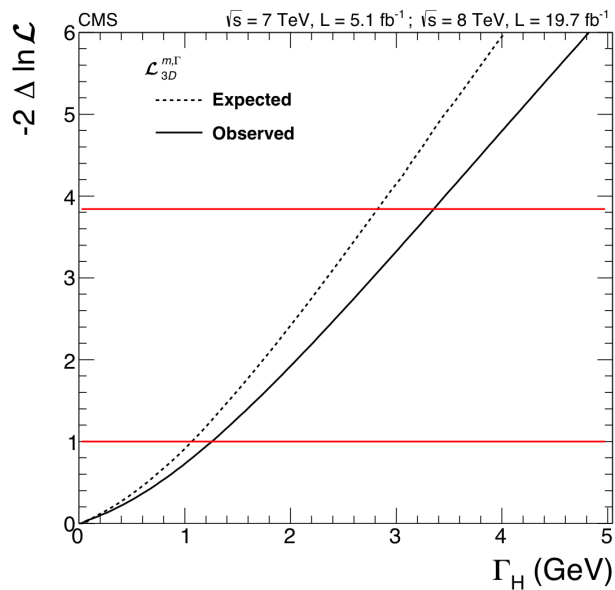


Figure 5.1 – Log-likelihood scan of the Higgs boson width. The horizontal lines at $-2\Delta \ln \mathcal{L} = 1$ and 3.84 correspond to the 68% and 95% C.L. respectively. Solid (dashed) line represent the observed (expected) result.

Using the same signal model and inputs as presented in the previous chapter, we can provide

direct measurement of the new boson width. In order to do so we profile the Higgs boson mass and signal strength as other nuisance parameters. The width parameter of the Breit-Wigner function on contrary is left floating. The resulting log-likelihood scan is shown in Fig. 5.1.

This measurement shows that the data is compatible with a narrow-width resonance. However the upper limit on the Higgs boson width is much higher than the SM Higgs boson width at the given mass. The measured value of the Higgs boson width is $\Gamma_H = 0.0_{0.0}^{+1.3}$ GeV and the upper limit at 95% C.L. is 3.4 GeV. Another direct measurement of the Higgs boson width, performed in the $H \rightarrow \gamma\gamma$ decay channel results in an upper limit of 2.4 GeV at 95% C.L. [54].

However recent theoretical investigations [55] have shown that indirect measurements based on the off-shell Higgs boson production could allow to constrain the Higgs boson width at the needed level of precision while being weakly model-dependent (e.g. allowing many beyond Standard Model scenarios). In this chapter we concentrate on bounding the Higgs boson width using the off-shell Higgs boson production and its decay to the 4ℓ final state. My personal contribution in this analysis is quite large. I was among the initiators of its experimental part. I developed an independent statistical tool which allowed to provide in a short timescale the first preliminary results, which I presented at the CMS week Higgs plenary meeting in December 2013. I then was most involved in the detailed analysis in view of the Moriond conference, and contributed in particular to the determination of the expected and observed event yields, cut-and-count cross check and evaluation of the systematic uncertainties.

5.1 Off-shell Higgs Production

In Ref. [56, 57] it has been shown that, when considering processes in which the Higgs boson decays to vector bosons (VV , where $V = W, Z$), the zero-width approximation (ZWA) is valid only in a small phase space region around m_H . Apart from the dominant contribution of the Higgs pole the integrated contribution of the off-shell production could be significant. In particular for $m_{4\ell} > 2m_{VV}$, theoretical calculations predict an enhancement of Higgs signal events which represent a sizable fraction (about 8%) of the on-peak cross-section. The gluon-induced diboson production followed by the decay to 4ℓ involves at tree level the two diagrams shown in Fig.5.2. The interference between these diagrams, which is needed in order to unitarize the di-boson scattering cross-section, is large and negative. Therefore it is taken into account in the analysis.

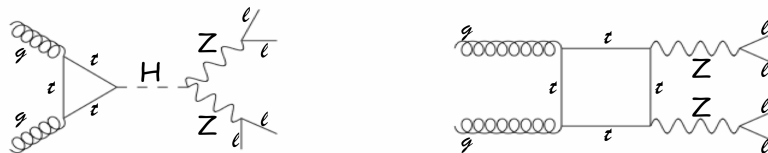


Figure 5.2 – Feynman diagrams for the process $gg \rightarrow 4\ell$.

5.1.1 Gluon-induced Higgs boson production

Let's consider the differential cross-section of $gg \rightarrow H \rightarrow 4\ell$, expressed in terms of the Higgs boson production, propagation and decay¹.

$$\frac{d\sigma_{gg \rightarrow H \rightarrow 4\ell}}{dm_{4\ell}^2} = \frac{1}{\pi} \sigma_{gg \rightarrow H} \frac{m_{4\ell}^2}{(m_{4\ell}^2 - m_H^2)^2 + m_H^2 \Gamma_H^2} \frac{\Gamma_{H \rightarrow 4\ell}(m_{4\ell})}{m_{4\ell}} \quad (5.1)$$

Applying the ZWA (i.e. integrating in the vicinity of m_H pole) one gets the usual result:

$$\begin{aligned} \sigma_{gg \rightarrow H \rightarrow 4\ell}^{\text{on-peak}} &\simeq \sigma_{gg \rightarrow H} m_H \Gamma_{H \rightarrow 4\ell}(m_H) \int_{m_H - n\Gamma_H}^{m_H + n\Gamma_H} \frac{1}{\pi} \frac{1}{(m_{4\ell}^2 - m_H^2)^2 + m_H^2 \Gamma_H^2} dm_{4\ell}^2 \\ &\simeq \sigma_{gg \rightarrow H} m_H \Gamma_{H \rightarrow 4\ell}(m_H) \frac{1}{m_H \Gamma_H} = \sigma_{gg \rightarrow H} \frac{\Gamma_{H \rightarrow 4\ell}(m_H)}{\Gamma_H} \end{aligned} \quad (5.2)$$

which, in terms of the κ scaling factors introduced in [58], $\kappa_g = g_{ggH}/g_{ggH}^{\text{SM}}$ and $\kappa_Z = g_{HZZ}/g_{HZZ}^{\text{SM}}$, and setting $r = \Gamma_H/\Gamma_H^{\text{SM}}$, becomes:

$$\sigma_{gg \rightarrow H \rightarrow 4\ell}^{\text{on-peak}} = \frac{\kappa_g^2 \kappa_Z^2}{r} (\sigma \cdot \text{BR})_{\text{SM}} \equiv \mu (\sigma \cdot \text{BR})_{\text{SM}} \quad (5.3)$$

From the Eq. (5.3) it is clear that scaling r of the width together with a scaling $r^{1/4}$ of each couplings would leave μ , defined as the measured signal strength, unchanged [59, 55].

Using the fact the Higgs boson is a narrow resonance we can rewrite the Eq. (5.1) in the off-peak region as follows:

$$\begin{aligned} \frac{d\sigma_{gg \rightarrow H \rightarrow 4\ell}^{\text{off-peak}}}{dm_{4\ell}^2} &= \frac{1}{\pi} \sigma_{gg \rightarrow H} \frac{m_{4\ell}^2}{(m_{4\ell}^2 - m_H^2)^2 + m_H^2 \Gamma_H^2} \frac{\Gamma_{H \rightarrow 4\ell}(m_{4\ell})}{m_{4\ell}} \\ &\simeq \kappa_g^2 \kappa_Z^2 \cdot \frac{1}{\pi} \sigma_{gg \rightarrow H}^{\text{SM}} \frac{m_{4\ell}^2}{(m_{4\ell}^2 - m_H^2)^2} \frac{\Gamma_{H \rightarrow 4\ell}^{\text{SM}}(m_{4\ell})}{m_{4\ell}} = \kappa_g^2 \kappa_Z^2 \cdot \frac{d\sigma_{gg \rightarrow H \rightarrow 4\ell}^{\text{off-peak, SM}}}{dm_{4\ell}^2} \end{aligned} \quad (5.4)$$

Thus, in the off-peak region the $gg \rightarrow H \rightarrow 4\ell$ cross-section is independent of Γ_H and depends only on coupling parameters. After the Higgs boson mass is fixed there is no other dependence on its parameters and one can constrain the coupling parameters using only Higgs boson mass measurements.

On the other hand, this relation can be interpreted on the other way around: a constraint on the total Higgs width could be made using fixed signal strength μ , provided by an external

¹The same logic, shown here on the example of $gg \rightarrow H \rightarrow 4\ell$, could be applied to any other production or decay mode.

source. Indeed, substituting Eq. (5.3) in (5.4) one obtains:

$$\frac{d\sigma_{gg \rightarrow H \rightarrow 4\ell}^{\text{off-peak}}}{dm_{4\ell}^2} = \mu r \frac{d\sigma_{gg \rightarrow H \rightarrow 4\ell}^{\text{off-peak,SM}}}{dm_{4\ell}^2} \quad (5.5)$$

For a fixed value of μ (for example $\mu = 1$, assuming the SM expectation in the peak, or from the results of the on-peak analysis [53]) the off-peak differential cross-section becomes proportional to the Γ_H .

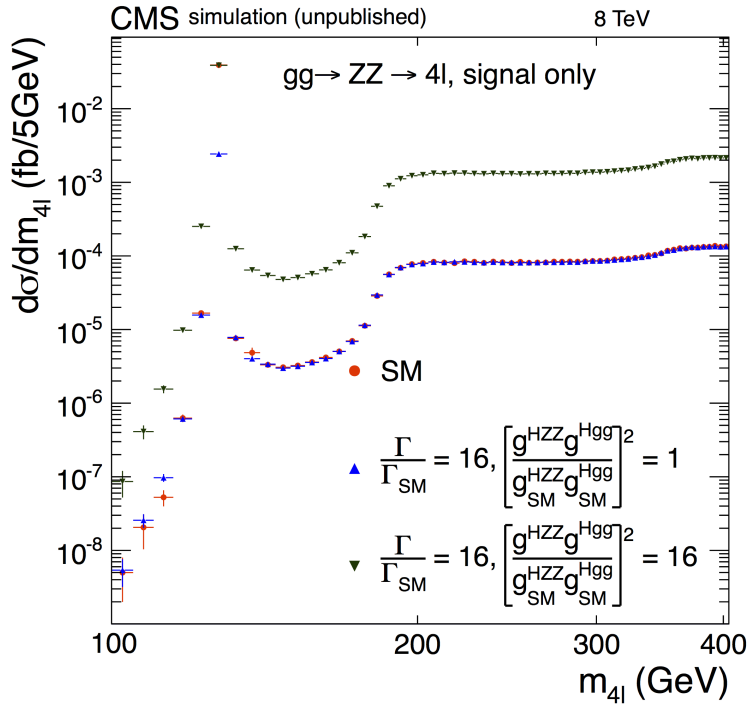


Figure 5.3 – Distribution of the generated four-lepton cross-section in mass range [100, 400] GeV for the $gg \rightarrow H \rightarrow 2e2\mu$ channel with different couplings and width scaling for a Higgs mass of 125.6 GeV.

An illustration of this result is given in Fig. 5.3. Under a scaling of the width only, the peak yield decreases by the scaling factor while the high mass part of the distribution stays unchanged. When scaling both the width and the coupling product squared, the yield in the peak is kept unchanged while an increase of the yield in the off-shell region by this scaling factor is expected.

Also one should notice that the cross-section is about constant in a region above the $2m_Z$ threshold. It has been shown that for $m_{4\ell} > 2m_Z$ [60]:

$$\frac{\Gamma_{H \rightarrow 4\ell}(m_{4\ell})}{m_{4\ell}} \propto m_{4\ell}^2. \quad (5.6)$$

Besides this, the following approximation is valid in the same region:

$$\frac{1}{(m_{4\ell}^2 - m_H^2)^2 + m_H^2 \Gamma_H^2} \simeq \frac{1}{(m_{4\ell}^2 - m_H^2)^2} \simeq \frac{1}{m_{4\ell}^4} \quad (5.7)$$

Putting these relations in the Eq. (5.1), we get that the $m_{4\ell}^4$ trends at the numerator and denominator cancel out. This effect allows us to have a non-negligible contribution from the off-shell Higgs boson production.

5.1.2 $gg \rightarrow ZZ$ continuum production

The $gg \rightarrow ZZ$ continuum doesn't appear as a main background ingredient neither in the peak region nor for the off-shell Higgs boson production because of dominating $q\bar{q} \rightarrow ZZ$, which despite the suppression due to the need for gluons in the initial state, is two orders of α_s larger. However this process plays a key role in Higgs boson width measurements due to its interference with the Higgs signal. This interference is destructive and effectively decreases the signal in the off-peak region. Taking into account both diagrams and interference term we can rewrite the equation for cross-section of the gluon-induced diboson production as in [55]:

$$\frac{d\sigma_{gg \rightarrow 4\ell}}{dm_{4\ell}} = \mu r \frac{d\sigma_{gg \rightarrow H \rightarrow 4\ell}}{dm_{4\ell}} + \sqrt{\mu r} \frac{d\sigma_{\text{interference}}}{dm_{4\ell}} + \frac{d\sigma_{gg \rightarrow ZZ \rightarrow 4\ell}}{dm_{4\ell}} \quad (5.8)$$

5.1.3 Contributions of other production mechanisms

Despite there are five main Higgs boson production mechanisms ($gg \rightarrow H$, VBF, ZH, WH, ttH), only two of them (gluon fusion and VBF) contributes at high mass and can lead to off-shell Higgs boson production above the $2m_Z$ threshold. The formalism presented in sections 5.1.2 and 5.1.1 for the gluon fusion production also applies to VBF production which is included in the analysis and adds to the overall sensitivity. Figure 5.4 (a) shows the cross-section for the VBF $\rightarrow 4\ell$ process including interference, as obtained from PHANTOM generator [61] for the VBF production and compared to gluon fusion for 8 TeV and for the $2e2\mu$ channel. In order to compare pure signal contributions the MCFM (gluon fusion) and MADGRAPH [62] (VBF) generators were used. The choice of different generators is motivated by the fact that PHANTOM generator does not consider signal and background processes only as "physical" and therefore is not able to produce pure signal. The shape of the VBF off-shell signal is similar to the shape of the gluon fusion, except the second enhancement of the cross-section at the $t\bar{t}$ threshold, as can be expected.

The ratio of VBF and gluon fusion contributions to the off-shell Higgs boson production is shown in Fig. 5.4 (b). The VBF fraction is below 10% at low mass and grows rapidly with $m_{4\ell}$ to reach ~ 1 at very high mass.

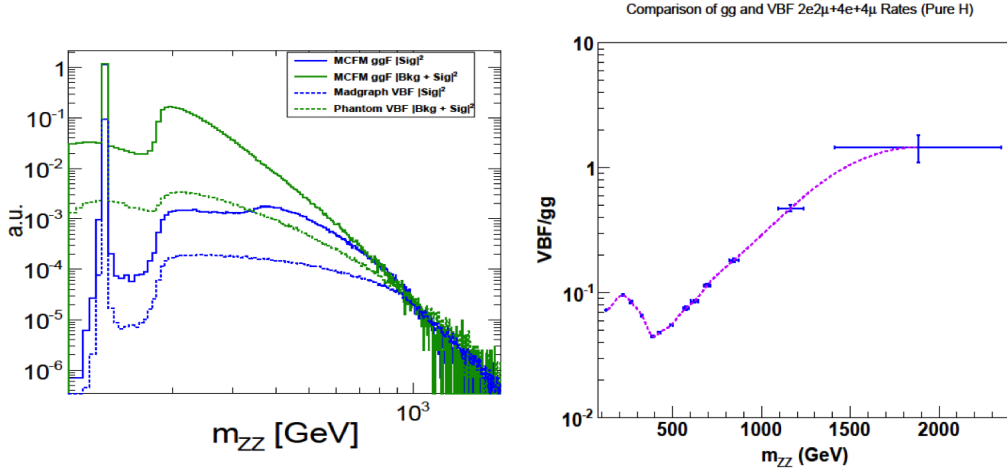


Figure 5.4 – Left: comparison of the VBF and gluon production processes: differential cross section for the sum of signal plus background plus interference contributions as obtained from PHANTOM for the VBF production and compared to gluon fusion from MCFM; differential cross section as obtained from MADGRAPH for the VBF production and for the signal only, and compared to gluon fusion from MCFM. The cross sections are for 8 TeV and for the $2e2\mu$ channel. Right: ratio of signal for VBF over gluon fusion as a function of $m_{4\ell}$ for the $H \rightarrow ZZ \rightarrow 4\ell$ decay channel.

5.2 Analysis Strategy

From the theoretical introduction given in the previous section it is natural to use the following parametrization in order to measure the Higgs boson width

$$\Gamma_H = r \times \Gamma_H^{SM}. \quad (5.9)$$

The analysis of off-shell production allows us to measure the product $r \times \mu$. Hence, in order to constrain r the signal strength should be known. Three possible μ estimations are considered:

- assume $\mu \equiv 1$;
- constrain μ from the low-mass $H \rightarrow ZZ \rightarrow 4\ell$ analysis;
- measure all couplings in a joined combined fit with all Higgs boson data.

The first option benefits from the independence on other measurements but makes a strong assumption that the signal strength at the peak matches exactly that of the SM. The second one is a self-contained measurement within the $H \rightarrow ZZ$ channel. It can be performed by combining the low-mass calculation (as in Sec. 4.6) and high-mass one (described in this chapter), keeping signal strength as a correlated parameter between the two. This approach also benefits from partial cancellation of the systematic uncertainties which are correlated

between low and high mass, such as the LHC luminosity, and the theory systematics which are common to the low mass and high mass regions. In order to avoid any further assumptions while using this method, we should also account for different μ measurements in the different production channels. Partial signal strengths for gluon fusion (μ_F) and VBF (μ_V) production are known in the ZZ channel [53], thanks to the VBF discriminant and $p_T(H)$ analysis, which allows to separate VBF-produced signal events. Other production modes are suppressed at high mass and therefore neglected in this analysis.

Finally, the third approach would be to measure κ_g , κ_Z and κ_W in a joined combined fit with all Higgs boson data in CMS. This approach is completely free from any assumptions on the relative signal strength, however it is outside the scope of this thesis.

We will describe the analysis methodology using both the first and second approaches and the final results will be presented for the second one.

5.3 Datasets

The data samples used in this analysis are exactly the same as those described in 4.1. The majority of simulated samples are also the same except the following improvements. $gg \rightarrow 4\ell$ events have been generated including the Higgs signal at 125.6 GeV, background production and interference between them using recent versions of two different LO MC generators: GG2VV 3.1.5 [56, 42] and MCFM 6.7 [59]. Two different generators were used in order to cross-check and validate the theoretical inputs. The leading order calculations were used due to the absence of beyond LO calculations for the fermion box $gg \rightarrow ZZ$ continuum process. The samples containing only Higgs signal and only continuum production were also generated in order to evaluate the differential distribution for each component in Eq. (5.8). Samples with scaled couplings corresponding to $r = 16, 25, 36, 49, 100$ have also been generated to check the normalization of the components in the model. The sample with $r = 25$ also underwent full simulation in order to cross check the correct modelling of the detector effects in the enhanced high-mass part of the signal.

All these samples have been generated with the following settings:

- CTEQ6L [63] LO parton density functions;
- Higgs mass as measured in [53] and corresponding SM width ($m_H = 125.6 \text{ GeV}$, $\Gamma_H = 4.15 \text{ MeV}$);
- “running” renormalization and factorization scales equal to $m_{4\ell}/2$ for MCFM samples. For technical reasons fixed scales equal to $m_H/2$ have been used for the generation of the GG2VV samples, but further reweighting was applied using an $m_{4\ell}$ dependent factor corresponding to the ratio of the running scale over the fixed scale cross sections.

In order to reduce the number of generated events which do not satisfy the detector acceptance

Chapter 5: The Higgs Boson Width Constraints From The Offshell Production

requirements (or just not used in the current analysis), the following preselection was applied at generator level:

- $m_{\ell\ell} > 4 \text{ GeV}$ where $m_{\ell\ell}$ is the invariant mass of any pair of opposite-sign same-flavor leptons in the event;
- $m_{4\ell} > 95 \text{ GeV}$;
- $p_T(\ell) > 3 \text{ GeV}$ and $|\eta(\ell)| < 2.7$ for all leptons;
- $p_T(\ell\ell) > 0.1 \text{ GeV}$ (with $\ell\ell$ defined as above) for the MCFM samples. For computational reasons, $p_T(\ell\ell) > 1 \text{ GeV}$ for different flavor final state ($2\ell 2\ell'$) and $p_T(\ell\ell) > 2 \text{ GeV}$ for same flavor final state (4ℓ) have been used for the GG2VV samples. Though no explicit cut on $p_T(\ell\ell)$ is applied at analysis level, it has been checked that the effect of this cut is negligible ($\leq 1\%$).

The details of the MC samples used are listed in Tables 5.1 and 5.2. All samples have been hadronized with PYTHIA and reconstructed using the same CMSSW releases as used in Sec.4.1.

Generator	sample name	σ_{LO} (fb)
gg2VV	GluGluTo4L_H_M-125p6_8TeV-gg2vv315-pythia6	0.586
gg2VV	GluGluTo2L2Lprime_H_M-125p6_8TeV-gg2vv315-pythia6	1.074
gg2VV	GluGluTo4L_Contin_8TeV-gg2vv315-pythia6	1.721
gg2VV	GluGluTo2L2Lprime_Contin_8TeV-gg2vv315-pythia6	3.486
gg2VV	GluGluTo4L_HContinInterf_M-125p6_8TeV-gg2vv315-pythia6	2.151
gg2VV	GluGluTo2L2Lprime_HContinInterf_M-125p6_8TeV-gg2vv315-pythia6	4.265
MCFM	GluGluTo4mu_SMH_M-125p6_8TeV-MCFM67-pythia6	0.163
MCFM	GluGluTo4mu_SMHContinInterf_M-125p6_8TeV-MCFM67-pythia6	0.592
MCFM	GluGluTo4mu_Contin_8TeV-MCFM67-pythia6	0.460
MCFM	GluGluTo4mu_BSMHContinInterf_M-125p6_8TeV-MCFM67-pythia6	0.808
MCFM	GluGluTo4e_SMH_M-125p6_8TeV-MCFM67-pythia6	0.163
MCFM	GluGluTo4e_SMHContinInterf_M-125p6_8TeV-MCFM67-pythia6	0.592
MCFM	GluGluTo4e_Contin_8TeV-MCFM67-pythia6	0.460
MCFM	GluGluTo4e_BSMHContinInterf_M-125p6_8TeV-MCFM67-pythia6	0.808
MCFM	GluGluTo2e2mu_SMH_M-125p6_8TeV-MCFM67-pythia6	0.326
MCFM	GluGluTo2e2mu_SMHContinInterf_M-125p6_8TeV-MCFM67-pythia6	1.185
MCFM	GluGluTo2e2mu_Contin_8TeV-MCFM67-pythia6	0.919
MCFM	GluGluTo2e2mu_BSMHContinInterf_M-125p6_8TeV-MCFM67-pythia6	1.616

Table 5.1 – List of new $gg \rightarrow ZZ \rightarrow 4\ell$ MC samples at 8 TeV, cross-sections of gg2VV are for $\ell = e, \mu, \tau$.

New samples of $qq' \rightarrow 4\ell qq'$ events have been also generated including Higgs signal at 125.6 GeV as well as background with interference using version 1.2.3 of PHANTOM. The calculation includes all EWK diagrams up to α_{EWK}^6 and therefore includes the interference of the VBF Higgs production with the VBF ZZ production through the fermion box diagram. Since

Generator	sample name	σ_{LO} (fb)
gg2VV	GluGluTo4L_H_M-125p6_7TeV-gg2vv315-pythia6	0.457
gg2VV	GluGluTo2L2Lprime_H_M-125p6_7TeV-gg2vv315-pythia6	0.837
gg2VV	GluGluTo4L_Contin_7TeV-gg2vv315-pythia6	1.293
gg2VV	GluGluTo2L2Lprime_Contin_7TeV-gg2vv315-pythia6	2.624
gg2VV	GluGluTo4L_HContinInterf_M-125p6_7TeV-gg2vv315-pythia6	1.624
gg2VV	GluGluTo2L2Lprime_HContinInterf_M-125p6_7TeV-gg2vv315-pythia6	3.252
MCFM	GluGluTo4mu_SMH_M-125p6_7TeV-MCFM67-pythia6	0.127
MCFM	GluGluTo4mu_SMHContinInterf_M-125p6_7TeV-MCFM67-pythia6	0.450
MCFM	GluGluTo4mu_Contin_7TeV-MCFM67-pythia6	0.344
MCFM	GluGluTo4mu_BSMHContinInterf_M-125p6_7TeV-MCFM67-pythia6	0.598
MCFM	GluGluTo4e_SMH_M-125p6_7TeV-MCFM67-pythia6	0.127
MCFM	GluGluTo4e_SMHContinInterf_M-125p6_7TeV-MCFM67-pythia6	0.450
MCFM	GluGluTo4e_Contin_7TeV-MCFM67-pythia6	0.344
MCFM	GluGluTo4e_BSMHContinInterf_M-125p6_7TeV-MCFM67-pythia6	0.598
MCFM	GluGluTo2e2mu_SMH_M-125p6_7TeV-MCFM67-pythia6	0.255
MCFM	GluGluTo2e2mu_SMHContinInterf_M-125p6_7TeV-MCFM67-pythia6	0.901
MCFM	GluGluTo2e2mu_Contin_7TeV-MCFM67-pythia6	0.689
MCFM	GluGluTo2e2mu_BSMHContinInterf_M-125p6_7TeV-MCFM67-pythia6	1.196

Table 5.2 – List of new $gg \rightarrow ZZ \rightarrow 4\ell$ MC samples at 7 TeV, cross-sections of gg2VV are for $\ell = e, \mu, \tau$.

the PHANTOM generator is not able to produce samples, containing only signal or only background, the samples with $r = 1, 10, 25$ have been generated in order to extract the normalized distributions of each component. Also the background-only sample has been produced by setting the Higgs mass to a negative value.

All $qq' \rightarrow 4\ell qq'$ samples have been generated with the following settings:

- CTEQ6L1 LO parton density functions;
- Higgs mass as measured in [53] and corresponding SM width ($m_{\text{H}} = 125.6 \text{ GeV}$, $\Gamma_{\text{H}} = 4.15 \text{ MeV}$);
- “running” renormalization and factorization scales equal to $m_{4\ell}/2$.

The same preselection was applied at the generator level as for the $gg \rightarrow 4\ell$ samples above, with the addition of a $m_{jj} \geq 130 \text{ GeV}$ requirement, applied to veto VH and VVH processes.

Since full simulation of PHANTOM sample is not available, we use two techniques to estimate the distributions of events after reconstruction.

- Reweighting of MCFM samples with the ratio between gluon-fusion and VBF generator-level cross section as a function of $m_{4\ell}$, as shown in Figure 5.4 (right).

- Smearing of lepton 4-momenta according to measured resolution [64, 65].

The shapes obtained in the two cases are very similar, and a systematic uncertainty is assigned for this difference. The reweighted MCFM samples are used as a baseline.

5.4 Signal and Background Cross-sections

In this section detailed description of the signal and background generation is provided. Quite a few samples were generated, part of them was subjected to the full detector simulation procedure while another part was used to estimate possible sensitivity and produce some preliminary results. This was needed in order to obtain a first expectation on the width constraint and further adjust more sophisticated analysis techniques in order to achieve the best performance. The details of the preliminary estimations will be given in Sec. 5.6.

The generator level differential cross-section as a function of four lepton invariant mass for the $2\ell 2\ell'$ final state and for 8 TeV c.o.m energy is shown in Figure 5.5. The factorization and renormalization scales are set here to $m_H/2$. Besides the basic preselection described in Sec. 4.1, a tighter kinematical selection was applied aiming to mimic the final analysis selection. We require $p_T(\ell) > 5$ (7) GeV for muons (electrons), $|\eta(\ell)| < 2.4$ (2.5) for muons (electrons), a transverse momentum $p_T(\ell) > 20$ (10) for the hardest (next-to-hardest) lepton and $m_{4\ell} > 100$ GeV. The invariant mass of a pair of same-flavor leptons closest to the Z -mass is required to be within $40 < m_{\ell\ell} < 120$ GeV and the invariant mass of the other pair should be within $12 < m_{\ell\ell} < 120$ GeV.

Apart from the differential cross-section for the full process (i.e. signal + background + interference between them) we show also the contributions of pure signal and pure continuum diagrams. The tail of the Higgs signal is visible starting from the $2m_Z$ threshold, at a level of about two orders of magnitude below the continuum at this mass. Despite the fact that the Higgs signal above the $2m_Z$ threshold is small, its contribution remains significant up to the very high masses. Starting from $m_{4\ell} \geq 600$ GeV it becomes even higher than the continuum contribution. The interference between the Higgs and the continuum diagrams is sizeable and negative as expected, the total cross section including the interference decreases faster than the Higgs signal at high mass and crosses the Higgs-only contribution at $m_{4\ell} \sim 700$ GeV.

The MCFM Monte Carlo generator is also used in the analysis. Fig. 5.6 presents the differential cross section as function of $m_{4\ell}$ for the Higgs signal obtained with MCFM and compared to the one obtained with gg2VV for different choices of the QCD scales. Identical generator level selection cuts and the same PDF are used in both simulations. An excellent agreement is found between the two generators when using the same scheme for the QCD scales.

Table 5.3 shows the comparison of the cross sections obtained with gg2VV in several mass bins with those obtained in [59] and in [55]. In these results the QCD scales are set to $m_H/2$ and the MSTW08 LO PDF are used. The selection described above is applied. An excellent

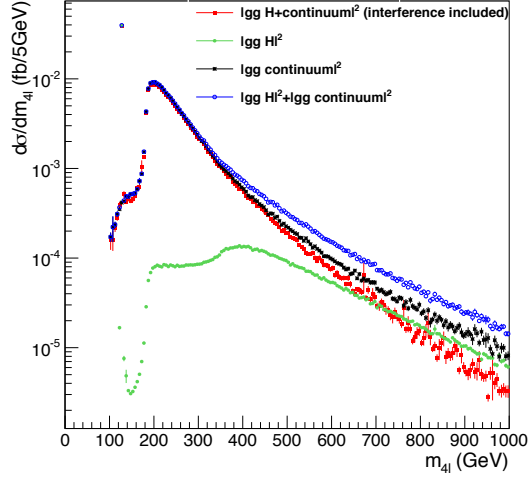


Figure 5.5 – Generator level differential cross-section at leading order as obtained from gg2VV for the $2\ell 2\ell'$ final state and for 8 TeV c.o.m. energy. The contribution of the Higgs-mediated and pure continuum diagrams are also shown separately, as well as the unphysical sum of the squared amplitudes.

agreement is found when using the same settings for the QCD scales and PDFs between gg2VV and MCFM. A difference is visible though for the interference term when comparing with [55], and understood to be due to the p_T^Z cut at 7 GeV which was applied in the gg2VV version used in [55].

generator	$m_{4l} < 130 \text{ GeV}$	$m_{4l} > 130 \text{ GeV}$		$m_{4l} > 300 \text{ GeV}$	
	σ_H^{peak} (fb)	σ_H^{off} (fb)	σ_I^{off} (fb)	σ_H^{off} (fb)	σ_I^{off} (fb)
gg2VV	0.258	0.060	-0.123	0.049	-0.068
Ref. [55]	0.255	0.061	-0.166	-	-
Ref. [59]	0.255	0.061	-0.118	0.049	-0.071

Table 5.3 – Integrated cross sections in different mass bins compared with results from [55] and [59]. QCD scales are set to $m_H/2$ and the MSTW08 LO PDFs are used.

Following the prescription given in [57] we set both scales to $m_{4\ell}/2$. This results in a decrease of the differential cross-section at very high masses as it is visible in Fig. 5.6.

5.4.1 Higher order corrections

As it was mentioned in Sec. 4.1, we are able to generate the $gg \rightarrow 4\ell$ events only at leading order. However, higher order corrections for the signal diagram are available as a function of $m_{4\ell}$ to NNLO [57]. The correction factor (K-factor) as a function of $m_{4\ell}$ is shown in Fig. 5.7. Unfortunately, only LO exact calculation exists for the box diagram which is responsible for the continuum background. Nevertheless, it has been recently shown in [66] that the soft

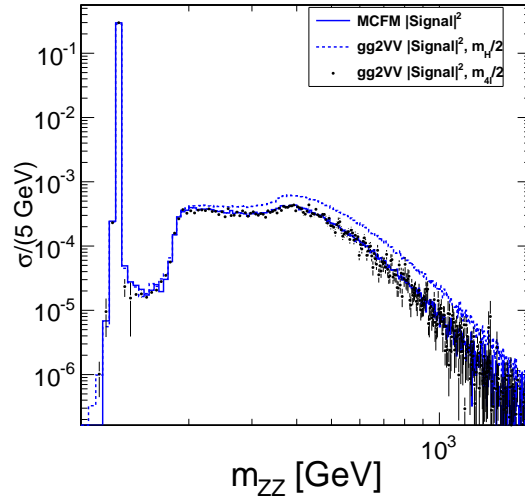


Figure 5.6 – Generator level differential cross-section as obtained from MCFM for the $2\ell 2\ell'$ final state and for 8 TeV c.o.m energy and compared to the cross section obtained with GG2VV. The factorization and renormalization scales are set here to $m_{4\ell}/2$ in case of MCFM and both $m_{4\ell}/2$ and $m_H/2$ in case of GG2VV.

collinear approximation works well enough at c.o.m energy around 8 TeV and thus can be used to assess the background higher order corrections. This opens the possibility to correctly scale the interference part of the process up to NNLO. Following [66], we assign to the LO background cross section a K-factor equal to the one used for the signal, and consequently also the same K-factor to the interference contribution. Dedicated systematic uncertainties are assigned due to this approximation and will be discussed in Sec. 5.10.

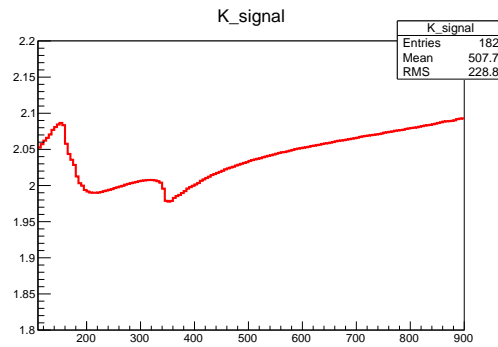


Figure 5.7 – NNLO/LO K-factor at 8 TeV.

5.4.2 Vector boson fusion samples

The PHANTOM generator, as it was mentioned, doesn't provide the possibility to generate "unphysical" samples containing only signal and only continuum processes. This was solved by generating the three samples with scaled couplings corresponding to $r = 1, 10, 25$ and extraction of the normalization of the components solving the matrix equation:

$$\begin{pmatrix} p_1 \\ p_{10} \\ p_{25} \end{pmatrix} = \begin{pmatrix} 1 & 1 & 1 \\ 10 & \sqrt{10} & 1 \\ 25 & 5 & 1 \end{pmatrix} \begin{pmatrix} S \\ I \\ B \end{pmatrix} \quad (5.10)$$

where p_1, p_{10}, p_{25} are the entries of any MC template distribution for the three samples and S, B and I the corresponding entries for signal-, background- and interference-only unphysical processes. Solving for S, B and I :

$$\begin{pmatrix} S \\ I \\ B \end{pmatrix} = \frac{1}{60 - 24\sqrt{10}} \begin{pmatrix} -5 + \sqrt{10} & 4 & 1 - \sqrt{10} \\ 15 & -24 & 9 \\ 50 - 25\sqrt{10} & 20 & -10 + \sqrt{10} \end{pmatrix} \begin{pmatrix} p_1 \\ p_{10} \\ p_{25} \end{pmatrix} \quad (5.11)$$

Finally, dedicated K-factors to obtain NNLO QCD description of 6% and independent of $m_{4\ell}$ [67, 68] are applied.

5.5 Backgrounds Estimation

The sources of background in this analysis are exactly the same as the ones described in Sec. 4.3. Thus, their treatment and contribution estimation is also essentially the same except some improvements obtained with most recent studies.

In the previous section we already described the treatment of the continuum background arising from the $gg \rightarrow ZZ \rightarrow 4\ell$ box diagram and the one coming from VBF. The missing pieces are therefore the reducible background and $q\bar{q} \rightarrow ZZ$. The reducible background is estimated exactly in the same way as in Sec. 4.3, whilst the $q\bar{q} \rightarrow ZZ$ treatment was improved.

Very recent calculations for NLO electroweak corrections to the $q\bar{q} \rightarrow ZZ$ process appeared in [69, 70, 71] were not considered neither in the POWHEG nor in MCFM simulations. These corrections predict negative $m_{4\ell}$ -dependent corrections to the cross-sections at order of -5% around 220 GeV up to about -20% at high mass. Moreover, these corrections are applicable only in case of both real Z bosons and hence no correction is provided at low mass. The corrections were obtained as a function of Mandelstam variables and quark flavour and are independent of \sqrt{s} . They were averaged over \hat{t} and the quark flavor using the generator-level information provided by POWHEG sample and results in $m_{4\ell}$ -dependent factor. This factor was applied as an event-by-event weight to the MC samples. The size of the correction is shown in Fig. 5.8.

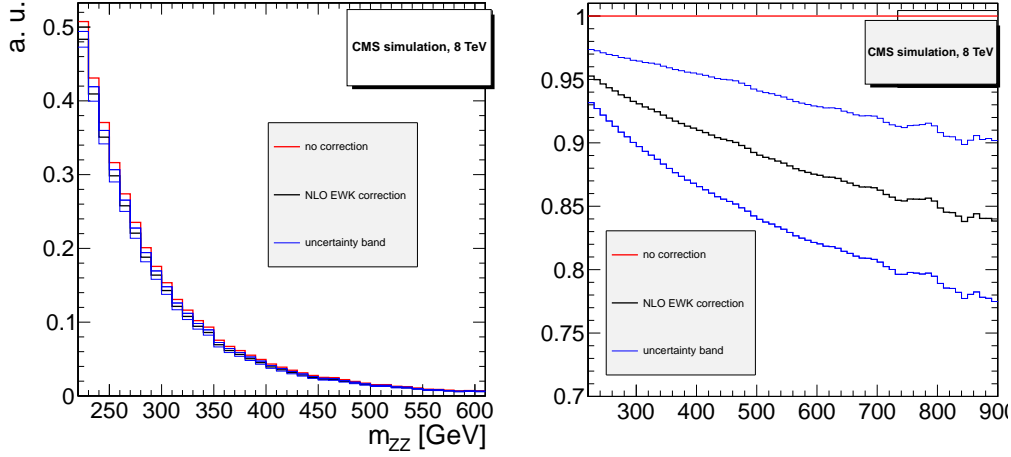


Figure 5.8 – $m_{4\ell}$ distribution after reconstruction and selection for the $2e2\mu$ final state at 8 TeV: before applying NLO EW correction (red), after applying (black) and with the relative uncertainties as explained in Sec. 5.10 (blue). On the right the same is shown as a ratio to the uncorrected distribution.

5.6 Reweighting Procedure

In order to perform the analysis we need in general the samples corresponding to each point in the width space we want to scan over. Since the full simulation procedure takes a lot of time we cannot perform it for a reasonable number of samples needed in this analysis. However a dedicated method, called the matrix element reweighting, was developed and allows to account properly all the effects. A closure test was done by comparing results from reweighted samples with the full simulation ones and a very good agreement is found. We show now how the reweighting was applied in the 1D case using $m_{4\ell}$ as a reweighting variable, while it could be generalized to the multidimensional case exploring the full kinematics of the event.

Denoting N_S the number of expected events in the high mass region from the Higgs signal only (Fig. 5.2, left), N_B the contribution from the continuum background (Fig. 5.2, right), and N_I the contribution from the interference between the two corresponding amplitudes, the total expected yield for the $gg \rightarrow 4\ell$ through diboson production process for any model with $r \neq 1$ (the alternative models) could be written as in [55] (assuming here $\mu = 1$):

$$N_{gg} = r \times N_S + \sqrt{r} \times N_I + N_B \quad (5.12)$$

where the N_I contribution is obtained by subtracting the pure signal and pure background contributions from the total one:

$$\sigma(I) = \sigma(S+B) - \sigma(S) - \sigma(B) \quad (5.13)$$

In the Fig. 5.9 the expected yields N_{gg} for the $2e2\mu$ final state and for $m_{4\ell} \geq 240$ GeV is shown

5.7. First Preliminary Results on the Width Constraints

as a function of $r = \Gamma_H/\Gamma_H^{SM}$, varying r from 1 up to 50. The line corresponds to the prediction from the parametrization of Eq. 5.12. The points are obtained by reweighting the SM distribution by the generator level cross sections obtained for various r . From this figure we see that Eq. 5.12 describes very well the expected yield for various alternative (i.e. $r \neq 1$) hypotheses.

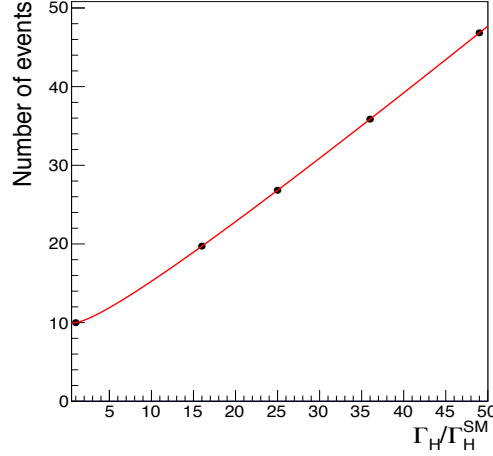


Figure 5.9 – Expected number of events from the $gg \rightarrow 2e2\mu$ through diboson production process for the SM and for alternative models corresponding to r varying up to 50. The line shows the parametrization of Eq. 5.12.

Using the above result we can now produce any alternative hypothesis point having SM yields for signal, continuum and interference. Figure 5.10 shows the comparison between the differential cross section obtained from the generator modifying the Higgs width and couplings and the differential cross section obtained by scaling the SM cross sections using parametrization from Eq. 5.12. The distributions here are shown for the example case of $r = 25$.

5.7 First Preliminary Results on the Width Constraints

In order to achieve the first perspective on the possible exclusion limit on the Higgs boson width a hypothesis-testing method based on a log-likelihood ratio in bins of the $m_{4\ell}$ distribution was implemented. The binning of $m_{4\ell}$ distribution was adjusted in compromise between benefiting from including the shape of the distribution in the analysis and having enough statistics in each bin. A bin size of 60 GeV is used for $m_{4\ell} > 220$ GeV and up to 1600 GeV phase space region. The CL_S criterion is defined as the ratio of the probabilities to observe under the hypotheses Γ_H a value of the test statistics

$$q = -2 \ln \mathcal{L}(\Gamma_H) / \mathcal{L}(\Gamma_H^{SM})$$

equal or larger than the one obtained under the SM assumption. An analytical curve representing the expected CL_S dependency on r was constructed. The analytical representation is

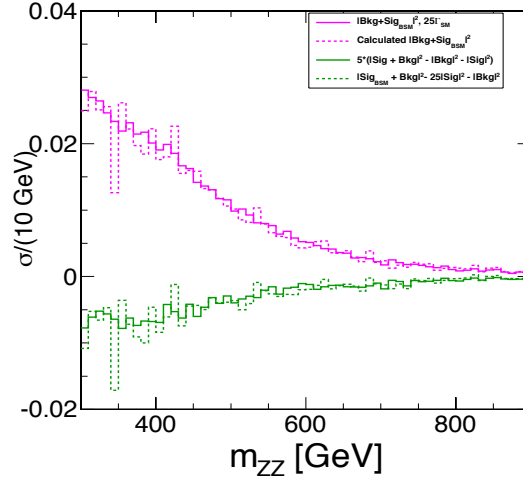


Figure 5.10 – Comparison between the differential cross section for the signal and for the interference obtained from the generator modifying the Higgs width and couplings as described above and the differential cross section obtained by scaling the SM cross section using Eq. 5.12. The distributions here are shown for the example case of $r=25$.

calculated as the cumulative distribution function of the poisson distribution of the number of expected events from the Eq. 5.12. After superimposing the analytical curve with the alternative hypotheses points for which we have the reweighted distributions we can extract the exclusion limit on r . Figure 5.11 presents the expected exclusion limits obtained using this log-likelihood ratio implementation. The presented results correspond to the 8 TeV dataset with no systematics. The expected upper limit on r is found to be 14.2 at 95% CL, which is in excellent agreement with the one obtained using the CMS combination tool (see Sec. 5.11).

Such result allows us to guess the final exclusion when doing the 2D analysis, exploring the special discriminant, which is described in the following section. The sensitivity of the 1D analysis with this discriminant is expected to be similar to the 1D $m_{4\ell}$ -based one. Combining both we expect about 30% improvement in sensitivity, which gives expected exclusion around $r = 10$. This result is further used in the discriminant adjustment.

5.8 Matrix Element Likelihood Approach

One of the most important features of the $H \rightarrow ZZ \rightarrow 4\ell$ channel is the fact that the final state products are fully reconstructable. In order to benefit from this a dedicated kinematic discriminant was developed following the same principles as described in Sec. 4.6.1. The discriminant is built from the probabilities \mathcal{P}_i for an event to come either from $gg \rightarrow ZZ$ or $q\bar{q} \rightarrow ZZ$ processes. The probability $\mathcal{P}_{gg,a}$ for the $gg \rightarrow ZZ$ process includes signal, background, and their interference, as introduced for the discriminant computation in [72]. For

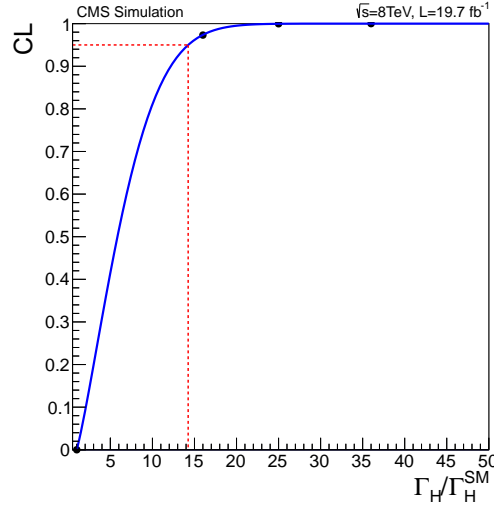


Figure 5.11 – Expected CLs as a function of Γ_H/Γ_H^{SM} from the hypothesis testing method based on the $m_{4\ell}$ distribution, with no systematics. The presented results correspond to the 8 TeV dataset.

each event one should calculate several effective probabilities:

$$\mathcal{P}_{gg,a}(\vec{\Omega}, m_1, m_2 | m_{4\ell}, m_H) = a \times \mathcal{P}_{\text{sig}}^{gg} + \sqrt{a} \times \mathcal{P}_{\text{int}}^{gg} + \mathcal{P}_{\text{bkg}}^{gg} \quad (5.14)$$

$$\mathcal{P}_{q\bar{q}}(\vec{\Omega}, m_1, m_2 | m_{4\ell}) = \mathcal{P}_{\text{bkg}}^{q\bar{q}}, \quad (5.15)$$

where \mathcal{P} is the probability as a function of angular and mass observables $(\vec{\Omega}, m_1, m_2)$ and calculated with the matrix element likelihood approach (MELA), and a is the strength of the enhancement due to the non-SM Higgs boson width with $a = 1$ corresponding to SM. The signal probability is calculated under the Higgs boson mass hypothesis $m_H = 125.6$ GeV.

Finally we construct the following observable:

$$\mathcal{D}_{gg,a} = \frac{\mathcal{P}_{gg,a}}{\mathcal{P}_{gg,a} + \mathcal{P}_{q\bar{q}}} = \left[1 + \frac{\mathcal{P}_{\text{bkg}}^{q\bar{q}}}{a \times \mathcal{P}_{\text{sig}}^{gg} + \sqrt{a} \times \mathcal{P}_{\text{int}}^{gg} + \mathcal{P}_{\text{bkg}}^{gg}} \right]^{-1} \quad (5.16)$$

where the $\mathcal{P}_{\text{bkg}}^{q\bar{q}}$ includes a correction factor $c(m_{4\ell})$ to account for the relative normalization of probabilities at a given value of $m_{4\ell}$. This correction factor does not affect the separation power.

The implementations of the matrix element approach is provided by the MELA package, which is based on JHUGen [39, 72] and MCFM [43] implementation of the signal and background processes, respectively, covering the gg and $q\bar{q}$ productions mechanisms for both signal and background.

There is still need to set the value of the signal strength a in the observable $\mathcal{D}_{gg,a}$, which has

to be optimized for analysis. As it was mentioned in the previous section, the preliminary results predict a sensitivity of order $r = 10$ which can be achieved from the analysis of the Run I data. Further studies confirmed that expected results do not vary strongly when we change a by a factor of 2 up or down. Hence we denote $\mathcal{D}_{gg} = \mathcal{D}_{gg,10}$ omitting the values of a in the discriminant notation.

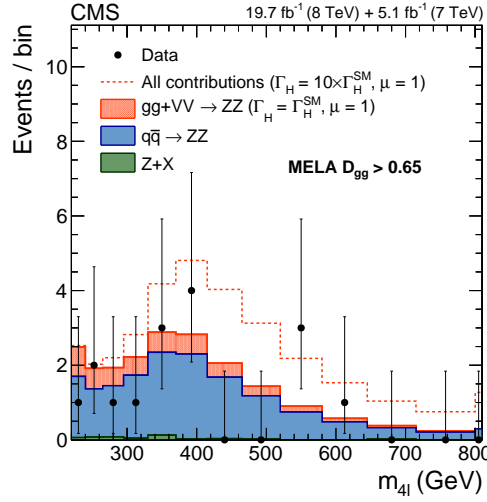


Figure 5.12 – Distribution of the four-lepton reconstructed mass in the full analysis mass range with a requirement on the MELA discriminant $\mathcal{D}_{gg} > 0.65$ to reject the ZZ background for the sum of the $4e$, 4μ , and $2e2\mu$ channels. Points represent the data, solid histograms represent the backgrounds and the dotted-shaded histogram is the $gg + VV \rightarrow ZZ$ expectations for a Higgs mass of 125.6 GeV, where VV represents VBF production. The expected distributions are presented as stacked histograms. The last bin includes overflow events.

Fig. 5.12 illustrates the separation power obtained by exploring both $m_{4\ell}$ and \mathcal{D}_{gg} variables. It shows the distribution of the four-lepton reconstructed mass in the full analysis mass range with a requirement on the MELA discriminant $\mathcal{D}_{gg} > 0.65$ to enhance the signal contribution. Although it is used for illustration purposes only, it clearly shows the difference between Standard Model prediction and the one with $\Gamma_H = 10 \times \Gamma_H^{SM}$. The separation power starts to be perceptible at $m_{4\ell} \sim 300$ GeV and increases with the invariant mass of the four leptons.

5.9 2D Statistical Model

A simultaneous maximum likelihood fit of the selected 4ℓ event candidates is performed both at low- and high-mass parts of the $m_{4\ell}$ spectrum. Following this approach we obtain the signal strength for gluon fusion and VBF production modes analysing the events in the peak and use them for the normalization of probability density functions (pdfs) at high mass. Following this,

we can write down the likelihood function in the following form:

$$\begin{aligned}
 \mathcal{L}_{\text{off-peak}} &= N_{\text{ggZZ}} \left[r \mu_F \times \mathcal{P}_{\text{sig}}^{\text{gg}} + \sqrt{r \mu_F} \times \mathcal{P}_{\text{int}}^{\text{gg}} + \mathcal{P}_{\text{bkg}}^{\text{gg}} \right] \\
 &+ N_{\text{VBF}} \left[r \mu_V \times \mathcal{P}_{\text{sig}}^{\text{VBF}} + \sqrt{r \mu_V} \times \mathcal{P}_{\text{int}}^{\text{VBF}} + \mathcal{P}_{\text{bkg}}^{\text{VBF}} \right] \\
 &+ N_{\text{q}\bar{\text{q}}\text{ZZ}} \mathcal{P}_{\text{bkg}}^{\text{q}\bar{\text{q}}} + N_{\text{ZX}} \mathcal{P}_{\text{bkg}}^{\text{ZX}}, \tag{5.17}
 \end{aligned}$$

The normalization of total probability is 1 when $r \times \mu = 1$. The individual components, such as $\mathcal{P}_{\text{int}}^{\text{gg}}$, may have both positive or negative values, since they do not correspond to observables, but the sum (which corresponds to the observed yield) is always positive-defined.

For the on-shell events we can instead write:

$$\begin{aligned}
 \mathcal{L}_{\text{on-peak}} &= N'_{\text{ggZZ}} \left[\mu_F \times \mathcal{P}'_{\text{sig}}{}^{\text{gg}} + \mathcal{P}'_{\text{bkg}}{}^{\text{gg}} \right] \\
 &+ N'_{\text{VBF+VH}} \mu_V \times \mathcal{P}'_{\text{sig}}{}^{\text{VBF+VH}} + N'_{\text{q}\bar{\text{q}}\text{ZZ}} \mathcal{P}'_{\text{bkg}}{}^{\text{q}\bar{\text{q}}} + N'_{\text{ZX}} \mathcal{P}'_{\text{bkg}}{}^{\text{ZX}}, \tag{5.18}
 \end{aligned}$$

where $\mathcal{P}'(m_{4\ell}, \mathcal{D}_{\text{bkg}}, p_T)$ or $\mathcal{P}'(m_{4\ell}, \mathcal{D}_{\text{bkg}}, V_D)$ is the normalized probability distribution for each process defined as a template of three observables [53, 73].

The implementation of the fit is based on the CMS Higgs combination tool. Although the final results are obtained with the 2D model fit, a 1D result using the $m_{4\ell}$ discrimination variable was produced and used to cross-check the implementation of statistical tool. The results are found to be in excellent agreement.

5.10 Systematic Uncertainties

Since the joint fit at low- and high-mass parts of the $m_{4\ell}$ spectrum is performed, we can split the systematic uncertainties into two categories: the ones which affect only the total normalization and others which affect both the shape and normalization of the variable distributions used in the analysis.

The uncertainties from the first category are treated as 100% correlated between the low- and high-mass events, and since they affect the $\mu_{V,F}$, they cancel completely in the determination of r . The following sources of uncertainties belong to this category: luminosity, trigger efficiency, identification and isolation efficiencies. Since we are fixing the signal strength from the measured yield in the peak, the theoretical uncertainties on the components normalization also cancel out.

In order to account for theoretical uncertainties on the gg-induced processes the following steps are done:

- We vary both the renormalization and factorization scales by factor two up and down from a nominal value of $m_{4\ell}/2$, applying a K-factor variation from [57] and keeping the

normalization unchanged

- Shape uncertainties from Parton-Density Function (PDF) variations are extracted by changing NLO PDF sets from CT10 to MSTW2008 and to NNPDF2.1. Fig. 5.13(left) shows the normalized ratio of the cross sections obtained using MSTW2008 and CT10. Same ratio between NNPDF2.1. and CT10 PDFs is shown in Fig. 5.13(right). A fit of the maximum observed deviation in the ratio yields a very small slope of $-7.51438 * 10^{-5} \text{ GeV}^{-1}$ which is used to derive alternative shapes (1-2%).
- For continuum $gg \rightarrow ZZ$, following [66], we assign to the LO background cross section a K-factor equal to the one used for the signal and additional systematic uncertainty of 10% following [66] is applied.

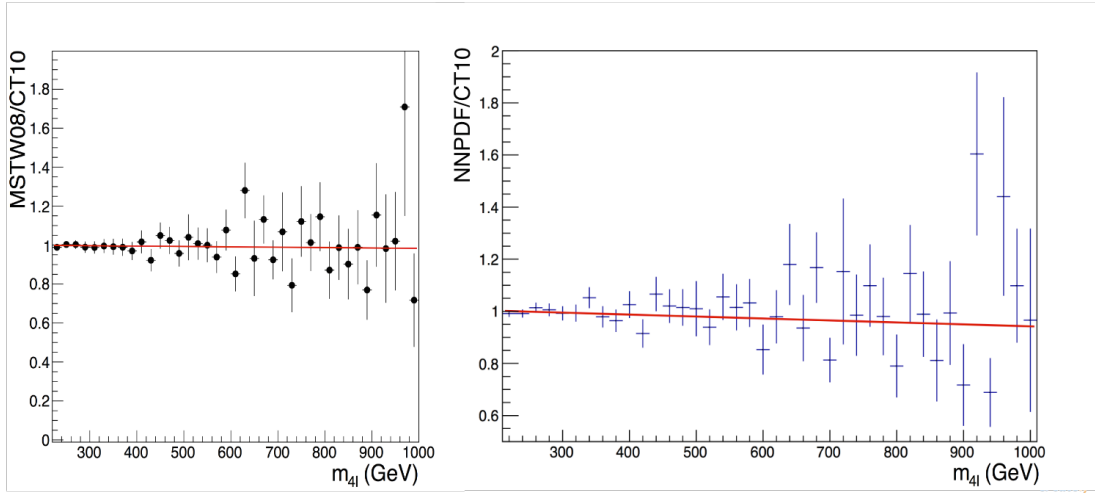


Figure 5.13 – Ratio of the gg differential cross section obtained using MSTW08 and CT10 PDFs (left) and NNPDF2.1 and CT10 PDFs (right). Both PDFs are taken at next-to-leading order. The line represents the result of a linear fit which is used to construct alternative shapes to describe the associated systematic uncertainty. Error bars correspond to the 1-sigma uncertainties on each point.

Similar procedure is used in order to evaluate the systematic uncertainties on the $q\bar{q} \rightarrow ZZ$ background cross-section. Theoretical uncertainties on the $q\bar{q} \rightarrow ZZ$ NLO electroweak corrections are assigned following [71]. Since the correlation between NLO QCD and NLO EW corrections is unknown, we take as uncertainty the product of these two NLO to LO corrections. The size of the resulting uncertainty is about 40% of the correction as it is shown in Fig. 5.8.

The systematic uncertainty on the amount of reducible background is evaluated following the methods developed in [53].

For VBF samples, which are not fully reconstructed, we assign a systematic due to the template shape differences in the two approximation approaches explained in Sec. 4.1. These are dominant with respect to shape uncertainties on QCD scales and PDFs.

5.11 Results

The reconstructed four lepton mass spectrum after passing all the selection requirements for both low- and high mass parts of the spectrum is shown in Fig. 5.14. It includes all the Higgs boson production mechanisms and all the scaling factors and corrections described above. The points represent the experimental data corresponding to the full 2011 and 2022 datasets. A good agreement between the data and Standard Model expectation is observed.

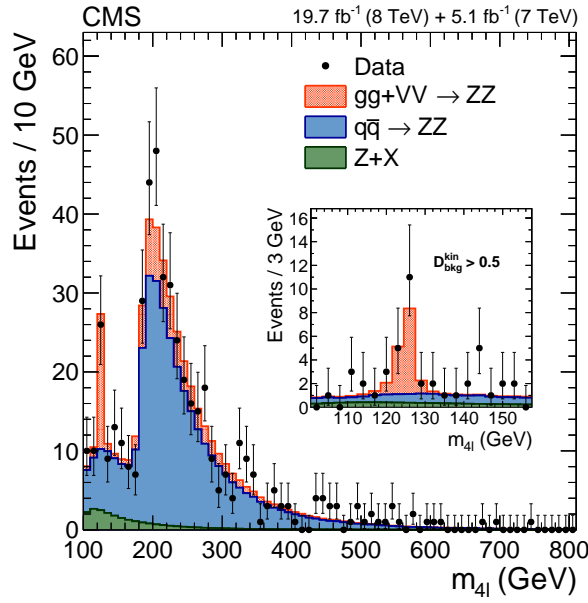


Figure 5.14 – Distribution of the four-lepton reconstructed mass in the full region for the summed $4e$, 4μ and $2e2\mu$ channels and for the full 2011 and 2012 datasets. Points represent the data, filled histograms represent the expected contributions from the reducible and the $q\bar{q} \rightarrow ZZ$ backgrounds, the solid line the contribution from $gg \rightarrow ZZ$ and $VV \rightarrow ZZ$ (including Higgs) for the SM. Zoom on the peak is in the inset, applying a loose discriminant cut $D_{bkg}^{kin} > 0.5$ as introduced in 4.6.1.

We first present the 1D fit results obtained using the measured mass distribution only (Fig 5.15, right) and the \mathcal{D}_{gg} discriminant only (Fig 5.15, left), where the two-dimensional templates are projected over the respective dimension. The expected upper limits for r at 95% CL are found to be of $\Gamma_H \leq 57.7$ MeV ($\Gamma_H \leq 13.9 \times \Gamma_H^{SM}$) for the $m_{4\ell}$ fit and $\Gamma_H \leq 44.3$ MeV ($\Gamma_H \leq 10.7 \times \Gamma_H^{SM}$) for the \mathcal{D}_{gg} fit. The corresponding observed limit are: $\Gamma_H \leq 112.5$ MeV ($\Gamma_H \leq 27.1 \times \Gamma_H^{SM}$) for the $m_{4\ell}$ fit and $\Gamma_H \leq 33.0$ MeV ($\Gamma_H \leq 8.0 \times \Gamma_H^{SM}$) for the \mathcal{D}_{gg} fit. In addition, the dash-dotted lines on the plots shows the expectation curves without the systematic uncertainties (i.e. fixing the nuisance parameters to their best fit values). The effect of the systematic uncertainties is quite small because of the partial cancellation of the correlated between on-shell and off-shell regions uncertainties. However, it is of primary importance to estimate correctly the systematic uncertainties, especially the ones arising from the $gg \rightarrow ZZ$ continuum diagram

since they enters in the signal yield through the interference term and can significantly affect the signal.

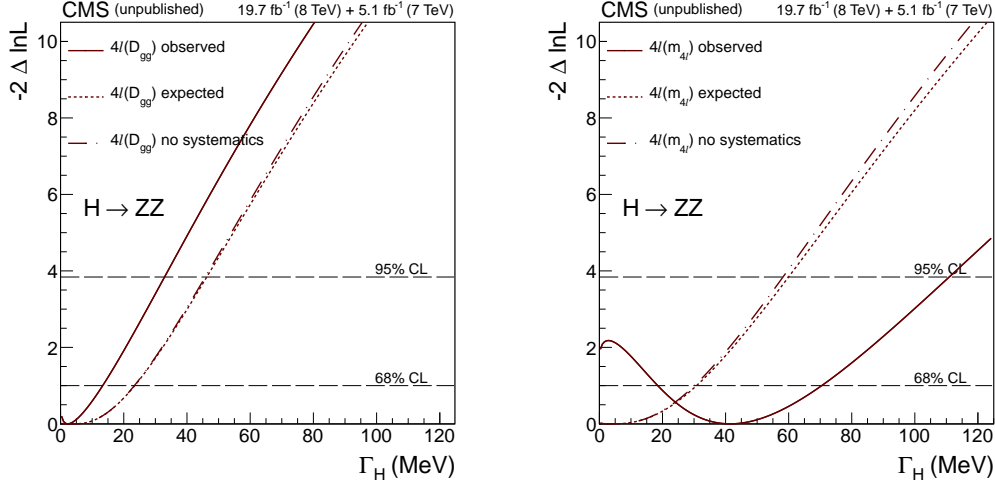


Figure 5.15 – Fit results for the 1D analyses using \mathcal{D}_{gg} (left) and $m_{4\ell}$ (right). The presented results correspond to the 7 and 8 TeV datasets.

Figure 5.16 presents the result of the 2D analysis using $m_{4\ell}$ and the \mathcal{D}_{gg} discriminant. The result is an expected exclusion of $\Gamma_H \leq 41.9$ MeV ($\Gamma_H \leq 10.1 \times \Gamma_H^{SM}$) and an observed limit of $\Gamma_H \leq 33.3$ MeV ($\Gamma_H \leq 8.0 \times \Gamma_H^{SM}$) at 95% CL with the systematic uncertainties included. The presented results correspond to the 7 and 8 TeV datasets.

5.11.1 Combination with the $2\ell 2\nu$ analysis

An analogous analysis was performed in the $2\ell 2\nu$ final state [74] using the data, collected by CMS experiment at $\sqrt{s} = 8$ TeV in 2012. Since the full invariant mass in this channel can not be reconstructed, the transverse mass, defined as:

$$M_T^2 = \left[\sqrt{p_{T,\ell\ell}^2 + m_{\ell\ell}^2} + \sqrt{E_{miss,T}^2 + m_{\ell\ell}^2} \right]^2 - \left[\vec{p}_{T,\ell\ell} + \vec{E}_{miss,T} \right]^2, \quad (5.19)$$

was used. The $H \rightarrow ZZ \rightarrow 2\ell 2\nu$ channel benefits from the higher branching fraction, but the background contribution is also much higher than in the 4ℓ final state. This leads to higher sensitivity to the systematic uncertainties. Using the Higgs combination tool, $2\ell 2\nu$ analysis is combined with the 4ℓ one to obtain the combined limit on the Higgs boson width.

We treat the systematic uncertainties as uncorrelated between the 4ℓ low/high mass and the $2\ell 2\nu$ analysis, with the exception of:

- theoretical uncertainties on the normalization of the $q\bar{q}$ background contribution

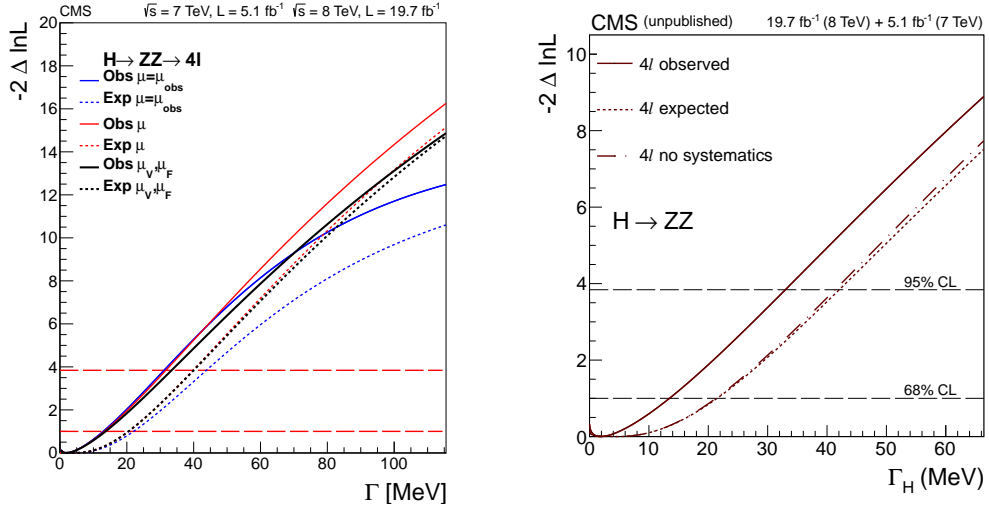


Figure 5.16 – Fit result for the 2D analysis ($m_{4\ell}$ and \mathcal{D}_{gg}). The presented results correspond to the 7 and 8 TeV datasets. The different lines, explained in the legend, correspond to observed (solid) and expected (dashed) results. The black line is the nominal analysis (r and $\mu_{V,F}$ floated), compared to the hypothesis $\mu_V = \mu_F = \mu$ (only two parameters floated, red) and the approach used for the results presented at the XLIXth Rencontres de Moriond conference, where μ is taken as an external input with Gaussian constraints. The right plot only contains nominal fits.

- limited knowledge on the background K-factor at NNLO
- variation of the scale used for factorization, normalization, and the K-factor
- shape uncertainties from Parton-Density Function (PDF) variations

The result of the combination is a $\Gamma_H \leq 22$ MeV ($\Gamma_H \leq 33$ MeV expected) 95% CL upper limit. This corresponds to $\Gamma_H \leq 5.4 \times \Gamma_H^{SM}$ ($\Gamma_H \leq 7.9 \times \Gamma_H^{SM}$ expected). The resulting likelihood scans are shown in Fig. 5.17.

5.11.2 Discussion and perspectives

The result achieved with this new method of width measurement is very tight. It was not expected at the start of the LHC that we could do this measurement at the level of few tens MeV. The approach used here is quite unusual and there is a very important question we should answer: the level of model dependency of the analysis. Let us remind the assumptions we have based on:

- validity of narrow-width approximation for the Higgs boson with $m_H \simeq 126$ GeV
- the main mechanism of the Higgs boson production is the gluon fusion with the top quark in the loop both in the peak region and off-peak

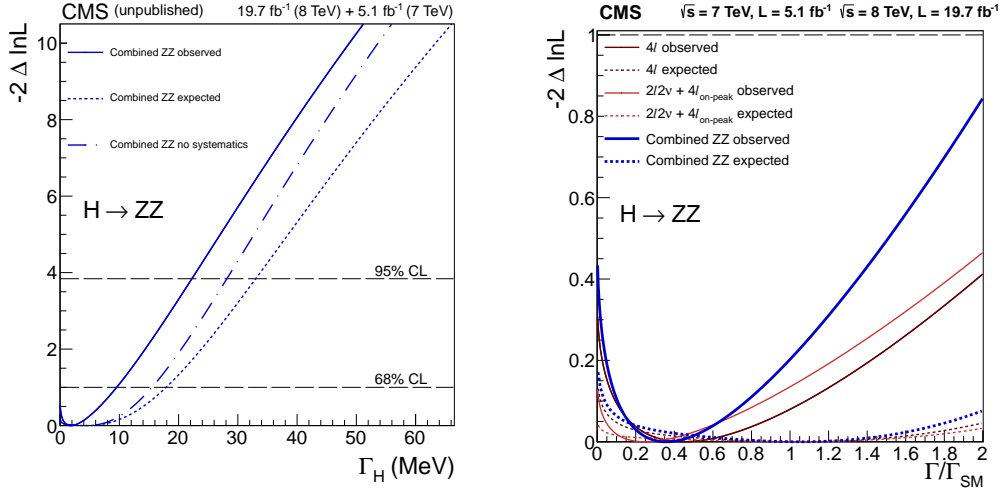


Figure 5.17 – Combined fit results for 4ℓ and $2\ell 2\nu$ analysis of [74] with and without systematic uncertainties (left). Zoom of the fit results for 4ℓ and $2\ell 2\nu$ analysis and the combined result with all systematic uncertainties included (right). The results corresponds to the 7 and 8 TeV datasets for 4ℓ and the 8 TeV dataset only for $2\ell 2\nu$.

- there is no contribution from BSM physics in the background

The first assumption doesn't bring any model dependency. Indeed, the assumption of narrow-width resonance is equivalent to the following condition:

$$(m_H \Gamma_H)^2 \ll (m_{4\ell}^2 - m_H^2)^2, \quad (5.20)$$

which in turn is equivalent to the condition $\Gamma_H \ll 2(m_{4\ell} - m_H)$. Considering $\Delta m = m_{4\ell} - m_H = 5$ GeV we end up with $\Gamma_H \ll 10$ GeV clause, which is well consistent with the direct limits on the Higgs boson width observed with the CMS experiment.

The second assumption is motivated by the fact that the signal strength at the peak region is very close to the SM prediction. However, this brings some model dependency because of existence of models which predict new particles which can bring non-negligible contribution in the off-peak region while keeping the on-peak cross-section unchanged. A possible example of such particle is heavy new physics colored state. The same arguments could be applied to the third bullet.

Finally, we discuss the interpretation of the results. We measure the signal strength μ in two parts of the phase space, on-shell ($\propto (g_{ggH} \times g_{HZZ} / \Gamma_H)^2$) and off-shell ($\propto (g_{ggH} \times g_{HZZ})$), and extract the limit on the Higgs boson width from the ratio of these two measurements. Since we assume no modification of the Higgs boson production at high mass, the only possible concern is the modification of the HZZ coupling due to extra terms in the Lagrangian. However the latter could only make the limit tighter and hence is not a needed assumption for the validity

of the width limit.

Summarizing the above, we can say that the model-dependence of the width limit is low and the assumptions are well motivated by the experimental data. This analysis doesn't require any constraints on the Higgs boson couplings and is valid for many of the BSM scenarios.

Looking forward for the perspectives of this analysis with the data of the LHC Run II, we can say that we will come closer to the nominal SM Higgs boson total width value. At the 13 TeV center-of-mass energy the expected tail/peak cross-sections ratio is ~ 2 times higher than at the 8 TeV. However, a very challenging task we foresee is the determination of the systematic uncertainties. Besides the higher instrumental uncertainties due to higher luminosity, the theoretical uncertainties should be also revisited. We will need full determination at next-to-next-to-leading order of the $gg \rightarrow ZZ$ continuum differential cross section. The very preliminary studies predict that we will be dominated by systematic uncertainties with about the same integrated luminosity as we have now. Nevertheless, the future work on reducing the systematic uncertainties may allow us to come quite close to the SM Higgs boson width value.

Conclusion and Outlook

The LHC Run I period went extremely well and delivered probably the most important achievement of the High Energy Physics in the recent years: the discovery of a new boson, candidating to be the Higgs boson. This was also a central event in the scope of the presented thesis work.

Prior to the announcement of a new boson observation in July 2012 I worked on improving the electron momentum determination. The results allowed to select a new population of electrons with mismeasured momentum in the tracker (about 2% of the total number of electrons in case of flat- p_T simulated sample) and to improve the energy scale and resolution uncertainties. The classification of electrons is subsequently used in the combination of the ECAL and tracker measurements and in the evaluation of the energy scale corrections. The ECAL-tracker combination algorithm was used to produce the results presented during the ICHEP 2012 and Moriond 2013 conferences. It was later replaced by a more sophisticated algorithm based on a multivariate regression. The energy scale corrections are time-dependent and have been evaluated for each data taking period. I developed a special software module which provides an interface for the energy scale correction implementation for Higgs boson analyses, including backward compatibility for the analyses which do not need the most precise momentum determination. Summarizing my work on the electron reconstruction I would like to underline that the resulting effective di-electron energy resolution for the electrons originated from $Z \rightarrow ee$ events varies from 2.7% (for the two well-measured electrons in the ECAL barrel) to 4.4% (for the two poorly-measured electrons in the ECAL endcaps) and the energy scale control is very good with an uncertainty on the electron energy scale below 2‰.

After the new boson discovery I contributed to the new boson mass measurement analysis. I worked on the propagation of the individual per-lepton uncertainties into the analysis benefiting from my expertise on the electron energy scale and resolution. I also provided the check of the error pulls compatibility as well as mass measurements cross-checks. Accurate measurements of the Higgs boson mass are extremely important in the survey of establishing the origin of the EWSB mechanism. In the Standard Model, the Higgs boson mass is the only undetermined parameter, therefore mass measurements allow us to predict the values of the other Higgs boson properties. Benefitting from the clean experimental signature of the $H \rightarrow ZZ \rightarrow 4\ell$ final state and excellent performance of electrons and muons reconstruction, we obtain a very precise mass measurement of the new resonance: $m_H = 125.6 \pm 0.4(stat) \pm$

0.2(*syst*) GeV, which is dominated by the statistical uncertainty.

Another very important characteristic of the Higgs boson is its total decay width. Given the measured Higgs boson mass, the Standard Model predicts its width to be very small, $\Gamma_H \simeq 4$ MeV. This magnitude is about three orders lower than the energy resolution we have and therefore it is impossible to provide precise direct measurements of the Higgs boson width. Nevertheless we can put very tight constraints on the Higgs boson width in an indirect way. The method used, which explores the off-shell Higgs boson production, was proposed in summer 2013. Following this method we can put bounds on the Higgs boson width by measuring the ratio of cross sections in the off-shell and on-shell regions. I was among the leading contributors to this analysis. The observed upper limit is 22 MeV at 95% CL which is very close to the Standard Model value. Such tight constraint on the width was not anticipated before and is the result of a completely different approach to the analysis.

Looking forward we expect more data with the Run II of the LHC. The collision energy will be almost twice higher than at the Run I, which is extremely important for all searches and possible better understanding of the EWSB. This run also looks very promising from the point of view of the statistics, however a large amount of preparation work is needed in order to retain the efficiency and accuracy of the analysis. With the new (increased) luminosity efficient triggers as well as an improved treatment of the pile-up will be needed. On the other hand we need new calculations on the theoretical cross sections of the interesting processes in order to avoid the domination of the systematic uncertainties. In application to the Higgs width analysis we expect the ratio of the signal strength in off-shell and on-shell regions to be about twice higher. However we need improved calculations from theory, in particular for the gluon fusion signal and continuum processes including the interference between them.

Appendix

Electron Energy Scale Corrections

Table 4 – Electron energy scale corrections on top of the energy regression for barrel electrons, $|\eta| < 1$ $R_9 < 0.94$.

ECAL Region	run range	correction factor
EB $ \eta < 1$ $R_9 < 0.94$	190645 - 190781	0.9952 ± 0.0003
EB $ \eta < 1$ $R_9 < 0.94$	190782 - 191042	1.0017 ± 0.0004
EB $ \eta < 1$ $R_9 < 0.94$	191043 - 191720	0.9960 ± 0.0002
EB $ \eta < 1$ $R_9 < 0.94$	191721 - 193833	0.9951 ± 0.0002
EB $ \eta < 1$ $R_9 < 0.94$	193834 - 194116	0.9953 ± 0.0002
EB $ \eta < 1$ $R_9 < 0.94$	194117 - 194427	0.9960 ± 0.0002
EB $ \eta < 1$ $R_9 < 0.94$	194428 - 194618	0.9954 ± 0.0002
EB $ \eta < 1$ $R_9 < 0.94$	194619 - 194789	0.9957 ± 0.0002
EB $ \eta < 1$ $R_9 < 0.94$	194790 - 195111	0.9969 ± 0.0002
EB $ \eta < 1$ $R_9 < 0.94$	195112 - 195377	0.9970 ± 0.0002
EB $ \eta < 1$ $R_9 < 0.94$	195378 - 195398	0.9956 ± 0.0002
EB $ \eta < 1$ $R_9 < 0.94$	195399 - 195657	0.9967 ± 0.0002
EB $ \eta < 1$ $R_9 < 0.94$	195658 - 195918	0.9971 ± 0.0002
EB $ \eta < 1$ $R_9 < 0.94$	195919 - 196198	0.9963 ± 0.0002
EB $ \eta < 1$ $R_9 < 0.94$	196199 - 196356	0.9972 ± 0.0002
EB $ \eta < 1$ $R_9 < 0.94$	196357 - 198115	0.9962 ± 0.0002
EB $ \eta < 1$ $R_9 < 0.94$	198116 - 198940	0.9960 ± 0.0002
EB $ \eta < 1$ $R_9 < 0.94$	198941 - 199317	0.9963 ± 0.0002
EB $ \eta < 1$ $R_9 < 0.94$	199318 - 199428	0.9957 ± 0.0002
EB $ \eta < 1$ $R_9 < 0.94$	199429 - 199697	0.9960 ± 0.0002
EB $ \eta < 1$ $R_9 < 0.94$	199698 - 199832	0.9964 ± 0.0002
EB $ \eta < 1$ $R_9 < 0.94$	199833 - 199960	0.9966 ± 0.0002
EB $ \eta < 1$ $R_9 < 0.94$	199961 - 200151	0.9969 ± 0.0002
EB $ \eta < 1$ $R_9 < 0.94$	200152 - 200490	0.9965 ± 0.0002
EB $ \eta < 1$ $R_9 < 0.94$	200491 - 200991	0.9974 ± 0.0002
EB $ \eta < 1$ $R_9 < 0.94$	200992 - 201201	0.9963 ± 0.0002

EB $ \eta < 1$ $R_9 < 0.94$	201202 - 201624	0.9970 ± 0.0002
EB $ \eta < 1$ $R_9 < 0.94$	201625 - 201707	0.9971 ± 0.0002
EB $ \eta < 1$ $R_9 < 0.94$	201708 - 202059	0.9969 ± 0.0002
EB $ \eta < 1$ $R_9 < 0.94$	202060 - 202204	0.9971 ± 0.0002
EB $ \eta < 1$ $R_9 < 0.94$	202205 - 202332	0.9979 ± 0.0002
EB $ \eta < 1$ $R_9 < 0.94$	202333 - 202972	0.9974 ± 0.0002
EB $ \eta < 1$ $R_9 < 0.94$	202973 - 203002	0.9964 ± 0.0003
EB $ \eta < 1$ $R_9 < 0.94$	203853 - 204099	0.9955 ± 0.0002
EB $ \eta < 1$ $R_9 < 0.94$	204100 - 204562	0.9965 ± 0.0002
EB $ \eta < 1$ $R_9 < 0.94$	204563 - 205085	0.9959 ± 0.0002
EB $ \eta < 1$ $R_9 < 0.94$	205086 - 205310	0.9964 ± 0.0002
EB $ \eta < 1$ $R_9 < 0.94$	205311 - 205617	0.9956 ± 0.0002
EB $ \eta < 1$ $R_9 < 0.94$	205618 - 205825	0.9963 ± 0.0002
EB $ \eta < 1$ $R_9 < 0.94$	205826 - 206207	0.9976 ± 0.0002
EB $ \eta < 1$ $R_9 < 0.94$	206208 - 206389	0.9964 ± 0.0002
EB $ \eta < 1$ $R_9 < 0.94$	206390 - 206483	0.9963 ± 0.0002
EB $ \eta < 1$ $R_9 < 0.94$	206484 - 206597	0.9966 ± 0.0002
EB $ \eta < 1$ $R_9 < 0.94$	206598 - 206896	0.9955 ± 0.0002
EB $ \eta < 1$ $R_9 < 0.94$	206897 - 207220	0.9972 ± 0.0002
EB $ \eta < 1$ $R_9 < 0.94$	207221 - 207315	0.9966 ± 0.0002
EB $ \eta < 1$ $R_9 < 0.94$	207316 - 207489	0.9971 ± 0.0002
EB $ \eta < 1$ $R_9 < 0.94$	207490 - 207919	0.9966 ± 0.0002
EB $ \eta < 1$ $R_9 < 0.94$	207920 - 208351	0.9964 ± 0.0002
EB $ \eta < 1$ $R_9 < 0.94$	208352 - 208686	0.9966 ± 0.0002

Table 5 – Electron energy scale corrections on top of the energy regression for barrel electrons, $|\eta| < 1$ $R_9 > 0.94$.

ECAL Region	run range	correction factor
EB $ \eta < 1$ $R_9 > 0.94$	190645 - 190781	0.9910 ± 0.0003
EB $ \eta < 1$ $R_9 > 0.94$	190782 - 191042	0.9976 ± 0.0004
EB $ \eta < 1$ $R_9 > 0.94$	191043 - 191720	0.9919 ± 0.0002
EB $ \eta < 1$ $R_9 > 0.94$	191721 - 193833	0.9910 ± 0.0002
EB $ \eta < 1$ $R_9 > 0.94$	193834 - 194116	0.9912 ± 0.0002
EB $ \eta < 1$ $R_9 > 0.94$	194117 - 194427	0.9919 ± 0.0002
EB $ \eta < 1$ $R_9 > 0.94$	194428 - 194618	0.9913 ± 0.0002
EB $ \eta < 1$ $R_9 > 0.94$	194619 - 194789	0.9916 ± 0.0002
EB $ \eta < 1$ $R_9 > 0.94$	194790 - 195111	0.9928 ± 0.0002
EB $ \eta < 1$ $R_9 > 0.94$	195112 - 195377	0.9929 ± 0.0002
EB $ \eta < 1$ $R_9 > 0.94$	195378 - 195398	0.9914 ± 0.0002
EB $ \eta < 1$ $R_9 > 0.94$	195399 - 195657	0.9925 ± 0.0002
EB $ \eta < 1$ $R_9 > 0.94$	195658 - 195918	0.9930 ± 0.0002

EB $ \eta < 1$ $R_9 > 0.94$	195919 - 196198	0.9922 ± 0.0002
EB $ \eta < 1$ $R_9 > 0.94$	196199 - 196356	0.9931 ± 0.0002
EB $ \eta < 1$ $R_9 > 0.94$	196357 - 198115	0.9921 ± 0.0002
EB $ \eta < 1$ $R_9 > 0.94$	198116 - 198940	0.9919 ± 0.0002
EB $ \eta < 1$ $R_9 > 0.94$	198941 - 199317	0.9921 ± 0.0002
EB $ \eta < 1$ $R_9 > 0.94$	199318 - 199428	0.9916 ± 0.0002
EB $ \eta < 1$ $R_9 > 0.94$	199429 - 199697	0.9918 ± 0.0002
EB $ \eta < 1$ $R_9 > 0.94$	199698 - 199832	0.9923 ± 0.0002
EB $ \eta < 1$ $R_9 > 0.94$	199833 - 199960	0.9925 ± 0.0002
EB $ \eta < 1$ $R_9 > 0.94$	199961 - 200151	0.9928 ± 0.0002
EB $ \eta < 1$ $R_9 > 0.94$	200152 - 200490	0.9924 ± 0.0002
EB $ \eta < 1$ $R_9 > 0.94$	200491 - 200991	0.9933 ± 0.0002
EB $ \eta < 1$ $R_9 > 0.94$	200992 - 201201	0.9922 ± 0.0002
EB $ \eta < 1$ $R_9 > 0.94$	201202 - 201624	0.9929 ± 0.0002
EB $ \eta < 1$ $R_9 > 0.94$	201625 - 201707	0.9930 ± 0.0002
EB $ \eta < 1$ $R_9 > 0.94$	201708 - 202059	0.9927 ± 0.0002
EB $ \eta < 1$ $R_9 > 0.94$	202060 - 202204	0.9929 ± 0.0002
EB $ \eta < 1$ $R_9 > 0.94$	202205 - 202332	0.9938 ± 0.0002
EB $ \eta < 1$ $R_9 > 0.94$	202333 - 202972	0.9932 ± 0.0002
EB $ \eta < 1$ $R_9 > 0.94$	202973 - 203002	0.9923 ± 0.0003
EB $ \eta < 1$ $R_9 > 0.94$	203853 - 204099	0.9914 ± 0.0002
EB $ \eta < 1$ $R_9 > 0.94$	204100 - 204562	0.9923 ± 0.0002
EB $ \eta < 1$ $R_9 > 0.94$	204563 - 205085	0.9918 ± 0.0002
EB $ \eta < 1$ $R_9 > 0.94$	205086 - 205310	0.9923 ± 0.0002
EB $ \eta < 1$ $R_9 > 0.94$	205311 - 205617	0.9914 ± 0.0002
EB $ \eta < 1$ $R_9 > 0.94$	205618 - 205825	0.9921 ± 0.0002
EB $ \eta < 1$ $R_9 > 0.94$	205826 - 206207	0.9935 ± 0.0002
EB $ \eta < 1$ $R_9 > 0.94$	206208 - 206389	0.9922 ± 0.0002
EB $ \eta < 1$ $R_9 > 0.94$	206390 - 206483	0.9922 ± 0.0002
EB $ \eta < 1$ $R_9 > 0.94$	206484 - 206597	0.9925 ± 0.0002
EB $ \eta < 1$ $R_9 > 0.94$	206598 - 206896	0.9914 ± 0.0002
EB $ \eta < 1$ $R_9 > 0.94$	206897 - 207220	0.9930 ± 0.0002
EB $ \eta < 1$ $R_9 > 0.94$	207221 - 207315	0.9925 ± 0.0002
EB $ \eta < 1$ $R_9 > 0.94$	207316 - 207489	0.9930 ± 0.0002
EB $ \eta < 1$ $R_9 > 0.94$	207490 - 207919	0.9925 ± 0.0002
EB $ \eta < 1$ $R_9 > 0.94$	207920 - 208351	0.9923 ± 0.0002
EB $ \eta < 1$ $R_9 > 0.94$	208352 - 208686	0.9925 ± 0.0002

Table 6 – Electron energy scale corrections on top of the energy regression for barrel electrons, $|\eta| > 1$ $R_9 < 0.94$.

ECAL Region	run range	correction factor
-------------	-----------	-------------------

EB $ \eta > 1$ $R_9 < 0.94$	190645 - 190781	1.0021 ± 0.0014
EB $ \eta > 1$ $R_9 < 0.94$	190782 - 191042	1.0076 ± 0.0017
EB $ \eta > 1$ $R_9 < 0.94$	191043 - 191720	1.0023 ± 0.0008
EB $ \eta > 1$ $R_9 < 0.94$	191721 - 193833	1.0035 ± 0.0008
EB $ \eta > 1$ $R_9 < 0.94$	193834 - 194116	1.0013 ± 0.0008
EB $ \eta > 1$ $R_9 < 0.94$	194117 - 194427	1.0029 ± 0.0008
EB $ \eta > 1$ $R_9 < 0.94$	194428 - 194618	1.0024 ± 0.0008
EB $ \eta > 1$ $R_9 < 0.94$	194619 - 194789	1.0028 ± 0.0008
EB $ \eta > 1$ $R_9 < 0.94$	194790 - 195111	1.0054 ± 0.0008
EB $ \eta > 1$ $R_9 < 0.94$	195112 - 195377	1.0038 ± 0.0008
EB $ \eta > 1$ $R_9 < 0.94$	195378 - 195398	1.0023 ± 0.0008
EB $ \eta > 1$ $R_9 < 0.94$	195399 - 195657	1.0045 ± 0.0008
EB $ \eta > 1$ $R_9 < 0.94$	195658 - 195918	1.0051 ± 0.0008
EB $ \eta > 1$ $R_9 < 0.94$	195919 - 196198	1.0032 ± 0.0007
EB $ \eta > 1$ $R_9 < 0.94$	196199 - 196356	1.0051 ± 0.0008
EB $ \eta > 1$ $R_9 < 0.94$	196357 - 198115	1.0019 ± 0.0007
EB $ \eta > 1$ $R_9 < 0.94$	198116 - 198940	1.0024 ± 0.0007
EB $ \eta > 1$ $R_9 < 0.94$	198941 - 199317	1.0031 ± 0.0007
EB $ \eta > 1$ $R_9 < 0.94$	199318 - 199428	1.0041 ± 0.0008
EB $ \eta > 1$ $R_9 < 0.94$	199429 - 199697	1.0023 ± 0.0007
EB $ \eta > 1$ $R_9 < 0.94$	199698 - 199832	1.0035 ± 0.0008
EB $ \eta > 1$ $R_9 < 0.94$	199833 - 199960	1.0024 ± 0.0008
EB $ \eta > 1$ $R_9 < 0.94$	199961 - 200151	1.0026 ± 0.0008
EB $ \eta > 1$ $R_9 < 0.94$	200152 - 200490	1.0029 ± 0.0007
EB $ \eta > 1$ $R_9 < 0.94$	200491 - 200991	1.0029 ± 0.0008
EB $ \eta > 1$ $R_9 < 0.94$	200992 - 201201	1.0031 ± 0.0008
EB $ \eta > 1$ $R_9 < 0.94$	201202 - 201624	1.0048 ± 0.0008
EB $ \eta > 1$ $R_9 < 0.94$	201625 - 201707	1.0035 ± 0.0008
EB $ \eta > 1$ $R_9 < 0.94$	201708 - 202059	1.0034 ± 0.0008
EB $ \eta > 1$ $R_9 < 0.94$	202060 - 202204	1.0024 ± 0.0008
EB $ \eta > 1$ $R_9 < 0.94$	202205 - 202332	1.0044 ± 0.0008
EB $ \eta > 1$ $R_9 < 0.94$	202333 - 202972	1.0035 ± 0.0008
EB $ \eta > 1$ $R_9 < 0.94$	202973 - 203002	0.9999 ± 0.0011
EB $ \eta > 1$ $R_9 < 0.94$	203853 - 204099	1.0029 ± 0.0009
EB $ \eta > 1$ $R_9 < 0.94$	204100 - 204562	1.0051 ± 0.0008
EB $ \eta > 1$ $R_9 < 0.94$	204563 - 205085	1.0048 ± 0.0008
EB $ \eta > 1$ $R_9 < 0.94$	205086 - 205310	1.0044 ± 0.0008
EB $ \eta > 1$ $R_9 < 0.94$	205311 - 205617	1.0022 ± 0.0009
EB $ \eta > 1$ $R_9 < 0.94$	205618 - 205825	1.0025 ± 0.0008
EB $ \eta > 1$ $R_9 < 0.94$	205826 - 206207	1.0050 ± 0.0009
EB $ \eta > 1$ $R_9 < 0.94$	206208 - 206389	1.0041 ± 0.0009

EB $ \eta > 1$ $R_9 < 0.94$	206390 - 206483	1.0033 ± 0.0008
EB $ \eta > 1$ $R_9 < 0.94$	206484 - 206597	1.0038 ± 0.0008
EB $ \eta > 1$ $R_9 < 0.94$	206598 - 206896	1.0024 ± 0.0009
EB $ \eta > 1$ $R_9 < 0.94$	206897 - 207220	1.0031 ± 0.0009
EB $ \eta > 1$ $R_9 < 0.94$	207221 - 207315	1.0035 ± 0.0009
EB $ \eta > 1$ $R_9 < 0.94$	207316 - 207489	1.0046 ± 0.0009
EB $ \eta > 1$ $R_9 < 0.94$	207490 - 207919	1.0044 ± 0.0008
EB $ \eta > 1$ $R_9 < 0.94$	207920 - 208351	1.0028 ± 0.0009
EB $ \eta > 1$ $R_9 < 0.94$	208352 - 208686	1.0045 ± 0.0007

Table 7 – Electron energy scale corrections on top of the energy regression for barrel electrons, $|\eta| > 1$ $R_9 > 0.94$.

ECAL Region	run range	correction factor
EB $ \eta > 1$ $R_9 > 0.94$	190645 - 190781	0.9902 ± 0.0015
EB $ \eta > 1$ $R_9 > 0.94$	190782 - 191042	0.9957 ± 0.0017
EB $ \eta > 1$ $R_9 > 0.94$	191043 - 191720	0.9904 ± 0.0008
EB $ \eta > 1$ $R_9 > 0.94$	191721 - 193833	0.9916 ± 0.0008
EB $ \eta > 1$ $R_9 > 0.94$	193834 - 194116	0.9894 ± 0.0008
EB $ \eta > 1$ $R_9 > 0.94$	194117 - 194427	0.9910 ± 0.0008
EB $ \eta > 1$ $R_9 > 0.94$	194428 - 194618	0.9905 ± 0.0008
EB $ \eta > 1$ $R_9 > 0.94$	194619 - 194789	0.9909 ± 0.0008
EB $ \eta > 1$ $R_9 > 0.94$	194790 - 195111	0.9935 ± 0.0009
EB $ \eta > 1$ $R_9 > 0.94$	195112 - 195377	0.9920 ± 0.0008
EB $ \eta > 1$ $R_9 > 0.94$	195378 - 195398	0.9904 ± 0.0009
EB $ \eta > 1$ $R_9 > 0.94$	195399 - 195657	0.9927 ± 0.0008
EB $ \eta > 1$ $R_9 > 0.94$	195658 - 195918	0.9933 ± 0.0009
EB $ \eta > 1$ $R_9 > 0.94$	195919 - 196198	0.9913 ± 0.0008
EB $ \eta > 1$ $R_9 > 0.94$	196199 - 196356	0.9933 ± 0.0009
EB $ \eta > 1$ $R_9 > 0.94$	196357 - 198115	0.9900 ± 0.0007
EB $ \eta > 1$ $R_9 > 0.94$	198116 - 198940	0.9905 ± 0.0008
EB $ \eta > 1$ $R_9 > 0.94$	198941 - 199317	0.9913 ± 0.0008
EB $ \eta > 1$ $R_9 > 0.94$	199318 - 199428	0.9922 ± 0.0008
EB $ \eta > 1$ $R_9 > 0.94$	199429 - 199697	0.9904 ± 0.0008
EB $ \eta > 1$ $R_9 > 0.94$	199698 - 199832	0.9916 ± 0.0008
EB $ \eta > 1$ $R_9 > 0.94$	199833 - 199960	0.9905 ± 0.0008
EB $ \eta > 1$ $R_9 > 0.94$	199961 - 200151	0.9907 ± 0.0008
EB $ \eta > 1$ $R_9 > 0.94$	200152 - 200490	0.9911 ± 0.0008
EB $ \eta > 1$ $R_9 > 0.94$	200491 - 200991	0.9910 ± 0.0008
EB $ \eta > 1$ $R_9 > 0.94$	200992 - 201201	0.9912 ± 0.0008
EB $ \eta > 1$ $R_9 > 0.94$	201202 - 201624	0.9929 ± 0.0009
EB $ \eta > 1$ $R_9 > 0.94$	201625 - 201707	0.9916 ± 0.0008

EB $ \eta > 1 R_9 > 0.94$	201708 - 202059	0.9915 ± 0.0008
EB $ \eta > 1 R_9 > 0.94$	202060 - 202204	0.9905 ± 0.0008
EB $ \eta > 1 R_9 > 0.94$	202205 - 202332	0.9925 ± 0.0008
EB $ \eta > 1 R_9 > 0.94$	202333 - 202972	0.9916 ± 0.0008
EB $ \eta > 1 R_9 > 0.94$	202973 - 203002	0.9879 ± 0.0011
EB $ \eta > 1 R_9 > 0.94$	203853 - 204099	0.9911 ± 0.0009
EB $ \eta > 1 R_9 > 0.94$	204100 - 204562	0.9932 ± 0.0009
EB $ \eta > 1 R_9 > 0.94$	204563 - 205085	0.9929 ± 0.0008
EB $ \eta > 1 R_9 > 0.94$	205086 - 205310	0.9926 ± 0.0009
EB $ \eta > 1 R_9 > 0.94$	205311 - 205617	0.9904 ± 0.0009
EB $ \eta > 1 R_9 > 0.94$	205618 - 205825	0.9906 ± 0.0008
EB $ \eta > 1 R_9 > 0.94$	205826 - 206207	0.9931 ± 0.0009
EB $ \eta > 1 R_9 > 0.94$	206208 - 206389	0.9923 ± 0.0009
EB $ \eta > 1 R_9 > 0.94$	206390 - 206483	0.9915 ± 0.0009
EB $ \eta > 1 R_9 > 0.94$	206484 - 206597	0.9919 ± 0.0009
EB $ \eta > 1 R_9 > 0.94$	206598 - 206896	0.9905 ± 0.0009
EB $ \eta > 1 R_9 > 0.94$	206897 - 207220	0.9913 ± 0.0009
EB $ \eta > 1 R_9 > 0.94$	207221 - 207315	0.9917 ± 0.0009
EB $ \eta > 1 R_9 > 0.94$	207316 - 207489	0.9928 ± 0.0009
EB $ \eta > 1 R_9 > 0.94$	207490 - 207919	0.9925 ± 0.0009
EB $ \eta > 1 R_9 > 0.94$	207920 - 208351	0.9909 ± 0.0009
EB $ \eta > 1 R_9 > 0.94$	208352 - 208686	0.9926 ± 0.0008

Table 8 – Electron energy scale corrections on top of the energy regression for endcap electrons, $|\eta| < 2$ $R_9 < 0.94$.

ECAL Region	run range	correction factor
EE $ \eta < 2 R_9 < 0.94$	190645 - 190781	0.9976 ± 0.0023
EE $ \eta < 2 R_9 < 0.94$	190782 - 191042	0.9980 ± 0.0029
EE $ \eta < 2 R_9 < 0.94$	191043 - 191720	0.9997 ± 0.0012
EE $ \eta < 2 R_9 < 0.94$	191721 - 193833	0.9993 ± 0.0012
EE $ \eta < 2 R_9 < 0.94$	193834 - 194116	0.9973 ± 0.0012
EE $ \eta < 2 R_9 < 0.94$	194117 - 194427	1.0003 ± 0.0012
EE $ \eta < 2 R_9 < 0.94$	194428 - 194618	0.9987 ± 0.0012
EE $ \eta < 2 R_9 < 0.94$	194619 - 194789	1.0007 ± 0.0012
EE $ \eta < 2 R_9 < 0.94$	194790 - 195111	1.0045 ± 0.0015
EE $ \eta < 2 R_9 < 0.94$	195112 - 195377	1.0043 ± 0.0012
EE $ \eta < 2 R_9 < 0.94$	195378 - 195398	0.9998 ± 0.0012
EE $ \eta < 2 R_9 < 0.94$	195399 - 195657	1.0021 ± 0.0012
EE $ \eta < 2 R_9 < 0.94$	195658 - 195918	1.0023 ± 0.0014
EE $ \eta < 2 R_9 < 0.94$	195919 - 196198	1.0030 ± 0.0012
EE $ \eta < 2 R_9 < 0.94$	196199 - 196356	1.0015 ± 0.0014

EE $ \eta < 2$ $R_9 < 0.94$	196357 - 198115	0.9984 ± 0.0010
EE $ \eta < 2$ $R_9 < 0.94$	198116 - 198940	1.0025 ± 0.0011
EE $ \eta < 2$ $R_9 < 0.94$	198941 - 199317	0.9990 ± 0.0011
EE $ \eta < 2$ $R_9 < 0.94$	199318 - 199428	1.0015 ± 0.0014
EE $ \eta < 2$ $R_9 < 0.94$	199429 - 199697	0.9978 ± 0.0011
EE $ \eta < 2$ $R_9 < 0.94$	199698 - 199832	0.9997 ± 0.0014
EE $ \eta < 2$ $R_9 < 0.94$	199833 - 199960	1.0017 ± 0.0012
EE $ \eta < 2$ $R_9 < 0.94$	199961 - 200151	0.9986 ± 0.0014
EE $ \eta < 2$ $R_9 < 0.94$	200152 - 200490	1.0009 ± 0.0012
EE $ \eta < 2$ $R_9 < 0.94$	200491 - 200991	1.0017 ± 0.0012
EE $ \eta < 2$ $R_9 < 0.94$	200992 - 201201	0.9961 ± 0.0011
EE $ \eta < 2$ $R_9 < 0.94$	201202 - 201624	1.0001 ± 0.0014
EE $ \eta < 2$ $R_9 < 0.94$	201625 - 201707	1.0004 ± 0.0014
EE $ \eta < 2$ $R_9 < 0.94$	201708 - 202059	1.0008 ± 0.0012
EE $ \eta < 2$ $R_9 < 0.94$	202060 - 202204	0.9995 ± 0.0012
EE $ \eta < 2$ $R_9 < 0.94$	202205 - 202332	1.0030 ± 0.0014
EE $ \eta < 2$ $R_9 < 0.94$	202333 - 202972	1.0003 ± 0.0014
EE $ \eta < 2$ $R_9 < 0.94$	202973 - 203002	0.9999 ± 0.0017
EE $ \eta < 2$ $R_9 < 0.94$	203853 - 204099	0.9982 ± 0.0014
EE $ \eta < 2$ $R_9 < 0.94$	204100 - 204562	1.0015 ± 0.0015
EE $ \eta < 2$ $R_9 < 0.94$	204563 - 205085	1.0023 ± 0.0012
EE $ \eta < 2$ $R_9 < 0.94$	205086 - 205310	1.0030 ± 0.0014
EE $ \eta < 2$ $R_9 < 0.94$	205311 - 205617	0.9994 ± 0.0014
EE $ \eta < 2$ $R_9 < 0.94$	205618 - 205825	1.0019 ± 0.0014
EE $ \eta < 2$ $R_9 < 0.94$	205826 - 206207	1.0043 ± 0.0014
EE $ \eta < 2$ $R_9 < 0.94$	206208 - 206389	0.9970 ± 0.0014
EE $ \eta < 2$ $R_9 < 0.94$	206390 - 206483	1.0033 ± 0.0014
EE $ \eta < 2$ $R_9 < 0.94$	206484 - 206597	1.0050 ± 0.0014
EE $ \eta < 2$ $R_9 < 0.94$	206598 - 206896	0.9982 ± 0.0014
EE $ \eta < 2$ $R_9 < 0.94$	206897 - 207220	0.9999 ± 0.0014
EE $ \eta < 2$ $R_9 < 0.94$	207221 - 207315	1.0013 ± 0.0014
EE $ \eta < 2$ $R_9 < 0.94$	207316 - 207489	1.0032 ± 0.0014
EE $ \eta < 2$ $R_9 < 0.94$	207490 - 207919	1.0013 ± 0.0012
EE $ \eta < 2$ $R_9 < 0.94$	207920 - 208351	1.0014 ± 0.0015
EE $ \eta < 2$ $R_9 < 0.94$	208352 - 208686	1.0037 ± 0.0011

Table 9 – Electron energy scale corrections on top of the energy regression for endcap electrons, $|\eta| < 2$ $R_9 > 0.94$.

ECAL Region	run range	correction factor
EE $ \eta < 2$ $R_9 > 0.94$	190645 - 190781	0.9895 ± 0.0023
EE $ \eta < 2$ $R_9 > 0.94$	190782 - 191042	0.9898 ± 0.0029

EE $ \eta < 2 R_9 > 0.94$	191043 - 191720	0.9916 ± 0.0013
EE $ \eta < 2 R_9 > 0.94$	191721 - 193833	0.9912 ± 0.0013
EE $ \eta < 2 R_9 > 0.94$	193834 - 194116	0.9892 ± 0.0013
EE $ \eta < 2 R_9 > 0.94$	194117 - 194427	0.9922 ± 0.0013
EE $ \eta < 2 R_9 > 0.94$	194428 - 194618	0.9906 ± 0.0013
EE $ \eta < 2 R_9 > 0.94$	194619 - 194789	0.9926 ± 0.0013
EE $ \eta < 2 R_9 > 0.94$	194790 - 195111	0.9964 ± 0.0015
EE $ \eta < 2 R_9 > 0.94$	195112 - 195377	0.9962 ± 0.0013
EE $ \eta < 2 R_9 > 0.94$	195378 - 195398	0.9917 ± 0.0013
EE $ \eta < 2 R_9 > 0.94$	195399 - 195657	0.9940 ± 0.0013
EE $ \eta < 2 R_9 > 0.94$	195658 - 195918	0.9942 ± 0.0014
EE $ \eta < 2 R_9 > 0.94$	195919 - 196198	0.9949 ± 0.0013
EE $ \eta < 2 R_9 > 0.94$	196199 - 196356	0.9934 ± 0.0014
EE $ \eta < 2 R_9 > 0.94$	196357 - 198115	0.9903 ± 0.0011
EE $ \eta < 2 R_9 > 0.94$	198116 - 198940	0.9945 ± 0.0012
EE $ \eta < 2 R_9 > 0.94$	198941 - 199317	0.9908 ± 0.0012
EE $ \eta < 2 R_9 > 0.94$	199318 - 199428	0.9934 ± 0.0014
EE $ \eta < 2 R_9 > 0.94$	199429 - 199697	0.9897 ± 0.0012
EE $ \eta < 2 R_9 > 0.94$	199698 - 199832	0.9916 ± 0.0014
EE $ \eta < 2 R_9 > 0.94$	199833 - 199960	0.9936 ± 0.0013
EE $ \eta < 2 R_9 > 0.94$	199961 - 200151	0.9905 ± 0.0014
EE $ \eta < 2 R_9 > 0.94$	200152 - 200490	0.9928 ± 0.0013
EE $ \eta < 2 R_9 > 0.94$	200491 - 200991	0.9936 ± 0.0013
EE $ \eta < 2 R_9 > 0.94$	200992 - 201201	0.9880 ± 0.0012
EE $ \eta < 2 R_9 > 0.94$	201202 - 201624	0.9919 ± 0.0014
EE $ \eta < 2 R_9 > 0.94$	201625 - 201707	0.9923 ± 0.0014
EE $ \eta < 2 R_9 > 0.94$	201708 - 202059	0.9927 ± 0.0013
EE $ \eta < 2 R_9 > 0.94$	202060 - 202204	0.9914 ± 0.0013
EE $ \eta < 2 R_9 > 0.94$	202205 - 202332	0.9949 ± 0.0014
EE $ \eta < 2 R_9 > 0.94$	202333 - 202972	0.9922 ± 0.0014
EE $ \eta < 2 R_9 > 0.94$	202973 - 203002	0.9918 ± 0.0017
EE $ \eta < 2 R_9 > 0.94$	203853 - 204099	0.9901 ± 0.0014
EE $ \eta < 2 R_9 > 0.94$	204100 - 204562	0.9934 ± 0.0015
EE $ \eta < 2 R_9 > 0.94$	204563 - 205085	0.9942 ± 0.0013
EE $ \eta < 2 R_9 > 0.94$	205086 - 205310	0.9949 ± 0.0014
EE $ \eta < 2 R_9 > 0.94$	205311 - 205617	0.9913 ± 0.0014
EE $ \eta < 2 R_9 > 0.94$	205618 - 205825	0.9938 ± 0.0014
EE $ \eta < 2 R_9 > 0.94$	205826 - 206207	0.9962 ± 0.0014
EE $ \eta < 2 R_9 > 0.94$	206208 - 206389	0.9889 ± 0.0014
EE $ \eta < 2 R_9 > 0.94$	206390 - 206483	0.9952 ± 0.0014
EE $ \eta < 2 R_9 > 0.94$	206484 - 206597	0.9969 ± 0.0014
EE $ \eta < 2 R_9 > 0.94$	206598 - 206896	0.9901 ± 0.0014

EE $ \eta < 2$ $R_9 > 0.94$	206897 - 207220	0.9918 ± 0.0014
EE $ \eta < 2$ $R_9 > 0.94$	207221 - 207315	0.9932 ± 0.0014
EE $ \eta < 2$ $R_9 > 0.94$	207316 - 207489	0.9951 ± 0.0014
EE $ \eta < 2$ $R_9 > 0.94$	207490 - 207919	0.9932 ± 0.0013
EE $ \eta < 2$ $R_9 > 0.94$	207920 - 208351	0.9933 ± 0.0015
EE $ \eta < 2$ $R_9 > 0.94$	208352 - 208686	0.9956 ± 0.0012

Table 10 – Electron energy scale corrections on top of the energy regression for endcap electrons, $|\eta| > 2$ $R_9 < 0.94$.

ECAL Region	run range	correction factor
EE $ \eta > 2$ $R_9 < 0.94$	190645 - 190781	1.0029 ± 0.0021
EE $ \eta > 2$ $R_9 < 0.94$	190782 - 191042	0.9954 ± 0.0020
EE $ \eta > 2$ $R_9 < 0.94$	191043 - 191720	0.9984 ± 0.0010
EE $ \eta > 2$ $R_9 < 0.94$	191721 - 193833	0.9989 ± 0.0011
EE $ \eta > 2$ $R_9 < 0.94$	193834 - 194116	0.9986 ± 0.0011
EE $ \eta > 2$ $R_9 < 0.94$	194117 - 194427	1.0012 ± 0.0011
EE $ \eta > 2$ $R_9 < 0.94$	194428 - 194618	0.9977 ± 0.0011
EE $ \eta > 2$ $R_9 < 0.94$	194619 - 194789	0.9996 ± 0.0011
EE $ \eta > 2$ $R_9 < 0.94$	194790 - 195111	1.0013 ± 0.0011
EE $ \eta > 2$ $R_9 < 0.94$	195112 - 195377	1.0030 ± 0.0011
EE $ \eta > 2$ $R_9 < 0.94$	195378 - 195398	0.9997 ± 0.0011
EE $ \eta > 2$ $R_9 < 0.94$	195399 - 195657	1.0019 ± 0.0011
EE $ \eta > 2$ $R_9 < 0.94$	195658 - 195918	1.0011 ± 0.0012
EE $ \eta > 2$ $R_9 < 0.94$	195919 - 196198	0.9999 ± 0.0010
EE $ \eta > 2$ $R_9 < 0.94$	196199 - 196356	1.0018 ± 0.0012
EE $ \eta > 2$ $R_9 < 0.94$	196357 - 198115	0.9979 ± 0.0009
EE $ \eta > 2$ $R_9 < 0.94$	198116 - 198940	1.0025 ± 0.0010
EE $ \eta > 2$ $R_9 < 0.94$	198941 - 199317	1.0006 ± 0.0011
EE $ \eta > 2$ $R_9 < 0.94$	199318 - 199428	1.0026 ± 0.0011
EE $ \eta > 2$ $R_9 < 0.94$	199429 - 199697	0.9995 ± 0.0009
EE $ \eta > 2$ $R_9 < 0.94$	199698 - 199832	1.0009 ± 0.0011
EE $ \eta > 2$ $R_9 < 0.94$	199833 - 199960	1.0026 ± 0.0011
EE $ \eta > 2$ $R_9 < 0.94$	199961 - 200151	1.0034 ± 0.0011
EE $ \eta > 2$ $R_9 < 0.94$	200152 - 200490	1.0012 ± 0.0010
EE $ \eta > 2$ $R_9 < 0.94$	200491 - 200991	1.0020 ± 0.0011
EE $ \eta > 2$ $R_9 < 0.94$	200992 - 201201	1.0031 ± 0.0010
EE $ \eta > 2$ $R_9 < 0.94$	201202 - 201624	1.0057 ± 0.0012
EE $ \eta > 2$ $R_9 < 0.94$	201625 - 201707	1.0033 ± 0.0011
EE $ \eta > 2$ $R_9 < 0.94$	201708 - 202059	1.0030 ± 0.0010
EE $ \eta > 2$ $R_9 < 0.94$	202060 - 202204	1.0038 ± 0.0011
EE $ \eta > 2$ $R_9 < 0.94$	202205 - 202332	1.0043 ± 0.0011

EE $ \eta > 2$ $R_9 < 0.94$	202333 - 202972	1.0031 ± 0.0011
EE $ \eta > 2$ $R_9 < 0.94$	202973 - 203002	1.0027 ± 0.0015
EE $ \eta > 2$ $R_9 < 0.94$	203853 - 204099	0.9987 ± 0.0011
EE $ \eta > 2$ $R_9 < 0.94$	204100 - 204562	1.0041 ± 0.0011
EE $ \eta > 2$ $R_9 < 0.94$	204563 - 205085	0.9990 ± 0.0011
EE $ \eta > 2$ $R_9 < 0.94$	205086 - 205310	1.0018 ± 0.0011
EE $ \eta > 2$ $R_9 < 0.94$	205311 - 205617	0.9981 ± 0.0011
EE $ \eta > 2$ $R_9 < 0.94$	205618 - 205825	0.9997 ± 0.0011
EE $ \eta > 2$ $R_9 < 0.94$	205826 - 206207	1.0042 ± 0.0011
EE $ \eta > 2$ $R_9 < 0.94$	206208 - 206389	0.9990 ± 0.0011
EE $ \eta > 2$ $R_9 < 0.94$	206390 - 206483	1.0033 ± 0.0011
EE $ \eta > 2$ $R_9 < 0.94$	206484 - 206597	1.0001 ± 0.0011
EE $ \eta > 2$ $R_9 < 0.94$	206598 - 206896	1.0000 ± 0.0011
EE $ \eta > 2$ $R_9 < 0.94$	206897 - 207220	1.0045 ± 0.0012
EE $ \eta > 2$ $R_9 < 0.94$	207221 - 207315	0.9994 ± 0.0011
EE $ \eta > 2$ $R_9 < 0.94$	207316 - 207489	1.0012 ± 0.0011
EE $ \eta > 2$ $R_9 < 0.94$	207490 - 207919	0.9988 ± 0.0010
EE $ \eta > 2$ $R_9 < 0.94$	207920 - 208351	1.0032 ± 0.0011
EE $ \eta > 2$ $R_9 < 0.94$	208352 - 208686	1.0026 ± 0.0009

Table 11 – Electron energy scale corrections on top of the energy regression for endcap electrons, $|\eta| > 2$ $R_9 > 0.94$.

ECAL Region	run range	correction factor
EE $ \eta > 2$ $R_9 > 0.94$	190645 - 190781	0.9928 ± 0.0021
EE $ \eta > 2$ $R_9 > 0.94$	190782 - 191042	0.9852 ± 0.0020
EE $ \eta > 2$ $R_9 > 0.94$	191043 - 191720	0.9884 ± 0.0010
EE $ \eta > 2$ $R_9 > 0.94$	191721 - 193833	0.9888 ± 0.0011
EE $ \eta > 2$ $R_9 > 0.94$	193834 - 194116	0.9886 ± 0.0011
EE $ \eta > 2$ $R_9 > 0.94$	194117 - 194427	0.9911 ± 0.0011
EE $ \eta > 2$ $R_9 > 0.94$	194428 - 194618	0.9876 ± 0.0011
EE $ \eta > 2$ $R_9 > 0.94$	194619 - 194789	0.9896 ± 0.0011
EE $ \eta > 2$ $R_9 > 0.94$	194790 - 195111	0.9913 ± 0.0011
EE $ \eta > 2$ $R_9 > 0.94$	195112 - 195377	0.9929 ± 0.0011
EE $ \eta > 2$ $R_9 > 0.94$	195378 - 195398	0.9896 ± 0.0011
EE $ \eta > 2$ $R_9 > 0.94$	195399 - 195657	0.9919 ± 0.0011
EE $ \eta > 2$ $R_9 > 0.94$	195658 - 195918	0.9911 ± 0.0012
EE $ \eta > 2$ $R_9 > 0.94$	195919 - 196198	0.9899 ± 0.0010
EE $ \eta > 2$ $R_9 > 0.94$	196199 - 196356	0.9917 ± 0.0012
EE $ \eta > 2$ $R_9 > 0.94$	196357 - 198115	0.9878 ± 0.0009
EE $ \eta > 2$ $R_9 > 0.94$	198116 - 198940	0.9924 ± 0.0010
EE $ \eta > 2$ $R_9 > 0.94$	198941 - 199317	0.9905 ± 0.0011

EE $ \eta > 2 R_9 > 0.94$	199318 - 199428	0.9926 ± 0.0011
EE $ \eta > 2 R_9 > 0.94$	199429 - 199697	0.9895 ± 0.0009
EE $ \eta > 2 R_9 > 0.94$	199698 - 199832	0.9909 ± 0.0011
EE $ \eta > 2 R_9 > 0.94$	199833 - 199960	0.9925 ± 0.0011
EE $ \eta > 2 R_9 > 0.94$	199961 - 200151	0.9934 ± 0.0011
EE $ \eta > 2 R_9 > 0.94$	200152 - 200490	0.9911 ± 0.0010
EE $ \eta > 2 R_9 > 0.94$	200491 - 200991	0.9919 ± 0.0011
EE $ \eta > 2 R_9 > 0.94$	200992 - 201201	0.9930 ± 0.0010
EE $ \eta > 2 R_9 > 0.94$	201202 - 201624	0.9957 ± 0.0012
EE $ \eta > 2 R_9 > 0.94$	201625 - 201707	0.9933 ± 0.0010
EE $ \eta > 2 R_9 > 0.94$	201708 - 202059	0.9929 ± 0.0010
EE $ \eta > 2 R_9 > 0.94$	202060 - 202204	0.9938 ± 0.0011
EE $ \eta > 2 R_9 > 0.94$	202205 - 202332	0.9943 ± 0.0011
EE $ \eta > 2 R_9 > 0.94$	202333 - 202972	0.9931 ± 0.0011
EE $ \eta > 2 R_9 > 0.94$	202973 - 203002	0.9926 ± 0.0015
EE $ \eta > 2 R_9 > 0.94$	203853 - 204099	0.9887 ± 0.0011
EE $ \eta > 2 R_9 > 0.94$	204100 - 204562	0.9941 ± 0.0011
EE $ \eta > 2 R_9 > 0.94$	204563 - 205085	0.9889 ± 0.0011
EE $ \eta > 2 R_9 > 0.94$	205086 - 205310	0.9917 ± 0.0011
EE $ \eta > 2 R_9 > 0.94$	205311 - 205617	0.9880 ± 0.0011
EE $ \eta > 2 R_9 > 0.94$	205618 - 205825	0.9897 ± 0.0011
EE $ \eta > 2 R_9 > 0.94$	205826 - 206207	0.9942 ± 0.0011
EE $ \eta > 2 R_9 > 0.94$	206208 - 206389	0.9889 ± 0.0011
EE $ \eta > 2 R_9 > 0.94$	206390 - 206483	0.9933 ± 0.0011
EE $ \eta > 2 R_9 > 0.94$	206484 - 206597	0.9901 ± 0.0011
EE $ \eta > 2 R_9 > 0.94$	206598 - 206896	0.9899 ± 0.0011
EE $ \eta > 2 R_9 > 0.94$	206897 - 207220	0.9945 ± 0.0012
EE $ \eta > 2 R_9 > 0.94$	207221 - 207315	0.9893 ± 0.0011
EE $ \eta > 2 R_9 > 0.94$	207316 - 207489	0.9912 ± 0.0011
EE $ \eta > 2 R_9 > 0.94$	207490 - 207919	0.9887 ± 0.0010
EE $ \eta > 2 R_9 > 0.94$	207920 - 208351	0.9932 ± 0.0011
EE $ \eta > 2 R_9 > 0.94$	208352 - 208686	0.9926 ± 0.0009

Table 12 – Additional smearings measured with the smearing method using the ele-tuned regression energy (new) and WP90_PU selection (90% selection efficiency, pile-up corrections applied), $E_t > 20$.

ECAL Region	σ_E/E (%) ele-tuned regression energy (new)
EB $ \eta < 1$ $R_9 > 0.94$	0.99 ± 0.03
EB $ \eta < 1$ $R_9 < 0.94$	0.68 ± 0.03
EB $ \eta > 1$ $R_9 > 0.94$	1.39 ± 0.14
EB $ \eta > 1$ $R_9 < 0.94$	2.00 ± 0.04
EE $ \eta < 2$ $R_9 < 0.94$	2.43 ± 0.04
EE $ \eta < 2$ $R_9 > 0.94$	2.58 ± 0.06
EE $ \eta > 2$ $R_9 < 0.94$	2.76 ± 0.04
EE $ \eta > 2$ $R_9 > 0.94$	2.88 ± 0.03

Bibliography

- [1] S.L. Glashow. Partial Symmetries of Weak Interactions. *Nucl.Phys.*, 22:579–588, 1961.
- [2] S. Weinberg. A model of leptons. *Phys. Rev. Lett.*, 19:1264–1266, Nov 1967.
- [3] A. Salam and J. C. Ward. Electromagnetic and weak interactions. *Phys.Lett.*, 13:168–171, 1964.
- [4] C. N. Yang and R. L. Mills. Conservation of isotopic spin and isotopic gauge invariance. *Phys. Rev.*, 96:191–195, Oct 1954.
- [5] F. Englert and R. Brout. Broken Symmetry and the Mass of Gauge Vector Mesons. *Phys.Rev.Lett.*, 13:321–323, 1964.
- [6] P. W. Higgs. Broken symmetries, massless particles and gauge fields. *Phys.Lett.*, 12:132–133, 1964.
- [7] S. Chatrchyan et al. Search for the fermiophobic model Higgs boson decaying into two photons. (CMS-PAS-HIG-12-002), 2012.
- [8] S. Chatrchyan et al. Searches for higgs bosons in pp collisions at in the context of four-generation and fermiophobic models. *Physics Letters B*, 725:36 – 59, 2013.
- [9] N. Cabibbo. Unitary Symmetry and Leptonic Decays. *Phys.Rev.Lett.*, 10:531–533, 1963.
- [10] M. Kobayashi and T. Maskawa. CP Violation in the Renormalizable Theory of Weak Interaction. *Prog.Theor.Phys.*, 49:652–657, 1973.
- [11] B. Pontecorvo. Mesonium and anti-mesonium. *Sov.Phys.JETP*, 6:429, 1957.
- [12] Z. Maki, M. Nakagawa, and S. Sakata. Remarks on the unified model of elementary particles. *Prog.Theor.Phys.*, 28:870–880, 1962.
- [13] M.A.B. Beg, C. Panagiotakopoulos, and A. Sirlin. Mass of the Higgs Boson in the Canonical Realization of the Weinberg-Salam Theory. *Phys.Rev.Lett.*, 52:883, 1984.
- [14] ALEPH, CDF, D0, DELPHI, L3, OPAL, SLD Collaborations, the LEP Electroweak Working Group, the Tevatron Electroweak Working Group, and the SLD Electroweak and Heavy

Bibliography

- Flavour Groups. Precision electroweak measurements and constraints on the Standard Model. 2010, 1012.2367.
- [15] R. Barate et al. Search for the standard model Higgs boson at LEP. *Phys.Lett.*, B565:61–75, 2003, hep-ex/0306033.
- [16] T. Aaltonen et al. Combined CDF and D0 Upper Limits on Standard Model Higgs Boson Production with up to 8.2 fb^{-1} of Data. 2011, 1103.3233.
- [17] M. Baak, M. Goebel, J. Haller, A. Hoecker, D. Ludwig, et al. Updated Status of the Global Electroweak Fit and Constraints on New Physics. *Eur.Phys.J.*, C72:2003, 2012, 1107.0975.
- [18] J. R. Ellis, M. K. Gaillard, and D. V. Nanopoulos. A Phenomenological Profile of the Higgs Boson. *Nucl.Phys.*, B106:292, 1976.
- [19] S Heinemeyer et al. Handbook of LHC Higgs Cross Sections: 3. Higgs Properties: Report of the LHC Higgs Cross Section Working Group. (arXiv:1307.1347. CERN-2013-004), 2013.
- [20] H. M. Georgi, S. L. Glashow, M. E. Machacek, and D. V. Nanopoulos. Higgs bosons from two-gluon annihilation in proton-proton collisions. *Phys. Rev. Lett.*, 40:692–694, Mar 1978.
- [21] S. Chatrchyan et al. The CMS experiment at the CERN LHC. *JINST*, 3:S08004, 2008.
- [22] S. Chatrchyan et al. Energy calibration and resolution of the cms electromagnetic calorimeter in pp collisions at $\sqrt{s} = 7 \text{ tev}$. *Journal of Instrumentation*, 8(09):P09009, 2013.
- [23] D. Futyan and C. Seez. Intercalibration of the CMS electromagnetic calorimeter crystals in ϕ using symmetry of energy deposition. *Journal of Physics G: Nuclear and Particle Physics*, 29(6):1299, 2003.
- [24] S. Chatrchyan et al. Electromagnetic calorimeter calibration with 7 TeV data. (CMS-PAS-EGM-10-003), 2010.
- [25] P. Adzic. Energy resolution of the barrel of the cms electromagnetic calorimeter. *Journal of Instrumentation*, 2(04):P04004, 2007.
- [26] G. L. Bayatian et al. *CMS Physics: Technical Design Report Volume 1: Detector Performance and Software*. Technical Design Report CMS. CERN, Geneva, 2006.
- [27] S. Chatrchyan et al. Particle-Flow Event Reconstruction in CMS and Performance for Jets, Taus, and MET. (CMS-PAS-PFT-09-001), Apr 2009.
- [28] R. Fruhwirth. Application of Kalman filtering to track and vertex fitting. *Nucl. Instrum. Meth.*, A262:444–450, 1987.
- [29] D. Stampfer, M. Regler, and R. Fruhwirth. Track fitting with energy loss. *Comput. Phys. Commun.*, 79:157–164, 1994.

-
- [30] S. Baffioni, C. Charlot, F. Ferri, D. Futyan, P. Meridiani, I. Puljak, C. Rovelli, R. Salerno, and Y. Sirois. Electron reconstruction in cms. *The European Physical Journal C*, 49(4):1099–1116, 2007.
- [31] Y. Chen et al. Electron energy reconstruction using a multivariate regression. *CMS AN*, 2012/327, 2012.
- [32] F. Beaudette et al. Electron momentum determination using boosted regression trees. *CMS AN*, 2013/209, 2013.
- [33] Pierini, M. Talk at the joint pvt/po meeting. <https://twiki.cern.ch/twiki/bin/viewauth/CMS/PdugMain>, 2011.
- [34] CMS Twiki. <https://twiki.cern.ch/twiki/bin/viewauth/CMS/ChangesEGMHLTAlgo2012>, 2012.
- [35] LHC Higgs Cross Section Working Group. Handbook of LHC Higgs Cross Sections: 1. Inclusive Observables. CERN Report CERN-2011-002, 2011, 1101.0593.
- [36] T. Sjöstrand, S. Mrenna, and P. Z. Skands. PYTHIA 6.4 Physics and Manual. *JHEP*, 05:026, 2006, hep-ph/0603175.
- [37] J. Alwall et al. MadGraph/MadEvent v4: The New Web Generation. *JHEP*, 09:028, 2007, 0706.2334.
- [38] S. Frixione, P. Nason, and C. Oleari. Matching NLO QCD computations with Parton Shower simulations: the POWHEG method. *JHEP*, 11:070, 2007, 0709.2092.
- [39] Y. Gao, A. V. Gritsan, Z. Guo, K. Melnikov, M. Schulze, et al. Spin determination of single-produced resonances at hadron colliders. *Phys.Rev.*, D81:075022, 2010, 1001.3396.
- [40] S. Bolognesi, Y. Gao, A. V. Gritsan, K. Melnikov, M. Schulze, et al. On the spin and parity of a single-produced resonance at the LHC. *Phys.Rev.*, D86:095031, 2012, 1208.4018.
- [41] Ian Anderson, Sara Bolognesi, Fabrizio Caola, Yanyan Gao, Andrei V. Gritsan, Christopher B. Martin, Kirill Melnikov, Markus Schulze, Nhan V. Tran, Andrew Whitbeck, and Yaofu Zhou. Constraining anomalous HVV interactions at proton and lepton colliders. 2013, 1309.4819.
- [42] T. Binoth, N. Kauer, and P. Mertsch. Gluon-induced QCD corrections to $pp \rightarrow ZZ \rightarrow \ell \bar{\ell} \ell' \bar{\ell}'$. In *Proceedings of the XVI Int. Workshop on Deep-Inelastic Scattering and Related Topics (DIS'07)*, 2008, 0807.0024.
- [43] J. Campbell, K. Ellis, C. Williams. MCFM - Monte Carlo for FeMtobarn processes. <http://mcfm.fnal.gov/>. 2011.
- [44] G. Aad et al. Measurement of hard double-parton interactions in $W(\rightarrow l\nu)+2$ jet events at $\sqrt{s}=7$ TeV with the ATLAS detector. *New J.Phys.*, 15:033038, 2013, 1301.6872.

Bibliography

- [45] H. L. Lai, M. Guzzi, J. Huston, Z. Li, P. M. Nadolsky, J. Pumplin and C. P. Yuan. New parton distributions for collider physics. *Phys.Rev.* D(82):074024, 2010.
- [46] A. D. Martin, W. J. Stirling, R. S. Thorne and G. Watt. Parton distributions for the LHC. *Eur. Phys. J.* C(63):189, 2009.
- [47] R. D. Ball, L. Del Debbio, S. Forte, A. Guffanti, J. I. Latorre, J. Rojo and M. Ubiali. A first unbiased global NLO determination of parton distributions and their uncertainties. *Nucl. Phys.* B(838):136, 2010.
- [48] S. Chatrchyan et al. Observation of a new boson at a mass of 125 GeV with the CMS experiment at the LHC. *Phys.Lett.*, B716:30–61, 2012, 1207.7235.
- [49] G. Aad et al. Observation of a new particle in the search for the Standard Model Higgs boson with the ATLAS detector at the LHC. *Phys.Lett.*, B716:1–29, 2012, 1207.7214.
- [50] R. D. Cousins. Why isn't every physicist a Bayesian? *Am.J.Phys.*, 63:398, 1995.
- [51] Yi Chen, Nhan Tran, and Roberto Vega-Morales. Scrutinizing the Higgs Signal and Background in the $2e2\mu$ Golden Channel. *JHEP*, 01:182, 2013, 1211.1959.
- [52] S. Chatrchyan et al. Study of the Mass and Spin-Parity of the Higgs Boson Candidate Via Its Decays to Z Boson Pairs. *Phys.Rev.Lett.*, 110:081803, 2013, 1212.6639.
- [53] S. Chatrchyan et al. Measurement of the properties of a Higgs boson in the four-lepton final state. *Phys.Rev.* D89:092007, 2014, 1312.5353.
- [54] V. Khachatryan et al. Observation of the diphoton decay of the Higgs boson and measurement of its properties. 2014, 1407.0558.
- [55] F. Caola and K. Melnikov. Constraining the Higgs boson width with ZZ production at the LHC. *Phys.Rev.* D88:054024, 2013, 1307.4935.
- [56] N. Kauer and G. Passarino. Inadequacy of zero-width approximation for a light Higgs boson signal. *JHEP*, 1208:116, 2012, 1206.4803.
- [57] G. Passarino. Higgs CAT. *Eur.Phys.J.*, C74, 2013, 1312.2397.
- [58] S. Chatrchyan et al. Combination of standard model Higgs boson searches and measurements of the properties of the new boson with a mass near 125 GeV. (CMS-PAS-HIG-13-005), 2013.
- [59] J. M. Campbell, R. K. Ellis, and C. Williams. Bounding the Higgs width at the LHC using full analytic results for $gg \rightarrow e^- e^+ \mu^- \mu^+$. *JHEP*, 1404:060, 2014, 1311.3589.
- [60] A. Bredenstein et al. Precise predictions for the Higgs-boson decay $H \rightarrow WW/ZZ \rightarrow 4$ leptons. *Phys. Rev. D*, 74:013004, 2006, hep-ph/0604011.

-
- [61] A. Ballestrero, A. Belhouari, G. Bevilacqua, V. Kashkan, and E. Maina. Phantom: A monte carlo event generator for six parton final states at high energy colliders. *Computer Physics Communications*, 180(3):401 – 417, 2009.
- [62] J. Alwall, R. Frederix, S. Frixione, V. Hirschi, F. Maltoni, et al. The automated computation of tree-level and next-to-leading order differential cross sections, and their matching to parton shower simulations. 2014, 1405.0301.
- [63] J. Pumplin, D.R. Stump, J. Huston, H.L. Lai, Pavel M. Nadolsky, et al. New generation of parton distributions with uncertainties from global QCD analysis. *JHEP*, 0207:012, 2002, hep-ph/0201195.
- [64] S. Chatrchyan et al. Performance of CMS muon reconstruction in pp collision events at $\sqrt{s} = 7$ TeV. *JINST*, 7:P10002, 2012, 1206.4071.
- [65] CMS Collaboration. Electron reconstruction and identification at $\sqrt{s} = 7$ tev. *CMS Physics Analysis Summary*, CMS-PAS-EGM-10-004, 2010.
- [66] M. Bonvini, F. Caola, S. Forte, K. Melnikov, and G. Ridolfi. Signal-background interference effects for $gg \rightarrow h \rightarrow w^+ w^-$ beyond leading order. *Phys. Rev. D*, 88:034032, Aug 2013.
- [67] P. Bolzoni et al. Higgs production via vector-boson fusion at NNLO in QCD. *Phys. Rev. Lett.*, 105:011801, 2010, 1003.4451.
- [68] LHC Higgs Cross Section Working Group. Handbook of LHC Higgs Cross Sections: 3. Higgs Properties. (CERN-2013-004), 2013, 1307.1347.
- [69] J. Baglio, L. D. Ninh, and M. M. Weber. Massive gauge boson pair production at the lhc: A next-to-leading order story. *Phys. Rev. D*, 88:113005, Dec 2013.
- [70] A. Bierweiler, T. Kasprzik, and . H. Kühn. Vector-boson pair production at the lhc to $\mathcal{O}(\alpha^3)$ accuracy. *Journal of High Energy Physics*, 2013(12), 2013.
- [71] S. Gieseke, T. Kasprzik, and . H. Kühn. Vector-boson pair production and electroweak corrections in HERWIG++. (arXiv:1401.3964), Jan 2014. Comments: 30 pages, 15 figures.
- [72] I. Anderson, S. Bolognesi, F. Caola, Y. Gao, A. V. Gritsan, et al. Constraining anomalous HVV interactions at proton and lepton colliders. *Phys.Rev.*, D89:035007, 2014, 1309.4819.
- [73] N. Amapane, I. Anderson, P. Avery, M. Bachtis, et al. Measurement of the production and decay of a higgs boson in the four-lepton final state. CMS Analysis Note AN-2013-108-v9, 2013.
- [74] D. Benedetti, D. Bortoletto, C. Caillol, G. Cerminati, et al. Bounding the higgs width using $zz \rightarrow \ell\ell\nu\nu$ events with high missing transverse energy. CMS Analysis Note AN-2013-411-v6, 2014.